Microwave-assisted Synthesis and Processing of Transparent Conducting Oxides and Thin Film Fabrication by Aerosol Assisted Deposition

By

D. S. Y. Jayathilake

A Doctoral Thesis Submitted in Partial Fulfilment of the Requirements for the Award of Doctor of Philosophy of Loughborough University

December 2017

Department of Chemistry
Loughborough University

EPSRC
Engineering and Physical Sciences Research Council

Acknowledgements:

I would like to express my gratitude to my supervisors Prof Upul Wijayantha and Dr Darren Southee for the continuous academic support of my project in addition to a wealth of guidance and encouragement given to me. I would also like to thank the United Kingdom Research Council (UKRC), for funding this work, without which it would not have been possible.

My PhD has been a wonderful experience thanks to all the members of the Energy Research Laboratory, especially, Dr Jagdeep Sagu, Dr Andrew McInnes, Dr Paul Brack, Jake Walls, Linda Shao, Diana Mehta and all the other members. You all have made me feel at home and part of a family and it has been great to work alongside all of you. Special thanks go to Jagdeep for the amazing support he has given me over the years and for being a wonderful friend. I would also like to give a big thanks to Andrew for proof-reading this thesis and his helpful comments. I would also like to thank Dr Shaghayegh Ghanizadeh, Dr Patrick Isherwood and Harminder Cheema for their kind help given during my studies.

I would like to give a very special thanks to my loving parents for their many sacrifices that have allowed me to build the life I have now. They are my pillars of success. I would also like to express my love and thanks to my mother and father-in-laws, for their kind help, guidance and encouragement during my postgraduate studies. I also really appreciate the loving support given to me by my two sister-in-laws and brother-in-laws, throughout my studies. Last but not least, a special thanks to my baby boy Shavin, who has brought light to my life and who has given me extra strength and motivation to get things done and also my loving thanks to my dearest husband Nirmal Peiris, for all of his endless care, continuous support and encouragement over the years. I can say for sure that I would not have got through this journey without him. He is my world and I dedicate this thesis to him.

Table of Contents

List of Figures

List of Tables

Abstract

Transparent conducting oxides (TCOs) have become an integral part of modern life through their essential role in touchscreen technology. The growing demand for cheap and superior transparent conducting layers, primarily driven by the smart phone market, has led to renewed efforts to develop novel TCOs. Currently, the most widely used material for transparent conducting applications is Sn-doped indium oxide (ITO), which has outstanding optical and electrical properties. This material is expensive though, due to the extensive use of In, and efforts to develop new low-cost transparent conducting oxides (TCO) have become increasingly important. Similarly attempts to reduce the cost of the fabrication and post-sintering steps used in making doped metal oxide thin films through innovative technologies have gained a lot of attention. With these points in mind, this research project has focused on the development of a novel low-cost aerosol assisted physical deposition method for TCO thin film fabrication and the development of new highly conducting materials to replace the expensive ITO for TCO applications.

In this study, a new and simple aerosol assisted vapour deposition technique (i.e AACT) is developed to fabricate TCO films using TCO nanoparticle suspensions. Firstly, to test the validity of the method, ITO thin films are fabricated on float glass substrates from a nanoparticle suspension. The influence of the deposition parameters on the structural and opto-electronic properties of the thin films are investigated to understand the intricacies of the process.

In order to investigate the fabrication of replacement materials for ITO, a range of doped zinc oxide powders are synthesised and processed using microwave radiation. Nominally, Al doped ZnO (AZO), Ga doped ZnO (GZO), Si doped ZnO (SZO), Cu doped ZnO (CZO) and Mn doped ZnO (MZO) singly doped ZnO powders are all investigated to determine the best metal dopants for transparent conducting ZnO. AZO and GZO pellets are found to present the best electrical conductivity for the singly doped microwave fabricated powders with values of 4.4×10^{-3} and 4.3×10^{-3} Ω.cm achieved reproducibly.

In an effort to further improve the properties of ZnO, co-doping experiments, utilising the two best dopants from the previous work (i.e. Al and Ga) is investigated. ZnO structures that are co-doped with Al and Ga (AGZO) are found to exhibit significantly

enhanced electrical properties than the singly doped powders. Typically, electrical conductivity value of 5.6 x 10^{-4} Ω.cm is obtained for AGZO pellets, which is an order of magnitude better than the previously fabricated materials.

Finally, the best AZO, GZO and AGZO materials are utilised to fabricate thin films using the previously verified AACT technique. Further investigations into the opto-electrical properties of the resulting thin films is presented prior to the utilisation of the best films in a practical application. Transparent heaters are fabricated using the best AGZO thin films, which are capable of reaching a mean temperature of 132.3 ˚C after applying a voltage of 18 V for 10 min. This work highlights the potential for using highly conducting AGZO, particularly fabricated by the microwave synthesis route, as a potential alternative for ITO in a wide variety of applications. The research also highlights the advantages of using microwaves in the thermal processing of TCO materials which significantly reduces the energy impact of the production process.

Chapter 1

Introduction

In the fast growing electronics market, transparent conducting oxides (TCOs) have become essential components in a large number of modern devices including touch screens, portable electronics, flexible electronics, optics, biochemical/environmental sensors, transparent heaters, multifunctional windows and solar cells.[1] The demand for all of these technologies is continuously increasing in the developed world.[2] The heavy use of TCOs in modern applications, the high cost associated with the current TCO materials and the potential opportunities for future applications has stimulated intense research interest over the diverse transparent conductor field and their electrical properties, as shown in figure 1a.

Transparent conducting oxides are metal oxides with high optical transmittance and high electrical conductivity.[3] They are also referred to as wide-bandgap oxide semiconductors (band gap > 3.2 eV). These materials have high optical transmission at visible wavelengths (400 - 700 nm) and electrical conductivity close to that of metals, which is often induced by doping with other elements. They also reflect the near infrared and infrared (i.e., heat) wavelengths.[4] Since the bandgaps of these materials lie in the ultraviolet wavelength region they do not absorb visible light, so they appear to be transparent to the human eye. These unique properties make TCOs widely applicable in current electronics which requires optical access behind electrical circuitry.

In recent years TCOs have gained significant attention as a substitute for plasmonic device applications and low emission (low-e) glasses due to their near-infrared (NIR) reflective properties.[5,6] Recent studies demonstrated that Ar and N2 post-deposition annealing atmosphere results in a notable tailoring of the TCOs' optical and structural properties and reduces their optical losses related to Au and Ag in the NIR.[6] Furthermore, research has revealed that ZnO also can be used as an efficient NIR reflecting material by tuning ZnO particle size and morphology. Hence, doped-ZnO transparent conducting thin films can be developed for a range of optoelectronic devices including plasmonic and metamaterial devices in the NIR region.[7]

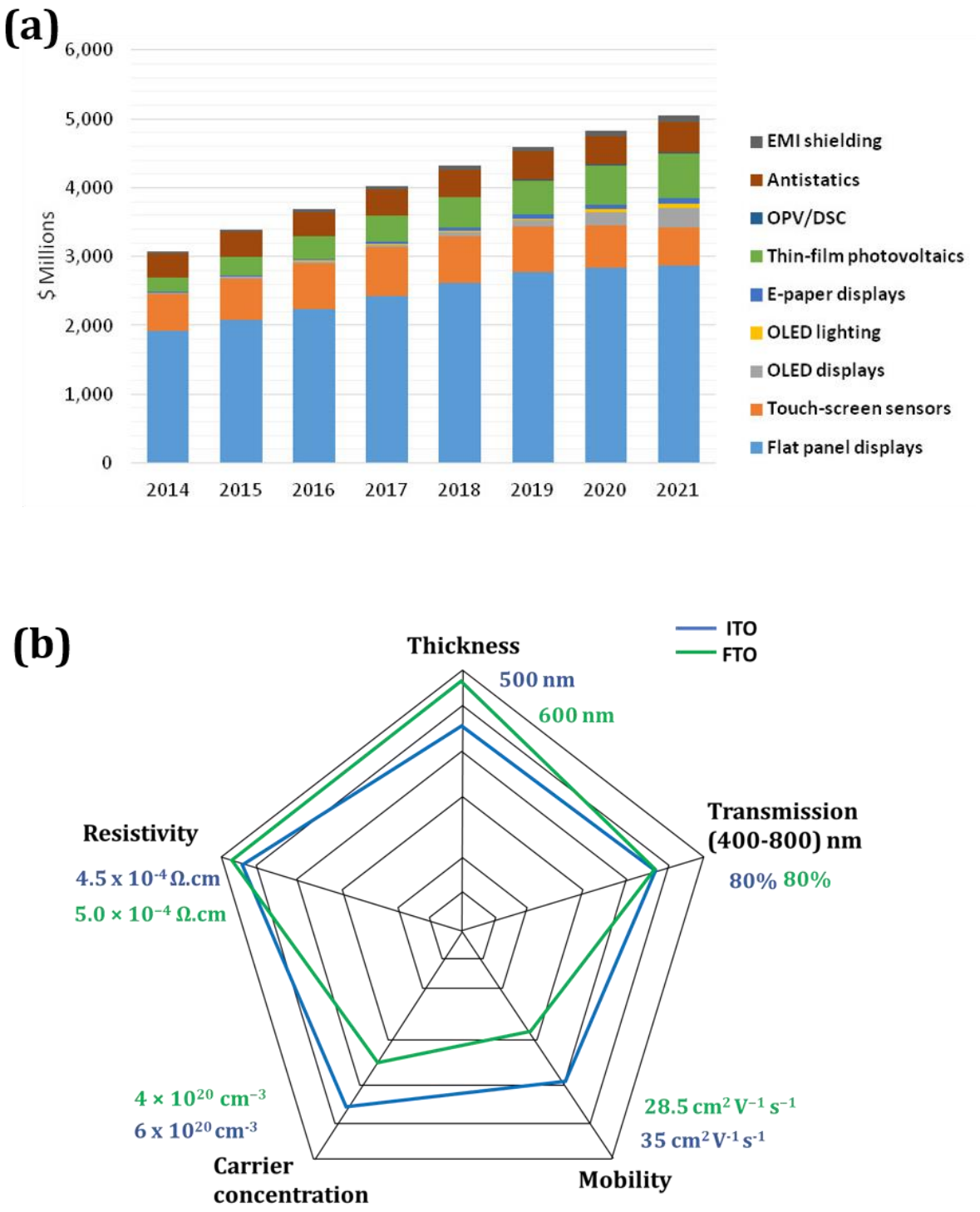

Figure 1 (a) Summary of transparent conductive materials by application and (b) the state of art values of standard TCOs.[2]

Over the last few decades the majority of TCO research has been focused on three main n-type materials: In_2O_3, SnO_2, and ZnO thin films.[8] Criteria for Choosing Transparent Conducting oxides are:

1) High electrical conductivity
2) High optical transmission at visible region
3) Thermal stability
4) Chemical durability
5) Low production costs
6) Toxicity
7) Minimum deposition temperature

Despite the intense research on the 3 listed materials, many other compounds meet some or all of these requirements for TCOs. Many binary oxides systems, primarily formed from p-block heavy metals, show good transparent conducting properties. Examples of these include SnO_2, In_2O_3, ZnO, CdO, Ga_2O_3, Tl_2O_3, PbO_2, and Sb_2O_5.[9,10] Recently it has been found that ternary and quaternary transition metal oxides such as Cd_2SnO_4, $CdSnO_3$, $CdIn_2O_4$, Zn_2SnO_4, $MgIn_2O_4$, Y-doped $CdSb_2O_6$, $ZnSnO_3$, $GaInO_3$, $Zn_2In_2O_5$, and $In_4Sn_3O_{12}$ are also good candidates for TCOs.[10] Out of this wide array, Sn-doped In_2O_3 (ITO) and F-doped SnO_2 (FTO) have become the most widely used TCOs in current industries, as they have superior electrical and optical properties. The state of art values of commercial ITO and best reported FTO are illustrated in figure 1(b).[11] However, the relative scarcity and high cost associated with indium are significant drawbacks for ITO; whilst FTO is far more cost effective, it requires higher deposition temperatures, which limit its applicability in flexible devices.[9]

Over Low cost, high durability and being non-toxic makes ZnO an attractive alternative to the commonly used ITO.[12] One of the key challenges in developing ZnO based TCOs is investigating the best metal dopants and the optimal dopant contents, in order to achieve the highest electrical conductivity. A report from Minami discussed the evolution of TCOs over the last 40 years. This indicated that unlike in SnO_2 and In_2O_3 based TCOs, efficient doping of group III elements into the ZnO structure could decrease

the resistivity significantly, potentially realising a future low cost TCO for electronic and optoelectronic applications.[13]

The electrical and optical properties of TCO thin films can be altered during the deposition and post-sintering steps, as they are frequently dependent on the film nanostructure, coverage and particle interconnectivity.[14,15] The cost of TCOs is not only dependent on the materials, but also on the film deposition process. TCO films have been fabricated through an extensive number of techniques, each of which has drawbacks.[16,17] TCO films have typically been deposited by magnetron sputtering or chemical vapour deposition methods. However these deposition techniques require a vacuum pressure ($\sim 10^{-6}$ Pa) or higher deposition temperatures (450 – 700 °C) both of which increase the energy demand and overall cost of the techniques.[18] In general, aerosol assisted deposition methods are considered to be one of the lower cost deposition techniques for TCO thin film fabrication as it does not require specially designed heated reactor lines or high vacuum systems.[19] However, the famous chemical vapour deposition technique, aerosol assisted chemical vapour deposition (AACVD) method require specially designed metal-organic precursors and high temperature heating zones. Therefore, due to the disadvantages in the current deposition techniques a great amount of attention has been committed to developing low cost and energy efficient deposition and post-sintering methods.

Significant interest has also been given to the synthesis of materials using microwave radiation as an alternative advanced material synthesis technique. The nature of the volumetric heating achieved through microwave radiation leads to faster reaction rates and rapid and uniform heating throughout the reaction mixture which is simply not possible with conventional radiant heating. Heat generation in materials by microwave energy is fundamentally different from conventional radiant heating, which relies on conduction or convection heating. In the microwave process, heat is generated from within the material itself (i.e. heat generation is due to an energy conversion process), instead of originating from external heating elements (by a heat transfer process). Due to these unique characteristics, inorganic materials synthesised by microwave irradiation often yield enhanced properties that cannot be achieved by conventional thermal processing methods.[20]

The use of microwave radiation for post-annealing of metal oxides, is a novel technological advancement and an alternative to conventional sintering.[21] This technique has recently gained particular momentum for the improvement of the chemical and physical properties of TCOs.[22,23] The improvement given by post-annealing with microwave irradiation is attributed to changes in the crystallinity and the particle necking properties and the densification of the TCO thin films. Recent examples demonstrate that microwave processing is a promising alternative to conventional sintering for thin film post treatments with better properties.[24]

The Main Objectives of this Project

Microwave assisted synthesis of novel low-cost conducting metal oxides, fabrication of thin films by a physical vapour deposition method and monitoring the influence of the deposition parameters on the structural and opto-electronic properties of the thin films to understand the intricacies of the process. Measurement of key TCO properties. Characterisation of TCO materials and deposited Films. Additionally, investigating the effect of the post-heat treatment of TCO pellets and thin films under microwave radiation is an important objective to achieve materials with similar or lower resistivity values than commercially available ITO transparent conducting films. Finally, assembly and characterization of functional TCO based devices, in order to test the practical applicability of the microwave synthesised best TCO material.

In order to achieve the above project objectives, the experiments were conducted to develop a low-cost physical deposition technique called aerosol-assisted chemical transport (AACT) (Chapter 4). Then a series of ZnO conducting materials were synthesised by doping with a range of elemental dopants using a microwave assisted synthesis method. (Chapter 5). The best doped-ZnO materials were investigated to evaluate the effect of microwave post-heat treatment on the opto-electrical properties (Chapter 6). Finally, thin films were fabricated using the best microwave synthesised materials by the AACT method (Chapter 7) and a potential application (i.e transparent heater) was demonstrated using the developed TCO material thin films. (Chapter 7).

Chapter 2

Theory and Literature review

2.1 Semiconductor Materials

A semiconducting material has a conductivity that falls in-between insulators (10^{-22} to 10^{-10} $ohm^{-1}.cm^{-1}$) and metals (10^{4} to 10^{6} $ohm^{-1}\cdot cm^{-1}$). However, the conductivity of these material can increase by increasing the temperature, impurity content or by light illumination.[25,26] The semiconductor electronic structure can be described with energy bands. The energy bands are formed by superposition of atomic orbitals of the individual atoms.[27] As a bulk material comprises of a large number of atomic orbitals, the energy difference between neighbouring orbitals is very small, hence they can be effectively considered a continuum of energy levels (i.e. a band). The highest and lowest energy levels of a band are named as the band edges. The valence band (E_{vb}) contains the highest occupied energy level and the conduction band (E_{cb}) contains the lowest unoccupied energy level. The band gap (E_g) is the energy between the upper edge of the valence band and the lower edge of the conduction band where electrons are forbidden from residing. This electronic structure is specific to the material and defines its properties. Conductivity occurs when electrons are present in the conduction band, through excitation or band overlap. For metals, the conduction and valence bands overlap, so the conduction band is readily occupied.[28] Due to the sufficiently large band gap in insulators, electrons are rarely promoted from the valence band to the conduction band. As the band gap is not as large in semiconductors, electrons can be moved into the conduction band with relative ease. (figure 2).

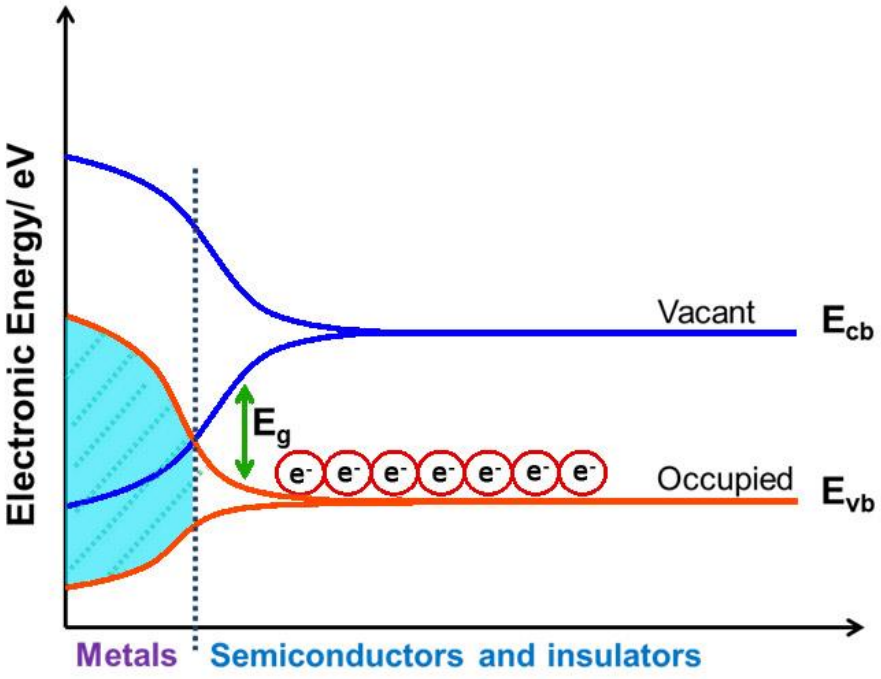

Figure 2 The electronic energies of metals, semiconductors and insulators.

An electron can be excited into the conduction band either thermally or via illumination, leaving behind a positively charged vacancy in the valence band, known as a hole. Doping is an alternate technique for permenantly creating charge carriers (i.e. electrons or holes) within a semiconductor. Doping is the incorporation of another element, which has different levels of charge into the semiconductor. The addition of a group V element (e.g., P, As, Sb) or a group III element (e.g., Al, Ga, In) into a group IV element (e.g., Si, Ge) is the most common example of doping. Doped semiconductors are called extrinsic semiconductors and they can be characterised into two types depending on their dominant charge carriers. The incorperation of group V elements into group IV elements provides occupied energy levels, which lie within the band gap close to the lower edge of the conduction band (E_D) within the group IV element. This allows facile promotion of electrons into the conduction band, as shown in figure 3(a). In this case the majority charge carriers are electrons, therefore these semiconductors are denoted as n-type semiconductors.

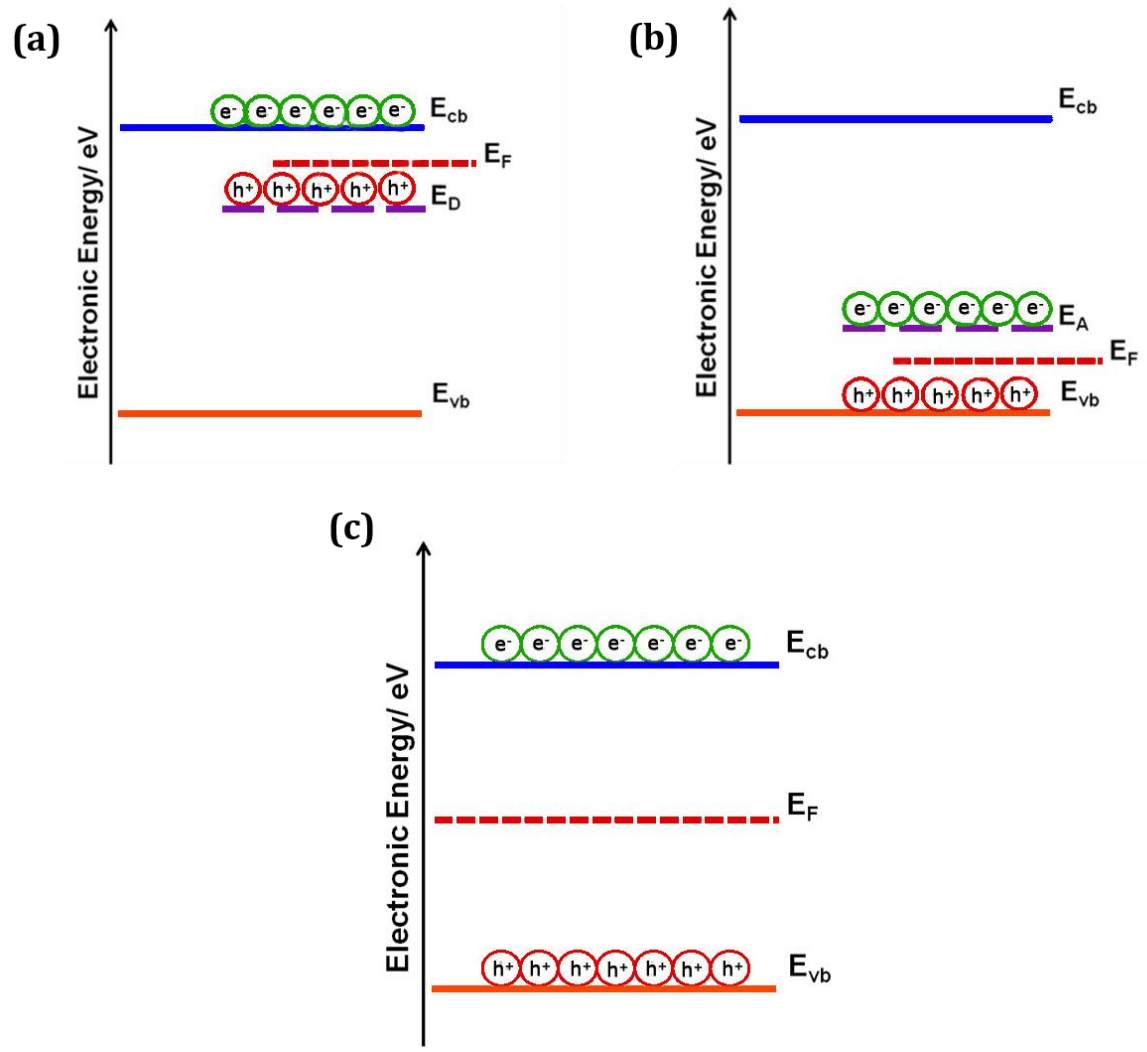

Figure 3 Schematic energy diagram of a (a) n-type semiconductor, (b) p-type semiconductor and (c) Schematic energy diagram of an intrinsic semiconductor.

The addition of group III elements into a group IV element would introduce vacant energy levels into the band gap close to the upper edge of the valence band (E_A). This leads to the formation of holes in the valence band, which become the majority charge carrier. This allows facile promotion of electrons from the valence band and such materials are known as P-type semiconductors. The figure 3(b) illustrates the schematic energy diagram of a p-type semiconductor. Un-doped semiconductors are referred to as intrinsic semiconductors and its band structure is showed in figure 3(c).

The Fermi level (E_F) is a theoretical energy level that has a 50% probability of being filled with electrons at absolute zero. Levels with lower energy than the Fermi level

would tend to be entirely filled with electrons, whilst energy levels higher than the Fermi would tend to be empty. For an intrinsic semiconductor, the Fermi level lies at the mid-point of the band gap (Figure 3(c)) whereas Fermi levels of n-type reside just below the conduction band (Figure 3(a)) and p-type semiconductors just above the valence band (Figure 3(b)).

2.2 Background of Transparent Conducting oxides

There is no doubt that TCO substrates are the basis of a broad range of optoelectronic and consumer devices. In order to be considered as a TCO substrate, the film needs to possess a low electrical resistivity (~10^{-3} - 10^{-4} Ω.cm) as well as a high optical transparency towards visible light (>80% transmittance), due to their wide band gap (>3.0 eV). In 1907, the first TCO material was found by Bädeker when he realised the electrical conducting properties of transparent CdO thin films prepared by a thermal oxidation of sputtered cadmium.[29]

In general, TCO thin films can be prepared by Pulse laser deposited (PLD),[30] chemical vapour deposition (CVD),[19,31–33] and radio frequency (RF) sputtering.[34–36] Table 1 gives an idea about different TCO films fabricated via various deposition techniques which are reported in the literature.

Table 1 An overview of different TCO materials and different deposition techniques reported in the literature.

Semiconductor	**Dopant**	**Synthesis/ deposition method**	**Resistivity**	**Reference**
ZnO	Al, Na and Al Na co-doped	Sol-gel	-	[37]
ZnO and $Zn_{1-x}Mg_xO$	Al	magnetron sputtering	Resistivity of 1 x 10^{-3} Ω.cm	[38]
NiO	Li	Combinatorial pulsed laser deposition	Resistivity of 7 x 10^{-1} Ω.cm	[39]

MgZnO	In	Pulse laser deposition	Resistivity of 10^{-2} Ω.cm	[40]
Cr_2O_3	Mg and N co-doped	Spray pyrolysis	Resistivity of 3.0 Ω.cm	[41]
$CuCrO_2$	Mg	Sol–gel	Resistivity of 0.38 Ω.cm	[42]
ZnO	Al	Solvothermal method	-	[43]
ZnO	Al	aqueous solution deposition (Al is immersed in the alkaline aqueous precursor solution)	Resistivity of 5 x 10^{-3} Ω.cm	[44]
ZnO	Al and Ga	sol–gel and spin-coating	Resistivity for Ga:ZnO is 5 x 10^{-2} Ω.cm and for Al:ZnO is 6 x 10^{-2} Ω.cm	[45]
ZnO	Al	Pulsed laser deposition	Resistivity of 8.54 x 10^{-5} Ω.cm	[30]
CuO	SnO_2	Sputtering	Resistivity of 4.3 x 10^{-2} Ω.cm	[36]
In_2O_3	Sn	Atomic layer deposition (ALD)	-	[46]
Cu_2O ($CuAlO_2$)	Al	Laser ablation (solid-state reactions of Cu_2O and Al_2O_3)	Resistivity of 1 Ω.cm	[47]
ZnO	As	magnetron sputtering and *in situ* rapid annealing	Resistivity of 6 Ω.cm	[48]
TiO_2	Nb	Sputtering	Resistivity of 2.3 x 10^{-4} Ω.cm	[49]
ZnO	In	Sputtering	Resistivity of 3 x 10^{-4} Ω.cm	[50]
$SrGeO_3$	La	Solid-state reactions	Resistivity of 2.5 x 10^{-3} Ω.cm	[51]
TiO_2 nanotubes	Nb	Electrochemical anodization	Resistivity of 6.5 × 10^{-1} Ω.cm	[52]
ZnO	Al	Sol-gel	Resistivity of 1.94x10^{-2} Ω.cm	[53]
ZnO	Al	Chemical spray	Resistivity of 1.8×10^{-2} Ω.cm	[54]
ZnO	Al	Magnetic sputtering and post annealing	Resistivity of 8.76 ×10^{-4} Ω.cm	[55]
ZnO	Al	Magnetron co-sputtering and	Resistivity of 8.30 ×10^{-4} Ω.cm	[56]

		post annealing		
TiO_2	W	Aerosol Assisted Chemical Vapor Deposition	Resistivity of 0.034 Ω.cm	[57]
In_2O_3	Sn	Microwave assisted synthesis/ solvent evaporation technique	Resistivity of pellets 1.1 $x10^{-2}$ Ω.cm and thin films 1.2$x10^{-2}$ Ω.cm	[58]
ZnO	Al	Microwave assisted nonaqueous sol-gel synthesis	Resistivity of 2.35 x 10^{-2} Ω.cm	[59]
ZnO	Si	Aerosol Assisted Chemical Vapor Deposition	Resistivity of 2.0 x 10^{-2} Ω.cm	[60]
ZnO	Al and Ga co-doped	High-throughput continuous hydrothermal flow synthesis	Resistivity of pellets 9 x 10^{-3} Ω.cm	[61]

The induction of electrical properties of TCOs can be understood by the semiconductor band theory. As already stated, for electrical conduction to occur within the semiconductor material, ground state electrons must be excited from the valence band to the conduction band minimum (CBM), across the band gap by absorbing photon energy. A wider band gap requires a higher-energy photon in order for an electron to become excited into conduction. Therefore, widening the band gap (i.e. Eg > 3.0 eV) in a material permits transparency to the visible portion of the spectrum by placing a greater separation between the valance band maximum (VBM) and CBM of the material, thus decreasing the probability of exciting an electron into conduction.[62]

TCOs have been developed by doping materials in order to facilitate the charge carrier generation within the structure. In the description of the band model, there is an important difference between the fundamental band gap such as that described above (i.e. the energy separation of the bulk E_{vb} and E_{cb}) and the optical band gap, which corresponds to the lowest-energy allowed for an optical transition. The optical band gap determines the transparency of a material which is important in TCO applications. In order to achieve n-type conducting properties, electrons are injected from a nearby defect donor level directly into the conduction band. The lattice defects in a metal oxide crystal, such as oxygen vacancies, proton interstitials and certain substitutional defects, effectively create an excess of electrons close to the defect site in n-type TCOs. If there is sufficient orbital overlap, it permits delocalisation of electrons from the defect sites

such that electronic states at the CBM become filled or in other words Fermi level shifts above the CBM (figure 4). This leads to an effect known as the Moss–Burstein shift, which effectively widens the optical band gap.

$$E_g = E_{CBM} - E_{VBM} \quad (1)$$

$$E^{opt}_g = E^{MB}_g + E_g = E_F - E_{VBM} \quad (2)$$

since the Moss–Burstein shift is:

$$E^{MB}_g = E_F - E_{CBM} \quad (3)$$

Where E_g is the fundamental energy gap separating the VBM and CBM, E^{opt}_g is the optical band gap corresponding to the smallest allowed optical transition from the VB to the CB, E^{MB}_g is the Moss–Burstein shift and E_F is the Fermi level. Thus, lattice defects in TCOs can simultaneously promote both electrical conductivity and optical transparency.

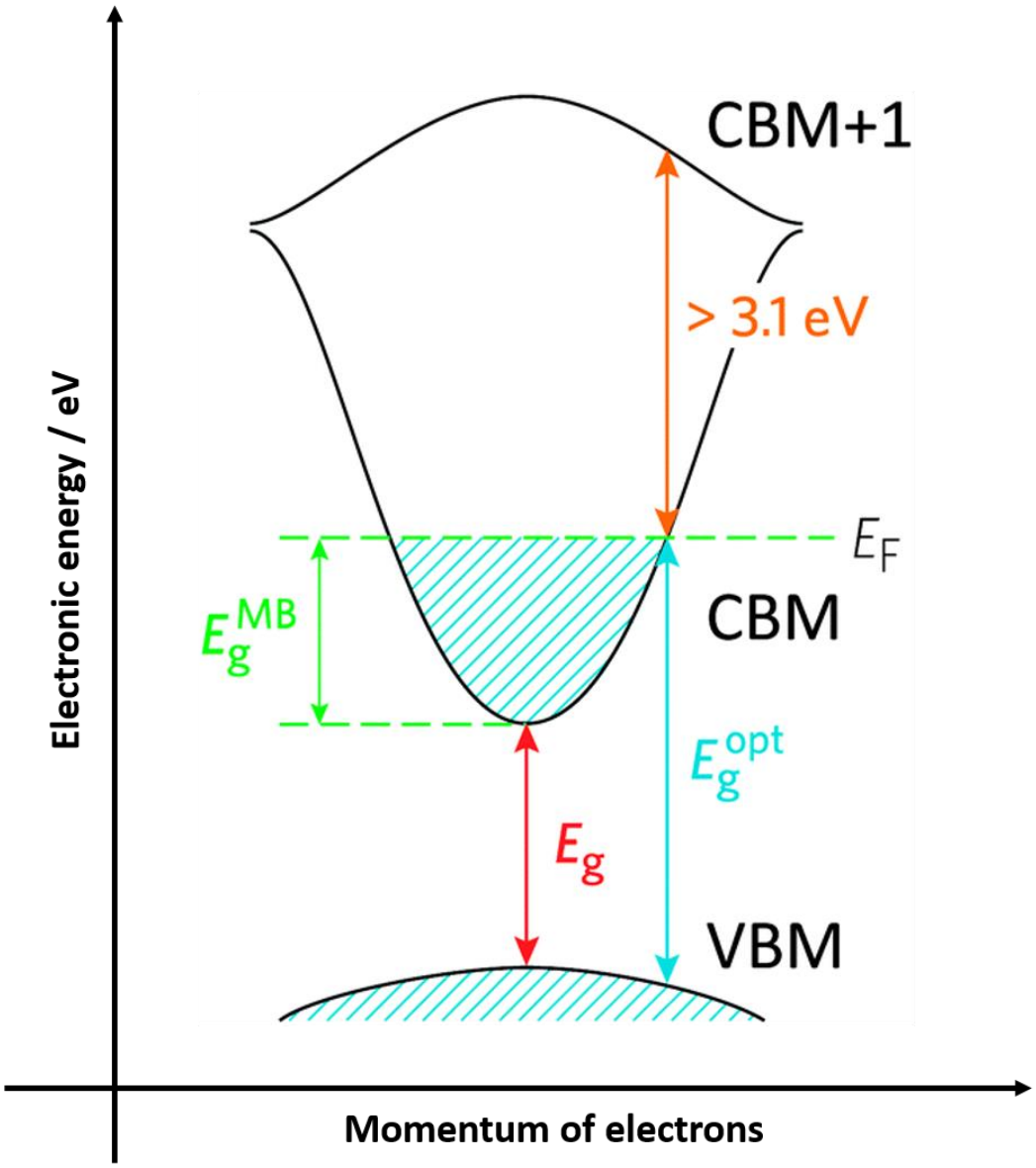

Figure 4 Diagram of the optical widening effect of the Moss–Burstein shift.[62]

The optical band gap is a key aspect of designing a TCO. However, the CBM depth or electron affinity (EA) in other words, the difference between vacuum energy and CBM which affects the 'dopability' of the TCO is also equally important in determining the conducting properties. A higher value of EA indicates greater ease of introducing charge carriers, i.e. a greater dopability.[63,64] A large separation (Eg > 3.0 eV) between the Fermi level in the conduction band and the next electronic energy level (CBM+1) helps to prevent excitation of electrons to higher states within the conduction band, which prevents undesirable optical absorption.[65]

The conductivity of a TCO is determined by the number of charge carriers and their mobility within the crystal lattice, which is inversely proportional to their effective mass. The effective mass is a quantity used to express the mass that the electrons appear to have when moving within a crystalline solid, in which their mobility is affected by their response to local forces within the crystal, expressed relative to their true mass (m_e). The local forces in TCO crystal lattice is controled by the orbital overlap between the metal cation in a host lattice and the oxygen. It has been observed that metal-oxide structures with prime s-character of the cation at the CBM are correlated with the lowest electron effective masses, suggesting that the degree of cation-oxide orbital hybridisation is a key feature in the TCO conductivity.[66] It is reported that the calculated conducton band with a lower effective mass is described as having higher dispersity and higher curvature at the band edges.[67] Therefore, a conduction band with a high curvature leads to a low electron effective mass, which in turn facilitates a high electron mobility. This helps to predict the electronic properties of prospective TCO formulations by calculating the electron effective mass using computationally modelled TCO band structures.

The electron mobility, electron density and conductivity of inorganic materials are linearly related as described in the Boltzmann equation:

$$\sigma = ne\mu \qquad (4)$$

where σ is the electrical conductivity defined in S cm^{-1}, n is the density of free charge carriers (*i.e.* electrons in an n-type TCO), e is the electronic charge and μ is the electron mobility. The electrical resistivity (ρ), expressed in Ω.cm, as below:

$$\rho = \frac{1}{\sigma} \qquad (5)$$

Figure 5 demonstrates that there are three distinct domains amongst inorganic materials regarding electrical properties: namely the semimetals (high carrier density, low electron mobility), highly conductive metals (both high carrier density and mobility) and semiconductors (low carrier density, high mobility). While the introduction of a donor level close to the conduction band permits a wide optical band gap from the VBM to the CBM, the optical absorption associated with the promotion of electrons from the CBM to higher states places an upper limit on the carrier concentration in the CBM, such

that the absorption coefficient α of the TCO is proportional to the density of free electrons *n* as found in equation 6:

$$\alpha = \sigma n \qquad (6)$$

where σ is the absorption cross-section and *n* is the carrier density.

Therefore, a compromise must be made when designing doped TCOs because of this relationship between the free electron density and the optical absorption.[19] With this limitation, ideal TCO materials need to have a high charge carrier mobility (typically μ = 50–70 $cm^2\ V^{-1}\ s^{-1}$) and a low electrical resistivity (ideally $\rho = 10^{-3}$ - 10^{-4} Ω.cm) whilst keeping the carrier concentration below 2×10^{21} cm^{-3}, to prevent undesired optical absorption.[62]

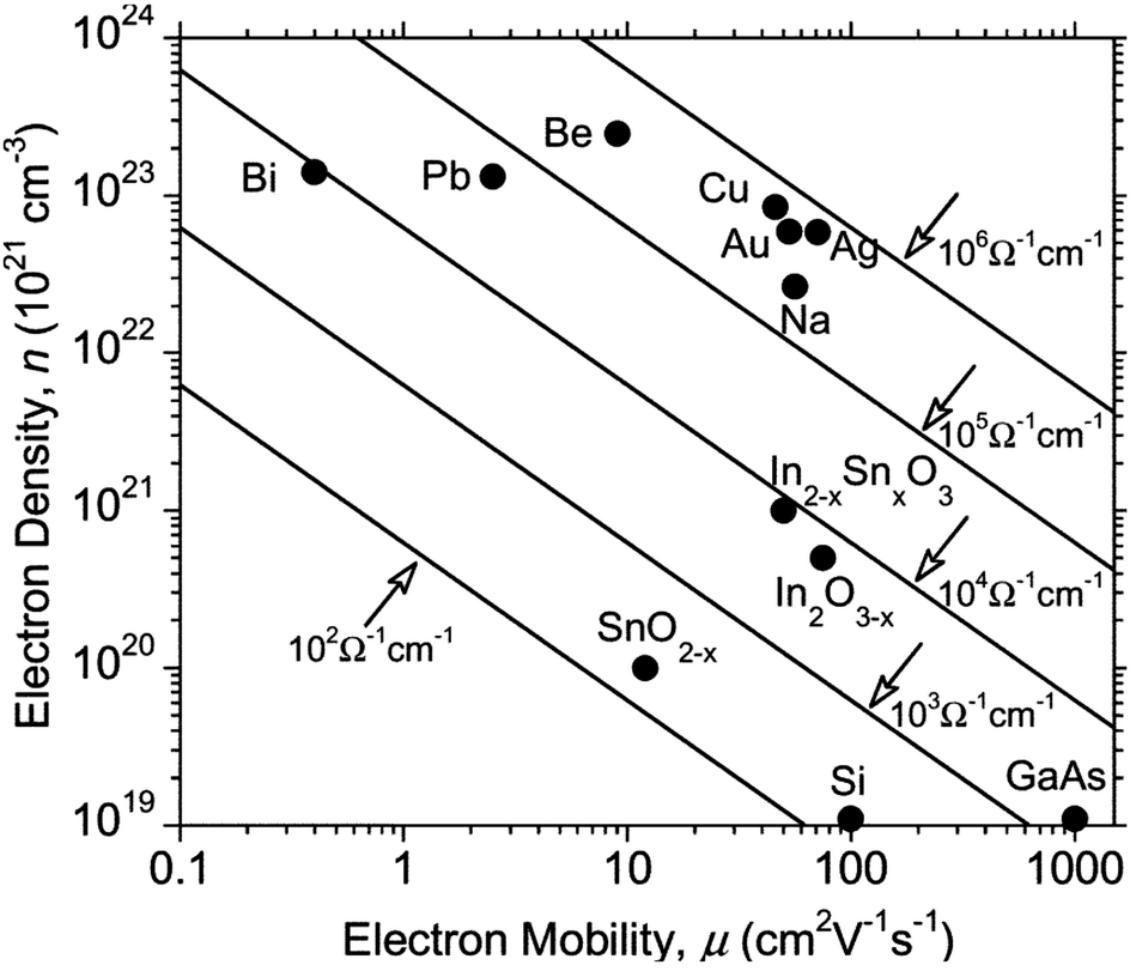

Figure 5 Boltzmann relation of electron density, mobility and hence, conductivity. The latter is displayed as straight-line contours.[67]

Similarly, increasing the dopant concentration of the TCO film also increases the density of defect (dopant) sites, hence increase the conductivity. However, this conductivity is limited by an electron scattering effect from the increased number of defects. Therefore, the film resistivity also increases with reduced mean free path length as it impacts on the free carrier relaxation time.[67] Figure 6 demonstrates the effect of film thickness on transmission and resistivity and a similar relationship can be inferred for increasing the dopant concentration.

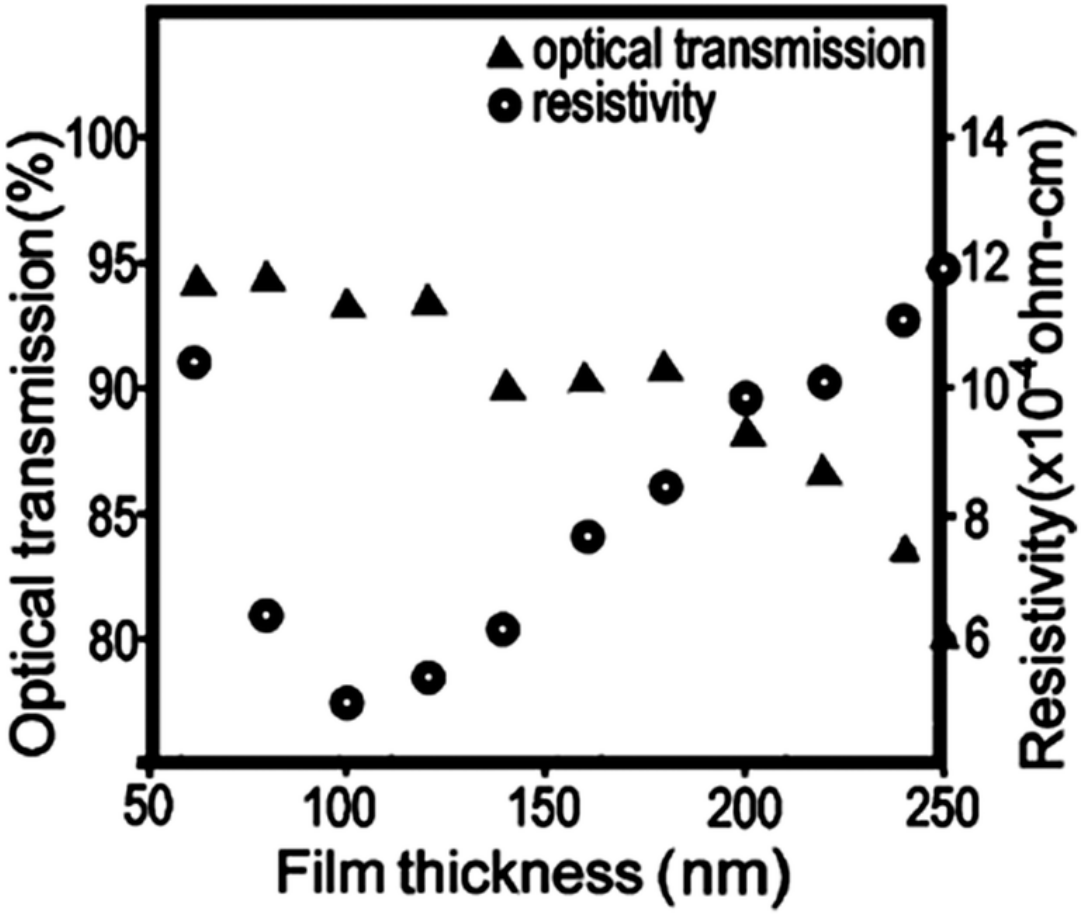

Figure 6 Effect on optical transmission and resistivity of increasing thickness of ITO film on PET substrate.[68]

2.3 Structures of ITO and ZnO

2.3.1 Structural Properties of ITO

Pure In_2O_3 can form in two crystalline structures, the bixbyite structure (bcc structure, a=10.117 Å) and the corundum structure (rhombohedron structure, a=5.487Å, c=14.510 Å) as illustrated in Figure 7(a) and Figure 7(b), respectively. ITO is also formed the same two crystalline structures. The bixbyite crystal structure is formed with a unit cell containing 40 atoms and two non-equivalent cation sites (Figure 7a). In this structure, indium cations are located in two different sixfold- coordinated sites. One quarter of the cations are located in trigonally compressed octahedra (b sites) whilst the remaining three quarters are located in highly distorted octahedral sites (d sites). Each cationic site can be described as a cube where two anion sites are empty at opposite vertices for sites b and d. These structural oxygen vacancies are located along the four (111) axes. ITO is essentially formed by substitutional doping of In_2O_3 with Sn^{4+} which replaces the In^{3+} ion in the cubic bixbyte structure of indium oxide.[69] The corundum structure in ITO is formed under high pressure (~1×10^5 MPa) or high temperature (≥ 800°C), or both.[70] However, ITO with corundum structure has some advantages compared to ITO with bixbyite structure. For instance, higher specific gravity, higher carrier density, and more stable conductivity which are favorable for TCO applications.[71] The lattice parameter of In_2O_3 varies with the Sn doping through the 10.12 Å to 10.31 Å range.

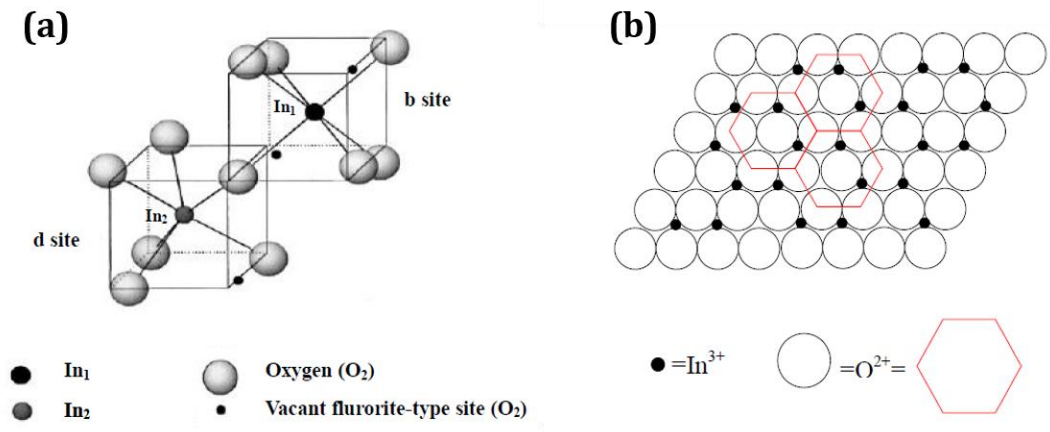

Figure 7(a) The bixbyite structure of In_2O_3 and (b) The corundum structure of In_2O_3.[70,72]

2.3.2 Opto-electrical Properties of ITO

Indium oxide is an n-type semiconductor with a wide energy gap (3.5 ~ 4.3 eV). The valence state of In_2O_3 has a direct effect on the conductivity. As Sn is doped into In_2O_3, SnO or SnO_2 is formed, where Sn has a valence state of +2 or +4, respectively. The lower valence state (Sn^{2+}) causes a net reduction in carrier concentration, as a hole is created which acts as a trap and reduces conductivity. If, on the other hand, a tetravalent cation (Sn^{4+}) is present, then electrons are donated to the conduction band, which increases the carrier concentration. Once the substitution is completed, an electron charge-compensation will be made as a result of different valences states of Sn^{4+} and In^{3+} as demonstrated below:

$$xIn_2O_3 + xSn^{4+} \rightarrow In_{2-x}^{3+}(Sn^{4+} \cdot e)_xO_3 + xIn^{3+} \quad (7)$$

This leads to a narrowing of the band gap with Sn^{4+} substitution into the In_2O_3 structure (Figure 8). The electrical conductivity of ITO increases with the increasing concentration of Sn^{4+} ions. Moreover, oxygen vacancies act as doubly ionised donors and contribute a maximum of two electrons to the electrical conductivity as shown in the below equation;[73]

$$O_0 \rightarrow V_0^{\cdot\cdot} + \frac{1}{2}O_2(g) + 2e^- \quad (8)$$

Hence, oxygen is also an important factor in controlling the electrical conductivity of ITO, which can essentially be described as $In_{2-x}Sn_xO_{3-2x}$.[74] However, due to the limited solubility of Sn in In_2O_3, only about 6–8 at.% of Sn can be incorporated into the In_2O_3 structure.[75,76]

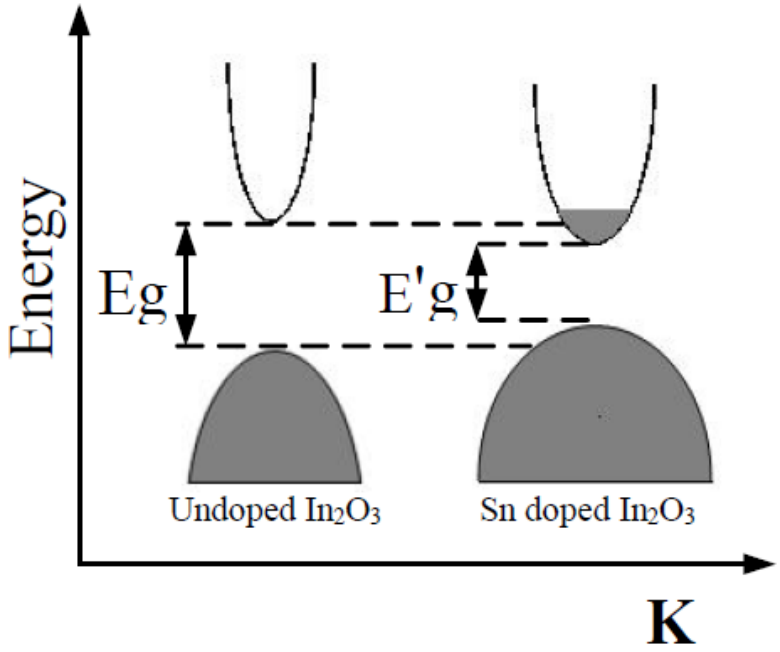

Figure 8 The energy band structure of ITO.[77]

ITO is transparent in the visible light range and reflective in the infrared spectral regions due to its wide optical energy gap.[78] An ITO film deposited by an oxygen ion-beam assisted deposition technique has been shown to display a transmittance of 85-98% in the visible region.[79] The same study showed that transmission decreased from 98% to 85% at 550 nm when the thickness was increased from 84 nm to 250 nm, due to a corresponding increase in absorption (Figure 9).

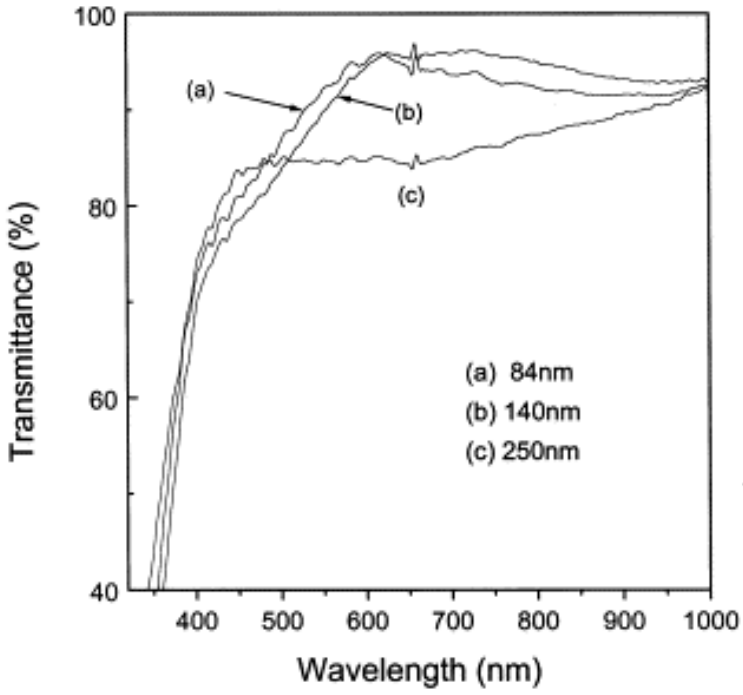

Figure 9 Variations of the optical transmittance of ITO thin films as a function of thickness.[79]

It is well-know that the optical and electronic properties of ITO films are highly dependent on the deposition parameters and methods used in the deposition. It is essential for the deposited film to contain a high density of charge carriers for it to electrically conduct. These carriers are free electrons from oxygen vacancies. High electrical conductivity is balanced against high transmittance in the visible region. Typically, the film sheet resistance should be maintained at less than 10 Ω/sq. with a visible transmittance of > 80%.[80]

2.3.3 Structural and Electrical Properties of ZnO

ZnO has been shown to be an extremely promising material for transparent conducting applications.[81] It has a wide and direct band gap in the near-UV spectral region, with a larger free-exciton binding energy and a higher electron effective mass which could give rise to high optical transparency. Also ZnO can persist excitonic emission processes at or even above room temperature, hence it is possible to prevent thermal excitation of electrons and avoid the unwanted optical absorption.[82] ZnO crystallizes in the wurtzite

structure, as shown in figure 10.[83] The properties of ZnO for semiconductor electronics have been widely studied, but the use of ZnO as a semiconductor in electronic devices has been hindered by the lack of control over its electrical conductivity.

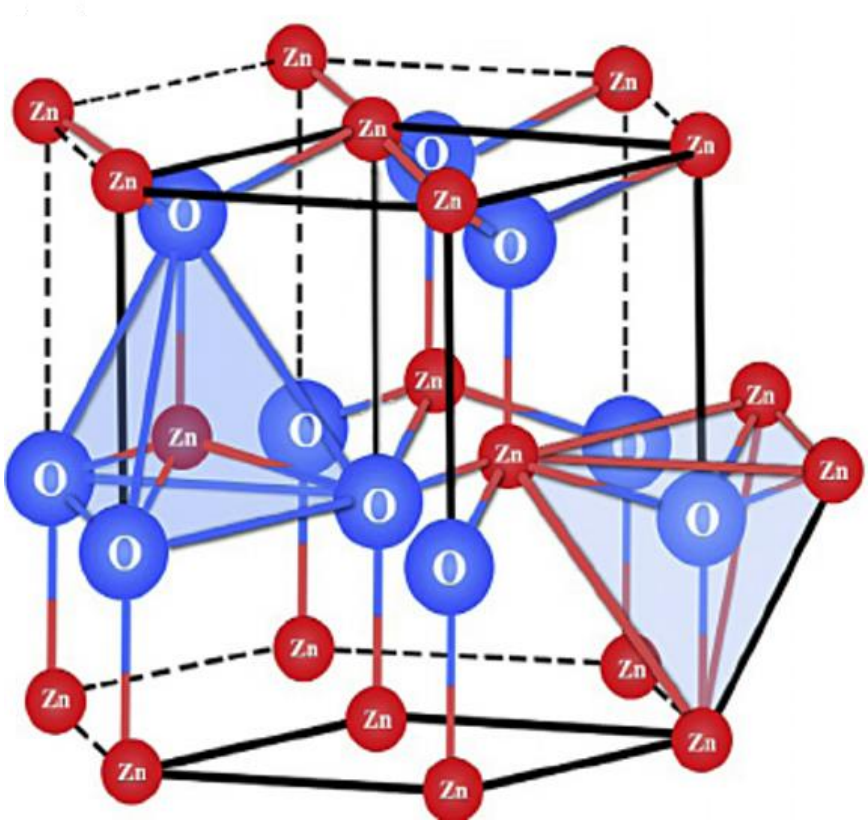

Figure 10 Hexagonal wurtzite crystal structure of ZnO.[84]

The n-type conductivity in ZnO thin films is mainly controlled by electrons generated by oxygen vacancies and charge donation.[81] However, theoretical studies, specifically first-principles calculations based on density functional theory (DFT), have also given a deeper understanding of the role of native point defects and impurities on the ZnO n-type conductivity.[82]

The native defects in the ZnO crystal lattice can influence the structure, which in turn affects the optical and electrical properties producing a naturally n-type material.[82] The structural defects of ZnO can be dependent on the atmosphere in which the material is grown as well as post synthesis annealing conditions. Therefore, characterising the

nature of defects in ZnO helps to tune the materials properties, including their conductivity.

Oxygen vacancies are the most discussed defect in ZnO, as it was once believed to be one of the main sources for the natural n-type behaviour. However, density-functionaltheory calculations disclosed that oxygen vacancies are very deep donors rather than shallow donors ("deep and shallow" in terms of the energy needed to remove an electron/hole from the trap to the valance or conduction band compared to the characteristic thermal energy kT, where k is the Boltzmann constant and T is absolute temperature) and consequently, cannot contribute to n-type conductivity.[82] Though, these deep donors can be manipulated under different annealing atmospheres (e.g. hydrogen) in order to change the electrical and optical properties.[85]

In n-type ZnO, zinc vacancies can easily form as a deep acceptor. Higher concentration of zinc vacancies are formed in oxygen rich atmospheres. Hydrogen rich atmospheres also have an effect on these zinc vacancies as the hydrogen is incorporated into the structure and passivates the charge state of the zinc vacancies. This in turn increases the n-type conductivity.[86]

Zinc interstitials carry two electrons above the conduction band minimum in order to stabilize its +2 charge state. Zinc interstitials are believed to be shallow donors because they always donate electrons to the conduction band as they have low ionization energy, but it is still unclear if it is related to sublattice defects or a zinc-interstitial complex. Zinc interstitials have shown mobility at room temperature, creating a complex with ambient nitrogen which also acts as a shallow donor and can increase the conductivity of ZnO.[82] Figure 11 illustrates main two defects Zinc oxide lattice.

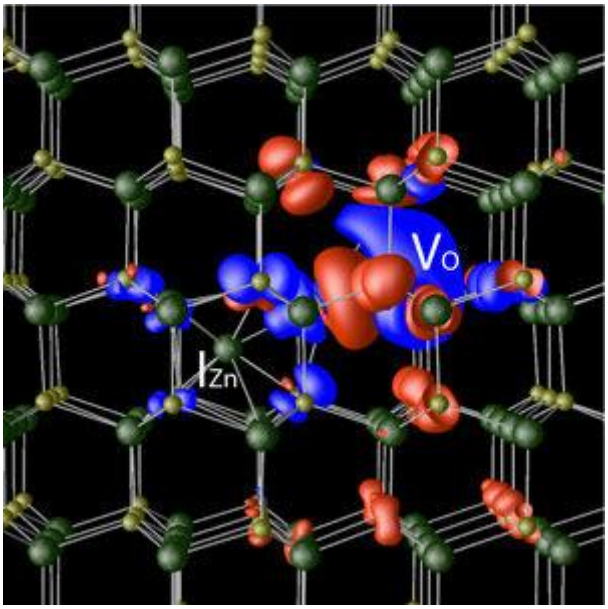

Figure 11 Zinc oxide lattice with an oxygen vacancy, V_o, and zinc interstitial, I_{Zn}, defects. These defects cause a redistribution in positive (blue) and negative (red) charges, ultimately resulting in an increase in n-type conductivity.[87]

The native defects such as zinc antisites, oxygen interstitials and oxygen antisites with higher formation energies are not expected to deliver n-type conductivity in ZnO under equilibrium conditions.[82]

2.4 Synthesis of Nanoparticles

2.4.1 General Introduction

Generally, nanoparticles are particles between 1 and 100 nm in size. They are characterized by having a large specific surface area and are widely used in fabricating functional thin films and catalysts. High performance, of thin films or catalysts, is often associated with having a large specific surface area.[88] There are several methods for preparing nanoparticles which are summarized in Figure 12. In general, two approaches can be taken in the preparation of ultrafine particles. The first is the breakdown method (top-down), which utilises an applied external force to break up a solid into smaller particles. The second is the build-up method (bottom-up), here

nanoparticles are fabricated from scratch using atoms of a gas or liquid undergoing atomic transformations or molecular condensations.[89]

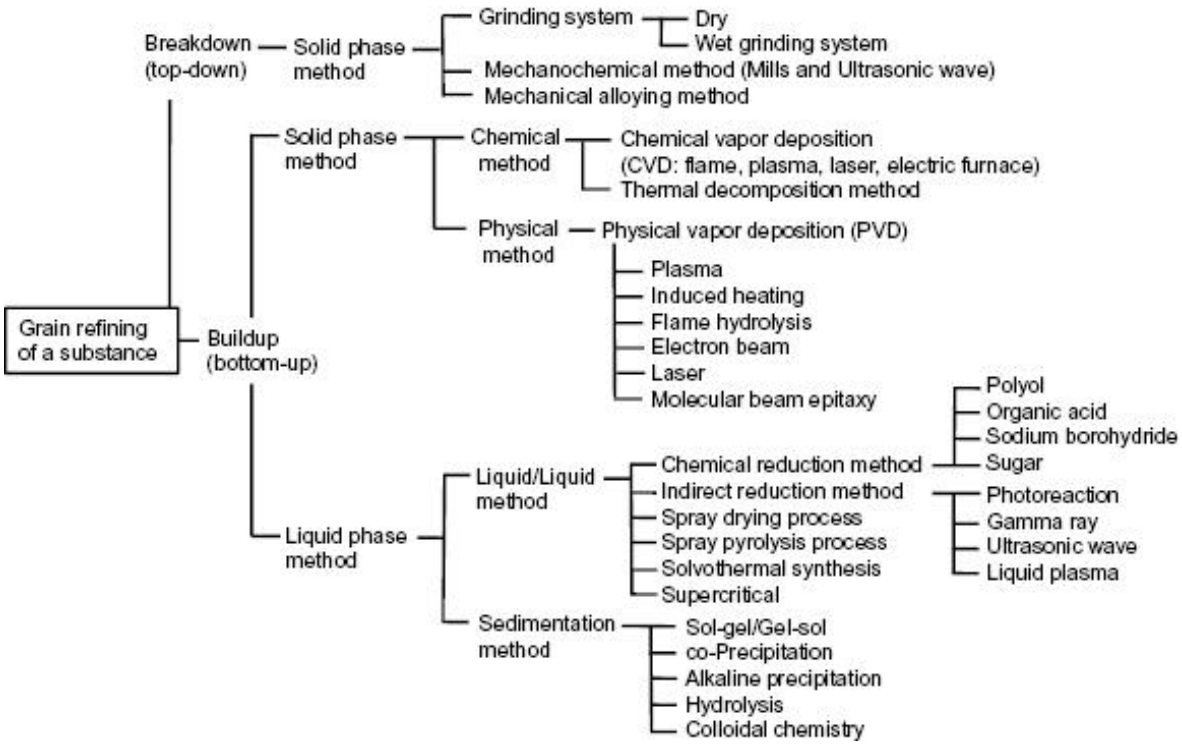

Figure 12 Typical synthetic methods for nanoparticles for the top-down and bottom-up approaches.[89]

Among the nanoparticle synthesis methods, liquid phase chemical reduction has been a widely used technique, as it is able to fine tune the shape and size of nanoparticles by using a correct reducing agent, dispersing agent, reaction time and temperature. The method is carried out by chemically reducing metal ions to their metallic state (i.e. $M^{n+} \rightarrow M^{0}$). The process uses simple equipment and instruments and can yield large quantities of nanoparticles at a low cost in a short time period. The use of microwave radiation as the heat source in these reactions not only improves the product quality but also reduces the production cost by completing the reactions over a significantly shorter period of time. In addition to the chemical reduction method, other reduction methods such as photoreduction by gamma rays, ultrasonic waves and liquid plasma can be used to prepare nanoparticles. In addition to these methods, co-precipitation, sol-gel synthesis as well as hydrothermal and solvothermal methods are also known for

nanoparticle synthesis, especially for transparent conducting oxide (TCO) nanoparticle synthesis. [90,91]

2.4.2 Polyol Mediated Route

Agglomeration of nanoparticles is practically inevitable in the absence of a stabilizer.[90] In most reactions, the organic capping agent normally used to prevent agglomeration also serves as a reducing agent in the synthesis. In polyol methods, multidentate and high-boiling point alcohols, such as diethylene glycol/DEG, ethylene glycol or glycerin, act as both the reaction solvent and the reducing agent in the synthesis of nanoparticles. The polar nature of the polyols makes them attractive as they not only dissolve the metal salts but can also play the role of a dispersing agent.[92] The previous studies on differential thermal analysis (DTA)/thermogravimetric (TG) confirmed that the adhered polyol on particle surfaces can be removed completely below 400 °C.[93]

The polyol method was originally developed by Fiévet et al. which involved the reaction of metal salts with polyalcohols.[94,95] However, in most of these reactions, a certain amount of water is added to transform the precursors into the corresponding metal oxides. As polyalcohols have high loss tangents, they are particularly susceptible to microwave heating.[96] The microwave absorbing characteristics of materials are discussed in detail in section 2.7.3. The application of microwave irradiation results in rapid heating of the reaction mixtures and thus rapid and nearly simultaneous precipitation of particles, which leads to a very small particle size and narrow size distribution.[90] Applying microwave-assisted heating of high-boiling solvents such as polyols has been advantageous with regard to particle morphology and material crystallinity.[97,98]

The water present in the reaction mixture helps to obtain zinc oxide from zinc acetate precursor. In addition, in microwave-assisted synthesis routes, the water enhances the microwave absorption and the heat generation, which can increase the final qualtity of the product. In order to increase the control over the nanoparticle shape, the polyol solvent can be combined with a surfactant. For instance, Tao et al. reported the synthesis of cerium dioxide nanoparticles in ethylene glycol, oleic acid and tert - butylamine.[89]

In principle, the boiling point of the polyols increases with the number of OH-functionalities and with increasing molecular weight. Similarly, the polarity and viscosity of the polyols increase with increasing molecular weight. Polyethelene glycols (PEGs) with comparably low molecular weight (<1000 g mol^{-1}), for instance, are viscous and colourless liquids, whilst high-molecular weight PEGs are waxy, white solids (>1000 g mol^{-1}). Perhaps the most important feature of the polyols is that they can achieve what can be considered as water-equivalent properties but with high-boiling points. The use of solvents with properties similar to water allows the use of simple, low-cost metal salts (e.g., halides, nitrates, sulfates) as starting materials. Moreover, the insolubility and precipitation of products in the polyol is determined by the polarity of the reaction mixture.[99] The low polarity of the reaction mixture is compensated by the chelating properties of the polyols as well as the small amount of water added in to the mixture. The chelating effect of the polyols is highly beneficial for controlling particle nucleation, particle growth and agglomeration of nanoparticles as the polyols adhere to the particle surface (especially on oxides) and serve as colloidal stabilisers.

In addition to the excellent colloidal stabilisation, the high boiling points of polyols are beneficial as they can be utilized for high synthesis temperatures (200–320 °C) without the requirement of high pressure heads and autoclaves.[100] Often, crystalline nanomaterials can be obtained right from the liquid phase with high temperature synthesis processes. Getting highly crystalline nanomaterials is essential for optimal materials properties for a wide range of applications.[100] As many applications rely on the absorption, emission and/or transport of electrons, defective solids have the potential to cause multiple competitive trap and loss processes which more crystalline materials do not.[101] In this regard, nanomaterials are anyway handicapped in comparison to infinite, periodic bulk compounds as already the particle surface itself represents a major defect.

2.4.3 Sol-gel Technique

Sol-gel chemistry allows the formation of an inorganic matrix by initially forming colloidal nanoparticles (sol) from a (metal salt or alkoxide) precursor in a (water or organic) based solvent and then converting it to a liquid phase (gel) by gelation. This involves chemical and physical steps associated with hydrolysis, polymerization,

gelation, condensation, drying and densification.[102] The sol-gel process is a well-established method for the synthesis of a variety of crystal size and shape controlled nanoparticles.[103,104,105] To avoid the precipitation and to form the homogenous gel, maintaining careful control of the pH of precursor solutions is extremely important. This can be achieved by the addition of acidic or basic solutions.[106] The discrete steps in sol-gel processing are shown in Figure 13.

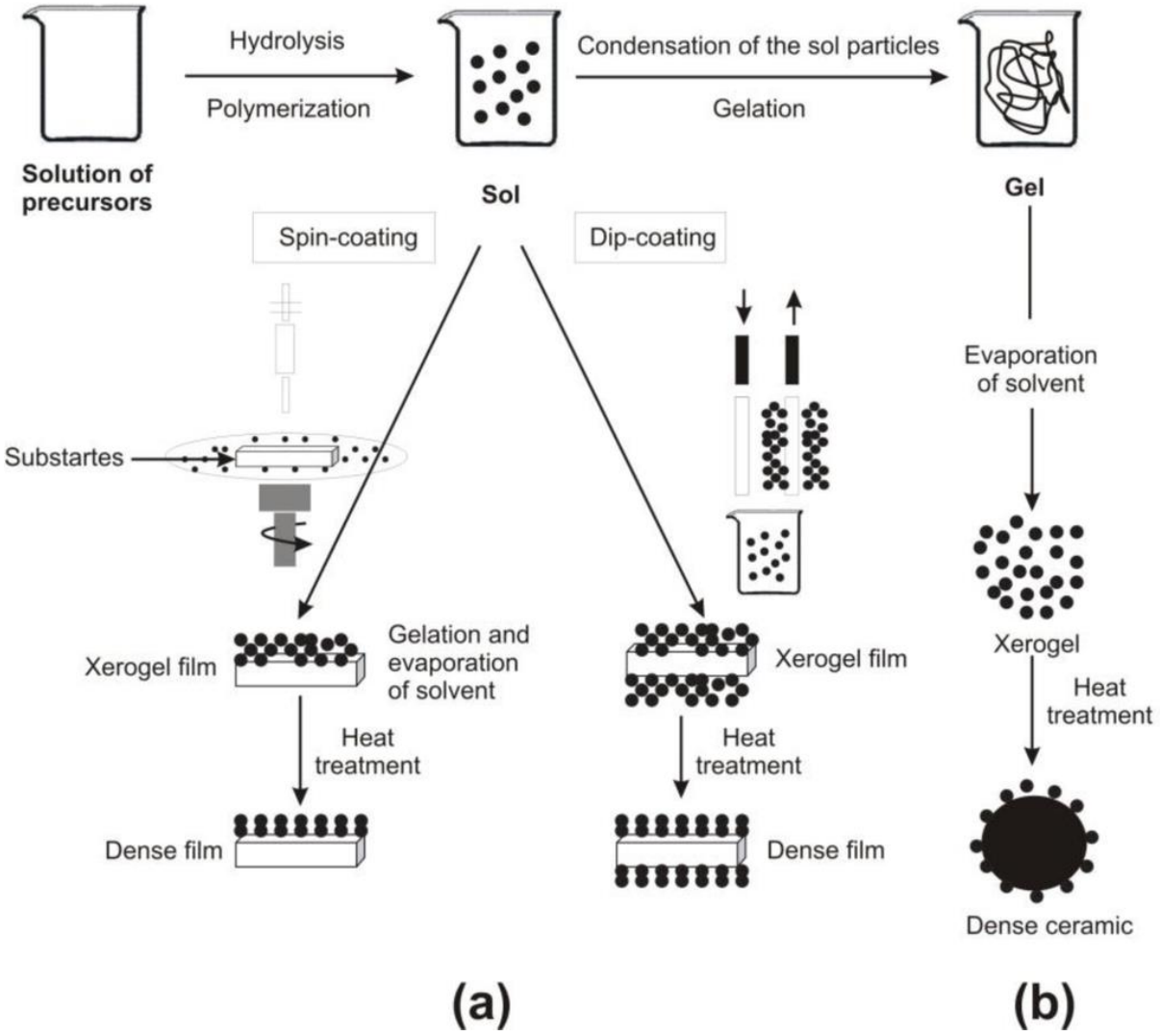

Figure 13 Overview of the sol-gel synthesis method: (a) films from a colloidal sol; (b) powder from a colloidal sol transformed into a gel.[107,108]

A particular advantage of the sol-gel methodis the facile control over the film composition and the ability to fabricate thin films over a large area at a low cost.[81] Luo *et al*.[59] developed a versatile film deposition process combining microwave-assisted

non-aqueous sol-gel processes with dip-coating. The resistivity of obtained films was a little high (minimum resistivity is 2.35×10^{-2} Ωcm) but their results were still promising on the way to the development of liquid phase routes. In order to produce good quality TCOs, every step of the sol-gel method has to be carefully optimised.

The major problem of sol–gel chemistry is that the products obtained are often characterized by low crystallinity. This problem is more pronounced in aqueous systems. Multi-metal oxides containing two or more metals are particularly difficult to access with high crystallinity and homogeneity.[89]

2.4.4 Co-precipitation Synthesis

In this process, the required metal cations from the precursor are co-precipitated, usually as hydroxides, carbonates, oxalates, formates or citrates.[109,110] The product is typically obtained after filtering, washing and drying steps. In many cases, the precipitate needs to be annealed at a certain temperature to obtain the final product of the desired chemical composition and crystalline phase.[111] In metal oxide synthesis, the material is co-precipitated as a hydroxide, which is generally amorphous.[112] When heat treated, the hydroxide transforms into an oxide via the loss of water at the same time as improving the crystallinity of the phases present.[113]

Qiao *et al*.[114] reported the production of ITO, where Indium (III) and tin (IV) hydroxides were synthesized by a co-precipitation method. The transformation of co-precipitated indium tin hydroxides to oxides of indium (III) and tin (IV) required thermal curing. Thermogravimetric analysis (TGA) and differential thermal analysis (DTA) techniques were used to analyse the phase transformation of hydroxides to oxides. It can be seen from the thermogravimetric (TG) curve in figure 14 that indium tin hydroxide converted to ITO completely at 314.7°C. DTA showed a series of endothermic and exothermic reactions, where the sharp peak temperature of 288.5°C was an endothermic reaction of 10 at.% tin doped indium hydroxide.

Co-precipitation often yields a product with a small particle size as it is an atomic scale mixing process.[115] However, reaction parameters such as pH, solution concentration, reaction temperature and stirring speed of the reaction mixture need to be carefully controlled in order to obtain the final product with the required properties.[116,117]

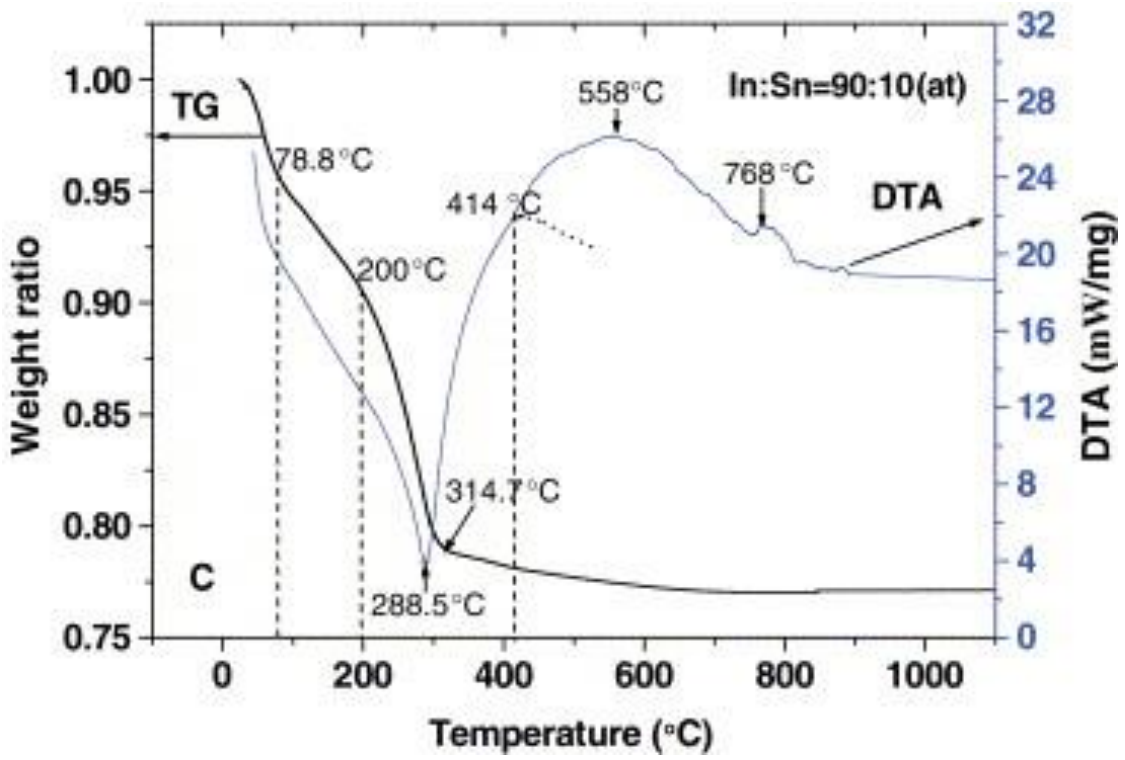

Figure 14 Thermal analysis of the ITO precursor sample with thermal temperature.[114]

2.4.5 Solvothermal and Hydrothermal Synthesis

Solvothermal synthesis is a method for synthesising a variety of materials such as metal oxides, semiconductors, ceramics, and polymers. The process involves the use of a solvent under moderate to high pressure (usually between 1 atm and 10,000 atm) and temperature (typically between 100°C and 1000°C) which facilitates the interaction of precursors during synthesis. If water is used as the solvent in the process, the method is called hydrothermal synthesis.[118] Solvothermal methods have gained much attention since particles with the desired characteristics can be prepared with this technique by controlling the solution pH, reaction temperature, reaction time, solute concentration and the type of solvent in a particular application.[119,120] The major advantages of this method are related to the homogeneous nucleation processes, which means it is possibile to eliminate the calcination step to produce very small grain-sized crystal particles with a narrow size distribution, good chemical homogeneity and high purity.[111,121] The corrosive nature of the hydrothermal slurries is often a drawback associated with this technique though.

It was found that ITO powders with a pure single cubic phase could not be produced by the conventional hydrothermal process as the technique didn't provide enough energy to break the bonds in the precursor molecules under the supercritical condition.[73] Hence organic solvents such as ethylene glycol ($C_2H_6O_2$), polyethylene glycol 600 ($H(OC_2H_4)_nOH$) and ethanol (C_2H_5OH) were substituted for water to move to a solvothermal method. Solvent viscosity in the solvothermal process strongly influences both electrical and optical properties of ITO. The ITO particle size increases with increasing solvent viscosity due to steric hindrance. At the same time, the shape of the synthesized ITO particles became more square with increasing solvent viscosity, because the preferred orientation of ITO materials for crystallization is fastest in the <100> direction.[73] However in order to synthesise ITO powders in a pure cubic crystalline phase the temperature of the solvothermal process is a key factor. Choi *et al*.[73] reported that 250°C was the critical temperature for forming a single oxide phase (figure 15).

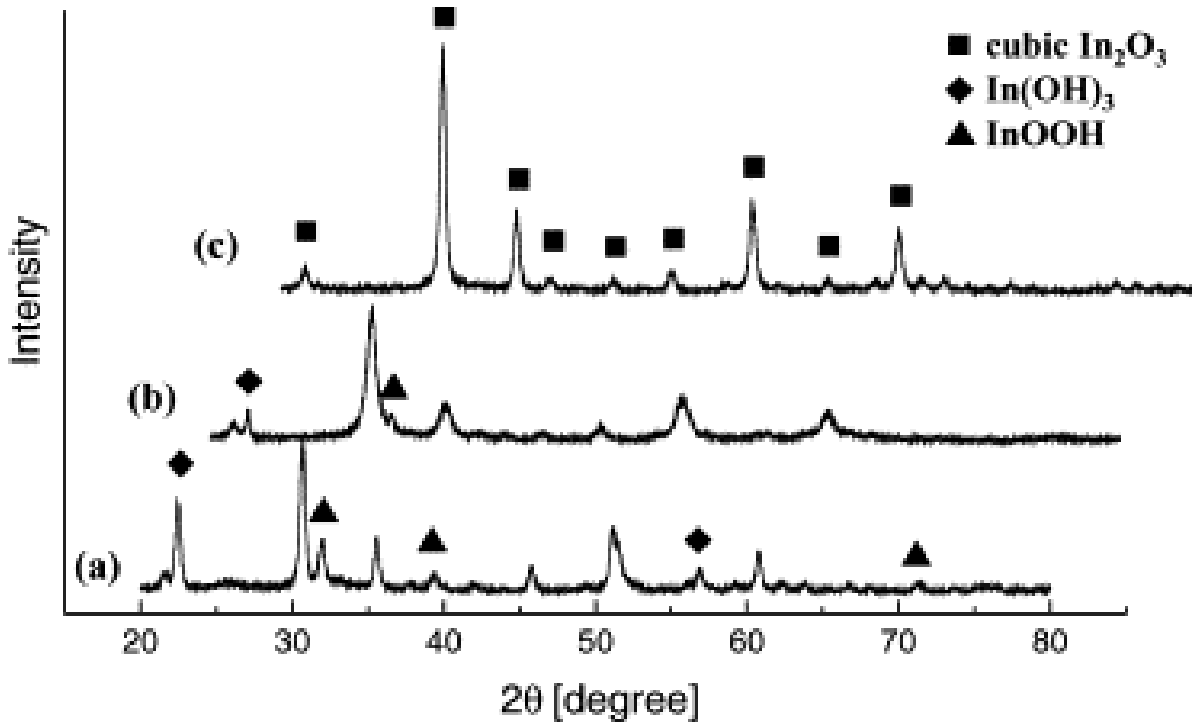

Figure 15 X-ray powder diffraction (XRD) patterns of ITO powders synthesized by the solvothermal process with ethylene glycol as a solvent: (a) at 210 °C, (b) 230 °C, and (c) 250 °C for 6 h, respectively.[73]

The colour of synthesized ITO powders varies according to the synthesis process. Solvothermally synthesized powders were blue and the powders synthesized by co-precipitation using calcination were yellow which indicates the wavelengths of light absorbed by the material.[122] It is known that blue ITO powders have a higher carrier concentration than yellow ITO powders, due to a greater number of oxygen vacancies, which is better for TCO applications.[73]

2.5 Thermal Processing of TCOs

It is a well known phenomenon that the electrical and optical properties of TCO thin films can be modified by carrying out post-deposition heat treatments.[123–125] The optical transmittance of a film is known to strongly depend on its surface morphology. K. Yim *et.al.* studied the effects of annealing on structure, resistivity and transmittance of Ga doped ZnO films.[126] J.F.Chang *et.al.* reported the effects of post-annealing on the structure and properties of Al-doped zinc oxide films.[55] According to their findings, improvement in the film transparency can be observed after the post-heat treatment of doped ZnO thin films, which is a result of the enhanced crystallinity and reduced surface roughness. As the grain size increases with the post-heat treatment, the boundary scattering tends to decrease. This effects the transmittance of the films favourably. Furthermore, annealing doped ZnO under a reducing atmosphere widens the optical band gap, whereas annealing in an oxidising atmosphere makes the optical band gap narrower. Figure 16 shows optical energy band gap variation of Ga doped ZnO thin films annealed under different atmospheres. The phenomenon that explains how the optical band gap increases with increasing carrier concentration in the conduction band is known as the Moss-Burstein effect, section 2.2. The Burstein relationship between the band gap shift ΔEg and the carrier concentration is linked in the following equation.[126]

$$\Delta E_g = \frac{h^2 n^{2/3}}{8 m_e^* \pi^{2/3}} \qquad (9)$$

where $m_e^*$is the effective mass of the electron, n is the electron concentration, and h is Planck's constant.

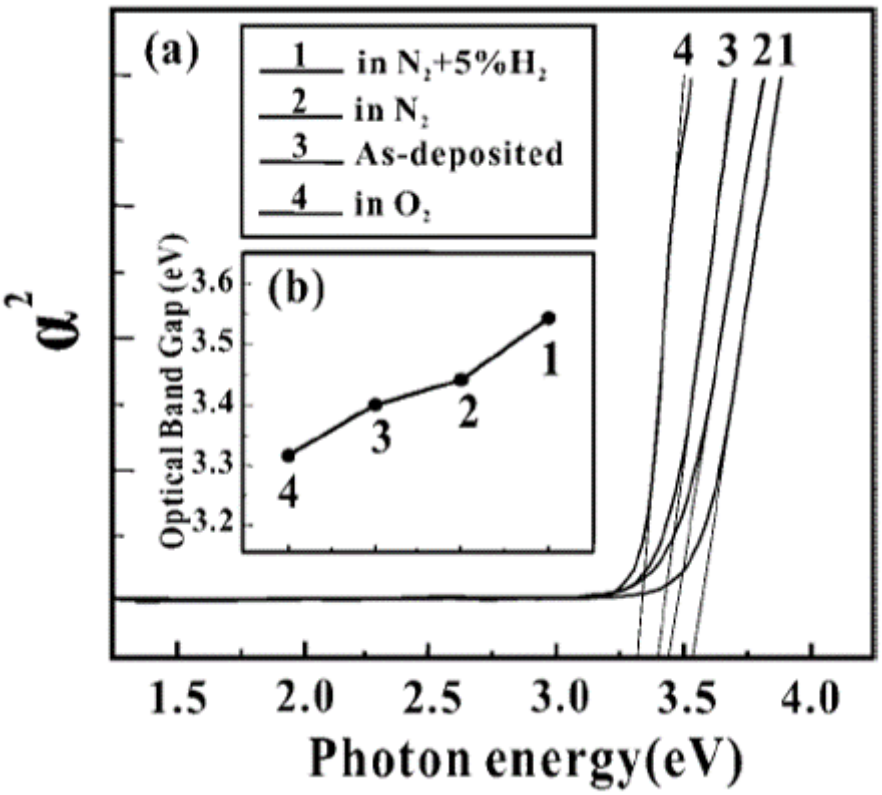

Figure 16(a) plot of α^2 versus photon energy and (b) optical energy band gap values of GZO thin films annealed in different atmospheres, determined by extrapolation of the α^2 versus photo energy curve.[126]

In addition to improving the transparency, post-heat treatment under a reduced atmosphere is also found to improve the electrical properties of terials.[126,125] This is ascribed to the passivation of grain boundaries and zinc ions resulting in increases in the carrier concentration and mobility in ZnO based materials. Negatively charged oxygen species reside at grain boundaries and act as trap sites. These negatively charged species form depletion regions near the grain boundary surfaces, decreasing the free-carrier concentration and Hall mobility. If these depletion regions in the TCO films were removed by the passivation of the grain boundary surfaces during the post-deposition annealing in a hydrogen atmosphere, the carrier concentration would increase, which in turn increases the conductivity (Figure 17).

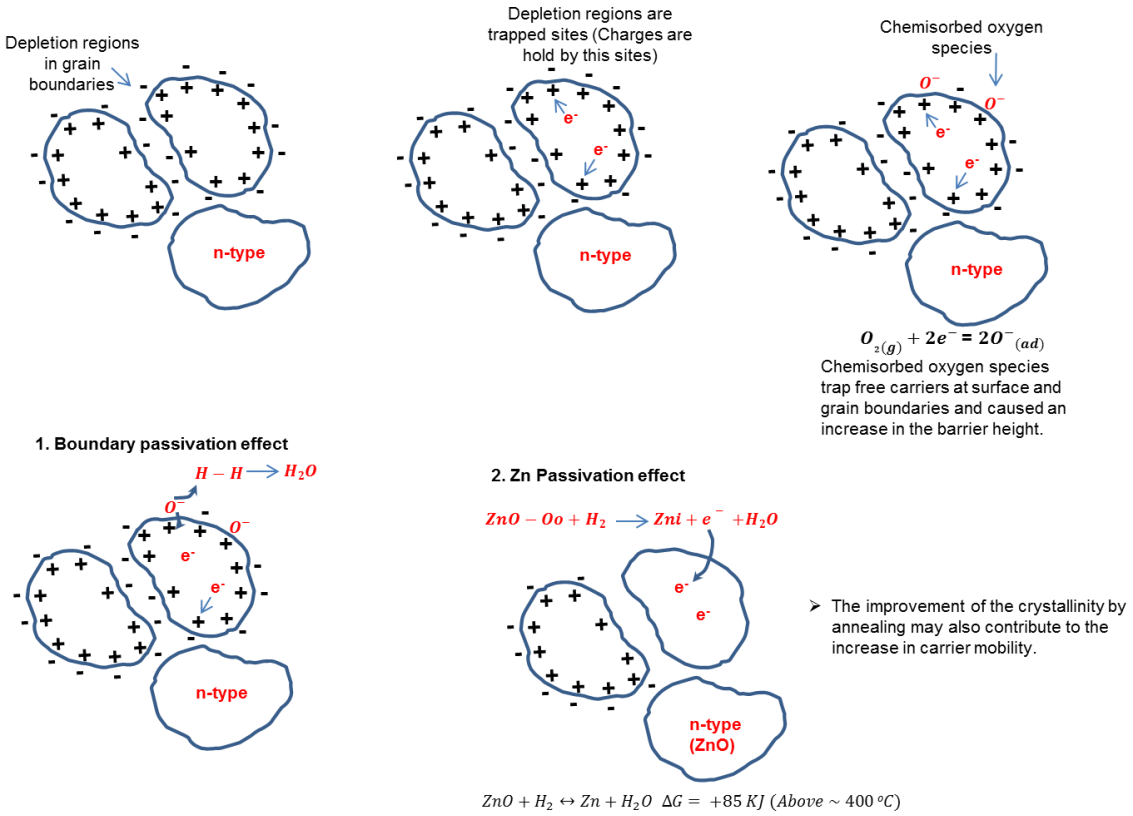

Figure 17 Effect of TCO annealing under a reduced atmosphere.

In contrast, N_2 rich atmospheres are more advantageous for ITO thin film processing compared to the reducing atmospheres used for ZnO.[127] As the Sn dopant and oxygen vacancies play a major role in ITOs conductivity, controlling the oxygen content is an important factor. According to the literature, N_2 can induce oxygen vacancies or remove oxygen interstitials through the incorporation of a reducible defect, giving rise to the conductivity.[128,129] Whilst the hydrogen treatment can form hydrogen oxygen links and stabilize oxygen in the ITO lattice, reducing the number of oxygen vacancies and increasing the resistivity.[130]

2.6 Microwave Assisted Synthesis and Processing of TCOs

2.6.1 Fundamentals of Microwaves

In the electromagnetic spectrum, microwaves are found in a transitional region between infrared and radio frequency radiation with wavelengths ranging from about 1

mm to 1 m in free space and frequencies between approximately 300 GHz to 300 MHz, respectively (Figure 18). This broad microwave region can be further classified into three bands: the ultra-high frequency (UHF) band with frequencies ranging from 300 MHz to 3 GHz, the super-high frequency (SHF) band with frequencies ranging from 3 to 30 GHz and the extremely-high frequency (EHF) band with frequencies ranging from 30 to 300 GHz.[131]

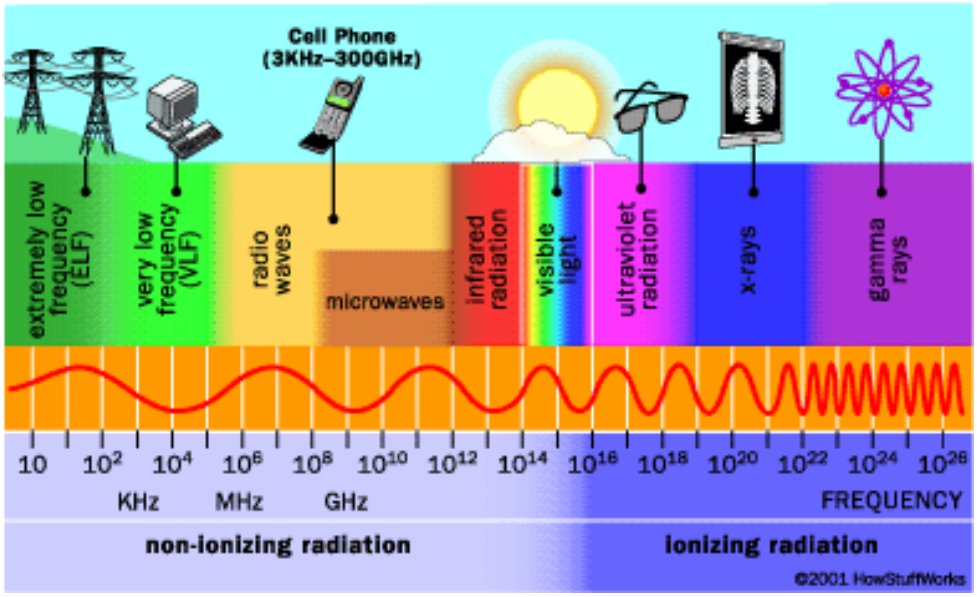

Figure 18 Electromagnetic spectrum.[132]

Although microwave radiation has a wide frequency range, most of the frequencies are restricted to government usage and telecommunication purposes, leaving only a limited range of frequencies available for use in industrial, scientific and medical applications.[133] Nowadays, narrow bands of frequencies centred at 915 MHz and 2.45 GHz are permitted by regulation for commercial usage. The microwave photon energy corresponding to 2.45 GHz is close to 0.00001 eV which is not sufficiently energetic even to break hydrogen bonds; it is also much smaller than that of Brownian motion.[134] Therefore, there is no possibility to break chemical bonds of materials by absorbing microwave energy. Microwaves are, however, capable of generating heat in materials through molecular interactions and collisions.

2.6.2 Conventional vs. Microwave heating

Heat generation in materials by microwave energy is fundamentally different from conventional radiant heating, conduction or convection heating. In the microwave process, the heat is generated within the material instead of originating from external heating elements. In other words, microwave heat generation is due to an energy conversion rather than a heat transfer process. As the material is being processed under microwaves, the absorbed radiation is converted to heat energy and the material becomes its own heating source. The temperature profiles of samples heated using conventional thermal heating, microwave heating and hybrid heating are illustrated in Figure 19.

For conventional thermal heating, the material always has a higher temperature at the surface compared to the core; this is due to heat being transferred from the heating element to the sample, then heat gradually transfers through the surface towards the core. The temperature profile for microwave heating is the reverse. As the heat is generated within the material, the temperature at the core of the sample is the greatest, but then decays towards the surface due to energy loss to the surroundings. Through the use of hybrid heating, it is possible to create uniform heating throughout the sample by carefully tuning the microwave and thermal power. The use of hybrid heating offers significant advantages compared to using thermal or microwave heating alone. By using hybrid heating, it is possible to create materials with more uniform properties. For example, if the phase of a material is dependent on the temperature, uneven heating could create a mixture of phases, which would lead to different properties, such as, differing levels of conductivity and catalytic activity, amongst others. As the dielectric constant of a material is temperature dependant, this offers significant opportunities for hybrid heating. For example, a material which does not absorb microwaves efficiently at room temperature, might, in fact, absorb much more efficiently at higher temperatures, opening up more possibilities to process low microwave absorbing materials.

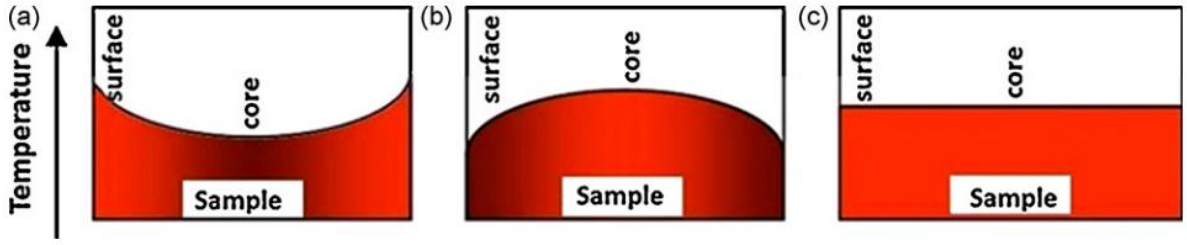

Figure 19 Temperature profile within a sample using (a) conventional thermal heating, (b) microwave heating and (c) hybrid heating.[135]

Not all materials are capable of absorbing microwaves under ambient conditions. Dielectric materials are capable of absorbing microwave radiation more efficiently than metals or insulators. The dielectric properties of a material can be described by the Maxwell Garnett theory. According to the Maxwell Garnett theory, the ratio ($\sigma/\omega\varepsilon'$) of a material is responsible in determining whether it is a conductor, insulator or dielectric material[136], where, σ is the electrical conductivity, ω is the angular frequency of molecules in the material and ε' is the dielectric constant of the material. In conductors, the ratio is much higher than unity while in dielectrics, it is much smaller than unity.

Microwaves pass through transparent or low dielectric loss materials (i.e. glass, ceramic, air etc.) with little attenuation, whilst opaque or conducting materials (i.e. most of metals including steel, Al, Cu etc.) reflect the radiation without penetration. Absorbing or high dielectric loss materials (i.e. SiC, CuO, $MoSi_2$ etc.) absorb microwave radiation in different levels based on their dielectric properties whilst magnetic materials (i.e. iron oxides, Fe, Ni, Mo, Co etc) interact with the magnetic component of microwaves. The heating effect mainly arises from the interaction of the electric field component of the microwaves with the charged species in the high dielectric loss materials. The microwave frequency is low enough that the charged species (dipoles or ions) have time to respond to the alternating electric field and rotate, but high enough that the rotation does not precisely follow the direction of the field and there is a lag, as illustrated in figure 20.

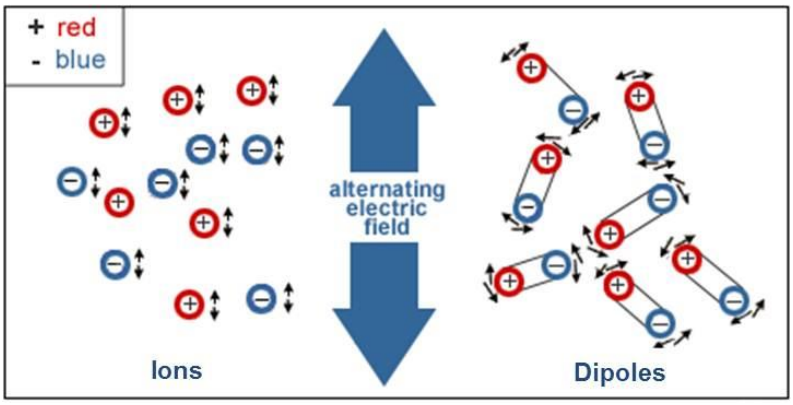

Figure 20 The response of ions and dipoles in materials under the alternating electric field of microwave radiation.[137]

2.6.3 Importance of Materials' Dielectric Properties

The microwave absorbing characteristics of materials are related to the dielectric and magnetic properties such as the electric permittivity (ε) and magnetic permeability (μ), whilst the extent of heat generation by absorbed energy is determined by the loss tangent (tan δ) of the material. Therefore, when microwaves are in contact with materials of different dielectric properties, they will selectively couple with the higher loss tangent material and generate heat. The application of microwave energy to various materials such as semiconductors, ceramics, metals and composites offers several advantages over conventional heating methods.[138] These advantages include unique microstructure, improved product yield, energy savings, reduction in manufacturing cost, synthesis of new materials.[20] Due to the fact that materials are heated volumetrically, materials with a uniform microstructure can be produced using microwave heating, if energy losses from the surface are minimized. The nature of microwave heating is also much more efficient in many ways compared to resistance heating.

In order for microwaves to interact with the material, a balanced combination of moderate dielectric constant (to permit adequate penetration) and high loss tangent (for higher energy to heat conversion) are required. Due to these characteristics of microwave heating, microwave irradiation has great potential for the synthesis and processing of different inorganic solids and semiconductor metal oxides which are used heavily in making many rigid and flexible electronic and optoelectronic devices.[139]

2.6.4 Microwave - Material Interactions

The interaction of electromagnetic radiation with dielectric materials can cause net polarization in materials. There are several mechanisms which are responsible for the polarization, including: ionic (P_i), dipolar(P_d), electronic(P_e) and interfacial (space-charge)(P_s) polarization. Therefore, for a dielectric material the net polarization, P, is determined by the sum of the contributions from each mechanism as shown in equation 10.

$$P = P_i + P_d + P_e + P_s \qquad (10)$$

Dipolar and ionic polarization mechanisms are the dominant mechanisms that cause heating in dielectric materials at microwaves frequencies.[140] Dipolar polarization arises due to the alignment of dipoles against the alternating electric field of microwaves (Figure 21a) whereas, ionic polarization takes place due to the displacement of positive and negative ions toward the changing electric field of microwaves until the net charge is balanced (Figure 21b). At the microwave frequency range, the alignment of these charged species lags behind the changing electric field which causes molecular friction and thus generates heat.

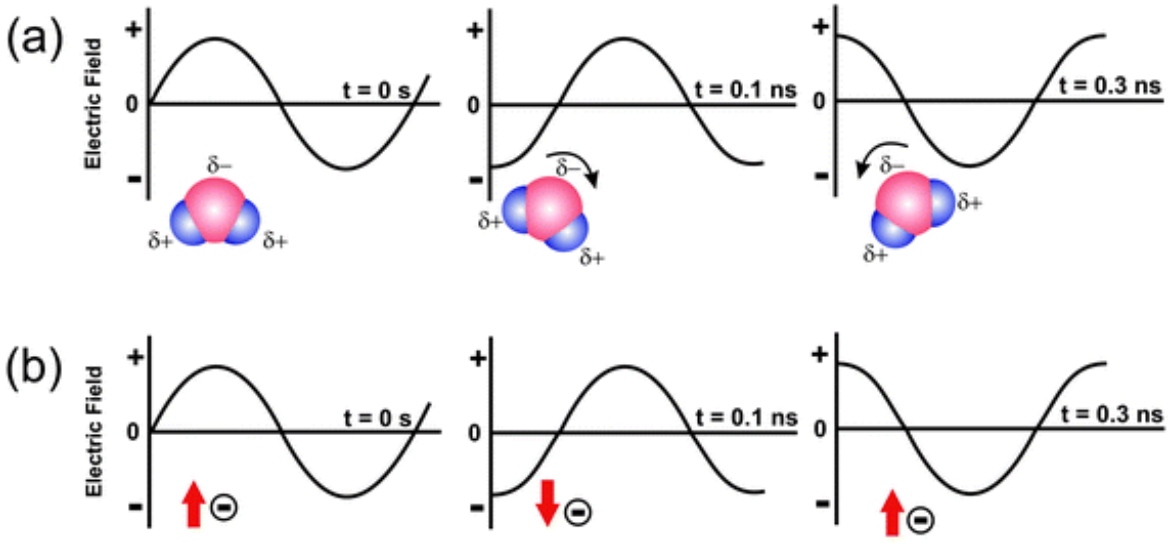

Figure 21 The dominant polarization mechanisms that cause heating of dielectric materials at microwaves frequencies (a) dipolar polarization and (b) ionic polarization.[141]

The exact nature of microwave-material interactions and hence heat generation depends upon the degree of polarization and the mobility of charges in dielectric materials. The degree of polarization (P) of dielectric materials is related to its dielectric properties through the relation in the equation 11,

$$P = \varepsilon_o(\varepsilon_r' - 1)E \qquad (11)$$

where $\varepsilon_o$is the permittivity of free space (ε_0 = 8·86 × 10^{-12} F m^{-1}), ε_r' is the relative permittivity of the material and E the applied electric field strength. If the charge carriers are mobile, the alternating microwave field gives rise to a current flow which could cause resistive heating in the material at the same time.[142]

2.6.5 Microwave Absorbing Characteristics of Materials

The interaction of microwaves with matter is quantified by two complex physical quantities; dielectric permittivity, ε, and permeability (magnetic susceptibility), μ.[143] In reality, the permittivity and permeability are complex quantities which are defined as ε^* and μ^* respectively as below equations 12 and 13,[144]

$$\varepsilon^* = \varepsilon' - i\varepsilon'' = \varepsilon_o\left(\varepsilon_r' - i\varepsilon_{eff}''\right) \qquad (12)$$

$$\mu^* = \mu' - i\mu'' = \mu_o\left(\mu_r' - i\mu_{eff}''\right) \qquad (13)$$

where ε' is the dielectric constant which represents the time-independent polarizability of a material in the presence of an external electric field, that is to say it measures the resistance encountered when forming an electric field in a medium. $\varepsilon''$is the dielectric loss or loss factor of the material, and indicates the time-dependent component of the permittivity which quantifies the ability of the material to convert absorbed energy into heat. ε_r' is the relative permittivity of the material which is the ratio of the permittivity of a substance to that of free space or vacuum. ε_{eff}'' is the effective relative loss factor. μ' is the magnetic permeability, μ'' magnetic loss factor, μ_o the permeability of free space (μ_o = 4π × 10^{-7} H m^{-1}), μ_r' is the relative permeability of the material and μ_{eff}'' is the effective relative magnetic loss factor.

The ratio of the dielectric loss to the dielectric constant is known as the loss tangent ($tan\delta$) or dissipation factor which is given in equation 14,[145]

$$tan\delta = \frac{\varepsilon''}{\varepsilon'} \qquad (14)$$

The angle δ represents the phase lag between the polarization of the material and the applied electric field. The loss tangent is an indicator of the ability of the material to convert absorbed energy into heat. A good microwave absorber has $tan\delta \geq 0.1$ while those with $tan\delta \leq 0.01$ are transparent to microwaves. The heat generation by microwave energy can be quantified by equation 15,[146]

$$P = \sigma|E|^2 = 2\pi f \varepsilon_o \varepsilon'' |E|^2 = 2\pi f \varepsilon_o \varepsilon' tan\delta |E|^2 \quad (15)$$

where, P is power dissipation (W/cm^3), σ is the total effective conductivity, E is the magnitude of the internal electric field, and f is the microwave frequency.

The intensity of heat evolution in a sample depends on the materials properties, the frequency and intensity of the applied field, penetration depth of microwaves into the substance and geometric size of the sample.[147] The distribution of energy within a material can be determined by the attenuation factor, α' expressed as equation 16,

$$\alpha' = \frac{2\pi}{\lambda}\left[\frac{\varepsilon'}{2}\left\{\sqrt{(1 + tan^2\delta)} - 1\right\}\right]^{1/2} \qquad (16)$$

The attenuation factor can be used to calculate the penetration depth (D) as suggested by von Hippel.[148] It is inversely proportional to the penetration depth of the material as shown in the below equation,

$$D = \frac{1}{\alpha'} \qquad (17)$$

Penetration depth is an important parameter which determines the heat generation of materials by microwaves. When microwaves are incident perpendicularly to the surface of the materials, its intensity decreases progressively due to dissipation inside the volume of the materials. The penetration depth is defined as the distance from the surface of the material at which the power drops to 1/e from its value at the surface. This can be also expressed by equation 18,[149]

$$D = \frac{3\lambda_0}{8.686\,\pi\,tan\delta\,\sqrt{\varepsilon'}} \qquad (18)$$

At a frequency of 2.45 GHz, the free space wavelength λ_0 is 12.24 cm. Penetration depth ranges between several micrometres to several tens of meters depending on the dielectric nature of the material.

In metals, microwave propagation is usually described in terms of skin depth (δ) which is defined as the depth at which the magnitude of electric field drops to 1/e of the value at the surface and it is expressed as,

$$\delta = \frac{1}{\sqrt{f\pi\mu_o\sigma}} \qquad (19)$$

In general, if the penetration depth exceeds the sample thickness, the material behaves as if it is transparent to microwaves. Volumetric heating only results when the penetration depth is comparable to the sample thickness. If the sample is too thick, absorption is limited to the surface.[150]

Microwave interaction with materials can be predicted if dielectric properties such as dielectric constant and dielectric loss are known. The loss tangent is an indicator of the ability of the material to convert absorbed energy into heat and the penetration depth determines the penetration ability of microwaves into the material. A list of reported dielectric properties and penetration depths of some useful materials are tabulated in table 2. Generally, the dielectric properties of a material are related to its temperature, moisture content, density and geometry.

Table 2 Reported dielectric properties of semiconductor oxides which are useful for microwave heating.

Material	ε'	ε''	tanδ	D / m	Ref.
SiC	10.5	11.0	1.05	0.004	[136]
γ-Al_2O_3	3.0	0.17	0.06	0.14	[151]
TiO_2	5.6	0.18	0.03	0.18	[152]
ZnO	3.4	0.19	0.06	0.13	[152]
ZrO_2	4.2	0.19	0.04	0.15	[153]
Fe_2O_3	7.4	0.22	0.03	0.17	[153]
CuO	3.3	0.17	0.05	0.14	[153]
V_2O_5	7.6	0.50	0.07	0.07	[153]
SiO_2	3.1	0.22	0.07	0.11	[153]

2.6.6 The Characteristics of Microwave Heating

Recent developments in the microwave processing of materials have shown significant advantages including energy savings, processing time, enhancement in the material properties and environmental remediation for a wide range of potential applications.[154] Microwave heating has drawn particular attention because of the advantages over conventional heating methods; the ability to achieve higher heating rates rapidly, short processing time, no direct contact between the heating elements and the material, selective heating abilities, greater control of the heating process, reduced equipment size and more environmentally friendly technology.

2.6.7 Microwave Equipment

Generally, microwave heating systems consist of four basic elements, a microwave generator to produce microwave radiation, waveguide components to transmit microwave energy, applicator (usually a cavity) to place the load and the control system to control the microwave power, temperature etc. The microwave generator is the device that generates microwave radiation. Microwave generators include magnetrons, power grid tubes, travelling wave tubes (TWTs), crossed field amplifiers (CFAs), klystrons and gyrotrons.[155] The selection of the appropriate type of microwave generator for a particular application depends on various factors including the power, frequency, efficiency, gain, bandwidth, phase, size, weight and cost. The magnetron is the most commonly used microwave generator because of its high efficiency, compact size and low cost. Magnetron tubes use resonant structures to generate an electromagnetic field, and, therefore, are only capable of generating a fixed frequency electromagnetic field.[156] A magnetron converts electrical energy to microwave radiation and typically operates at a frequency of 2.45 GHz and they are widely used in microwave ovens and radar systems. A cross-section of a typical magnetron is shown in figure 22.

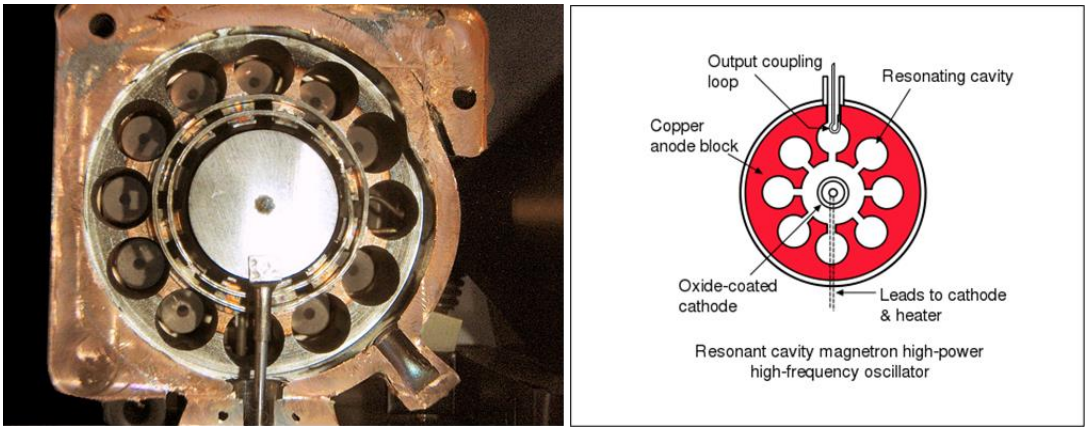

Figure 22 A cross-section of a typical magnetron.[20]

In the magnetron, heated cathodes act as a source of electrons. The cathode is surrounded by a circular anode having an array of radial slots acting as resonators tuned to the desired operating frequency. The electric field created by the applied DC voltage draws electrons from the cathode to the anode region. In the presence of a magnetic field, the electrons cannot travel radially outward to the anode but they are

forced to rotate circularly in the coaxial space between the cathode and the anode. Consequently, bunching of the electron clouds occurs.[157] The electron clouds would appear as a rotating spoke wheel. In the presence of an electromagnetic field, the electrons entering the positive microwave electric field gradient accelerate and those entering the negative gradient will decelerate. The change in the kinetic energy of the electrons leaving the cathode and arriving at the anode results in the generation of the microwaves. The transfer of power from the DC power input to the microwave power is extremely efficient. The microwaves are then directed towards a target with the use of microwave guides which are usually made of sheet metals. The output microwave power can be generated in two ways; pulsed or continuous. Pulsed magnetrons produce an output power of kilowatts to several megawatts for short durations while continuous magnetrons produce an output power of a few watts to kilowatts continuously.

2.6.8 Microwave-assisted Synthesis

In recent years, microwaves have been explored as an efficient alternative energy source to traditional forms of heating (i.e. isomantles, oil baths, hot plates etc.) in materials synthesis.[158] It has been shown that the use of microwave radiation for material synthesis has shown promising results over conventional heating methods in terms of the product yield and the reaction rate.[159] Over the past few decades, most of the microwave heating in chemistry has been limited to organic synthesis. More recently the use of microwave radiation for heating reactions in the laboratory has expanded to inorganic and materials chemistry. Reviews by Bilecka [141] and Rao [160] give an overview of microwave-assisted liquid phase routes to synthese inorganic nanomaterials. A recent review by Kitchen et al,[161] analyses the significant advances in the area of solid-state microwave synthesis. A review by Hoz et al. provides an overall picture of non-thermal microwave effects on organic synthesis[162] whilst Lidström[140] delivers a critical review on microwave assisted organic synthesis and its advantages over conventional synthesis methods.

In organic and inorganic material synthesis, some or all of the reactants involved in the reaction should have a high coupling efficiency with microwaves. This provides adequate energy to overcome the activation energy barrier, allowing the reaction to proceed. The microwave absorbing properties of the reactants facilitate the rapid

heating and lead to the successful synthesis of the target material within a very short period of time. In microwave-assisted synthesis, one often selects alternative reactants with favourable dielectric properties in order to achieve the maximum product yield. If there are no alternative microwave absorbing reactants available for material synthesis, it is usually possible to find a secondary material that can act as a heat source; this is commonly referred to as a microwave susceptor. Microwave susceptors are substances that have the ability to absorb microwave energy and convert it to heat. In other words, a susceptor is a material that has a high dielectric loss tangent. Graphitic or amorphous carbon, silicon carbide and copper (II) oxide are some examples of commonly used susceptors.[20] These susceptor materials can be kept either in direct contact with the sample (by mixing with the other regents) or placed outside (surrounding the sample). In some cases, adding a susceptor into a reaction mixture can cause problems with the final product purity, yield and reaction rate. Microwave susceptors can also be used in material post heat treatments to ramp up the temperature of poorly microwave absorbing materials. In such cases, the penetration depth plays a vital role in the heat generation. If the penetration depth exceeds susceptor thickness, the susceptor behaves as if it is transparent to microwaves. Volumetric heating only occurs when the penetration depth is comparable to the sample thickness. If the sample is too thick, absorption is limited to the surface. The physical nature of materials, such as particle size, density and the medium the material is present in, also determines the microwave penetration depth.[163] The variation of the penetration depth of SiC with the above physical properties is shown in figure 23.

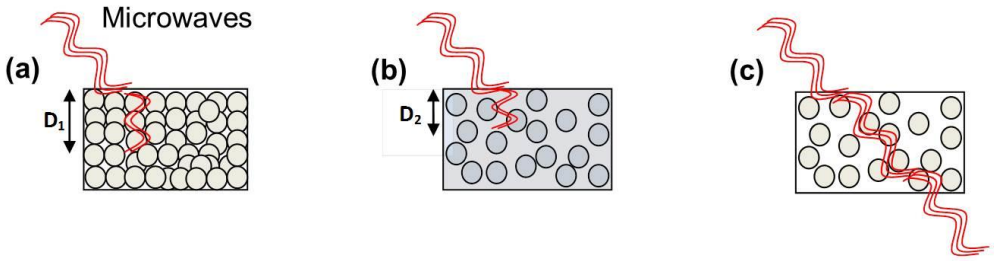

Figure 23 The variation in the penetration depth of m icrowaves with the density and the dispersion medium of SiC (a) Highly dense SiC (Tile) (b) SiC particles dispersed in a dielectric medium (c) SiC particles dispersed in air.[20]

As indicated in figure 23, the penetration depth of microwaves in to SiC varies with the density and the nature of the particle dispersion in the medium. This affects the microwave coupling and heat generation. Generally, SiC is an abrasive material with a high density. The microwaves couple with SiC as a whole and penetrate well into the material to generate heat effectively because of its high density (figure 23a). When the SiC particles are dispersed in a dielectric medium, (such as water, ethanol etc.) microwaves interact with SiC particles as well as the dielectric medium to generate heat. Since both media couple well with microwaves, the penetration depth of such a system (which is determined by the sum of the contributions from each material's dielectric properties) are reasonably high, and this leads to heat generation (figure 23b). In the case of SiC powders the voids between the particles are filled with air, which is transparent to microwaves. Thus, heat generation is only influenced by the particle size of SiC (figure 23c). In order to generate volumetric heating in SiC powders the penetration depth of microwaves needs to be comparable with the particle size of the SiC (diameter of the particles). Therefore, it is not possible to heat SiC nanoparticles (< 100 nm) by microwaves unless they are mixed with another dielectric matrix.

Over the past decade many colloidal inorganic metal nanocrystals, metal oxides and chalogenides have been synthesised using microwave radiation. Table 3 gives an idea about the transparent conducting metal oxides synthesised using microwave radiation. In most of the literature it is claimed that use of microwaves in microwave-assisted synthesis shortens the reaction times and reaction temperatures significantly compared to conventional synthetic techniques.[164] As discussed earlier, the thermal gradient in a microwave processed material is the reverse of that in a material processed by conventional heating.[165] The temperature profiles of microwave and conventional annealing for a reaction are shown in figure 24.

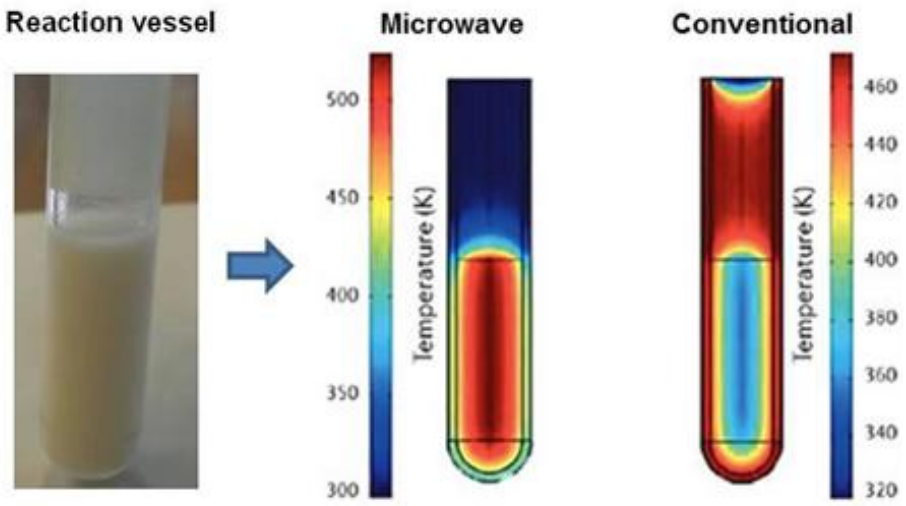

Figure 24 The temperature profiles of microwave and conventional annealing methods of the reaction mixture in the vessel.[166]

Table 3 Transparent conducting metal oxides synthesised using microwave radiation are listed by the dopant, synthesis/thin film fabrication method, reported conductivity/resistivity with the references.

Metal Oxide	**Dopant**	**Synthesis method and additives**	**Precursors**	**Specialty and reaction cond.**	**Reference**
ZnO	Al	Glycolysis, H_2O DEG	$Zn(OAc)_2$ $AlCl_3$	Spheres ca. 12 nm MW - 30 min 200°C	[167]
ZnO	In	Glycolysis, H_2O DEG	$Zn(OAc)_2$ $InCl_3$	Spheres 15 nm, 30 min 200°C	[167]
In_2O_3	Sn	Alkaline hydrolysis DMF/EtOH $N(CH_3)_4OH$	$InCl_3$ $SnCl_4$	Irregular polyhedrons 25 nm, 3–15 s 300°C	[168]
In_2O_3	Sn	Glycolysis,	$InCl_3$	Spheres	[58]

		DEG $N(CH_3)4OH$	$SnCl_4$	15–19 nm 120 min 200°C, 1 atm	
$ZnGa_2O_4$	Cu	Alkaline Hydrolysis, H_2O NH_4OH	$Ga_2(SO_4)_3$ $ZnSO_4$ $CuCl_2$	Aggregates of spherical 10– 20 nm particles 30 min 150°C	[169]
ZnO	Au	Alkaline hydrolysis EtOH NaOH, PEG	$Zn(NO_3)_2$, $H[AuCl_4]$	Nanoods 10–15 nm x 100–600 nm 10 min (MW cycles: 10 s on/20 s off)	[170]
TiO_2	La, Zr	Acidic hydrolysis iPrOH AcOH, citric acid, PEG, H_2O	$Ti(OiPr)_4$, $ZrCl_4$ $La(NO_3)_3$	Aggregates of 15–25 nm particles 4 min	[171]

2.7 TCO Thin Film Fabrication

A large number of methods are used for the production of high quality, uniform thin films.[172,173,174] Each technique falls into one of three general types: wet chemical deposition, physical vapour deposition or chemical vapour deposition. Crystallinity, morphology and other properties of the resultant film can be controlled by selecting the appropriate deposition technique and careful optimization of the deposition parameters.[175]

2.7.1 Wet Chemical Deposition Techniques

Wet-chemical methods are liquid-based coating techniques, such as spin-coating and dip coating, which are easily scaled up for mass production in industry.

2.7.1.1 Dip Coating

The dip coating technique can be described as a process where the substrate to be coated is immersed in a dispersion and then withdrawn with a well-defined withdrawal speed. The steps of the dip-coating process are shown in figure 25. The coating thickness is mainly defined by the withdrawal speed, the solid content and the viscosity and evaporability of the solvent. The faster withdrawal speeds, higher solid concentrations and solvents with higher evaporation points result in thicker films. This is a low-cost and simple technique to deposit multilayer films. Post-heat treatment of the film is usually necessary to sinter the particles, especially into transparent conducting oxides.[176]

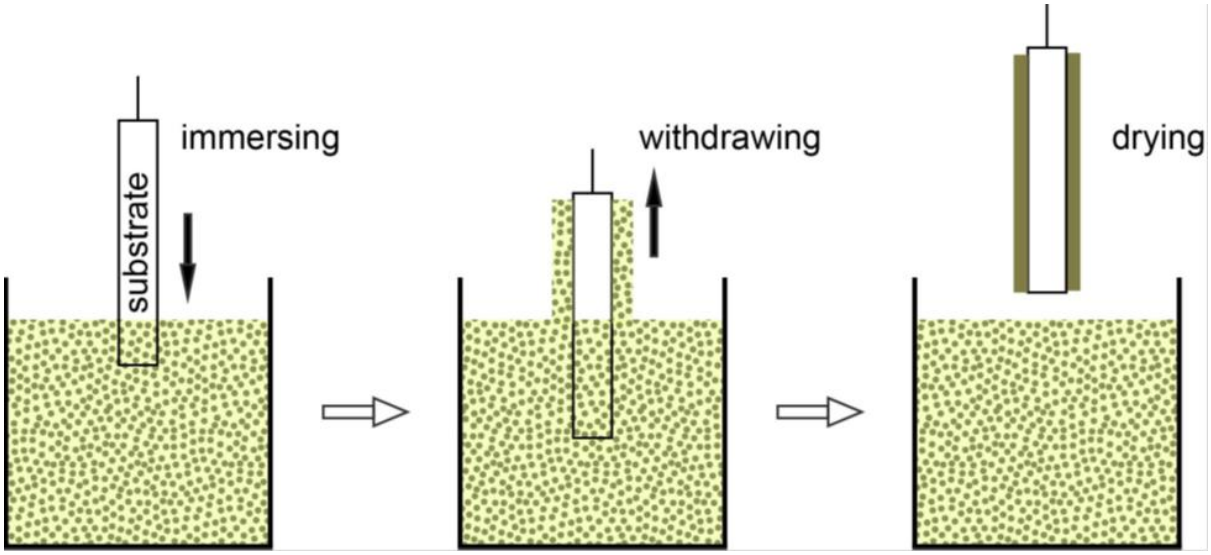

Figure 25 Diagram of the steps in dip-coating process.[176]

2.7.1.2 Spin Coating

Spin coating has been used for several decades as a method for fabricating homogeneous thin films. A typical process involves depositing a small puddle of a fluid material onto the center of a substrate and then spinning the substrate at high speed. Centripetal acceleration will cause most of the material to spread out and eventually drop off from the edge of the substrate, leaving a thin film of material on the surface. A separate drying step is often added after the high speed spin step in TCO thin film fabrication in order to remove the solvent from the film (figure 26).[177]

The final thickness and other properties of the film will depend on the nature of the fluid material (viscosity, drying rate, surface tension) and the parameters such as spin rate in revolutions per minute (rpm) and time in the spin process. One of the key challenges in spin coating is reproducibility, as subtle variations in the parameters that define a spin-coating process can result in drastic variations in the coated film.

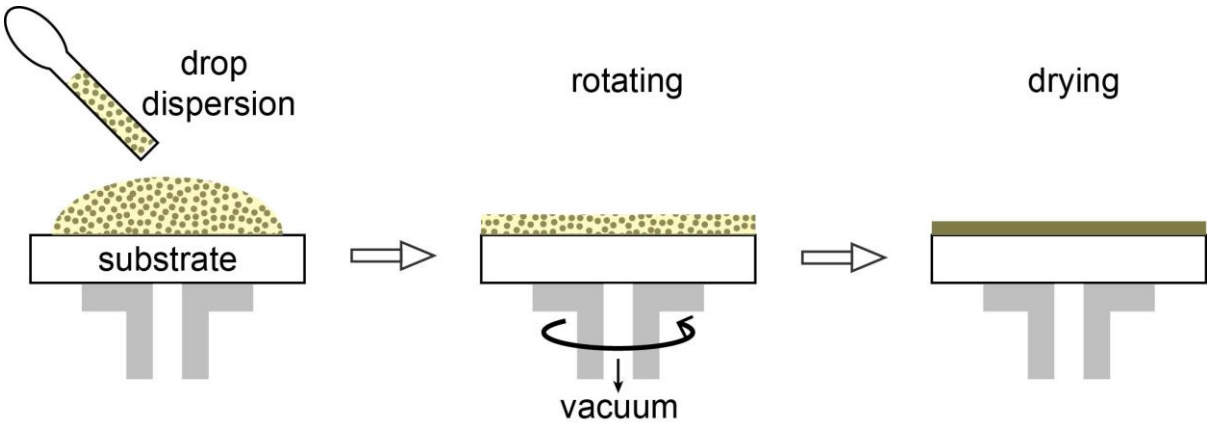

Figure 26 Diagram of the steps in dip-coating process.[178]

2.7.2 Chemical Vapour Deposition

Chemical Vapour Deposition (CVD) is perhaps the most widely used technique to fabricate thin film TCO materials. It involves the deposition of a thin solid film onto a substrate via chemical reactions of precursors in the vapour phase.[178] The chemical reactions can occur either homogeneously in the gas phase or heterogeneously on the substrate. It is the chemical reaction which distinguishes CVD from physical vapour deposition processes.[179,180]

CVD requires the dispersal of the precursor into a gas stream, transport of the precursor towards a substrate and the application of energy to cause a reaction. The key steps of CVD are listed below.[181,182,183]

- Evaporation and transport of reagents in the bulk gas flow region into the reactor.
- Mass transport of the reactants to the substrate surface.
- Adsorption of the reactants on the substrate surface.
- Surface diffusion to growth sites.
- Nucleation and surface chemical reactions leading to film growth.
- Desorption and mass transport of remaining fragments of the decomposition away from the reaction zone.

Other than the chemistry in the gas phase, the substrate temperature and the pressure of the reactor affect the film growth rate in thermal CVD. At lower substrate temperatures, the film growth rate is determined by the kinetics of the chemical reactions taking place either in the gas phase or on the substrate surface. This is known as surface reaction limited film growth. As the temperature is increased, the film growth rate becomes virtually independent of temperature and the growth is determined by the mass transport of the precursors through the boundary layer to the growth surface as shown in figure 27. This is known as mass transport limited film growth.

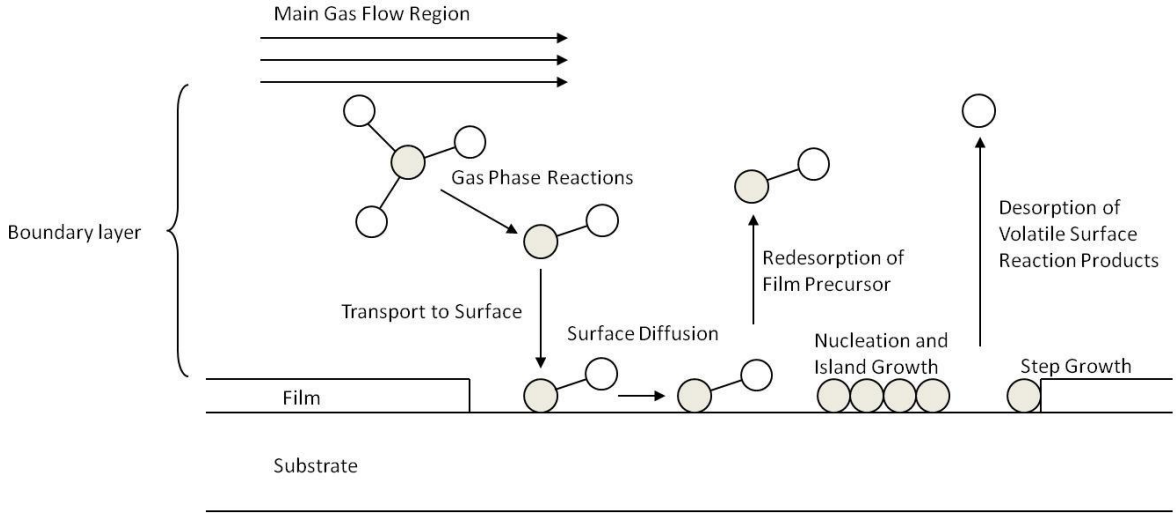

Figure 27 Schematic diagram of the CVD process.[173]

There are a wide range of CVD techniques which differ through changes in several parameters.

Pressure - CVD can either be carried out at atmospheric pressure chemical vapour deposition (APCVD) or under low pressure chemical vapour deposition (LPCVD).[184,185,186]

Precursor decomposition - The energy supplied to initiate the chemical reaction can be delivered in the form of heat, light, radio frequency, plasma or another method.

Number of precursors - The amount of precursor required for the deposition can either be from a single precursor (single source) which contains a preformed bond of

the desired product, or multiple precursors (dual or multiple sources) to form the bonds required in the desired film.

Precursor transport - The precursor can be introduced into the gas phase via heating, liquid injection or through the formation of an aerosol.[31,187,188]

Type of reactor - The reaction chamber can be hot walled or cold walled with a horizontal, vertical or dynamic substrate.

A distinct advantage of CVD is that it can be performed as a continuous process, which has a low consumption of energy, and is therefore achievable on an industrial scale. CVD is a non-line of sight process, so is able to give uniform conformal coatings which are usually chemically bonded to the substrate, giving high adhesion. Crystal structure, morphology and orientation of the deposited material can be controlled by careful selection of process parameters. Highly dense and pure materials can be produced by controlling the deposition rate and the precursor solutions.[189]

2.7.3 Physical Vapour Deposition

Physical vapour deposition (PVD) processes are atomistic deposition processes in which material is vaporized from a solid or liquid source in the form of atoms or molecules and transported in the form of a vapour through a vacuum, typically through a low pressure carrier gas (or plasma) environment directed at a substrate, where it condenses.[190] Unlike CVD, there are no chemical reactions that take place in the process.[191] The main types of PVD techniques are;

Evaporative deposition - resistive heating is used to vaporise the material which is then allowed to deposit onto a substrate.

Electron beam vapour deposition- a high energy beam of electrons bombards the sample material causing vaporisation, which is then subsequently deposited onto the desired substrate.[192]

Sputter coating - involves the use of a plasma discharge to vaporise the material and then condense onto a substrate.

Pulsed laser deposition - a high energy laser pulse causes evaporation of the material, prior to deposition on the substrate.[193]

Chapter 3

Experimental Methods and Materials Characterization

3.1 Experimental Methods

3.1.1 Aerosol-assisted Chemical Transport (AACT) Deposition

A novel PVD technique that utilises an ultrasonically generated aerosol containing TCO nanoparticles from a suspension, which is directed at a heated substrate. The nanoparticles are deposited on the substrate through evaporation of the solvent (figure 28). All the relevant reaction and deposition parameter details are discussed in the respective chapers, as they were different from one experiment to another.

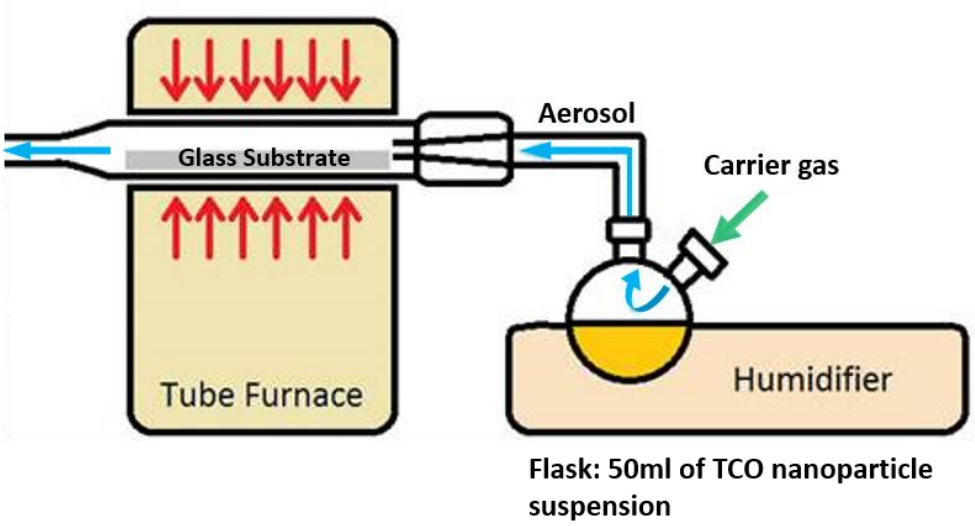

Figure 28 Schematic diagram of the aerosol assisted chemical transport (AACT) set-up.

3.1.2 Microwave-assisted Synthesis of TCOs

A One-pot synthesis of nanoscale ZnO based TCOs was carried out by dissolving a suitable metal precursor (acetate or halogenide) in diethylene glycol (DEG). A defined amount of water was added to the reaction mixture to initiate the hydrolysis. This mixture was then rapidly heated to 200 °C at a ramp rate of 20 °C min^{-1} to form the oxide from the hydroxide. At acertain temperature, precipitation of the metal doped

ZnO happens. DEG is a chelation agent and instantly complexes with the growing particles. As a result the grain growth is limited and the agglomeration of particles is prohibited.[194] The suspensions were heated for at the maximum ramp temperature, 200 °C for 30 mins. The average particle diameter can be agested by manipulating precursor concentration, water content and the duration of the reaction. An increase in any one of these parameters leads to particle fusing.[194] Furthermore, the type of metal precursor has to be selected carefully for each target TCO material. The minimum particle diameter is limited by the solubility of the components in DEG. Below a certain precursor concentration, no precipitation was found to occur. Synthesis of very large particles (> 1 μm) resulted in a more inhomogeneous size distribution. Upon cooling, the powders were collected by centrifuge and were washed with ethanol and dried in an oven for 1 hour at 60 °C to evaporate the solvent completely. The dried ZnO powders were annealed at 450 °C for an hour using a hotplate to remove the DEG from the powdered samples. All the relevant reaction details are discussed in the respective chapers.

The microwave-assisted synthesis was performed in an Anton Paar Multiwave PRO reactor in 100 mL fluorocarbon polymer (TFM) vessels. Figure 29 demonstrates the Anton Paar Multiwave PRO reactor which was used to the synthesis the AZO, GZO and AGZO powders reported in this report.

Figure 29 Anton Paar Multiwave PRO reactor.[195]

3.1.3 Microwave Assisted Thermal Processing of TCOs

TCOs (ITO thin films and doped ZnO pellets) were heat treated after fabrication using microwave assisted heating methods. Microwave assisted annealing of TCOs was performed using a microwave oven (Microwave research Applications Inc. BP-211/50, USA) operating at the 2.45GHz frequency with a maximum power of 3000W (figure 30). An IR temperature transmitter (M67S) is placed on top of the furnace and the temperature was recorded during the microwave treatment of samples. The samples were placed inside high purity insulator blocks to minimise the heat loss during the microwave processing. The gas environment can be modified within the microwave chamber using a specially designed quartz container as shown in figure 30b.

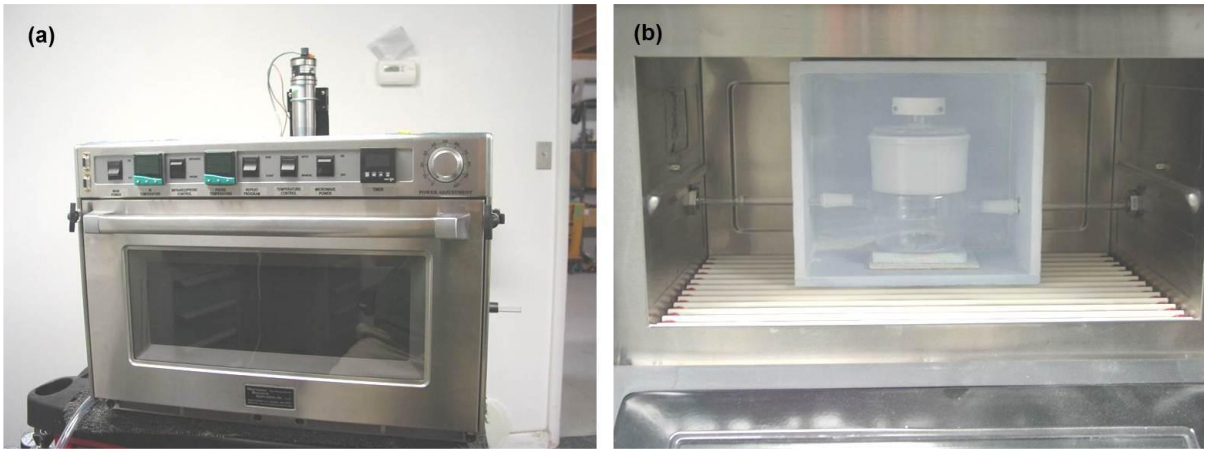

Figure 30 The images of (a) custom processing BP-211/50 microwave furnace with M67S IR temperature transmitter. (b) Microwave furnace chamber and the insulation.

3.1.4 Conventional Thermal Processing of TCOs

Conventional thermal annealing was carried out in a tube furnace (MTF-10-25-130, Carbolite Hope Valley, UK) with a ramp rate of 15ºC/min to the desired temperature. Both ends of the tube were kept open to allow for the flow of gas. After annealing the furnace was turned off and the samples were left in the furnace to cool down. An image of MTF-10-25-130 tube furnace is shown in figure 31. (Specific details about the experiments are discussed in relevant chapters).

Figure 31 Conventional thermal MTF-10-25-130 tube furnace.

3.2 Material Characterisation

3.2.1 X-ray Diffraction

X-ray diffraction (XRD) is one of the primary techniques that can be used to determine the crystalline structure of solid materials. When the X-rays interact with atoms in the crystal lattices of a solid, a diffraction pattern is generated. Since, each crystalline material has a unique atomic architecture, the generated XRD pattern is characteristic of the material from which is obtained and can be used as a fingerprint to identify the crystalline phases and its nature (i.e. packing density of the atoms, crystalline state, shape, stresses in the crystal lattice and size of the unit cell etc.).

English physicists Sir W.H. Bragg and his son Sir W.L. Bragg developed a relationship in 1913 to explain why the incident X-ray beams reflect at certain angles when they interact with atoms of crystalline phases. When X-rays interact with atoms in two lattice planes, and the path length difference between rays equals a whole multiple of the wavelength of the radiation, constructive interference occurs (Figure 32). Bragg's law describes the conditions for constructive interference in certain directions and the production of diffracted scattered X-rays:

$$n\lambda = 2d'sin\theta \quad (20)$$

Where n = an integer, λ = the wavelength of the X-rays, *d'* = the lattice spacing of a bragg (h,k,l) plane, θ = the angle between the incoming X-ray and the atomic layer. X-rays are scattered by atoms in the different crystalline planes (hkl) and are picked up by the detector, which then converts them in to intensity against 2θ spectrum. The XRD analysis enables to identify the material without destroying the sample.

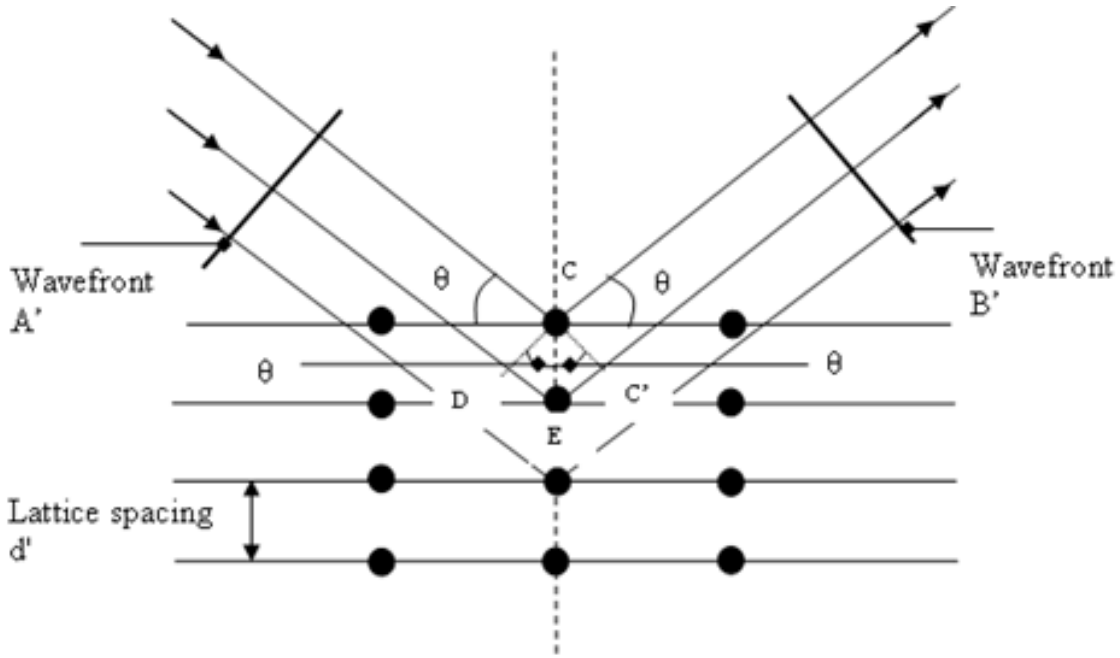

Figure 32 An X-ray diffraction beam schematic diagram showing the incident and scattered X-rays from a pair of atoms in different lattice planes.[196]

3.2.2 X-ray Photoelectron Spectroscopy

X-ray photoelectron spectroscopy (XPS) is a surface-sensitive quantitative spectroscopic technique. It can be used to characterise the surface (within ~ 1-10 nm usually) of materials. XPS can provide the elemental composition and the chemical or electronic state of each element in the surface. When the sample (placed in a vacuum environment) is irradiated with a photon beam in the X-ray energy range, an electron can be ejected from the surface of the material. The energy of these ejected electrons is measured over a range of kinetic energies and peaks appear in the spectrum from atoms emitting electrons of a characteristic energy. The kinetic energy of the electrons depends on the photon energy (from the irradiated beam) and on the binding energy of the electron (the energy required to remove the electron from the atom). The binding energy is dependant on the element from which the electron has been ejected, the orbital it has been ejected from and the chemical environment of the atom. Thus, analysis of the binding energy can allow elemental analysis of the surface of a material.

3.2.3 Field Emission Gun Electron Microscope (FEG-SEM) and EDX

This technique uses to investigate surface topography and particle morphology, as well as the cross-sectional thickness of the thin films. The sample is required to be clean, vacuum compatible and electrically conductive. While the electrodes fulfil the first two criteria, the third is not achieved, as the samples are constructed from a wide band gap semiconductor. Therefore, a thin layer of gold is sputter coated on to the surface of the electrode to accomplish this requirement. The system works by scanning the surface of the sample with a focused beam of electrons, which frees electrons from the atoms at the surface (from a depth of a few nm), as well as being reflected back from the sample. These emitted electrons are called secondary electrons and are considered to be electrons with energies less than 50eV. Secondary electrons are collected by an Everhard-Thornley detector and are converted in to a signal which is processed in to an image of the surface. Reflected electrons have energies greater than 50eV and can be collected by a second detector. These electrons are commonly referred to as backscattered electrons and provide elemental analysis as elements with large atomic numbers generate a higher number of back scattered electrons than those with lower atomic numbers. When secondary electrons are knocked out of an inner energy orbital, the atom is left in an excited state, however as the atom relaxes an electron from a higher energy level may drop in to this orbital. In doing so, the electron releases energy which can be in the form of x-rays (figure 33). As these x-rays are unique for each element, elemental analysis of the sample can be conducted. This technique is known as energy dispersive x-ray analysis (EDX). However, in this instance only the secondary electrons were collected to provide thickness and morphology information.

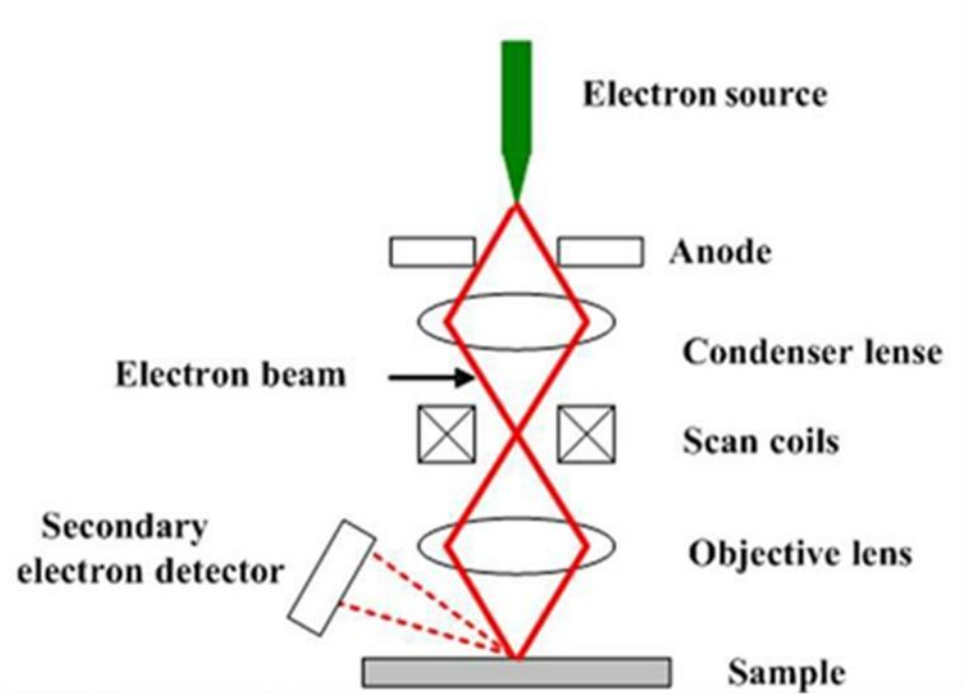

Figure 33 A schematic diagram of scanning electron microscope.[197]

3.2.4 UV-VIS Optical Absorbance

Optical transmittance measurements were conducted using a UV-VIS spectrometer. The system was blanked with plain glass for TCO thin film measurements. The light source was provided by a tungsten and deuterium lamp to provide the light with wavelengths ranging from 900 nm to 300 nm, so that near-infrared, visible and ultra violet regions of light were transmitted. The light passes through a series of slits and gratings before it is split into two equal beams (i.e. the dual beams). Consequently, the light that passes through the samples travels in one direction and little scattering occurs. As the light travels through the sample, some of the light is absorbed by the various layers in the electrode. The light that is transmitted is detected by the photodiode, which generates an electrical current proportional to the amount of light absorbed at different wavelengths resulting in an absorbance versus wavelength spectrum.

Spectrophotometry is used for both qualitative and quantitative analysis. The wavelength at the maximum of the absorption band will give information about the structure of the molecule or ion and the extent of the absorption is proportional to the amount of the species absorbing the light.[198] Quantitative measurements are carried out using the Beer-Lambert law (equation 21).

$$A = \varepsilon c l \qquad (21)$$

A is absorbance ($A = \log_{10}(I_0/I)$, where I_0 is the incident light's intensity and I is the light intensity after it passes through the sample. ε is molar absorbance or absorption coefficient (in $dm^3mol^{-1}cm^{-1}$). c is the concentration (molarity) of the compound (in $moldm^{-3}$). l is the path length of light in the sample (in cm).

3.2.5 Four Point Probe

A four-point probe is a simple apparatus for measuring the sheet resistance of a conducting material by passing a current through two outer probes and measuring the voltage through the inner probes (figure 34). This technique assumes that a thin film has a negligible thickness, is laterally homogeneous and is infinite in the XZ plane.

Probes with uniform spacing (s) typically around 0.5 to 1 mm apart, are placed on a material with t representing the thickness of the thin film. Below equation gives the R_S (in Ω/□) for shallow layers.

$$Rs = \frac{\rho}{t} \qquad (22)$$

Where the resistivity ρ (Ω.cm) given by,

$$\rho = \frac{\pi t}{\ln 2}\frac{V}{I} \qquad s \gg t \qquad (23)$$

In the above equations V is the measured voltage drop and I is the current passing though the probes. $\pi/ln2$ is equal to 4.53236, hence the if the applied current is in mA then the output measured in mV is equal to the sheet resistance.[199]

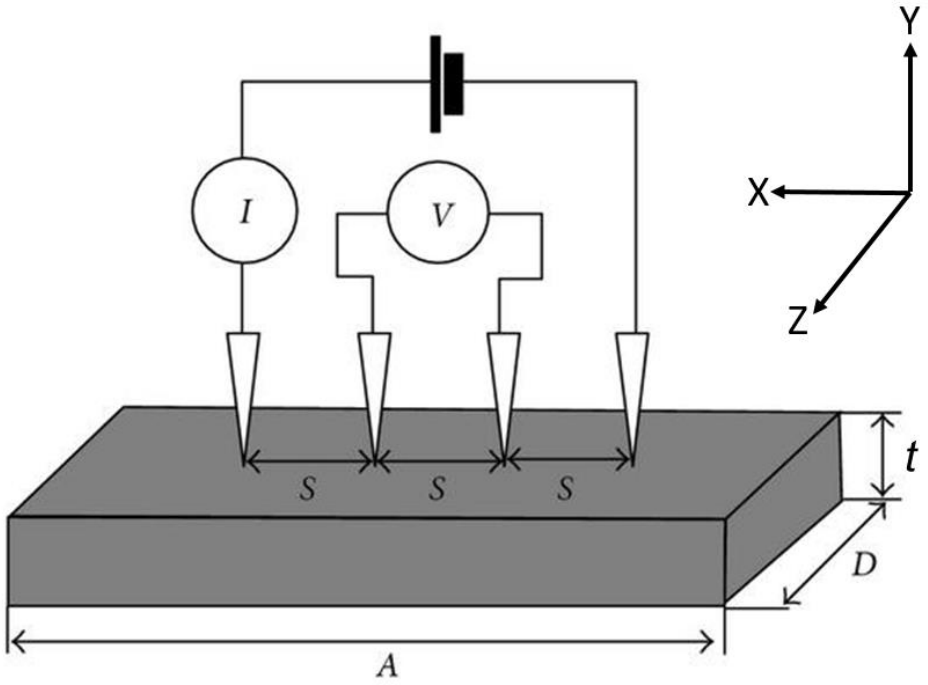

Figure 34 Schematic diagram of a test circuit in the four-point probe equipment. *A* and *D* are the length and the width od the sample.[200]

3.2.5.1 The Difference between Surface (Sheet) Resistivity and the Bulk (Volume) Resistivity

Surface resistivity is a measure of resistivity of a material along the plane or surface of the sheet. It is a useful measurement when measuring a thin film of material with a uniform thickness. The unit Ω/□ is only used for sheet resistance since it is dimensionally the same as Ω; it leaves no room for misinterpretation with the bulk resistance. Bulk resistivity, thus is a measurement of the resistivity of a material perpendicular to the plane. As explained in section 2.2, the volume resistivity (in Ω.cm) can be obtained, when sheet resistance is multiplied by the thickness (in cm) of the material. The difference between two resistivity measurements is shown in figure 35.

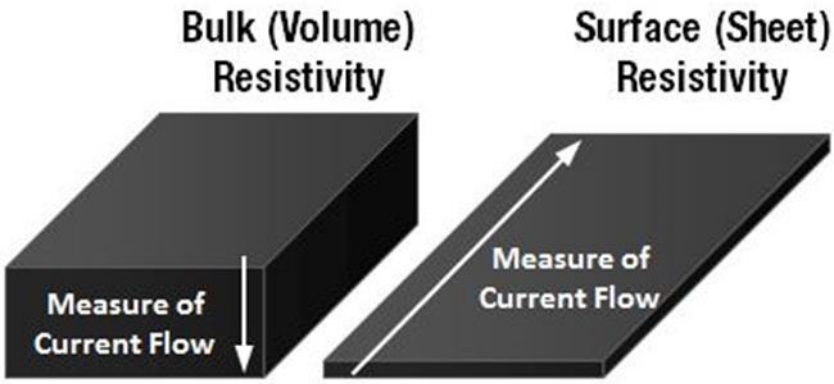

Figure 35 Bulk resistivity vs. surface resistivity.[201]

3.2.6 The Van der Pauw Hall Mobility Method

The van der Pauw Hall mobility method helps to calculate the properties of materials such as resistivity, doping type, carrier concentration and mobility.[199] It was first reported in 1958 by Leo J. van der Pauw.[202] This method employs a four-point probe placed around the perimeter of the sample, in contrast to the linear four point probe. Using four probes disregards measurement errors due to the probe resistance, the spreading resistance under each probe, and the contact resistance between each metal probe and the sample. As a high impedance voltmeter draws little current, the voltage drops across the probe resistance, spreading resistance, and contact resistance are very small, which minimise the overall error in the measurements.

The method involves appling a current via four small contacts on the circumference of a flat, arbitrarily shaped sample of uniform thickness and the voltage is measured. This technique is mostly useful for measuring very small samples as the geometric spacing of the contacts is insignificant. Effects due to a sample's size, which is the approximate probe spacing, are irrelevant. Therefore, this provides an average resistivity of the sample than in the sensing direction. This difference becomes important for anisotropic materials, which can be properly measured this method.

The resistance for each measurement is calculated using below equation according to the ohm's law,

$$R = \frac{V}{I} \qquad (24)$$

Where V is the measured voltage drop and I is the applied current. In the van der Pauw method, two average values, Ra and Rb are obtained for each pair of contacts opposite to each other. The sheet resistance can then be found by solving the van der Pauw equation as below,

$$e^{-\pi R_a/R_s} + e^{-\pi R_b/R_s} = 1 \qquad (25)$$

The resistivity is calculated calculated by multiplying the R_s with the thickness of the film in centimetres.

In order to, measure the carrier concentration, the sample is placed in a perpendicular magnetic field of known value and a known direct current is passed between one set of diagonally facing contacts. The Hall voltage between the second set of the diagonally facing contacts is then measured which is defined by the following equation,

$$V_H = IH/eNd \qquad (26)$$

Where H is the magnetic field, I is the applied current, N is the film carrier density, d is the film thickness and e is the elementary charge. Measuring the Hall voltage therefore enables the calculation of the film carrier density, which can be converted into the bulk carrier concentration by dividing the result by the thickness of the sample. Once the resistivity and carrier concentration are known, the mobility (μ) can be calculated using the equation below,

$$\mu = 1/eN_T\rho \qquad (27)$$

Where N_T is the material bulk carrier concentration (carriers/cm^3) and ρ is the resistivity.

3.2.7 Profilometer

A profilometer is used to measure the film thickness by the difference between the high and low points of the surface in nanometres. This is done mechanically with a feedback loop that monitors the force from the sample pushing up against the probe as it scans along the surface. A feedback system is used to keep the arm with a specific amount of

torque on it, known as the 'set point'. The changes in the *Z* position of the arm holder can then be used to reconstruct the surface. This technique requires force feedback and physically touching the surface, so while it is an extremely sensitive technique and provides the highest resolution, it is also sensitive to soft surfaces and the probe can become contaminated by the surface. This technique can also be destructive to some surfaces, as the needle drags along the surface. This technique involves physical movements in *X*, *Y* and *Z* while maintaining contact with the surface, so it can be much slower than non-contact techniques (figure 36).[203]

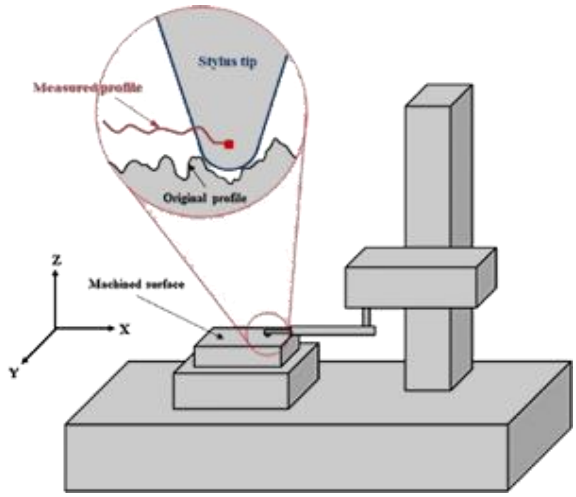

Figure 36 Schematic diagram of a Stylus Profilometer.[203]

3.2.8 Zeta Potential and Particle Size Measurements

The zeta potential is a measure of the electrostatic potential at the hydrodynamic plane of shear between a stationary liquid and a charged surface made up of a moving particle and the ions moving together with it.[204,205] This potential determines the net interparticle forces and is therefore an important property when investigating colloidal stability. It is normally measured as a function of pH or the amount of added surface stabilizer. The point where the zeta potential and thus the net interparticle forces are zero is called the isoelectric point (IEP), or point of zero charge (PZC). The movement of a charged particle relative to a stationary liquid under the influence of an applied electric field is called electrophoresis, whereas electro-osmosis refers to the motion of a liquid relative to a stationary charged surface. The velocity *v* of a particle in electrophoretic motion is given approximately by,

$$v = \frac{\varepsilon \zeta E}{f \pi \eta} \quad (28)$$

Where ε is the dielectric constant of the dispersion medium, ζ is the zeta potential, E is the electric field at the particle, f is a shape factor, and η is the viscosity of the medium. The ratio v/E is termed the electrophoretic mobility.

For nonconductive particles, where the extent of the ionic double layer around them is small relative to the radius of the particle, the applied electric field lines conform to the shape of the particles. For particles with conductivity equal to the bulk liquid, which is much smaller than the thickness of the ionic double layer, the applied field lines run straight between the electrodes, without conforming to the shape of the particles.

When measuring the electrophoretic velocity of dispersion, electro-osmotic effects also have to be taken into account, since the electro-osmotic flow is superimposed on the electrophoretic movement of the particles in the cell. At a certain point or level in the suspension – the stationary level – the resultant velocity of the osmotic flow is zero. Here, the electrophoretic mobility can be accurately measured. Another solution is to apply an alternating field of sufficiently high frequency to suppress electro-osmotic flows. Colloidal particles respond to the electric field much faster than the time it takes for the electro-osmotic flows to develop. Hence the mobility of particles can be measured within a short time interval before the electro-osmosis has started.

The electrophoretic velocity is measured with the laser Doppler method and utilizes electrophoretic light scattering (ELS). The output of a laser is split into two coherent beams which are cross-focused in the cell to illuminate the sample. The light scattered by the particle, together with the reference beam, is detected by a photomultiplier. Since the Doppler shift often is too small to detect due to the slow motion of the particles, the phase shift is instead detected.

Chapter 4

Aerosol-assisted fabrication of tin-doped indium oxide ceramic thin films from nanoparticle suspensions

4.1 Overview

Metal oxide ceramics have attracted significant attention due to their wide use in electronic and optoelectronic applications.[206,207] Among them, transparent conducting metal oxide (TCO) ceramics have received particular attention due to their applications in modern electronic devices such as touch panel displays, smart windows, optics, biochemical and environmental sensors as well as transducers.[38,208,209] Generally TCO thin films require high optical transparency in the visible light spectrum and high electrical conductivity, which is not possible in an intrinsic stoichiometric material.[210] TCOs are prepared by addition of dopants at various concentrations into a crystal lattice of pure semiconductors, thereby altering the optical and electrical properties of the material. The electrical and optical properties of TCO ceramics, can be controlled during the deposition and post-deposition heat-treatment steps asthey are dependent on the film nanostructure, coverage and particle connections.[14,15] Pulsed laser deposition (PLD),[30] chemical vapour deposition (CVD),[19,31,32,211] and radio frequency (RF) sputtering[34–36] are thin film deposition techniques commonly used in depositing TCO films. Typically, these deposition techniques require a vacuum pressure ($\sim 10^{-6}$ Pa) or higher deposition temperatures (450 – 700 ^{o}C) over a long period of time, hence, the energy demand and overall production cost are high. Therefore, there is a considerable interest in developing low and inexpensive film fabrication methods and processing technologies to improve the optical and electrical properties.

Aerosol assisted[20,212] and sol-gel[213–215] deposition methods are considered to be simple and inexpensive routes for thin film fabrication as they do not require specially designed heated reactor lines and high vacuum systems. For example, already known methods such as aerosol assisted chemical vapour deposition (AACVD), atmospheric pressure chemical vapour deposition (APCVD) and sol-gel deposition do not require

specially designed metal-organic precursors and high temperature zones.[13,19,22] Aerosol-assisted chemical transport (AACT), a physical vapour deposition method, was used to deposit TCO thin films in this study using nanoparticle suspensions at relatively low temperatures. In the AACT technique, aerosol droplets containing nanoparticles can be generated by nebulising a nanoparticle suspension using an ultrasonic generator, the droplets are then transported onto the substrate at a relatively low temperature (i.e. 50 ^{o}C) using an inert carrier gas, thus depositing a thin film of nanoparticles on the substrate due to solvent evaporation. The AACT method has been previously used in our laboratory to deposit CuI thin films on glass substrates,[217] which were then suitably heat-treated post-deposition by conventional radiant heating.

Post-deposition heat-treatments are important for strengthening particle-particle and particle-substrate connections in the film and improve the conductive properties of the deposited film. However, conventional radiant annealing can lead to the breakdown of the film nanostructure and its physical nature, leading to poor conductivity. Hence, a great deal of interest has been directed in recent years towards microwave irradiation as an alternative material annealing technique in place of conventional radiant sintering.[218] This technique is capable of improving particle necking and crystallinity with minimal effect on the surface texture, due to the fact that microwave irradiation generates a volumetric heating profile compared to radiant sintering.[32,219] Furthermore, there are many unique characteristics of microwave assisted sintering, including its ability to achieve higher heating rates, short processing times, selective heating and greater control of the heating process, which helps to improve the crystallinity as well as inter-particle and particle-substrate connections in the film.[220]

This chapter demonstrates a new and simple aerosol assisted physical vapour deposition technique (i.e. AACT) to fabricate TCO films by using TCO nanoparticle suspensions which is conducted for the first time. Sn-doped In_2O_3 (ITO) thin films were fabricated on float glass substrates from a nanoparticle suspension using a new and inexpensive aerosol-assisted chemical transport (AACT) process. The influence of the solvent type, loading level and film deposition time on the structural, electrical and optical properties of the deposited thin films was investigated. In addition, the effect of post-deposition heat-treatment of ITO films on the film resistivity and transparency was investigated using microwave radiation and compared with conventional radiant heat-

treated films; in particular, the microwave heat treatment was relatively shorter, which significantly reduced the energy input for that step compared to more conventional radiant heating. The SEM images of the films prepared using a 30 min deposition time with 0.20% (wt/vol%) methanolic ITO suspension provided better surface coverage compared to the other deposition times investigated. The optimised ITO films were heat-treated after deposition by either conventional radiant or microwave assisted heating methods in order to improve the inter-particle connections and film adherence. The films heat-treated after deposition by microwave annealing exhibited an average transmittance of >85% in the visible region with a resistivity of 12 Ω.cm and a carrier concentration of -3.7 x 10^{16} cm^3, which was superior to films that were heat-treated using more conventional thermal processing (despite the shorter processing time for the microwave process). The resistivity of ITO films was further decreased to 6.0 x 10^{-2} Ω.cm with an increased carrier concentration of -8.0 x 10^{18} cm^3 when ethyl cellulose was added to the ITO suspension prior to the AACT deposition. The enhanced conductivity of this film is due to the improved particle-particle and particle-substrate connections as observed by SEM imaging. Furthermore, the resistivity of the microwave heat treated AACT ITO films showed comparable results to the films reported by sol-gel method.[213,215]

4.2 Experimental Details and Characterization Techniques

4.2.1 ITO Nanoparticle Synthesis

ITO nanoparticles (with 10 at% Sn) were directly synthesised using a continuous hydrothermal flow synthesis (CHFS) method as discussed in a previous report.[221] Briefly, a solution of 0.09 M indium(III) nitrate (99 %, Alfa Aesar, Lancashire, UK) was pumped to meet a flow consisting of a combined solution of 0.01 M potassium stannate trihydrate (99.9 %, Sigma Aldrich, Dorset, UK) and 0.3 M KOH (Fisher Scientific, Leicestershire, UK) at room temperature in a low volume stainless steel T-piece. Each of these precursor feeds was pumped at a flow rate of 25 mL min^{-1}. Separately, a 80 mL min^{-1} flow of deionised water was heated to 450 °C and then mixed with a 20 mL min^{-1} flow of 1 M formic acid (≥95 %, Sigma Aldrich, Dorset, UK), before mixing with the combined precursor feeds within a confined jet mixer,[222] resulting in rapid precipitation

of nanoparticles. The resulting suspension was cooled in-line by passing it through a pipe-in-pipe heat-exchanger. The blue slurry product was then collected at the outlet of the back-pressure regulator (Tescom). The material was purified by three cycles of centrifugation and washing with deionised water, before being freeze-dried at 13 Pa with slow heating from −60 to 25 ^{o}C (over 24 h) to a form a free-flowing blue powder.

4.2.2 ITO Suspension Preparation

A series of ITO suspensions with different loadings were made by adding 0.02, 0.04, 0.06, and 0.1 g of nano-ITO powder (made as detailed above via CHFS) to 50 mL of each solvent followed by 15 min of sonication using a sonicator probe (S-4000, Misonix, Inc, USA). The solvents used were methanol (100%, VWR Chemicals), ethanol (99.9%, VWR Chemicals), propan-2-ol (99.9%, VWR Chemicals) and acetone (100%, VWR Chemicals). Each suspension with corresponding wt/vol percentages of 0.04%, 0.08%, 0.12% and 0.20% was used to fabricate ITO thin films by the AACT technique. The particle size and the zeta potential of the suspensions were recorded using a Zetasizer-nano (Malvern Instruments Ltd, UK).

4.2.3 ITO Thin Film Deposition by AACT Method

ITO films were deposited on 1 x 2 cm^2 float glass (NSG, Pilkington, UK) substrates held at 50 ˚C by AACT. The glass substrates were ultrasonically cleaned with doubly distilled water, acetone, propan-2-ol, and then stored in ethanol prior to the deposition. Figure 28 shows a schematic diagram of the AACT set-up (in section 3.1.1).

In this deposition method, an ultrasonically generated aerosol containing ITO nanoparticles was directed via an argon gas flow (BOC, UK) at a flow rate of 108 mL min^{-1} towards the substrate, which was held at 50 ^{o}C in a tube furnace (MTF-10-25-130, Carbolite, UK). The ITO films were optimised for higher surface coverage of the substrate by varying the solvent type, loading level and the deposition time.

In some experiments, 0.01 g of ethyl cellulose (Sigma-Aldrich) was added in to the 50 mL of nanoparticle suspension and stirred until it fully dissolved prior to the deposition in order to improve the binding properties of the ITO particles.

4.2.4 Post-deposition Heat Treatment of ITO Films

The ITO films prepared by AACT method were post-deposition heat-treated using conventional radiant as well as microwave- assisted heating methods. Conventional radiant heating was carried out in a tube furnace (MTF-10-25-130, Carbolite, UK) with a ramp rate of 15 ˚C min^{-1} to 600 ˚C and then held for 3 hrs under a steady N_2 flow of 1825 mL min^{-1} (N_2 purity > 99 %, BOC). After heat-treatment, the furnace was turned off and the samples were allowed to cool down to room temperature in the tube furnace under continuous N_2 flow. Alternatively, microwave-assisted annealing was performed using a microwave oven (Microwave research Applications Inc. BP-211/50, USA) operating at 2.45 GHz frequency with a maximum power of 3000 W. The sintering of the ITO films was assisted by placing the samples between SiC susceptor tiles and the heat loss during annealing was minimized by shielding the sample with insulator blocks.[223] The microwave sintering of the films was conducted under a constant gas flow of N_2 at 1825 mL min^{-1} (BOC, UK) and the sintering was conducted for 90 s. During the sintering, the temperature of the SiC susceptor was monitored using an infrared temperature probe (Mikron infrared Inc. M67/M67S series, USA) with an error of ± 5 ^{o}C. After 90 s, the temperature of the susceptor reached 600 ^{o}C.

4.2.5 Characterisation of ITO Thin Films

The microstructure and surface morphology of the ITO thin films were investigated using a field emission gun scanning electron microscope (FEG-SEM, Jeol, Hertfordshire, UK) operating at an accelerating voltage of 5 keV and a working distance of 5 mm. The phase and crystallinity of the as-deposited and sintered films were studied using a Bruker D8 XRD, operating with monochromatic Cu K_α (k = 1.54 Å) radiation and a position sensitive detector. The optical transmittance measurements were conducted using a dual beam Perkin-Elmer Lambda 35 UV-Vis spectrometer (Perkin Elmer, Massachusetts, US) over the wavelength range of 300 nm – 800 nm. A standard scotch tape test was conducted to assess the film adherence.[224] The sheet resistance was measured by a four point probe conductivity meter (Jandel, HM20, Jandel Engineering Ltd., Linslade, UK) and the film thickness was measured using an Ambios XP2 stylus profilometer in order to calculate the film resistivity. Hall effect measurements were

carried out using the Van der Pauw method to determine the bulk resistivity of the films. The films were subjected to an input current of 1 μA and a calibrated magnetic field of 0.58 T. The transverse voltage was then measured. The measurement was repeated by reversing the direction of the magnetic field and the current. For the measurements, we used ECOPIA Hall effect measurement system (HMS-3000).

4.3 Results and Discussion

4.3.1 ITO Suspension Preparation

Preparation of a stable nanoparticle suspension in a suitable solvent is very important in order to deposit ITO thin films by the AACT technique. Herein, the solvent was required to evaporate under the operational/deposition temperature of the experiment. The suspensions of 0.04, 0.08, 0.12 and 0.20 wt/vol% were prepared by adding the corresponding weight of ITO powder to 50 mL of each solvent used in this study, followed by 15 min of sonication using a sonicator probe. ITO suspensions made in both methanol and ethanol showed the best stability for a period over 30 min, which was sufficient to complete the deposition cycle. The particle size distribution and the surface charge of the particles were monitored with a Zetasizer-nano. For example, the recorded particle size distribution and the zeta potential distribution curves of the 0.20 wt/vol% ITO methanolic suspension are shown in figures 37 and 38 respectively. The average ITO particle size in the methanolic suspension was observed to be around 130 nm, whereas the average zeta potential value (at pH 5) was +25 mV. These values indicated that there is less chance of agglomeration of ITO particles in the methanol media as the positive surface charge of the ITO particles causes particles to separate from each other due to repulsion. However, due to the high surface energy of these nanoparticles, they tend to agglomerate during the evaporation of the solvent.[225] The addition of surfactants or binders lowered the surface energy of nanoparticles, thereby preventing the particle agglomeration.[226]

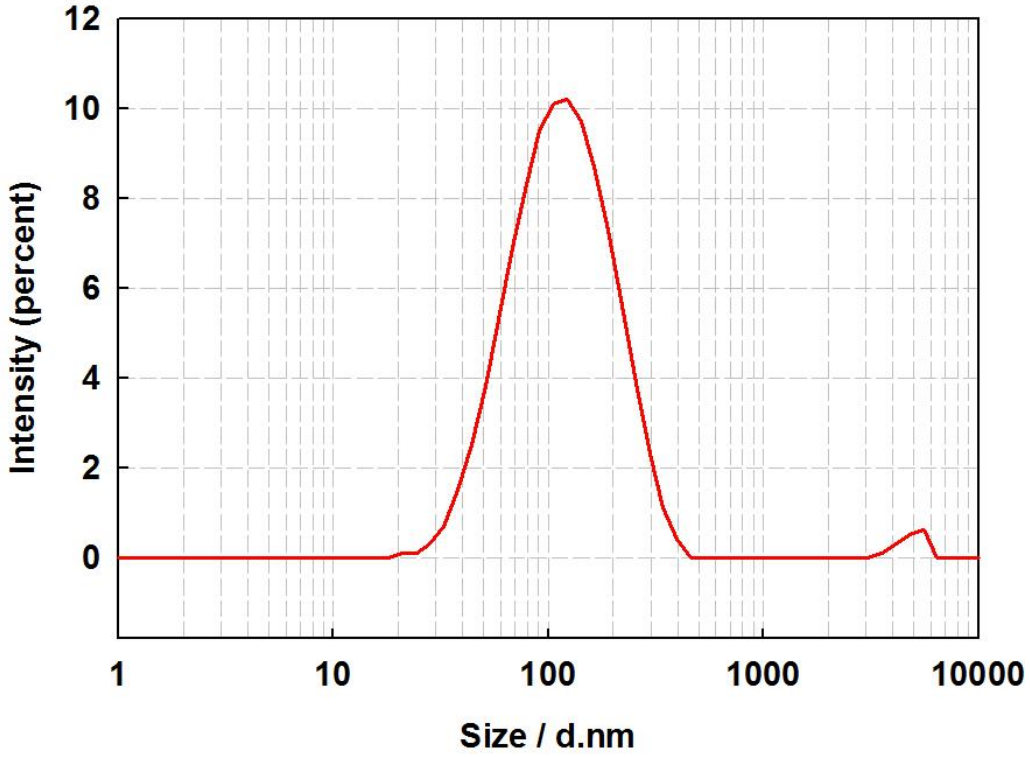

Figure 37 Particle size distribution of the 0.20 wt/vol % ITO suspension in methanol.

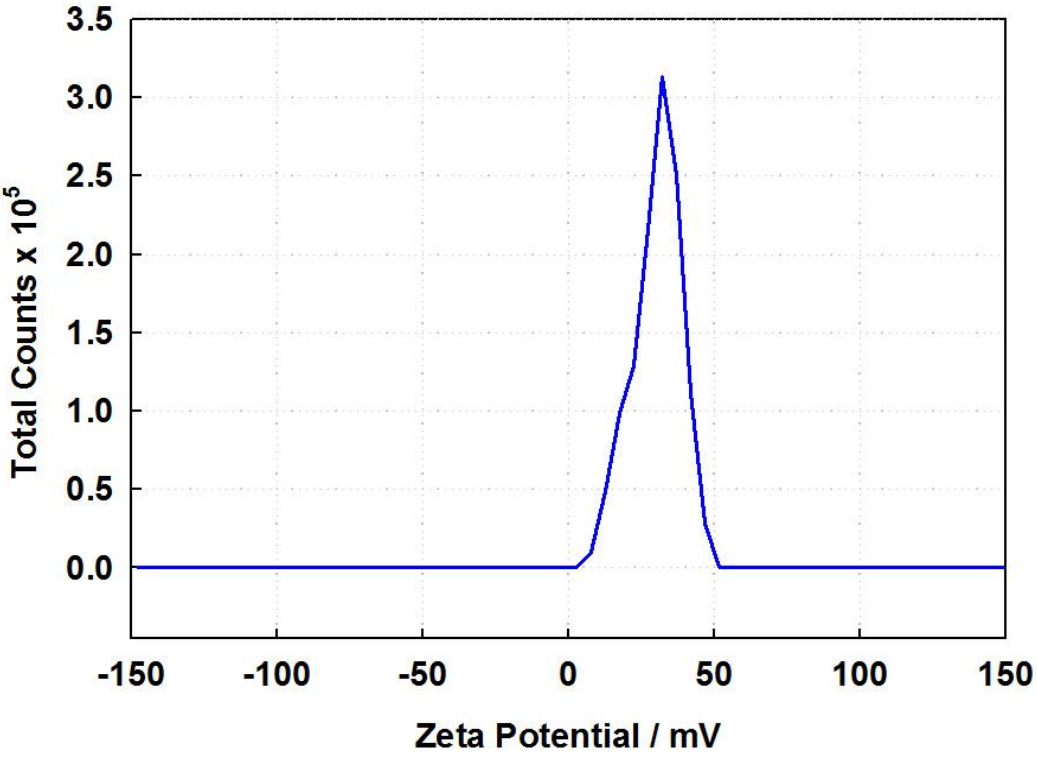

Figure 38 Zeta potential distribution curves for the 0.20 wt/vol % ITO suspension in methanol.

4.3.2 ITO Thin Film Fabrication using AACT and Optimisation for Surface Coverage

ITO thin films were deposited at 50 ^{o}C on glass substrates using the AACT technique. The deposition parameters were systematically investigated in order to control nanoparticle surface coverage. The surface coverage of nanoparticles in the film was controlled by means of solvent type, loading level and deposition time. The FEG-SEM images (figure 39) show the surface morphology of ITO thin films deposited using 0.20 wt/vol% suspensions in methanol, ethanol, propan-2-ol and acetone. The films deposited using methanol (figure 39a) and ethanol (figure 39b), showed good surface coverage compared to those deposited using propan-2-ol (figure 39c) and acetone (figure 39d). Since these suspensions contain no binders, the nanoparticles in the films were aggregated. The SEM images showed the randomly oriented, nano-scale spherical particles along with some nanoparticle clusters in the film. In fact, the clusters were more prominent in the films deposited using propan-2-ol and acetone, leading to patchy coverage. The SEM investigation confirmed that the best ITO nanoparticle coverage on glass substrates was obtained for the films deposited using methanolic and ethanolic suspensions.

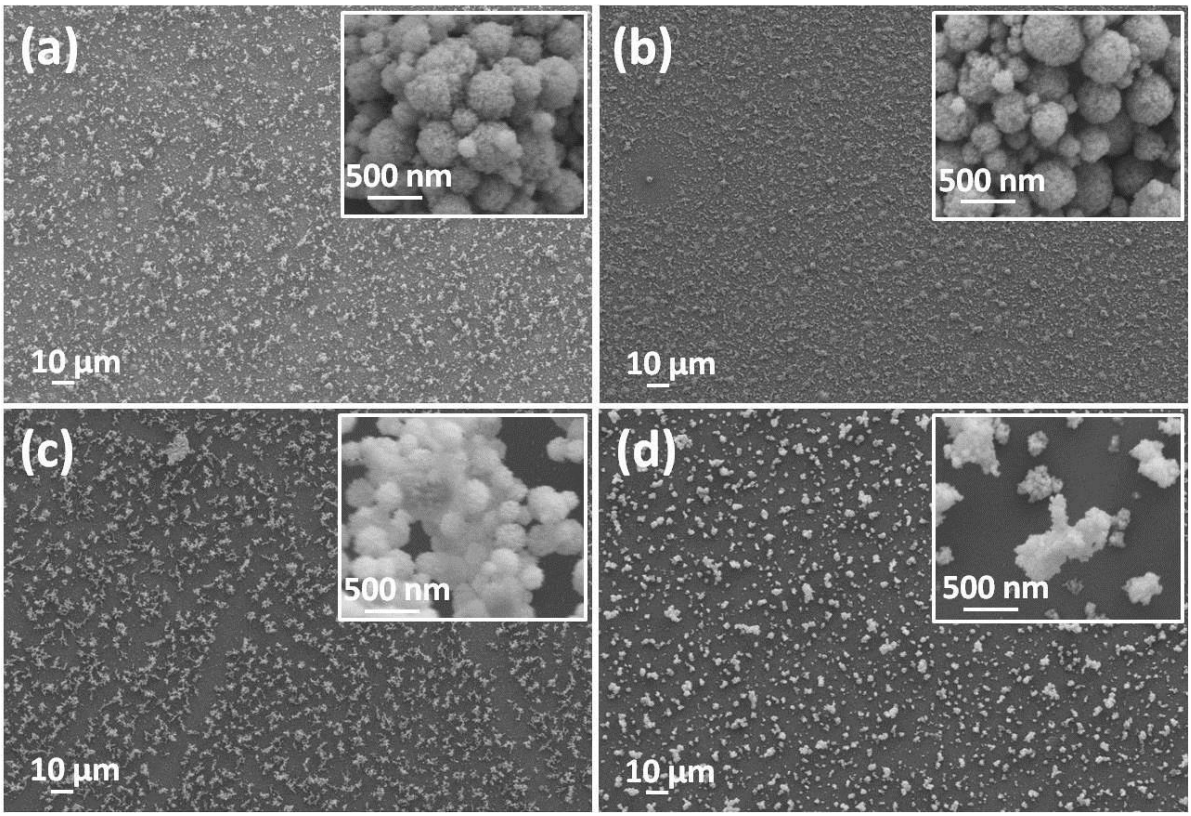

Figure 39 The FEG-SEM images of ITO thin films deposited for 30 min using 0.20 wt/vol% suspensions made with (a) methanol, (b) ethanol, (c) propan-2-ol, and (d) acetone.

The films deposited using methanol and ethanol suspensions illustrated agglomerates on a uniform layer of nanoparticles. The higher magnified surface topographic images of the films deposited by these suspensions, shown in figure 40, confirmed that a relatively good ITO nanoparticle coverage can be obtained when methanol was used as the solvent (figures. 40a-c).

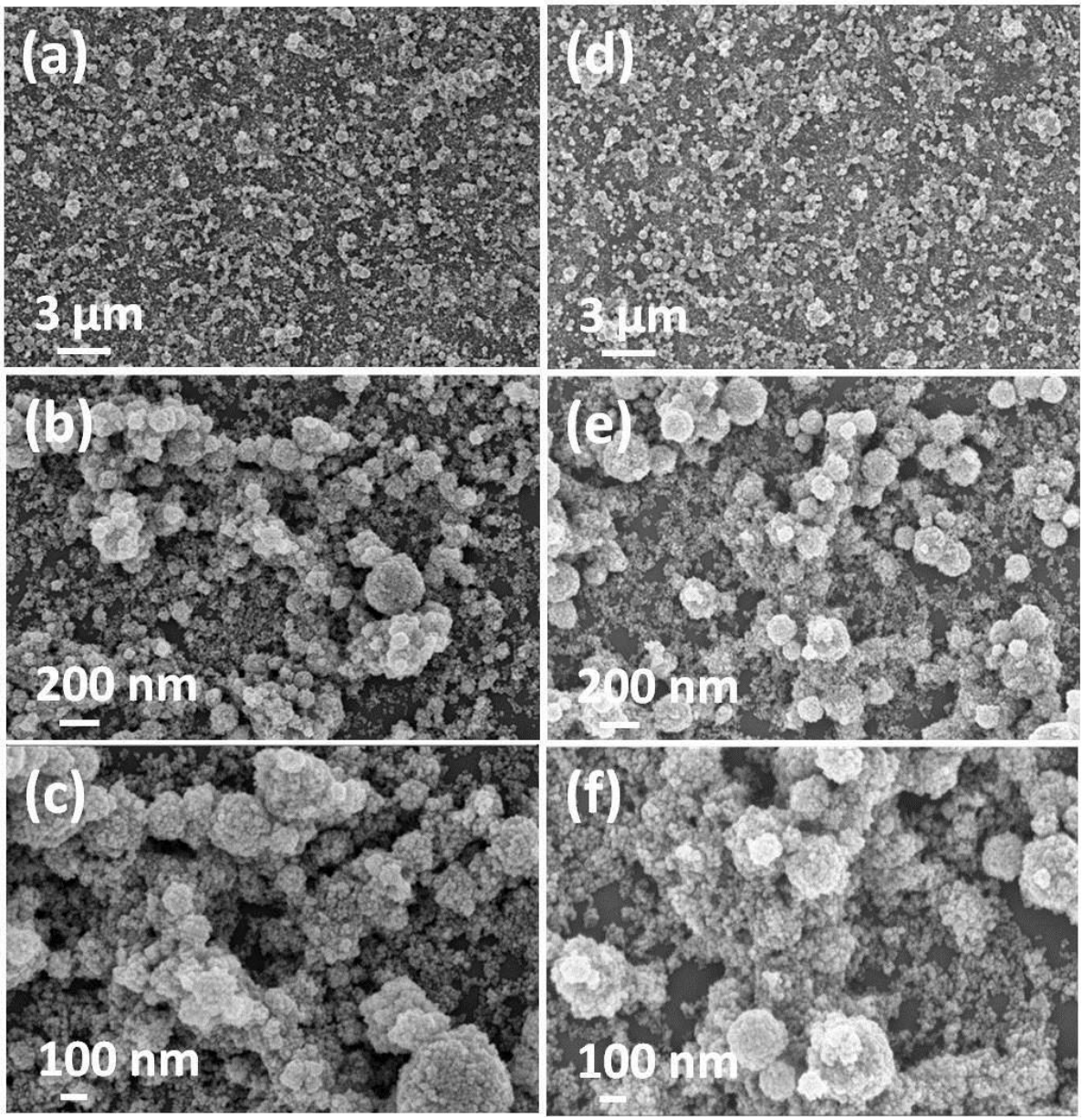

Figure 40 FEG-SEM images at different magnifications of the ITO thin films deposited for 30 min using 0.20 wt/vol% suspensions made with methanol (a-c) and ethanol (d-f).

The effect of the loading level of the methanolic ITO nanoparticle suspension on the film coverage was also studied. The SEM surface morphologies of films deposited using suspensions with loadings between 0.04 - 0.20 by wt/vol% are shown in figure 41. The images indicated that the film coverage not only dependent on the solvent type, but also on the ITO loading level in the suspension. It was apparent that at relatively low loadings (i.e. 0.04 - 0.12 wt/vol%), the resulting films had poor nanoparticle coverage

(figures 41a, 41b and 41c). This may be due to the low nanoparticle content in the aerosol droplets. When the suspension loading was further increased to 0.20 wt/vol%, the deposited film showed improved surface coverage (figure 41d).

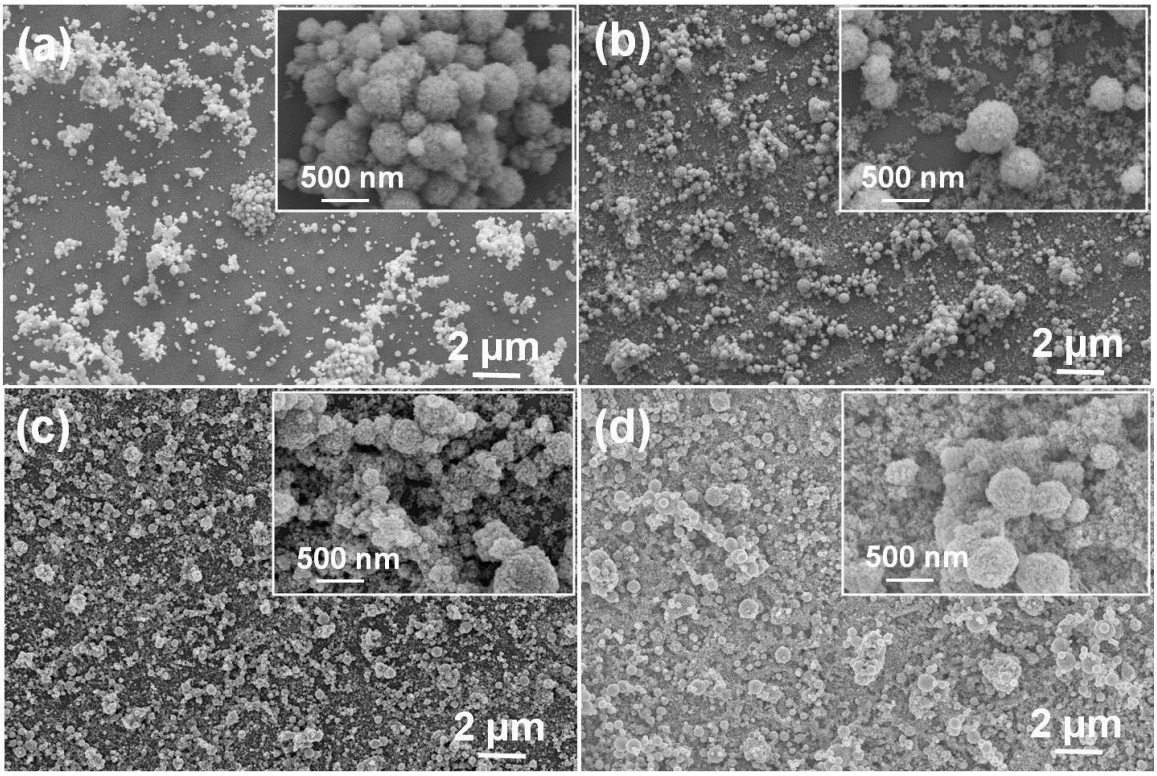

Figure 41 FEG-SEM images of ITO thin films deposited for 30 min by AACT using methanolic suspensions with loading levels of (a) 0.04%, (b) 0.08%, (c) 0.12% and (d) 0.20% by wt/vol%.

Along with the solvent type and solid loading, the deposition time is another key parameter that affects the nanoparticle coverage of the film. Therefore, studies were conducted to investigate the influence of the deposition time on the nanoparticle coverage. Since our investigation thus far showed that films deposited from methanolic suspension with a 0.20 wt/vol% loading had a better coverage, those conditions were adopted to study the effect of the deposition time.

Figure 42 shows the surface topographical SEM images of ITO films deposited at different deposition times by AACT. The deposition time was varied from 5 to 45 mins, whilst maintaining a constant deposition rate. As shown in figure 42b, it was found that

the films prepared over 30 and 45 min deposition times, had a complete nanoparticle surface coverage than the film deposited for 5 min. However, the film deposited over 45 min was appeared to be powdery which could be due to pronounced nanoparticle aggregation in the film. The application of the standard adherence test resulted in removal of the film (figure 42d), which was evidence of the powdery nature of the film.

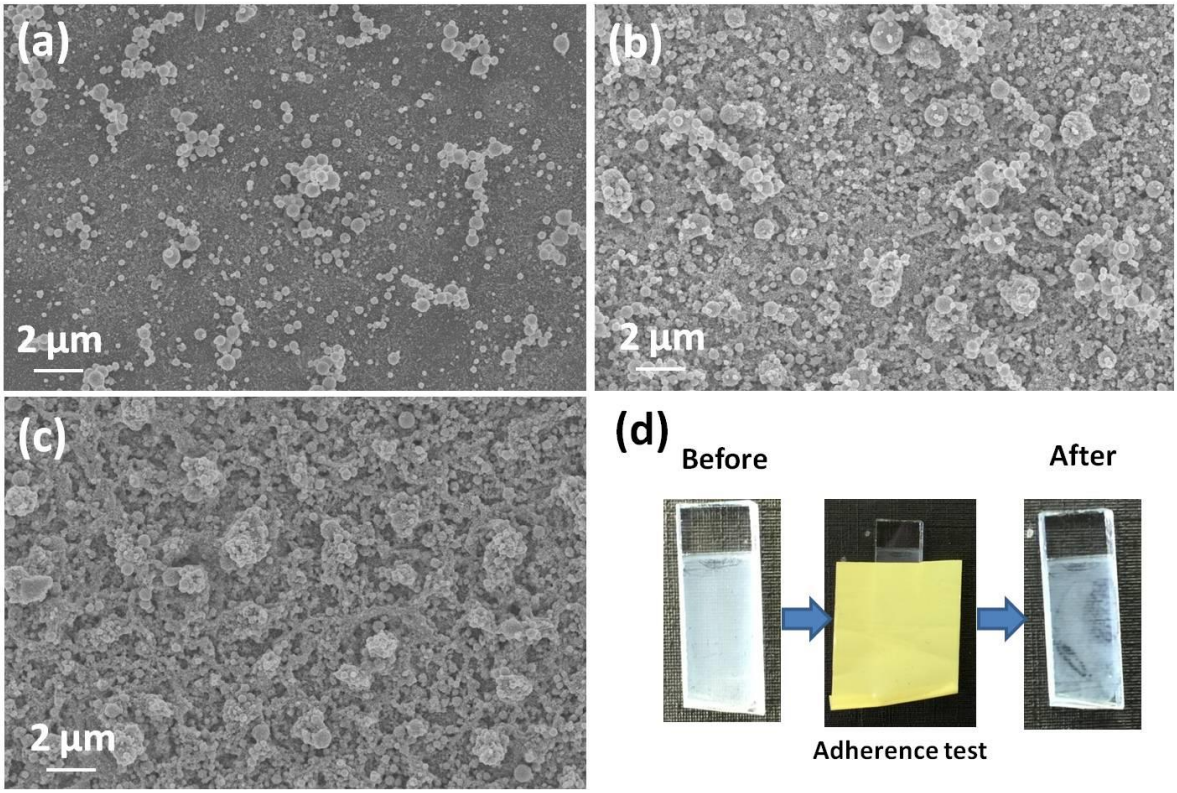

Figure 42 Surface topographical FEG-SEM images of ITO thin films deposited by AACT using a 0.20 wt/vol% methanolic suspension for different deposition times (a) 5 min, (b) 30 min, (c) 45 min and (d) images of the scotch tape test for the 45 min deposited film.

4.3.3 Post-deposition Sintering of AACT Deposited ITO Films

Post-deposition sintering of ceramics is a key processing technique that can be used to enhance the electrical connection between individual particles themselves, as well as particle-substrate interactions, which also eventually improves the crystallinity and nanostructure in the film.[227] In recent years, a great deal of interest has been focused on irradiation with microwaves as an alternative ceramic post-deposition sintering

technique to conventional radiant annealing. It is capable of improving particle necking and crystallinity with a minimal effect on the material's original nanostructure formed after the drying step.[228,229] Figure 43 shows the surface morphology of as-deposited, microwave and conventional radiantly heat-treated ITO films, which were deposited for 30 min by AACT using a 0.20 wt/vol% methanolic ITO suspension. It is intriguing that the edges of the crystallites of microwave treated ITO films were well-defined and smoother compared to those in the more conventional radiantly heated film (Figure 43b).

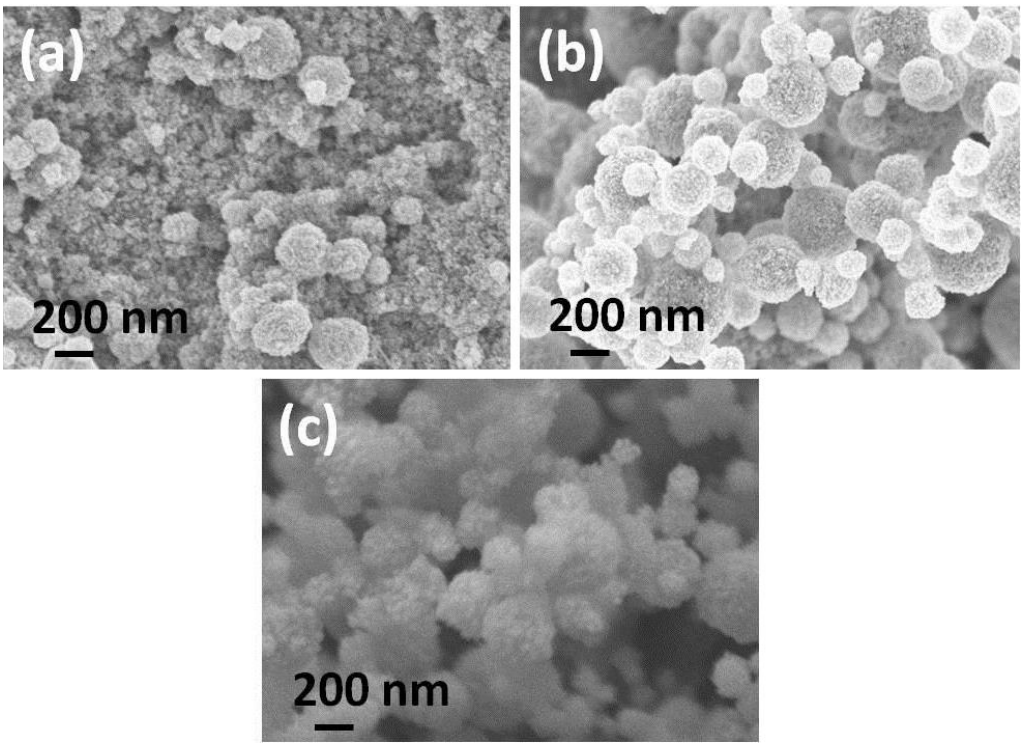

Figure 43 FEG-SEM images of ITO thin films deposited by AACT for 30 min using a 0.20 wt/vol% methanolic suspension (a) as-deposited, (b) post-deposition heat-treated to 600 ^{o}C from 90s by microwaves, (c) conventional radiant post-heated for 600 ^{o}C for 3 hrs.

As shown in figure 43b, the best ITO films obtained in this study so far still contained agglomerates. The addition of surfactants or binders is known to lower the surface energy of nanoparticles and thereby reducing particle agglomeration.[226] Therefore, we

have investigated the effect of ethyl cellulose (EC) in the nanoparticle suspension; when EC was added to the ITO nanoparticle suspension used in the AACT process, the textural nature of the resulting films were more compact with better inter-particle necking compared to the ITO films without EC as shown in tilted SEM images in figure 44.

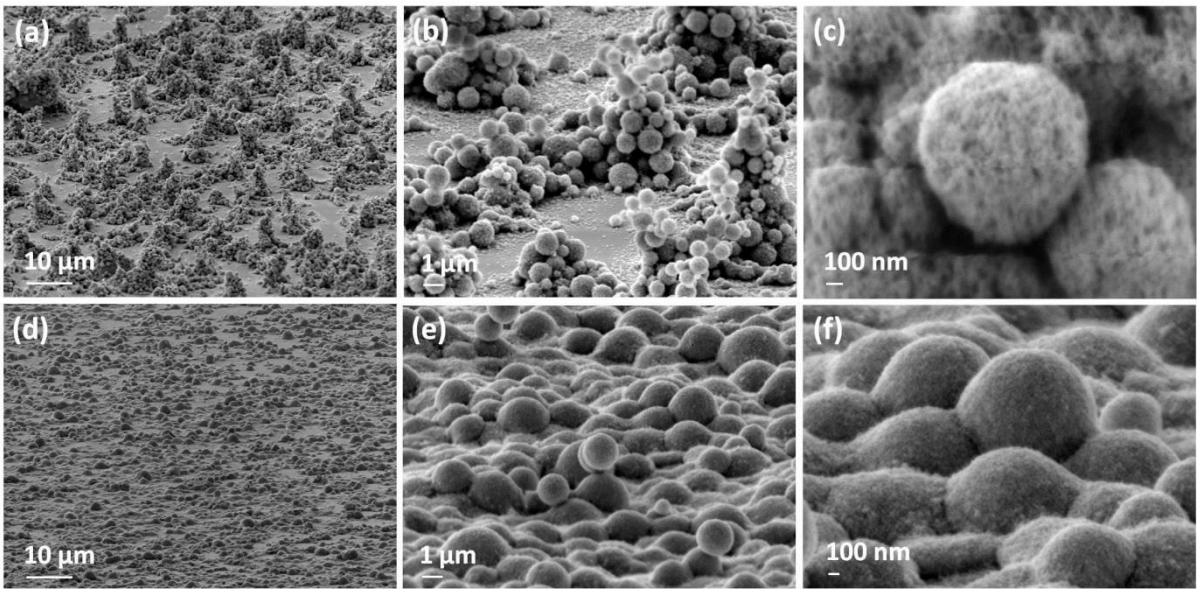

Figure 44 The tilted FEG-SEM images of as-prepared ITO thin films by AACT for 30 min using 0.20 wt/vol% methanolic suspension (a-b) different magnified images without adding the EC binder (b) different magnified images of ITO films deposited including 0.01 g of EC as a binder.

After the post-deposition heat-treatment step, a significant change in the film morphology with the addition of EC was observed (figure 45), suggesting during post-deposition heat-treatment, new binding mechanisms between the agglomerates and binder may have resulted in a more compact film, albeit with more cracks. According to the reported dielectric properties of EC,[230] heat generation by absorbing microwave radiation can be expected in the ITO films with EC. Generally, the dielectric properties of materials vary with the temperature. Due to the increase in the dielectric properties at the elevated temperatures, microwave absorption increases and enhances the heat generation in materials. Therefore, we believe that during the microwave heat treatment, EC molecules in the films could absorb microwaves and generate heat locally

until the substrate temperature reached the EC decomposition temperature. Hence, the particles around the EC molecules may experience slightly higher temperature due to this local heat generation by EC molecules exist in the film. However, the EC molecules will burn off when the temperature reached above its decomposition temperature result in voids where the EC was present in the films. As the temperature of the ITO particles around the voids is slightly higher than the bulk, therefore better sintering can be expected in such films under microwave heat treatment compared to conventional radiant annealing.

Furthermore, it is evident that addition of EC helped to improve the necking between the particles as well as with the substrate, which was demonstrated by a standard scotch tape test. The images further show that the crystallized grains of microwave sintered film were more uniform (figure 45a) than the conventionally sintered ITO film, despite the fact that the required microwave processing time (90 s) being much shorter than that of the radiant annealing time of 3 hrs (figure 45b).

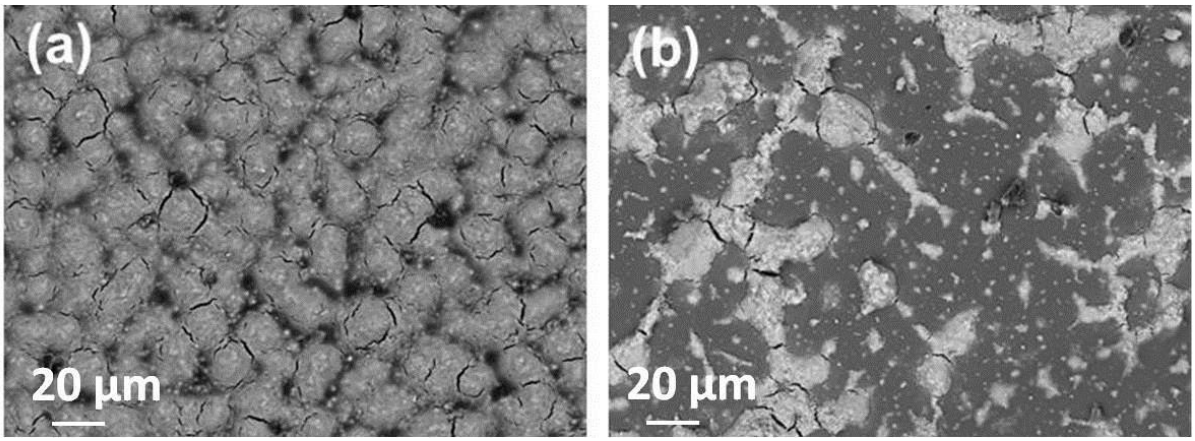

Figure 45 FEG-SEM images of ITO thin films deposited by AACT for 30 min using 0.20 wt/vol% methanolic suspension including 0.01 g of ethyl cellulose as a binder (a) post-deposition heat-treated to 600 ^{o}C from 90s by microwaves, (b) conventional radiant annealed at 600 ^{o}C for 3 hrs.

4.3.4 Materials Characterization

Powder X-ray diffraction (XRD) data collection and analysis were employed to determine the crystalline structure of the ITO powder sample and the films deposited by AACT. XRD diffractograms of the ITO powder, as deposited film and post sintered powder are shown in figure 46(a). The XRD diffractograms of the as-prepared and as-deposited ITO show reflections for both In_2O_3 and InOOH phases. For the ITO powder annealed at 600 ^{o}C for 3 hrs under N_2 atmosphere (figure 46b), the diffraction peaks correlated well with the lattice planes of the pure cubic structure of In_2O_3 (JCPDS 76-0152). Figure 46c illustrates the XRD diffractograms of as deposited and microwave heat treated ITO films with the addition of EC. The higher intensity in the In_2O_3 reflections of the microwave heat-treated sample indicated the InOOH phase transformation, enhancement in the crystal size and the improved crystallinity of the films.

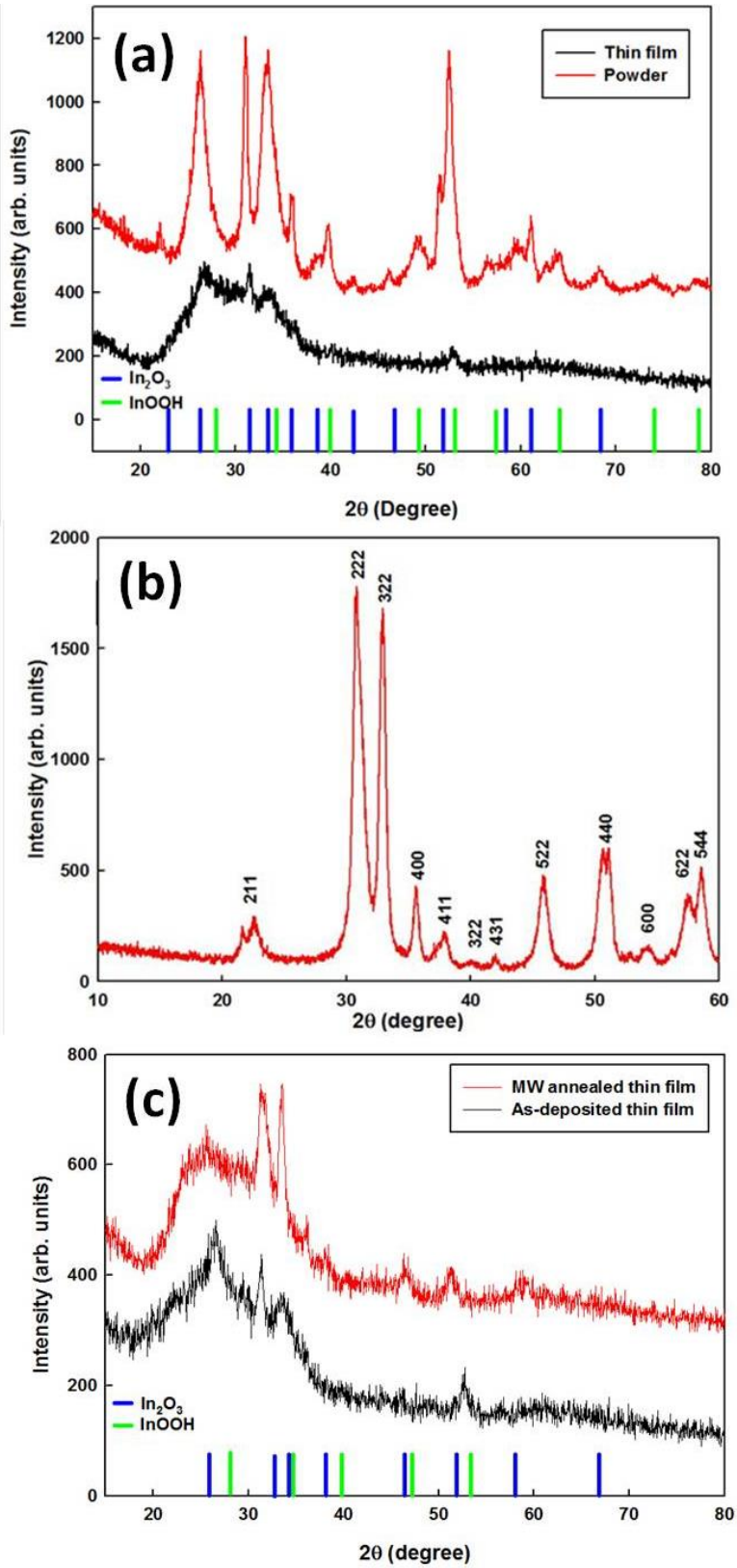

Figure 46 XRD diffractograms of (a) as-prepared powder and as-deposited thin film, (b) after post-heating of the as prepared ITO powder at 600 ^{o}C and (c) as-prepared and microwave heat treated films with EC.

4.3.5 Optical Transmittance and film resistivity

The optical transmission spectrum of an ITO thin film deposited by AACT from a 0.20 wt/vol% methanolic suspension is shown in figure 47. In general, all films were >85% transparent through the visible portion of the electromagnetic spectrum (400-700 nm). The thickness of the films was measured by a profilometer, which measures the difference between the film and the substrate in nanometres. The measured thicknesses of as-deposited and post-deposited and heat-treated ITO films were ca. 800 and 600 nm, respectively.

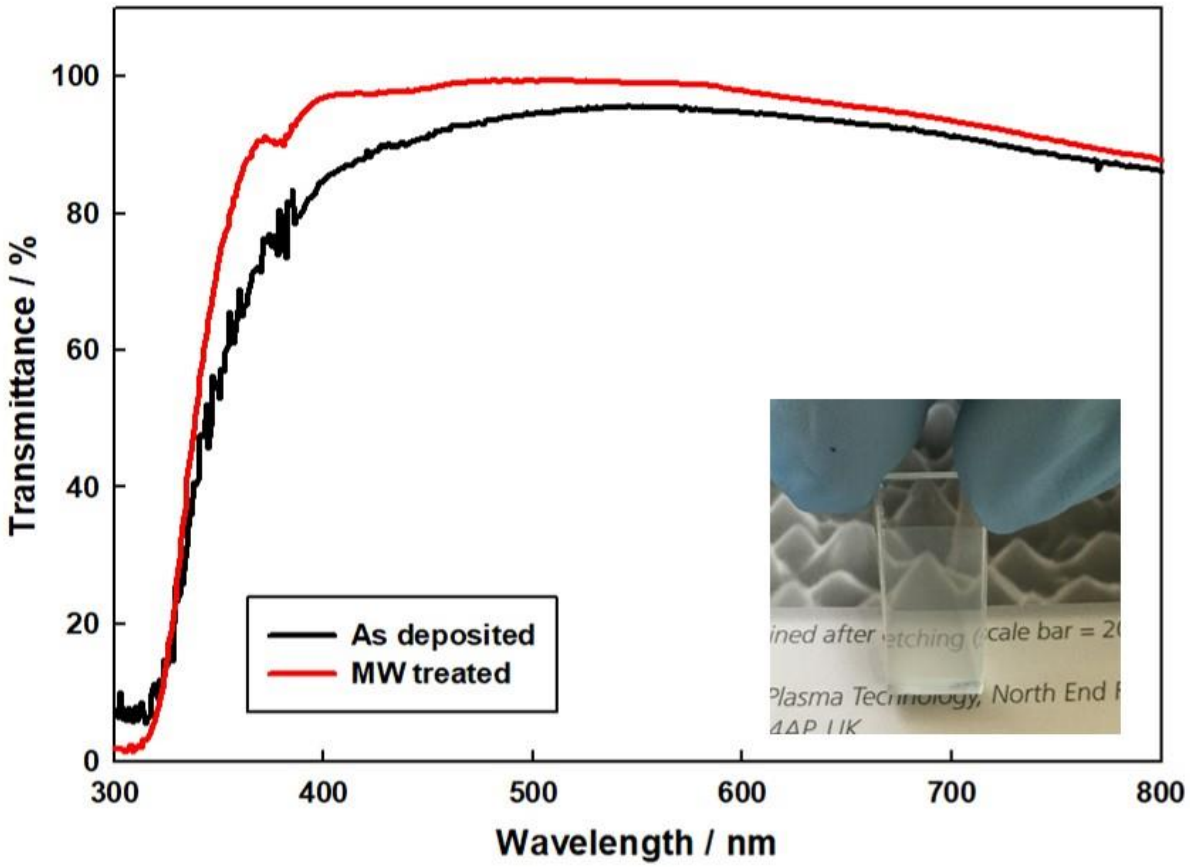

Figure 47 Optical transmission spectrum of ITO thin film deposited for 30 min by AACT using 0.20 wt/vol% methanolic suspension before and after heat treated using microwave radiation. Inset is a photograph of the microwave heat treated glass sample showing the optical transmission.

The sheet resistance was measured by a four-point probe conductivity meter and the resistivity of the films was calculated by taking in to account the measured sheet resistance and the film thickness. The sheet resistance (R), resistivity (ρ), Hall mobility (μ) and carrier concentration (n) values of ITO films with and without addition of EC are given in table 4. A higher carrier concentration of -80.46 x 10^{17} cm^3 was found for the microwave heat treated films with ethyl cellulose which could be due to the improved particle necking properties. However, a low Hall mobility of 2.19 $cm^2V^{-1}S^{-1}$ was observed for the same sample due to the enhanced carrier-carrier scattering taking place at higher carrier concentrations.[231,232]

Table 4 Properties of the AACT deposited ITO films; Sheet resistance (R), resistivity (ρ), Hall mobility (μ) and carrier concentration (n).

		R / $\Omega\square^{-1}$	ρ /Ωcm	μ / $cm^2V^{-1}S^{-1}$	n/ x 10^{17} cm^3
As-deposited	Without EC	40 x 10^6	3.2 x 10^2	1.32	0.12
	With EC	50 x 10^6	4.0 x 10^2	2.92	0.02
Microwave annealed (90s)	Without EC	0.2 x 10^6	1.2 x 10^1	11.74	0.37
	With EC	1.0 x 10^3	6.0 x 10^{-2}	2.19	80.46
Radiant annealed (3hrs)	Without EC	0.4 x 10^6	2.4 x 10^1	22.70	0.18
	With EC	5.0 x 10^3	3.0 x 10^{-1}	2.18	59.80

According to the resistivity values given in table 4, it is clear that both microwave and conventional radiant post-deposition heat-treatments significantly reduced the resistivity, especially when EC was present due to enhanced inter-particle connections and film adherence caused during the sintering step. However, the lowest resistivity of 6.0 x 10^{-2} Ω cm was obtained using microwave radiation for post-deposition heat-treatment due to the improved particle-particle and particle-substrate connections by the volumetric heating. The best resistivity values reported in the literature are based on solution processed ITO nanoparticle films and are of the order of 10^{-3} Ω cm.[233] However, in that work the films were spin coated followed by a radiant annealing step

(250 – 950 ^{o}C) under partial oxygen (1.3 x 10^{-4} – 2.1 x 10^{4} Pa) over a long period (1 – 3 hr). The methods used herein and the optimised conditions, provided an alternative, novel and significantly cost-effective route for manufacturing TCO films. Further work on improving the conductivity of the TCO films deposited by the AACT method is being carried out by varying other parameters such as flow rate, deposition temperature, doping level, post-processing parameters etc., to build from these initial promising results.

4.4 Conclusions

In this study, we introduced a simple and low cost deposition method to fabricate thin films from nanoparticle suspensions. We demonstrated the use of aerosol-assisted chemical transport (AACT) to fabricate Sn-doped In_2O_3 (ITO) thin films on glass substrates. The surface morphological images confirmed that by choosing an appropriate solvent (methanol) and the loading level (0.20 wt/vol%), a significant improvement in the film nanoparticle coverage can be obtained. The XRD diffractograms illustrated that post-deposition heat treatment of ITO films, helped to improve the phase purity of the films, as well as the inter-particle connections and film adherence. The required microwave processing time was much shorter than the radiant annealing time. The lowest resistivity of 6.0 x 10^{-2} Ω cm, Hall mobility of 2.19 $cm^2V^{-1}S^{-1}$ and a higher carrier concentration of -8.046 x 10^{18} cm^3 for the microwave heat-treated ITO films were assisted in the presence of ethyl cellulose binder in the initial aerosol. Furthermore, transmission plot showed over 85% transmission in the visible region for the microwave heat-treated films ITO films.

Chapter 5

Structural Analysis and Electronic Screening of Microwave Synthesised Metal-doped ZnO Materials

5.1 Overview

Due to the high cost and the demand associated with In, the industry has substantial need to find novel, low cost and readily available alternatives for ITO. Fortunately, ZnO is a promising substitute as it is inexpensive, non-toxic and an earth abundant material.[12] ZnO has a direct and wide band gap in the near-UV spectral region and a large free-exciton binding energy so that excitonic emission processes can persist at or even above room temperature.[82] It's properties have been greatly studied for many years, however the use of pure ZnO as a semiconductor in electronic devices has been limited due to the poor control over its electrical conductivity.

The electrical and optical properties of semiconductors, can be significantly affected even by relatively low concentrations of native point defects and impurities (down to 10^{-14} cm^{-3} or 0.01 ppm).[234–237] Hence, understanding the role of native point defects (i.e. vacancies, interstitials, and antisites) and the incorporation of impurity dopants is key toward tuning the conductivity in ZnO. For a long period, it has been hypothesised that the unintended n-type conductivity in ZnO is caused by the presence of oxygen vacancies or zinc interstitials. Though, recent state-of-the-art density functional calculations and optically detected electron paramagnetic resonance measurements of high quality ZnO crystals have exhibited that this provenance to native defects cannot be correct. It has been shown that oxygen vacancies are deep donors and cannot contribute to n-type conductivity. Moreover, it was found that the other point defects (e.g. Zn interstitials and Zn antisites) are also unlikely to cause the n-type conductivity in ZnO.[82]

Instead, the unintentional incorporation of impurities which act as shallow donors, is the most likely cause. An example of such unintentional incorporation could be hydrogen, which exists in almost all growth and processing environments.[238,239] Density

functional theory has demonstrated that interstitial H forms a strong bond with O in ZnO and acts as a shallow donor, contrary to the amphoteric behaviour of interstitial H in conventional semiconductors.[238] Moreover, recent findings suggest that H can also substitute for O in the ZnO structure and act as a shallow donor.[239] Other shallow donors which give rise to the n-type conductivity in ZnO are impurity dopants such as Al, Ga, Cu, In or Se. However, these elements are not usually present in ZnO samples thus intentional doping will be required to alter the conductivity.

It has been shown that it is very difficult to obtain p-type doping in ZnO, mainly due to its tendency towards n-type conductivity.[240–244] Additionally, the above-mentioned defects play a role as compensating centres in p-type doping, reducing its effect. Furthermore, there are very few candidate shallow acceptors for ZnO.[82] Group 1 metals (Li, Na, K) on the Zn site can be considered as either deep acceptors or stable like interstitial donors which compensate p-type conductivity.[120,245,246] Group 11 metals (Cu, Ag, Au) are deep acceptors hence do not contribute to p-type conductivity. As O is an electronegative element, only N is possible to result in a shallow acceptor level in ZnO. Group 15 elements (P, As, Sb) act as deep acceptors when substituted on to O sites in ZnO.[246] Even though, there are reports on obtaining p-type doping through the incorporation of N, the reproducibility and the stability of this p-type doped ZnO is still under debate.[82]

This chapter reports the metal doping of ZnO using Al, Ga, Si, Cu and Mn elements (i.e. co-doping) to improve the conductivity and detect the best metal dopants among them. Al doped ZnO (AZO) has arisen as an earth abundant alternative to ITO since around the mid-1990s.[247] Ga doped ZnO (GZO) has attracted particular attention, as the use of Ga a potential dopant is favourable due to the close matching ionic radii of Ga^{3+} and Zn^{2+}. Additionally, both GZO and Mn doped ZnO (MZO) have been suggested to exhibit a relatively low electron effective mass, hence increasing their potential for improved electrical properties in n-type TCOs.[62] Sato *et al*. reported that ZnO doping with group 14 elements (Si, Ge, Ti, Zr and Hf) leads to low resistivity and high visible range transmittance.[248] Given the earth abundance of silicon and its non-toxic nature, n-type Si doped ZnO (SZO) shows great promise for yielding high electrical activity and high transparency.[249] Similarly, among other promising transition metal dopants, Cu is also known to be preferable because of its abundance and low toxicity. Recently, Cu-doped

ZnO (CZO) has shown a noteworthy enhancement in relevant properties such as electrical, magnetic, photocatalytic performance and gas sensing.[250]

AZO, GZO, SZO, CZO and MZO powders were synthesised and processed using microwave radiation and subsequently evaluated to determine their electrical properties. The respective dopant amounts were varied to tune the conductivity. Resistivity trends were constructed to detect the optimal doping of the powders. Subsequent measurements of the carrier density and electron mobility of the pellets were obtained using the van der Pauw method. In addition, structural and surface analysis was carried out by using XPS, XRD and SEM for the optimally doped ZnO powders. Moreover, particle size measurements were carried out for the suspensions of as-synthesised powers in DEG. Among all the microwave synthesised singly doped-ZnO powders, AZO and GZO showed the lowest resistivity values of 4.4 x 10^{-3} and 4.3 x 10^{-3} Ω.cm, respectively. The superlative electrical properties were achieved for the pelleted co-doped AGZO powder using the optimised Al and Ga dopant levels.

5.2 Experimental Details and Characterization

5.2.1 Powder Synthesis

Doped ZnO powders were prepared by microwave synthesis. In this method, $Zn(CH_3COO).2H_2O$ (1.00 g) (BDH Chemicals) was used as the ZnO precursor. Suitable atomic percentages from (0.5 – 2.5) at.% of Al^{3+}, Si $^{4+}$, Cu^{2+}, Mn $^{2+}$ and Ga^{3+} were introduced to the Zn^{2+} precursor in the form of their salt (i.e $AlCl_3.6H_2O$, $Ga(NO_3)_3.xH_2O$, $Mn(CH_3COO)_2{\cdot}4H_2O$, $Cu(CO_2CH_3)2{\cdot}H_2O$ and $Si(OCOCH_3)_4$ from Sigma-Aldrich) which was dissolved in diethylene glycol (DEG) (45 mL) (Sigma-Aldrich) and deionized water (5 mL). The solution was stirred for 1 hour to get a clear, transparent solution. The clear solution was transferred to a fluorocarbon polymer (TFM) vessel after purging with Ar for 5 min. The vessel was sealed after purging with Ar prior to being placed in the microwave synthesizer (Anton Paar Multiwave PRO, 2.45 GHz, 1500w) at 200 °C for 30 minutes. The microwave heating ramp rate was 20 °C/min, and the timing of the reaction was started when the vessel reached the desired temperature of 200 ˚C. After the reaction was completed, the vessel was allowed to cool to room temperature before removal of the reaction product mixture from the microwave reactor. Temperature,

pressure and microwave power profiles for a typical reaction are given in Figure 53. After the reaction had taken place, the clear reaction solution mixture had transformed to an opaque suspension, which was then centrifuged, washed with ethanol and placed in an oven at 60 °C for 1 hour to evaporate the solvent completely. The dried powder was annealed at 450 ºC for another hour using a hotplate. The powders were then compressed into pellets using a specac manual hydraulic press under a 10 ton load. The annealed, metal doped powder was then used to prepare pellets. Figure 54 provides a step-by-step scheme of microwave synthesis of doped ZnO powder.

5.2.2 Post-synthesis Heat Treatment of Pellets

The pellets prepared using microwave synthesised powders were treated by a microwave assisted heating technique. The microwave assisted annealing was carried out using a microwave oven (Microwave research Applications Inc. BP-211/50, USA) operating at 2.45 GHz frequency with a maximum power of 3000 W. The microwave heat treatment was facilitated by using SiC susceptor tiles, placed on both sides of the doped ZnO pellets. The heat loss was minimized by shielding the sample within thermally insulating blocks.[251,223] The pellets, SiC tiles and insulating blocks were placed inside a custom made quartz vessel fitted with a gas inlet and outlet and a zirconium oxide window to allow monitoring of the temperature using an IR thermometer. Prior to the microwave annealing, the quartz vessel containing the TCO pellet was purged with the 5% H_2/N_2 gas mixture at 1825 mL min^{-1} (BOC, UK) for 5 mins. The microwave heat treatment was provided under a constant gas flow of 5% H_2/N_2 for 90 s. During the heat treatment, the temperature of the SiC susceptor was monitored using an infrared temperature probe (Mikron infrared Inc. M67/M67S series, USA) with an error of ± 5 ºC. After 90 s, the temperature of the susceptor reached 600 ºC. Once the 90 s microwave annealing step was completed, the gas flow was maintained until the pellets cooled down to room temperature.

5.2.3 Characterization

The structural and surface analysis was carried out for the optimally doped powders. The surface compositions were studied by XPS analysis. The measurements were

conducted using Thermo Scientific (model K-Alpha) spectrometer for a 400×400 μm^2 area. Particle size distributions of the as-synthesised powders in the reaction mixtures were monitored using a Zeta-nano from Malvern Instruments. The surface morphology of the powders was investigated using a Leo 1530 VP field emission gun scanning electron microscope (FEG-SEM) at an accelerating voltage of 5 kV and a working distance of 5 mm. The phase and crystallinity of the TCO powders were characterized using a Bruker AXS Advance X-ray diffractometer with primary monochromatic high intensity Cu Kα (λ = 1.541 Å) radiation and a position sensitive detector. To calculate the *c* and *a* lattice parameters, the Rietveld analysis technique was used.[252,253] The electrical properties were measured by a four-point probe conductivity meter (Jandel, HM20, Jandel Engineering Ltd., Linslade, UK) and by a Hall effect measurement system, using the Van der Pauw method to determine the bulk resistivity of the TCOs. The pellets were subjected to an input current of 10 mA and a calibrated magnetic field of 0.58 T. The transverse voltage was then measured. The measurement was repeated by reversing the direction of the magnetic field and the current. For the measurements, an ECOPIA Hall effect measurement system (HMS-3000) was used.

5.3 Results and Discussion

5.3.1 Composition, Structure and Surface Morphology

Figure 48 shows the X-ray diffraction spectra of microwave synthesised pure ZnO, MZO, SZO, CZO, AZO, GZO and AGZO powders. All the samples displayed only the reflections for polycrystalline ZnO, with (101) preferred orientation crystallized in the wurtzite structure.[218] Furthermore, microwave synthesis has yield phase pure ZnO with all the different types of doping systems.

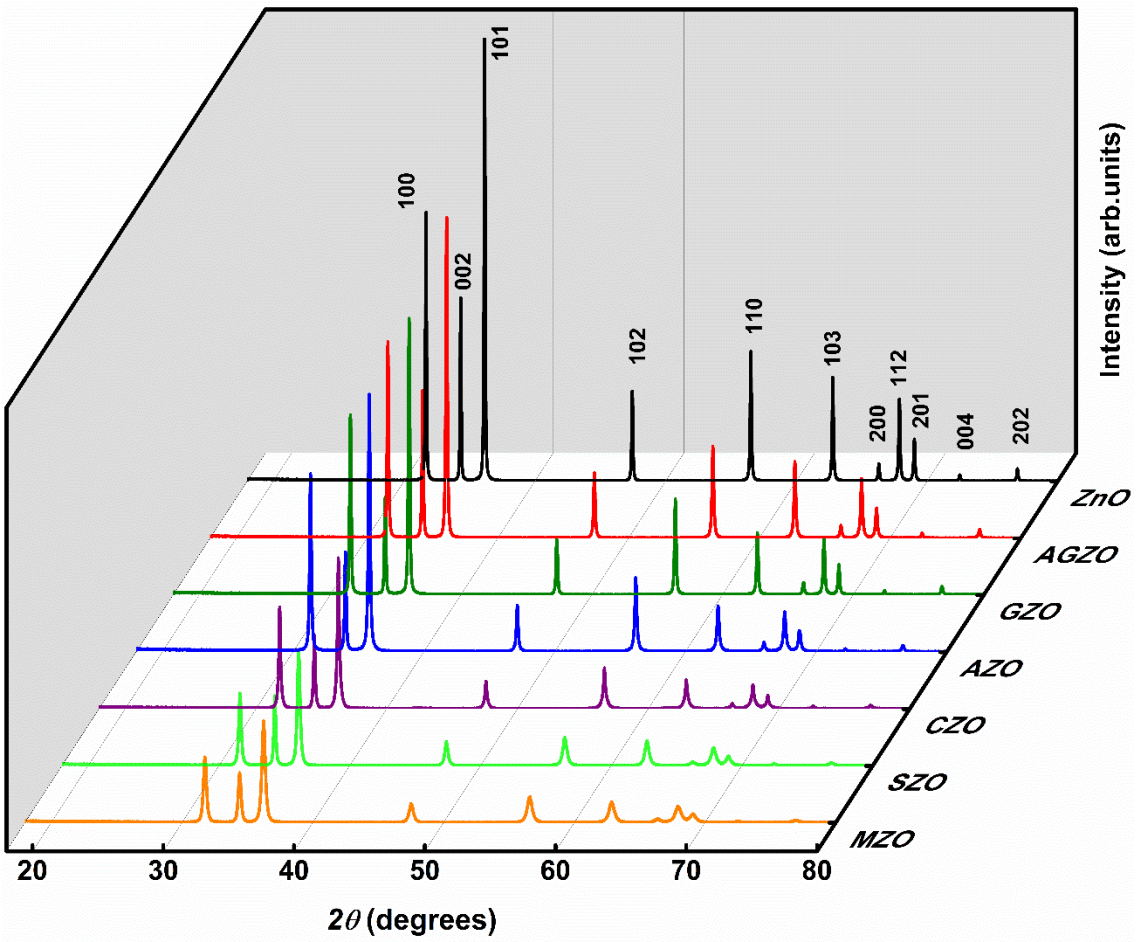

Figure 48 XRD diffraction spectra of microwave synthesised 1.5 at.% SZO, 2.0 at.% MZO, 1.5 at.% CZO, AGZO, 1.5 at.% GZO and 1.5 at.% AZO powders.

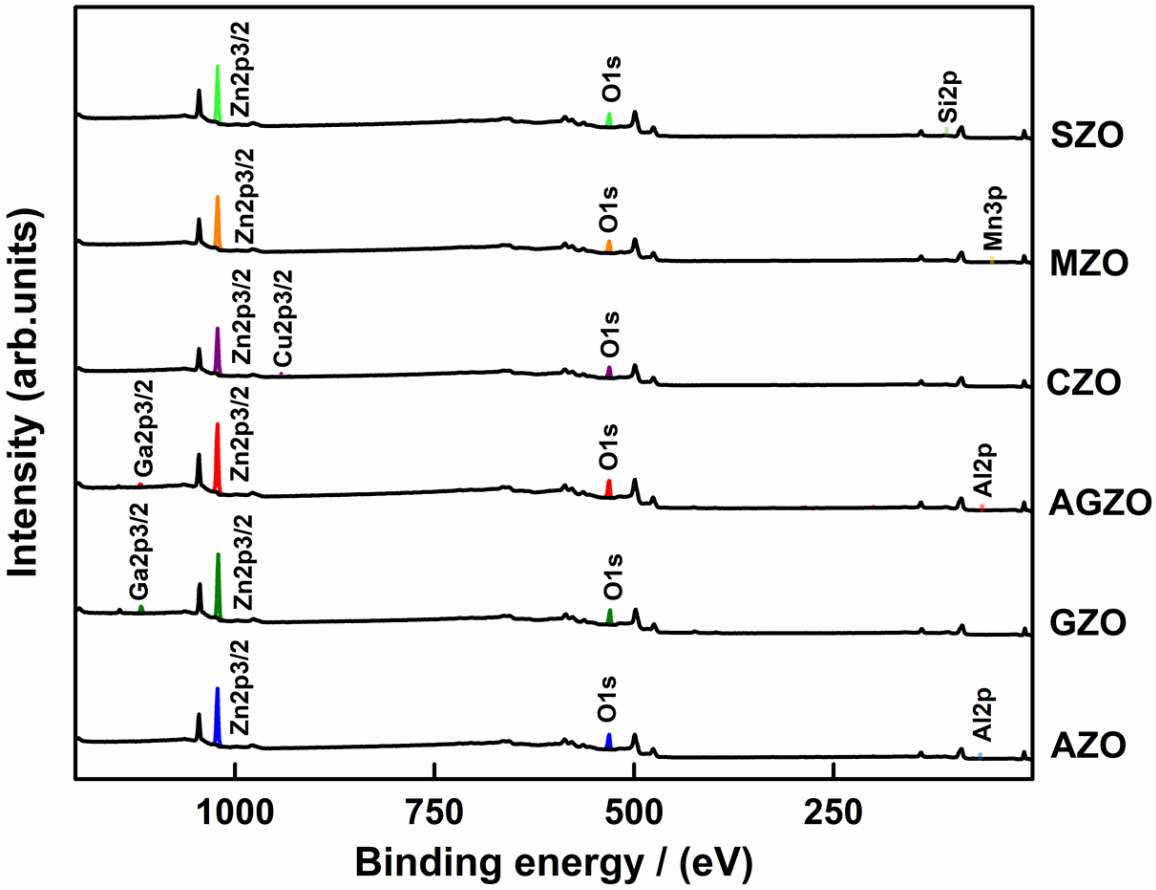

Figure 49 XPS analysis of 1.5 at.% SZO, 2.0 at.% MZO, 1.5 at.% CZO, AGZO, 1.5 at.% GZO and 1.5 at.% AZO powders.

The chemical bonding states of Al, Ga, Si, Cu, Mn, Zn and O elements on the surface of the optimally doped ZnO powders were studied by XPS surface analysis (figure 49). As shown in the figure, the intensive peaks of O 1s and Zn 2p3/2 (with binding energies ~ 531 eV and 1022 eV, respectively) are observed on the survey XPS spectra of all the powders studied. Apart from that, small peaks were observed in the samples, which correspond to the oxide forms of the dopant elements in each powder, confirming that dopants are present in the ZnO host lattice.[254] The rest of the peaks appearing in the XPS spectra are auger peaks of the above stated elements. No other additional peaks were detected, indicating that there is a single phase of ZnO in the samples, which is in good agreement with the XRD results.

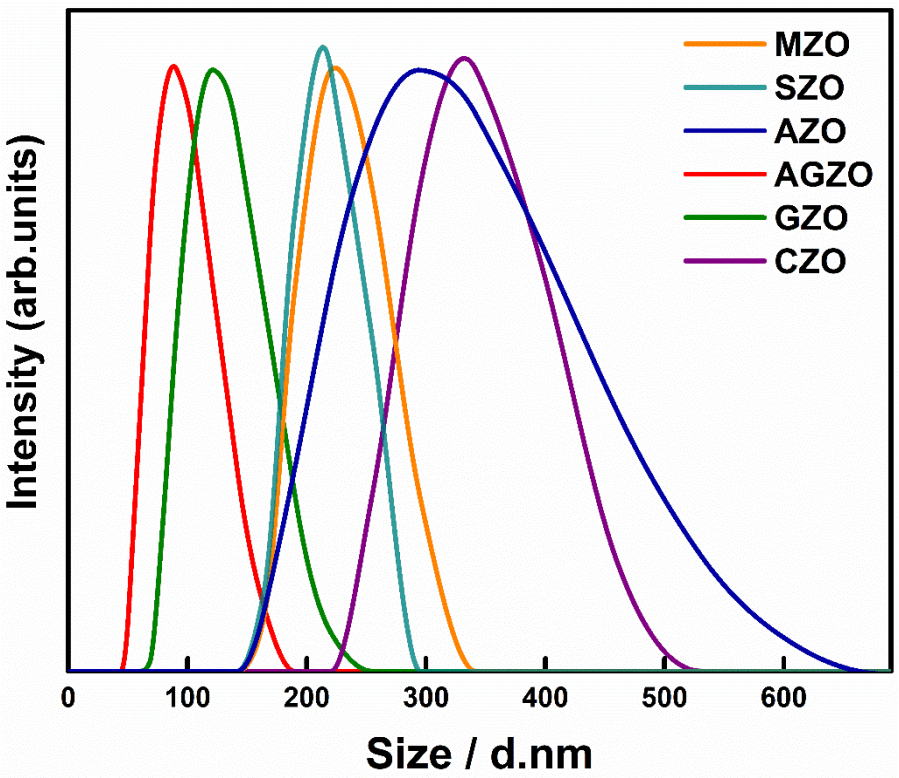

Figure 50 Particle size distribution of as-synthesised 1.5 at.% SZO, 2.0 at.% MZO, 1.5 at.% CZO, AGZO, 1.5 at.% GZO and 1.5 at.% AZO powders in diethylene glycol.

The particle size distributions of the as-synthesised powder suspensions with 0.025 moldm^{-3} concentration, were measured using dynamic light scattering (DLS) in diethylene glycol (figure 50). The measurements were carried out using suspensions that were diluted enough (0.001g/L) to deter particle-to-particle interactions. The lowest average particle size was found to be ~85 nm for co-doped ZnO powders. The average particle size values for singly-doped GZO, SZO, MZO, AZO and CZO were 105 nm, 194 nm, 232 nm, 244 nm and 342 nm respectively.

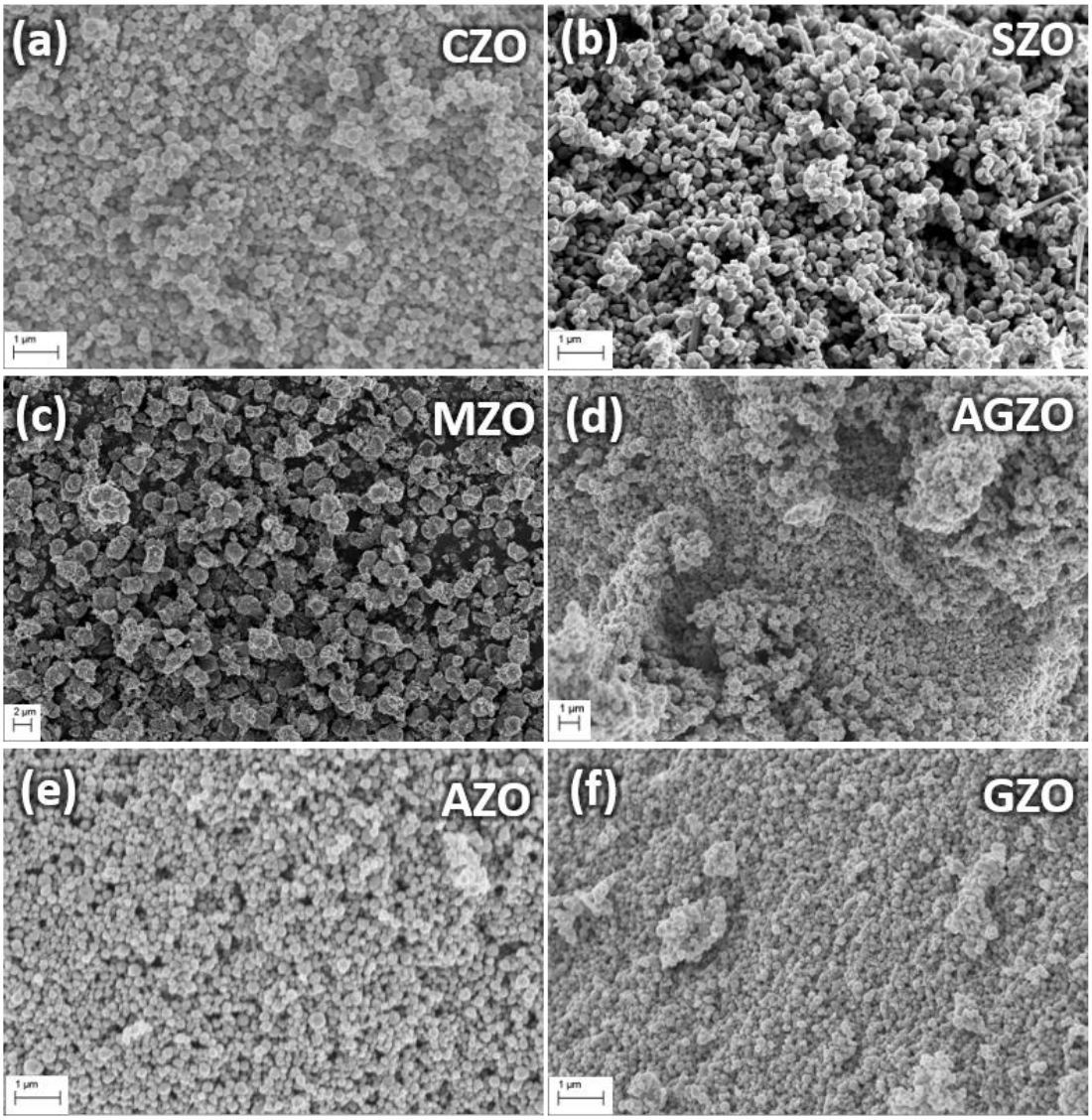

Figure 51 FEG-SEM images microwave synthesised 1.5 at.% SZO, 2.0 at.% MZO, 1.5 at.% CZO, AGZO, 1.5 at.% GZO and 1.5 at.% AZO powders.

Figure 51 shows the surface morphology of as-synthesised optimal doped-ZnO powders. Apart from MZO, all the other powders show a structure of mostly agglomerated spherical nanoparticles. MZO exhibited a much broader particle size distribution compared to the other powders. Formation of these agglomerated clusters are most possibly due to the solvent evaporation of the suspensions.[255]

5.3.2 Electrical Properties of Pellets

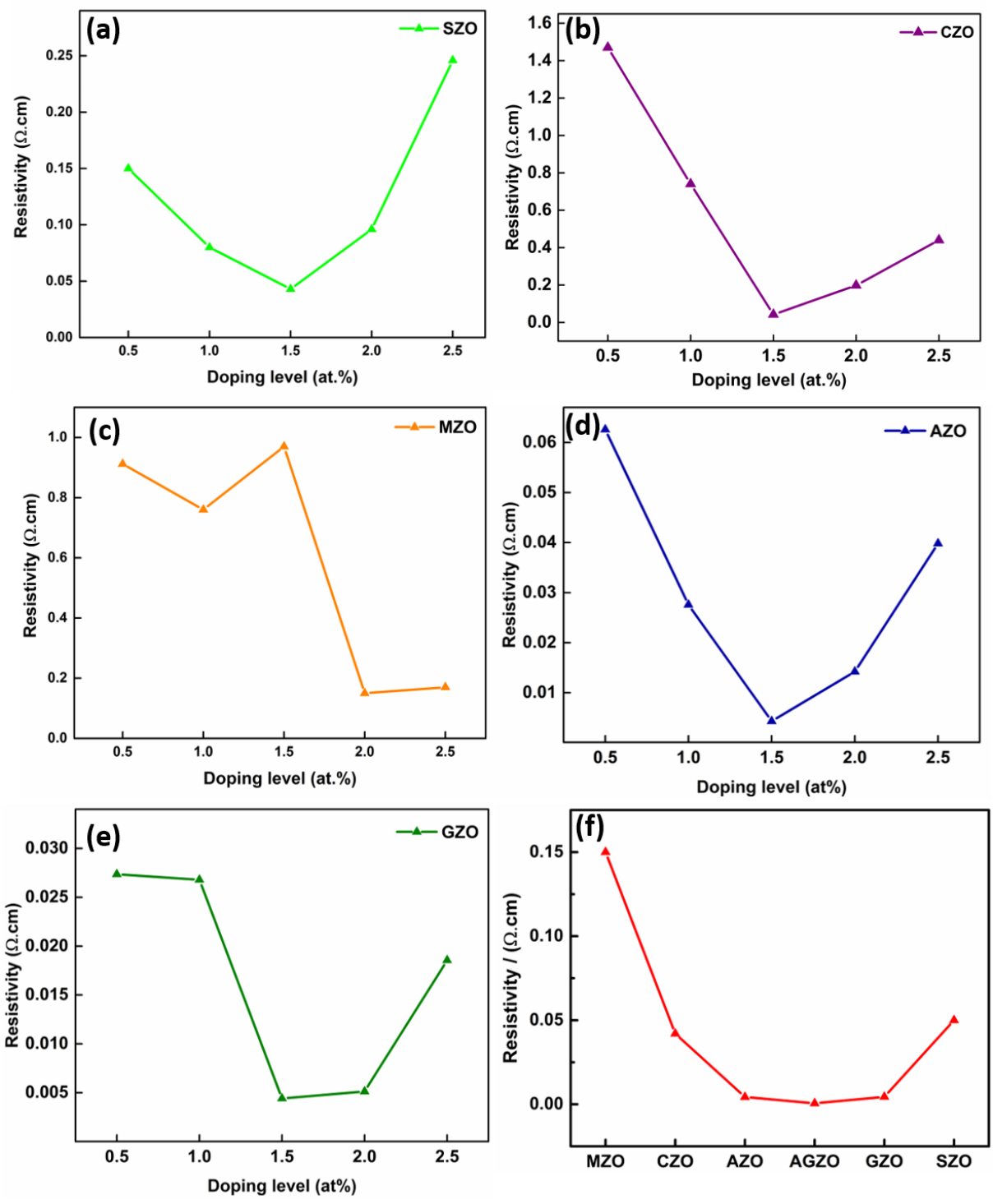

Figure 52 Resistivity values of microwave annealed (a) SZO, (b) CZO, (c) MZO, (d) AZO, (e) GZO pellets with different dopant levels and (f) resistivity values comparison of all the 1.5 at.% SZO, 2.0 at.% MZO, 1.5 at.% CZO, AGZO, 1.5 at.% GZO and 1.5 at.% AZO powders.

The resistivity (ρ) values of microwave annealed ZnO pellets are summarized in figure 52(a-f). Post-synthesis heat treatments were carried out to densify the pellets, as the pellets made from as-synthesised powders were not robust enough to allow assessment of the electrical properties. The general resistivity trends found an initial decrease in the resistivity upon increase of the dopant content, to a point, whereby further increases in dopant concentration led to an increase in the resistance. This phenomenon might possibly be related to the kinetic equilibrium process where the high contents of metal dopants could be nucleated with oxygen ions by itself to form bigger particles. Hence, it could be difficult for the dopant ions to be incorporated into ZnO lattice at higher concentrations.[256]

Once the optimal dopant levels were determined from the resistivity trends, the Hall measurements were carried out for the pellets prepared with optimally doped powders to obtain the Hall mobility (μ) and carrier concentration (*n*) values. The electrical properties of the pellets with the optimal dopant levels are listed in table 5.

Table 5 Average values of electrical properties of doped-ZnO pellets.

Material	ρ (Ω.cm)	n (cm^3)	μ ($cm^2V^{-1}s^{-1}$)
CZO	0.0420	4.705×10^{18}	1.741
AZO	0.0043	9.607×10^{18}	10.380
MZO	0.1500	4.559×10^{17}	1.702
GZO	0.0044	7.835×10^{19}	18.197
SZO	0.0500	1.891×10^{18}	1.855
AGZO	0.0005	8.100×10^{20}	8.320

The conductivity of a material is a combined effect of the carrier concentration and the donor Hall mobility. The electrical properties of doped-ZnO are governed by the effective dopant substitution of the metal ions into the ZnO structure, which is mainly dependant on the ionic radii of the metal ions.[257] If the mismatch of the ionic radii is significant, the doping will cause more crystal strain within the ZnO lattice. This can lead to a degradation of the crystallinity, resulting in poor electrical properties.[258] The ionic radii of Zn^{2+}, Mn^{2+}, Cu^{2+}, Ga^{3+}, Al^{3+} and Si^{4+} are 0.74 Å, 0.83 Å, 0.73 Å, 0.62 Å, 0.54 Å

and 0.42 Å respectively.[259,60,257,260] Since the ionic radius of Mn^{2+} is larger than Zn^{2+} effective doping is difficult. This is likely the reason for the lower carrier concentration observed in MZO. The higher mismatch in size between Si^{4+} and Zn^{2+}could also be causing the high resistivity in SZO. Compared to the rest of the above-mentioned metal ions, Cu^{2+}, Ga^{3+} and Al^{3+} ions could give higher dopant solubility in the ZnO structure due to their close matching ionic radii, hence improved electrical properties can be expected. However, the unexpected high resistivity observed for the CZO could be possibly due to the poor stability of Cu doped ZnO.[261]

Out of all the analysed singly doped-ZnO powders, AZO and GZO exhibited the lowest resistivity values. It was therefore logical to investigate co-doping ZnO with both Al and Ga to see if the properties could be further enhanced by co-doping. Hence, AGZO was synthesised utilizing the optimal dopant concentrations that were determined for the Al and Ga singly doped powders. The superlative electrical properties observed for AZO, GZO and co-doped AGZO are discussed in depth in the next chapter (chapter 6).

5.4 Conclusions

AZO, GZO, SZO, CZO and MZO singly doped-ZnO powders were synthesised and processed using microwave radiation, to investigate the best metal dopants for transparent conducting ZnO. Systematic variation of the dopant levels was used to vary the conductivity. The apparent optimum dopant concentrations for each case were determined through analysis of the resistivity trends. Subsequent structural and surface analysis was carried out to assess the suitability of each optimally doped ZnO powder. XPS and XRD confirmed that all the doped powders were pure phase ZnO. From the electrical testing, it was evident that Al and Ga doped ZnO powders had significantly better properties than the other doped powders. These exceptional properties require more in-depth study, as does the potential for co-doping ZnO. Hence, AZO, GZO and AGZO were carefully chosen as the ZnO based TCO materials to further investigate the structural, electrical and optical properties; which is discussed in detail in following chapters (chapter 6 and chapter 7).

Chapter 6

Microwave-Assisted Synthesis and Processing of Al-Doped, Ga-Doped, and Al, Ga Co-doped ZnO for the Pursuit of Optimal Conductivity for Transparent Conducting Film Fabrication

6.1 Overview

Transparent conducting oxides (TCOs) are of great importance in modern life due to their applications as coatings in electronic and opto-electronic devices such as solar cells, touch screen displays, flat panel displays, automobile/aircraft windows and organic light emitting diodes (OLEDs).[81] Typically, indium tin oxide (ITO) is the TCO of choice, however the cost of ITO has steadily increased recently due to the rarity of In. Therefore, research has intensified to find sustainable alternatives to ITO, with doped-ZnO showing many favourable characteristics, most notably low cost. Various methods including co-precipitation, hydrothermal processes, sol-gel, spray pyrolysis, aerosol assisted methods, pulsed laser deposition and magnetron sputtering have been widely used to develop ZnO based TCOs.[123,124,262,263]

Controlling atomic level doping during the synthesis of ZnO is challenging due to native defects present in the hexagonal wurtzite structure, which alter the optical and electrical properties of the material.[264–266] Structural defects also can be dependent on the atmosphere in which the ZnO material is grown and the post-synthesis heat treatment.[267,268] Oxygen vacancies can be filled or manipulated by changing the annealing atmosphere. For instance, annealing under an O_2 atmosphere could reduce the number of oxygen vacancies in the lattice and hence cause a reduction in the number of charge carriers present in ZnO films.[264] On the other hand, annealing under reductive atmospheres (i.e. H_2-rich atmospheres) increases the *n*-type conductivity of ZnO by passivating the Zn vacancies.[269] In this condition, hydrogen also can be substituted on an oxygen site and form a multicenter bond with the four nearest-neighbour Zn atoms. The substitutional hydrogen has a low formation energy andacts as

a shallow donor.[270] Additionally, zinc interstitials can form complexes with ambient nitrogen, which act as shallow donors to further increase the conductivity of ZnO.[271] Alongside atmospheric conditions, annealing time and temperature are two other parameters that can have an influence on the electrical properties of doped ZnO films.[266,272–274] Even though these effects are extensively reported by many researchers, the exact effect of the annealing time on the structural and optoelectronic properties of doped ZnO is still unclear and widely debated.

Extensive efforts have been taken to improve the transparent conducting properties of ZnO and it has been shown that various elements, such as Al, Ga, Cu, In or Se can be used as dopants which considerably enhance the electrical properties of ZnO.[275] Al doped ZnO (AZO) has shown poor humidity stability compared to Ga doped ZnO (GZO). However, conducting GZO is not an ideal alternative TCO due to the high cost associated with Ga.[13,276] Therefore, research has focussed on the co-doping of ZnO with Al and Ga (AGZO) as a sustainable TCO material with enhanced electrical properties. For instance, both Al and Ga are simultaneously introduced into the ZnO structure as dopants. Zhang et al. investigated the structural and electronic properties of AGZO powders synthesised by chemical co-precipitation. They observed a smaller grain size in AGZO powders compared to AZO, suggesting that the co-doped material is better for high quality ceramic target preparation. Their sintered AGZO pellets exhibited a resistivity of 2.518 x 10^{-3} Ω.cm.[277] Furthermore, a resistivity value of 9.0 x 10^{-3} Ω.cm was reported for AGZO powder synthesised using the continuous hydrothermal flow synthesis (CHFS) method followed by sintering the pellets by conventional radiant annealing under 5% H_2/N_2 gas flow at 500 ˚C for 3 hours.[61]

In recent years, a great deal of interest has been received for the synthesis of materials under the irradiation of microwaves as an alternative advanced material synthesis technique. Volumetric heating by microwave radiation leads to fast reaction rates, rapid and uniform heating throughout the reaction mixture, which cannot be achieved by conventional radiant annealing methods. Heat generation in materials by microwave energy is fundamentally different from conventional radiant heating, conduction or convection heating. In the microwave process, heat is generated within the material itself, instead of originating from external heating elements. In other words, microwave

heat generation is due to an energy conversion process rather than a heat transfer process. Thus, the microwave synthesis technique has produced inorganic materials with unique properties that cannot be achieved by other methods which use conventional thermal processing.[20]

Recent reports indicate that microwave synthesised TCO materials possess significantly improved conducting properties by enhancing crystallinity and modifying the intrinsic defects. For example, Feldmann et al. reported the microwave synthesis of ITO and AZO pelleted powders in polyol media with resistivity values of 1.1 x 10^{-2} Ω.cm and 5.1 x 10^{-1} Ω.cm, respectively.[58,167] Niederberger et al. synthesised AZO by a microwave-assisted non-aqueous sol–gel route in benzyl alcohol and then processed it into a TCO thin film. They reported a minimum resistivity value of 2.35 x 10^{-2} Ω.cm for their AZO thin film after post-synthesis heat treatment.[59] However, to the best of our knowledge, there are very few literature reports available on microwave assisted synthesis of TCOs.

In this study, a single-step microwave assisted synthesis method was used to synthesise conducting AZO, GZO and co-doped AGZO powders. The conductivity of the powders was tuned by varying the Al and Ga dopant amounts. The lowest resistivity values of 5.6 x 10^{-4} Ω.cm and 5.7 x 10^{-3} Ω.cm were achieved for Al (1.5 at.%) and Ga (1.5 at.%) co-doped pellets and thin films, respectively. Furthermore, the resistivity and the transparency of the AGZO reported in this work show promising signs of utilizing this cost-effective alternative to replace expensive ITO.

6.2 Experimental Details and Characterization Techniques

6.2.1 Powder Synthesis

AZO, GZO and AGZO powders were prepared by microwave synthesis. In this method, $Zn(CH_3COO).2H_2O$ (1.00 g) (BDH Chemicals) was used as the ZnO precursor. Appropriate atomic percentages of Al^{3+} and Ga^{3+} were added to the ZnO precursor in the form of $AlCl_3.6H_2O$ (Sigma-Aldrich) and $Ga(NO_3)_3.xH_2O$ (Sigma-Aldrich), which were dissolved in diethylene glycol (DEG) (45 mL) (Sigma-Aldrich) and deionized water (5 mL). The solution was stirred for 1 hour to get a clear, transparent solution. The clear

solution was transferred to a fluorocarbon polymer (TFM) vessel after purging with Ar for 5 min. The vessel was sealed after purging with Ar prior to being placed in the microwave synthesizer (Anton Paar Multiwave PRO, 2.45 GHz, 1500w) at 200 °C for 30 minutes. The microwave heating ramp rate was 20 °C/min, and the timing of the reaction was started when the vessel reached the desired temperature of 200 ˚C. After the reaction was completed, the vessel was allowed to cool to room temperature before removal of the reaction product mixture from the microwave reactor. Temperature, pressure and microwave power profiles for a typical reaction are given in figure 53.

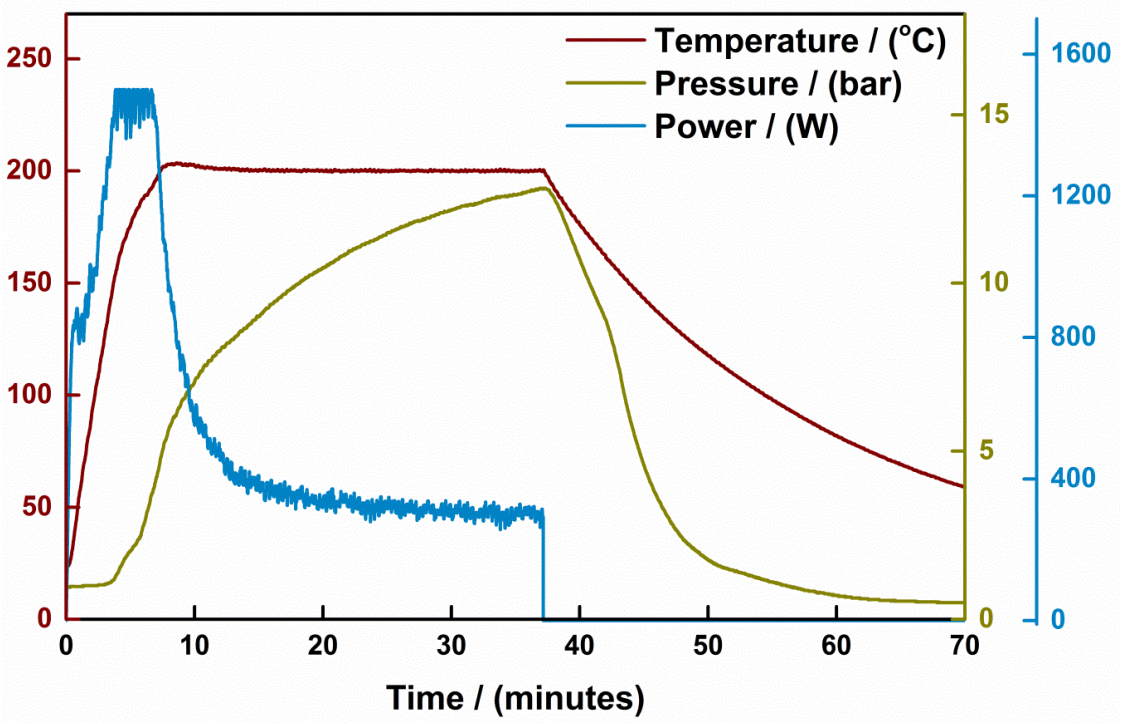

Figure 53 Temperature, pressure and microwave power profiles for the microwave synthesis.

After the reaction had taken place, the clear reaction solution mixture had transformed to an opaque suspension, which was then centrifuged, washed with ethanol and placed in an oven at 60 °C for 1 hour to evaporate the solvent completely. The dried powder was annealed at 450 ºC for another hour using a hotplate. The powders were then compressed into pellets using a Specac manual hydraulic press under a 10 ton load. The annealed, metal doped powder was then used to prepare pellets. Figure 54 provides a step-by-step scheme of microwave synthesis of doped ZnO powder.

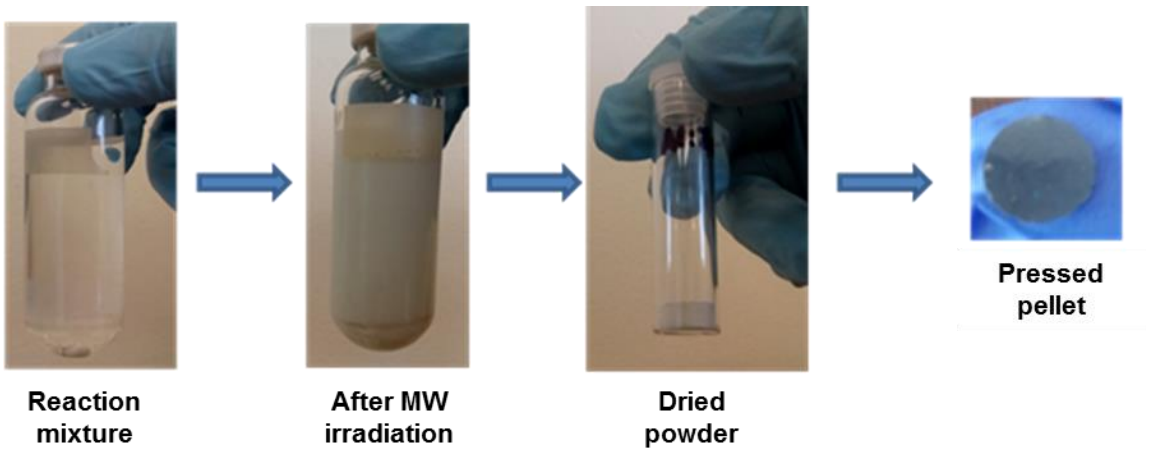

Figure 54 Step-by-step scheme of microwave synthesis of doped ZnO powder.

6.2.2 Post-synthesis Heat Treatment of Pellets

The pellets prepared using microwave synthesised AZO, GZO and AGZO powders were treated by both conventional radiant and microwave assisted heating techniques. Conventional radiant heating was conducted in a tube furnace (MTF-10-25-130, Carbolite, UK) with a ramp rate of 15 ºC min^{-1} to 600 ºC and then held for 3 hrs under a steady 5% H_2/N_2 flow of 1825 mL min^{-1} before letting cool down to room temperature under the same gas flow. The microwave assisted annealing was carried out using a microwave oven (Microwave research Applications Inc. BP-211/50, USA) operating at 2.45 GHz frequency with a maximum power of 3000 W. The microwave heat treatment was facilitated by using SiC susceptor tiles, placed on both sides of the doped ZnO pellets. The heat loss was minimized by shielding the sample within thermally insulating blocks.[251,223] The pellets, SiC tiles and insulating blocks were placed inside a custom made quartz vessel fitted with a gas inlet and outlet and a zirconium oxide window to allow monitoring of the temperature using an IR thermometer. Prior to the microwave annealing, the quartz vessel containing the TCO pellet was purged with the 5% H_2/N_2 gas mixture at 1825 mL min^{-1} (BOC, UK) for 5 mins. The microwave heat treatment was provided under a constant gas flow of 5% H_2/N_2 for 90 s. During the heat treatment, the temperature of the SiC susceptor was monitored using an infraredtemperature probe (Mikron infrared Inc. M67/M67S series, USA) with an error of ± 5 ºC. After 90 s, the temperature of the susceptor reached 600 ºC. Once the 90s

microwave annealing step was completed, the gas flow was maintained until the pellets cooled down to room temperature.

6.2.3 Characterization

The structural and surface analysis was carried out for the optimally doped AZO, GZO (i.e 1.5 at.%) and AGZO powders. The surface compositions were studied by XPS analysis. The measurements were conducted using Thermo Scientific (model K-Alpha) spectrometer for a 400×400 μm^2 area. Particle size distributions of the as-synthesised powders in the reaction mixtures were monitored using a Zeta-nano from Malvern Instruments. The surface morphology of the powders was investigated using a Leo 1530 VP field emission gun scanning electron microscope (FEGSEM) at an accelerating voltage of 5 kV and a working distance of 5 mm. The phase and crystallinity of the TCO powders were characterized using a Bruker AXS Advance X-ray diffractometer with primary monochromatic high intensity Cu Kα (λ = 1.541 Å) radiation and a position sensitive detector. To calculate the *c* and *a* lattice parameters, the Rietveld analysis technique was used.[252,253] The electrical properties were measured by a four-point probe conductivity meter (Jandel, HM20, Jandel Engineering Ltd., Linslade, UK) and by a Hall effect measurement system, using the Van der Pauw method to determine the bulk resistivity of the TCOs. The pellets were subjected to an input current of 10 mA and a calibrated magnetic field of 0.58 T. The transverse voltage was then measured. The measurement was repeated by reversing the direction of the magnetic field and the current. For the measurements, an ECOPIA Hall effect measurement system (HMS-3000) was used.

6.3 Results and Discussion

6.3.1 Composition, Structure and Surface Morphology

The bonding states of Al, Ga, Zn and O on the surface of the optimal (1.5 at.%) AZO, GZO and AGZO powders were investigated by XPS surface analysis (Figure 55a). The intense peak at 1022.27 eV was assigned to the Zn $2p_{3/2}$ corresponding to ZnO (Figure 55b).

Since the peak is relatively narrow and symmetric, it is believed that Zn predominantly exists in an oxidized state as also confirmed by XRD.[278,247] The Al 2p peaks located at 75.22 eV and 75.01 eV in Figure 56a corresponds to the Al-O bond in AZO and AGZO respectively. The characteristic peak of metallic Al (72.7 eV) was not observed in both powders.[279] The XPS spectra of GZO and AGZO (figure 56b) show peaks present at 1117.79 and 1118.71 eV, respectively, which are characteristic of Ga $2p_{3/2}$ in Ga-O.[280] Metallic Ga with a binding energy of 1116.70 eV was not observed in any of these two powder samples confirming the presence of Ga^{3+} as dopants. In addition, small amounts of C (284.90-285.89) eV and Cl (200.09 eV) were also present at impurity levels. The rest of the peaks present in the XPS spectra are auger peaks of the elements mentioned above.

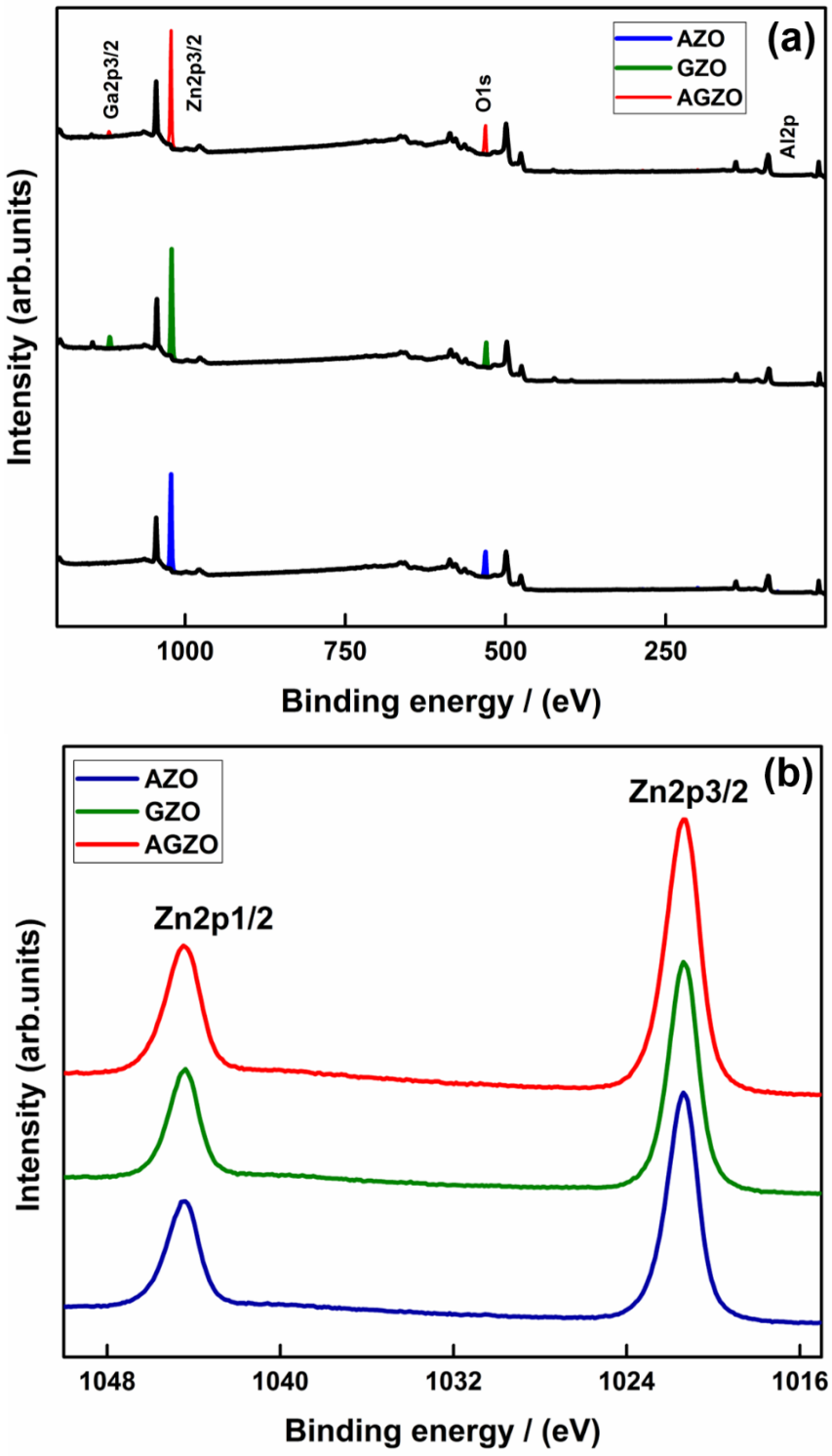

Figure 55 XPS analysis of (a) 1.5 at.% Al doped ZnO, 1.5 at.% Ga doped ZnO and co-doped ZnO, (b) Zn peaks in 1.5 at.% (Optimum) AZO, GZO and 1.5 at.% Al, 1.5 at.% Ga containing AGZO.

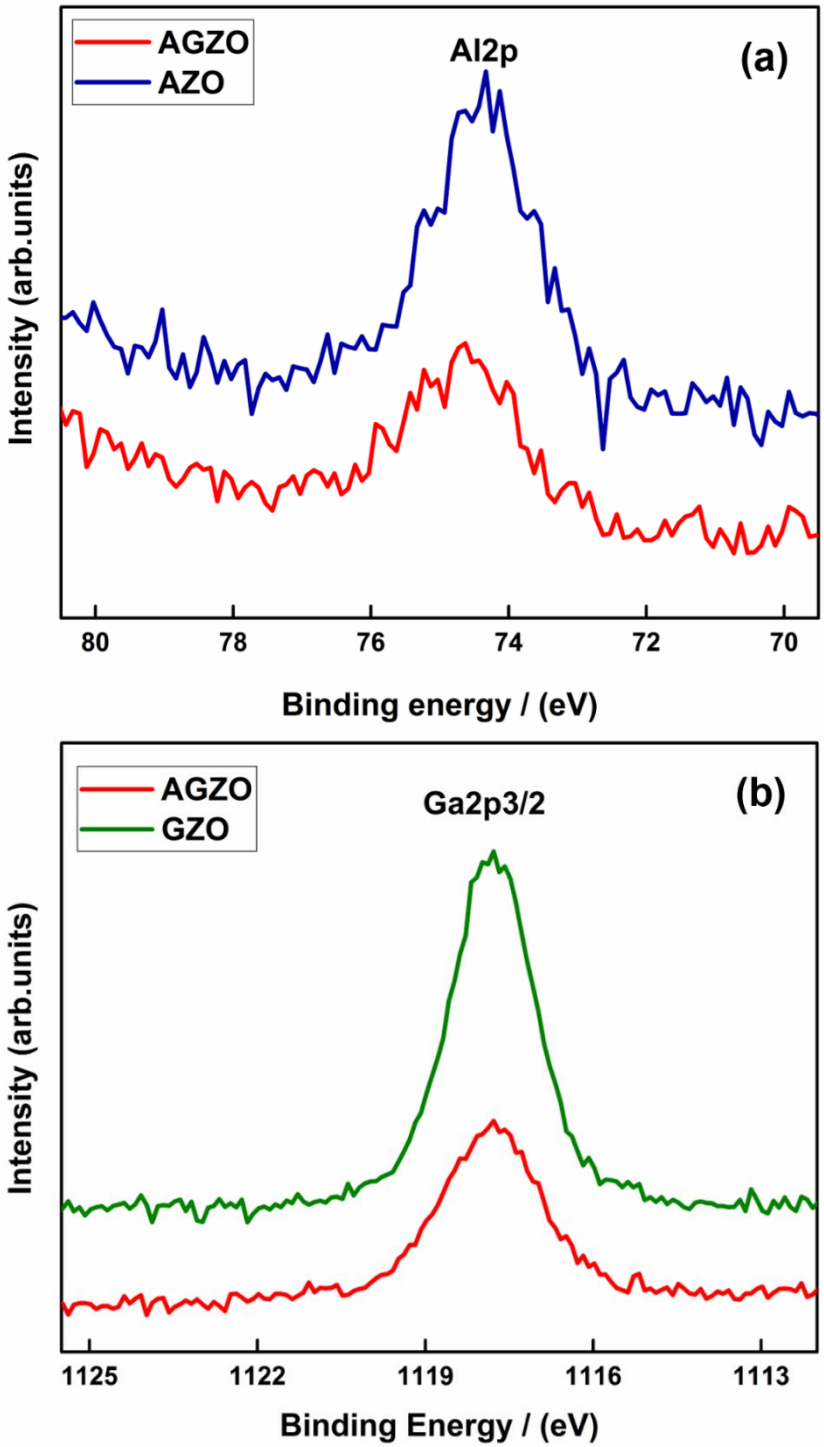

Figure 56(a) XPS data of Al2p in 1.5 at.% AZO and AGZO, (b) XPS data of Ga $2p_{3/2}$ in 1.5 at.% GZO and AGZO.

The O 1s spectra recorded for all three powder samples (Figure 57) can be fitted to show three Gaussian binding energy components, denoted O_I, O_{II} and O_{III}, respectively. The lower energy peak located at 530.37-531.12 eV corresponds to O^{2-} ions at the intrinsic sites on wurtzite structure of hexagonal Zn^{2+} (with substituted Al^{3+}/Ga^{3+}) array (O_I). The O_{II} peak (531.60-531.85 eV) is generally assigned to O^{2-} ions in the oxygen deficient regions. The higher energy peak O_{III} located at 532.76-533.00 eV is usually attributed to the presence of loosely bound oxygen on the surface.[281,282] It is noteworthy that the O_I peak was found to be the dominant peak in the O 1s spectrums in all three doped ZnO powder samples which is indeed the expected pattern.

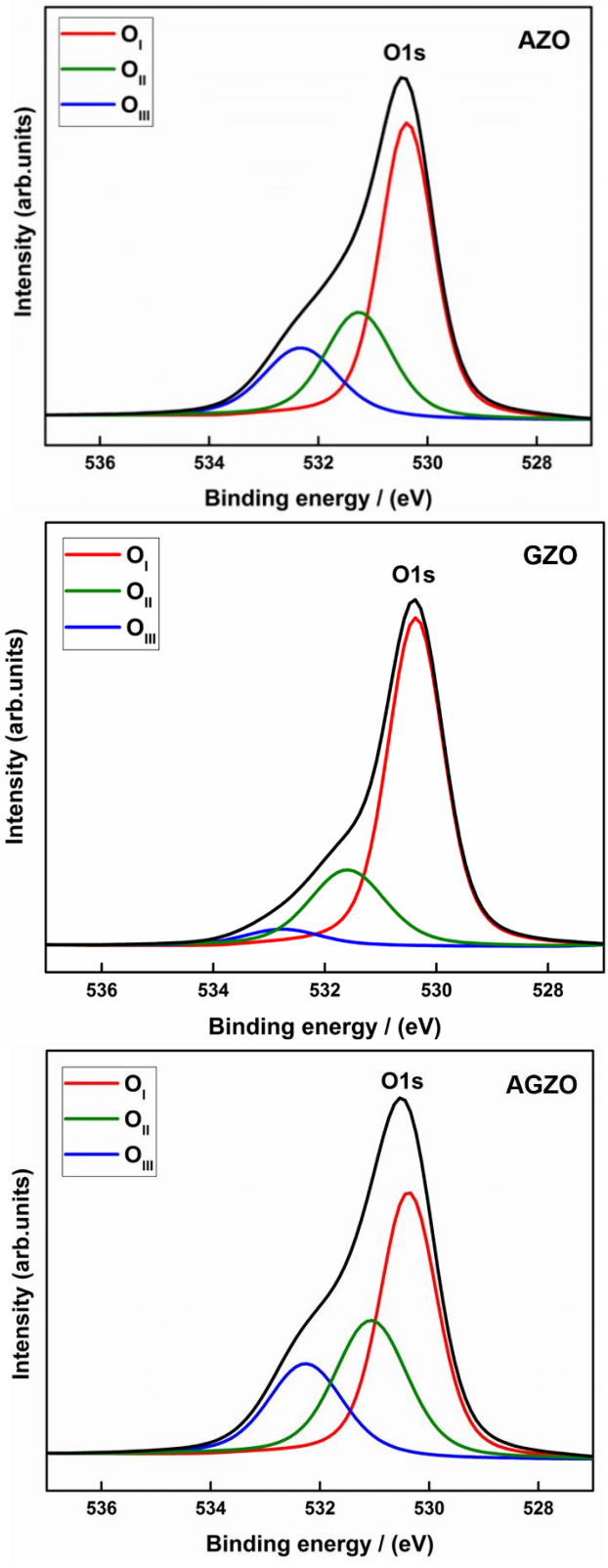

Figure 57 XPS data of O 1s in optimum1.5 at.% AZO 1.5 at.% GZO and AGZO.

Table 6 shows the elemental composition of the singly doped and co-doped powders from the XPS measurements.

Table 6 The XPS data of the singly doped and co-doped ZnO powders.

Al/Ga doped ZnO powder (at.%)	Elemental Composition (at.%)				
	Al 2p	Ga $2p_{3/2}$	Zn $2p_{3/2}$	O 1s	C 1s
0.5 AZO	2.04	-	47.62	45.54	4.8
1.0 AZO	4.16	-	45.02	46.82	3.96
1.5 AZO	5.02	-	40.45	43.67	10.87
2.0 AZO	5.80	-	42.78	48.89	2.53
2.5 AZO	6.21	-	36.46	44.07	9.78
0.5 GZO	-	2.29	48.98	44.30	4.43
1.0 GZO	-	4.95	47.56	44.39	3.09
1.5 GZO	-	5.72	45.29	46.56	2.43
2.0 GZO	-	8.22	43.02	46.40	2.36
2.5 GZO	-	9.80	40.49	46.94	2.76
AGZO	2.91	2.69	41.16	45.63	7.40

As expected, the Al and Ga content of AZO and GZO increases, respectively, with increasing dopant concentration in the precursor solutions. However, the dopant levels in the powder from the XPS measurements were found to be higher than expected from the initial concentrations in the precursor solutions, indicating that the dopants are more concentrated at the surface of the nanoparticles compared to the bulk.

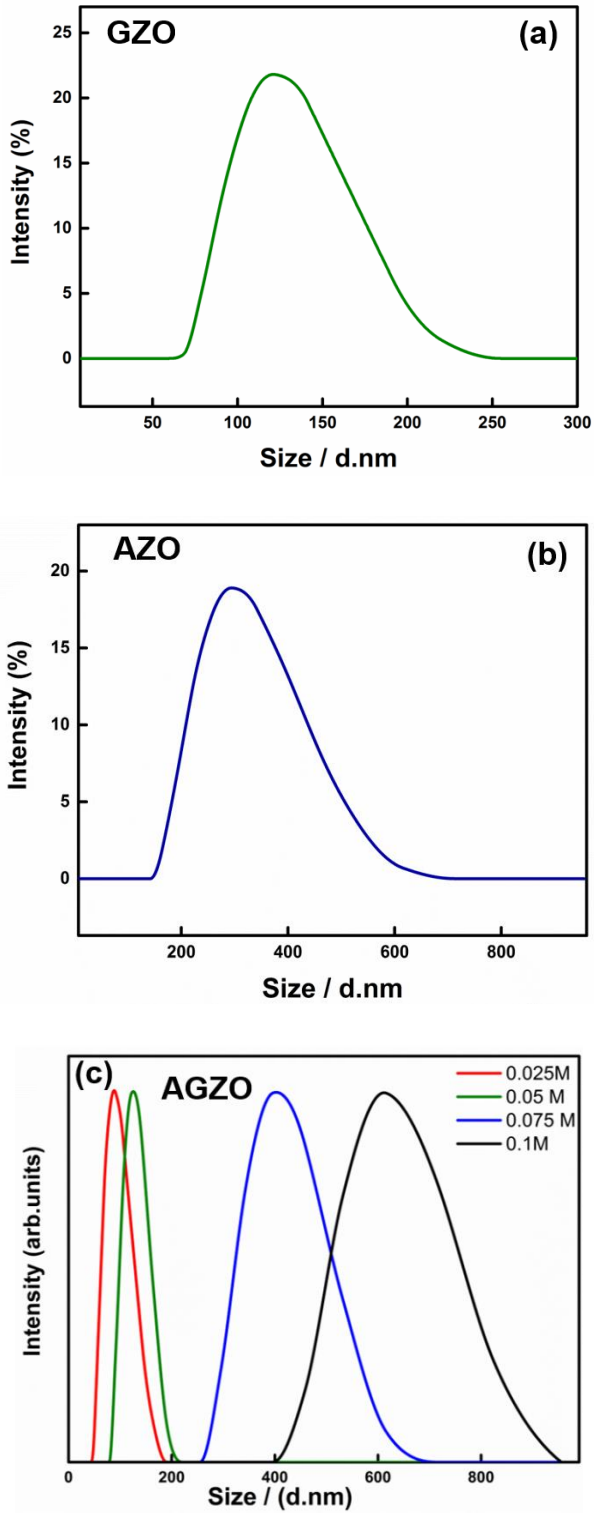

Figure 58 Particle size distribution of as-synthesised powders in diethylene glycol (a) 1.5 at.% GZO (b) 1.5 at.% AZO (c) AGZO with different precursor concentrations.

The particle size distributions of the as-synthesised powders were measured using dynamic light scattering (DLS) in diethylene glycol (Figure 58). The measurements were carried out using suspensions that were diluted enough (0.001g/L) to deter particle-to-particle interactions. The average particle size of GZO and AZO were 100 nm and 250 nm, respectively, for the optimum 1.5 at.% doping level. The effect of precursor concentration on the average particle size distribution was investigated for the optimized AGZO powder, with different concentrations of precursor varying from (0.025-0.1) moldm^{-3}. It was observed that reducing the concentration results in smaller average particle size distribution. The lowest average particle size (~85 nm) was detected for the suspension with 0.025 moldm^{-3} concentration, which was stable as a colloid for more than a month. Suspensions of conducting materials with this level of stability could be used in developing TCO ink formulations for inkjet printing which is beyond the scope of the present work.

Figure 59 shows the morphology and structural features of as-synthesised optimal AZO, GZO and AGZO powders. Both singly doped and co-doped powders exhibited a broad size distribution with particles around (100-200) nm. The FEG-SEM images of powders clearly show polycrystalline clusters of nanoparticles which are mostly spherical. Formation of these agglomerated spherical clusters is most likely due to the high surface energy of individual nanoparticles.[225]

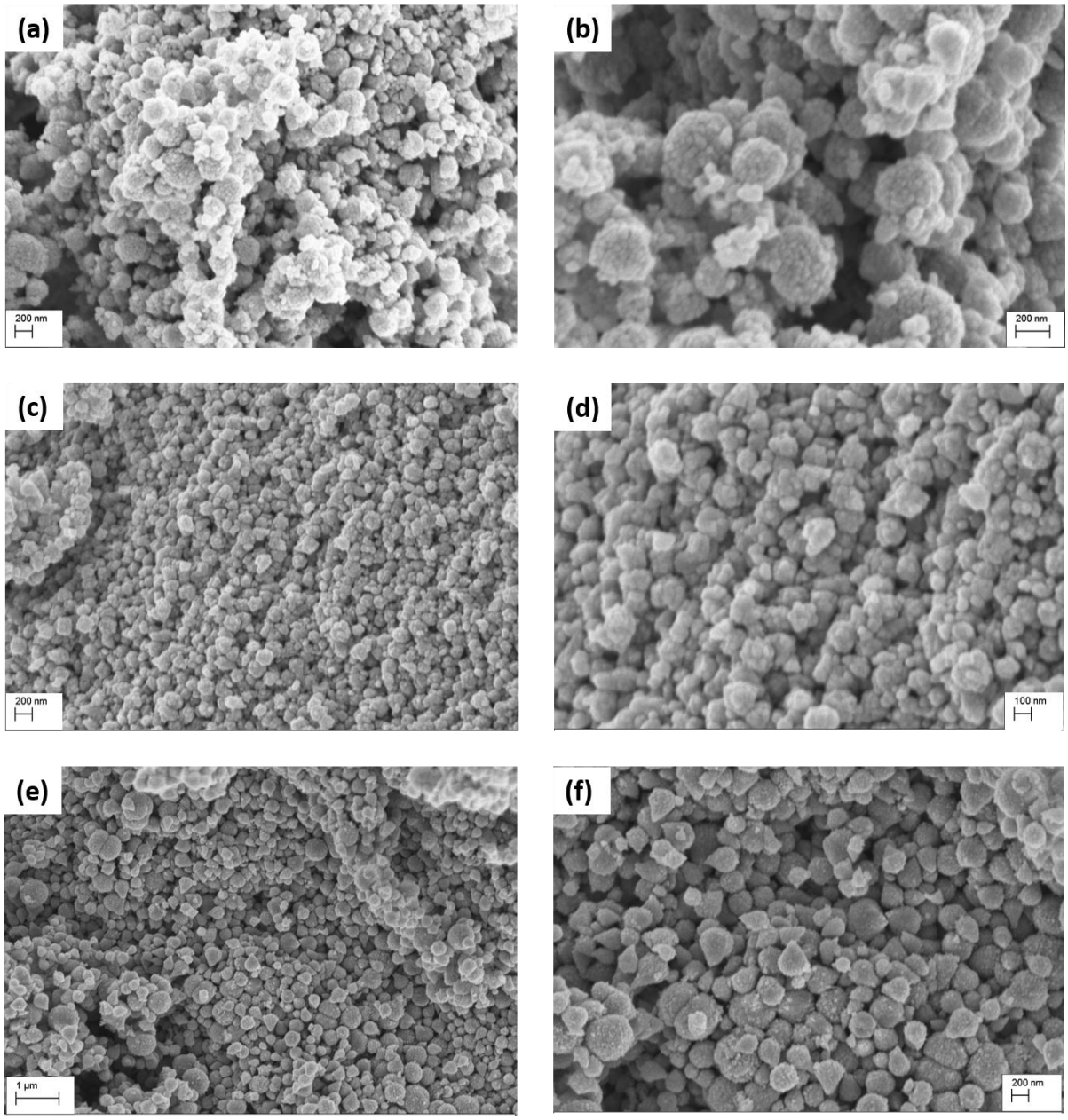

Figure 59 FEG-SEM images as-synthesised powders (a) and (b) 1.5 at.% Al doped ZnO (c) and (d) 1.5 at.% Ga doped ZnO (e) and (f) Al, Ga co-doped ZnO.

Figure 60 shows the surface morphology of AGZO pellets subjected to 90s microwave sintering and 3 hours radiant annealing at 600 °C. No cracks were seen through the pellets surfaces. However, cavities are visible between the grains in both pellets after heat treatment. A colour change in pellets (Figure 61) was observed after heat treatment, implying a shift from lower density to higher density.[283]

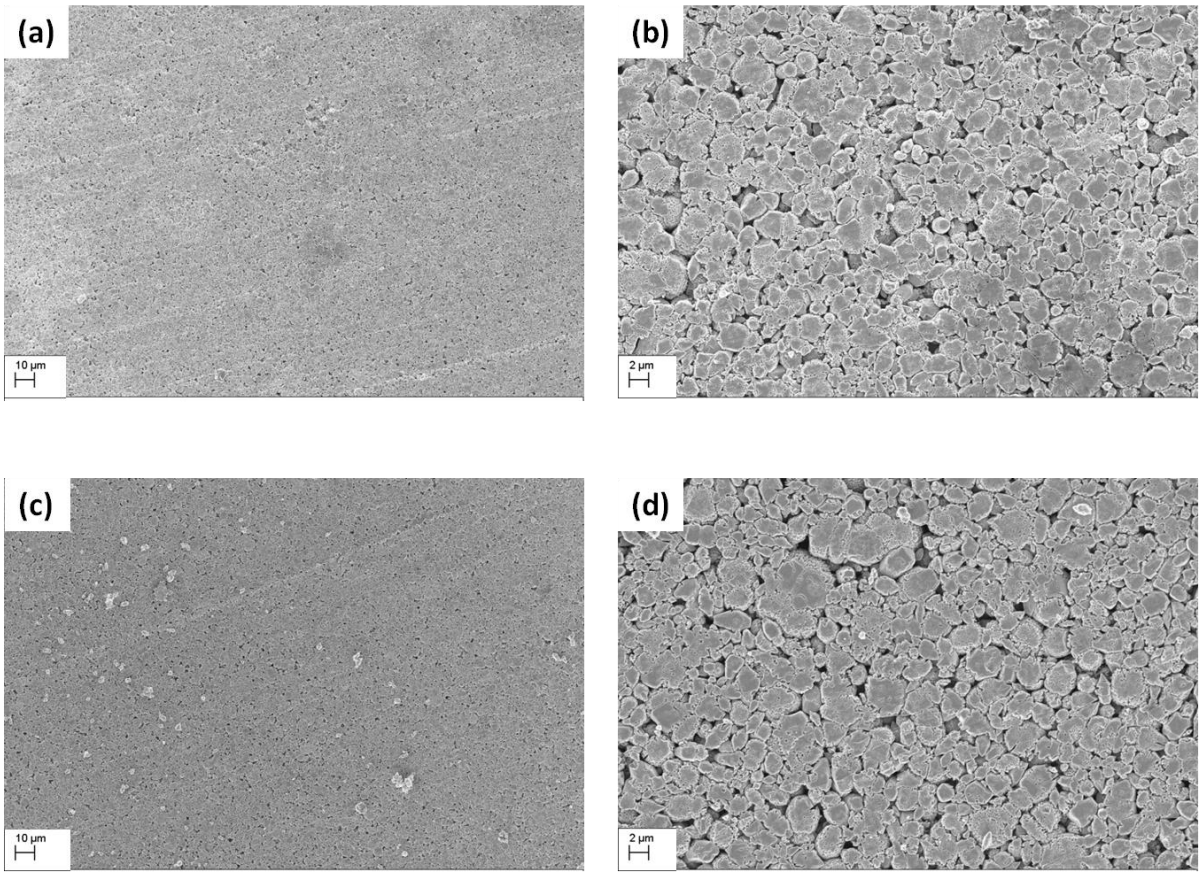

Figure 60 FEG-SEM images of AGZO Pellets (a) and (b) microwave post-synthesis heat treated (c) and (d) conventionally post-synthesis heat treated.

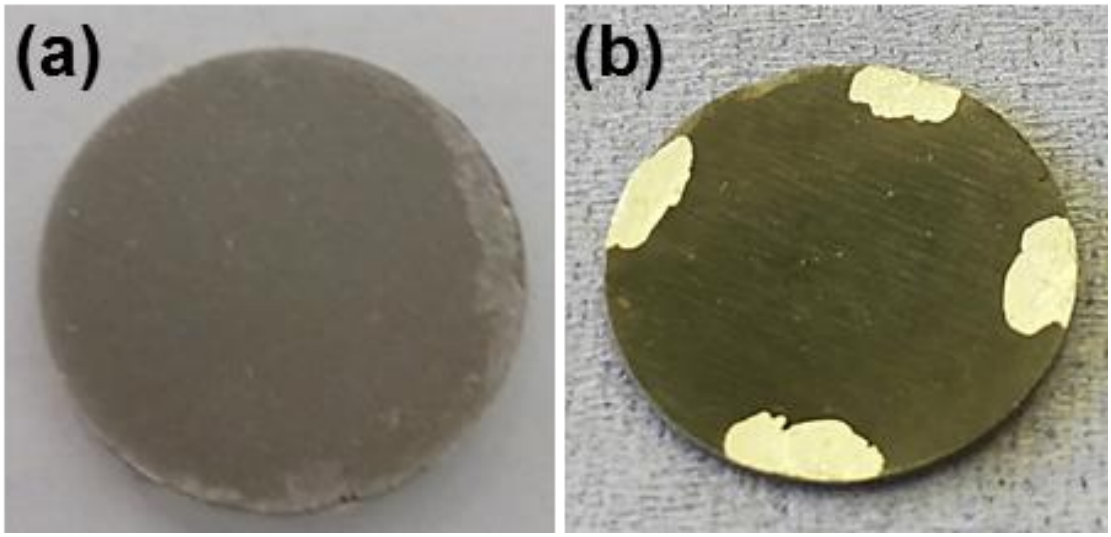

Figure 61 Colour change in AGZO pellets (a) before annealing (b) after annealing.

Figure 62 shows the X-ray diffraction spectra of microwave synthesised pure ZnO, and the best singly doped and co-doped powders which gave the lowest resistivity values. The powder samples exhibited only the polycrystalline ZnO reflections, with a preferred orientation of (101), indicating a preferential orientation of the crystals along the *a* and *c* axes.[284,167,59] All doped and un-doped powders crystallized in the wurtzite structure.[218] No other phases were detected in the XRD data. The high crystallinity of the microwave synthesised powders was implied by the narrow peak width and the relatively high intensity of the reflections in the XRD patterns. It is well-known that volumetric heating by microwaves produces materials with a greater level of crystallinity than those produced by many other conventional synthesis methods.[285,286]

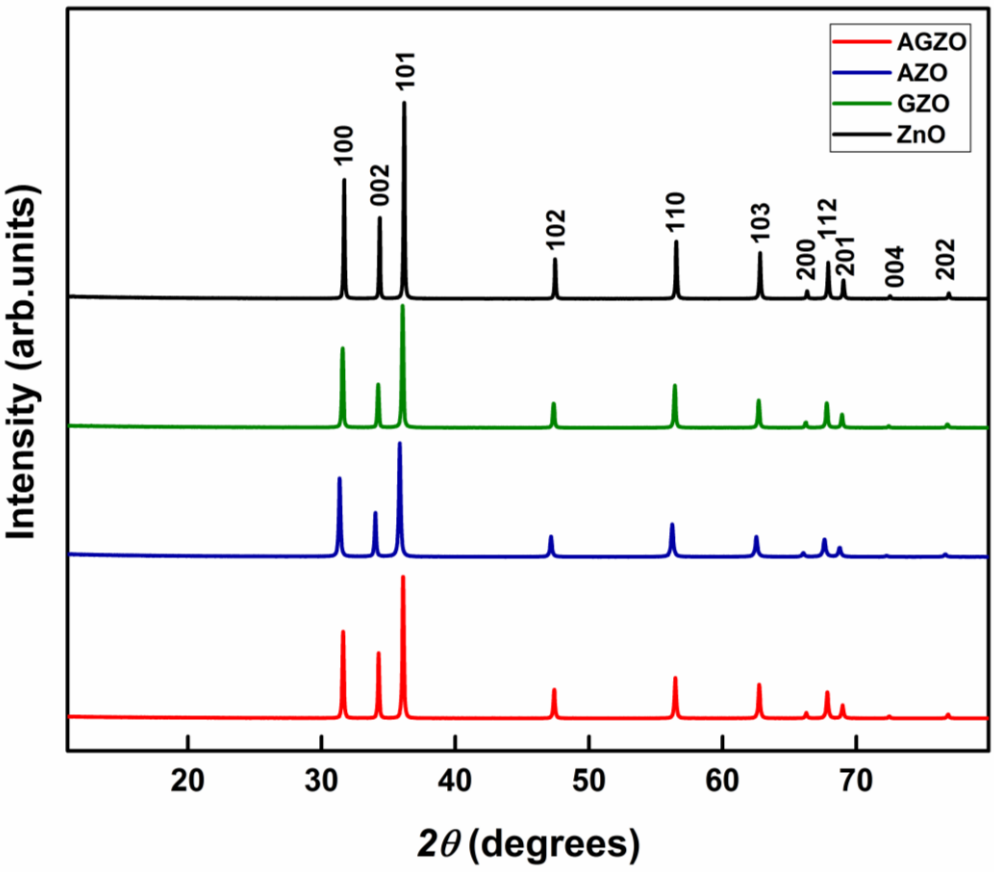

Figure 62 XRD patterns of as-synthesised ZnO, best singly doped and co-doped powders.

In order to compare the crystallinity and the average crystallite sizes, full width half maximum (FWHM) values were obtained for the (101) dominant reflection planes for the best AZO, GZO and AGZO powders which were then used to calculate the crystallite size using the Scherrer Equation.[287] Furthermore, the unit cell volumes were calculated using GSAS and EXPGUI, and are shown in table 7.

Table 7 Summary of structural properties of the best Al and Ga doped as-synthesised powders.

Sample	FWHM (°)	*a* (Å)	*c* (Å)	*c/a*	V (Å^3)	d (nm)
AGZO	0.1500	3.25244(9)	5.2099(2)	1.6018	47.723(3)	55.6530
1.5 at.% GZO	0.1520	3.2521(9)	5.209(1)	1.6017	47.71(4)	54.8878
1.5 at.% AZO	0.1980	3.251(1)	5.208(1)	1.6019	47.68(4)	42.1738
ZnO	0.1320	3.2520(8)	5.210(1)	1.6021	47.72(3)	63.2471

Highly crystallized polycrystalline materials with larger grains, show strong XRD reflections and a narrow FWHM.[288] AGZO and GZO showed similar FWHM values and crystallite sizes. The higher FWHM and the lower crystallite size in the AZO powder imply reduced crystallinity in AZO compared to GZO and AGZO. The wurtzite structure of ZnO has a hexagonal unit cell with two lattice parameters, *a* and *c*.[289] ZnO lattice parameters (*a* = 3.2520 Å, *c* = 5.2101 Å) and their ratio (*c*/*a* = 1.6021) are similar to the values for the hexagonal close-packed (hcp) crystal structure. A variation in the lattice parameters and the unit cell volumes are observed after doping, due to the difference in the ionic radii of the dopants compared to that of Zn^{2+}, as explained in detail later.

6.3.2 Electrical Properties of Pellets

The resistivity (ρ), Hall mobility (μ) and carrier concentration (*n*) values of microwave annealed and conventional radiant annealed, singly doped pellets are summarized in figures 63 and 64. The electrical properties of the as-synthesised powder pellets could not be assessed due to the low robustness of the pelleted samples. Therefore, post-synthesis heat treatment was carried out to densify the pellets, improve their inter-particle connections and mechanical stability.[277] The resistivity of the pellets decreased upon increasing the doping content up to a certain amount, but further addition of

dopants gave rise to a higher resistivity. At the dopant content of 1.5 at.% both AZO and GZO pellets gave the lowest resistivity of 4.4×10^{-3} and 4.3×10^{-3} Ω.cm respectively, after the microwave post-synthesis heat treatment. Interestingly, the resistivity values of the pellets obtained from both heat treatment methods were comparable.

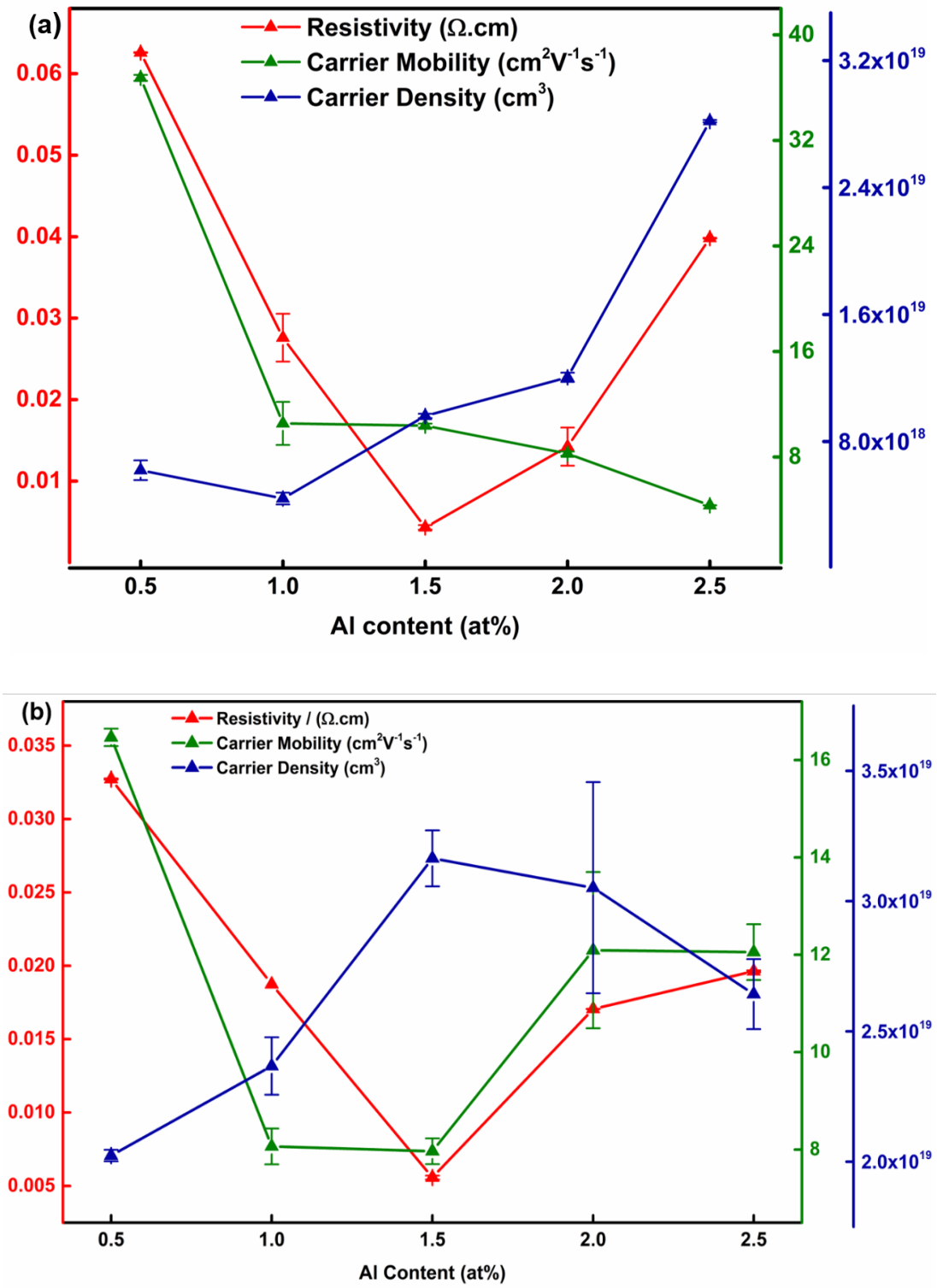

Figure 63 Electrical properties of (a) microwave annealed and (b) radiant annealed AZO pellets.

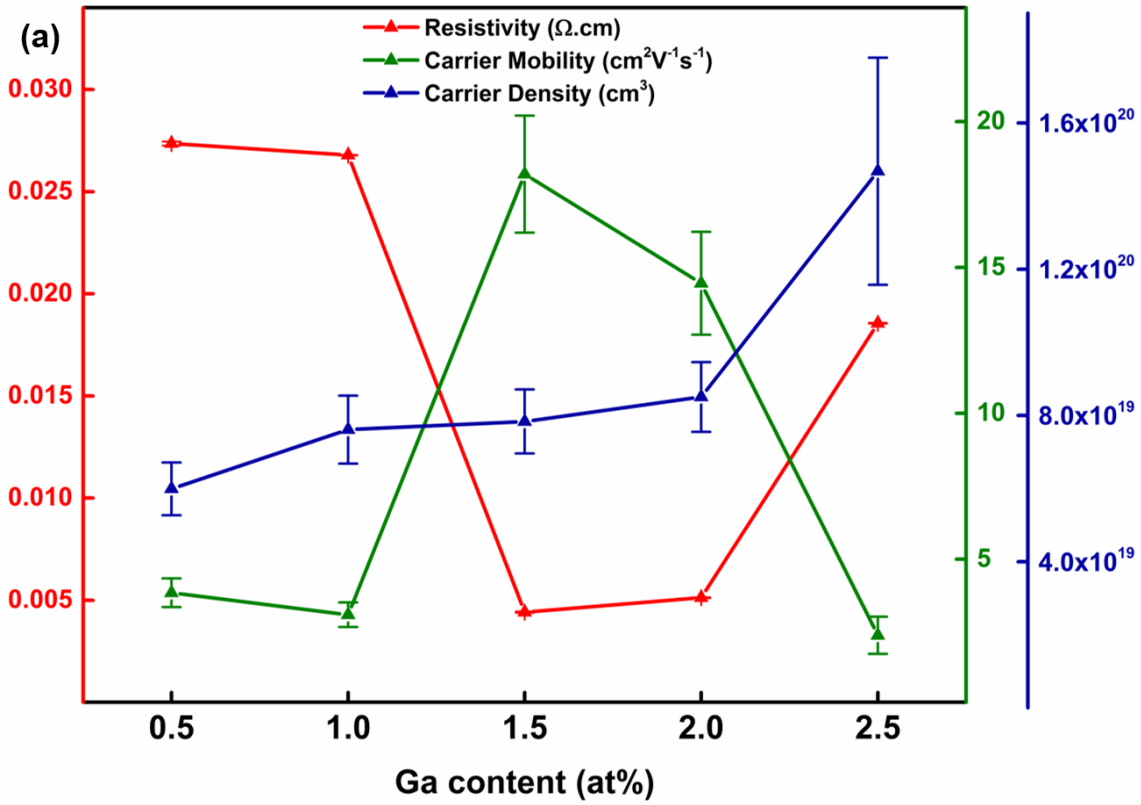

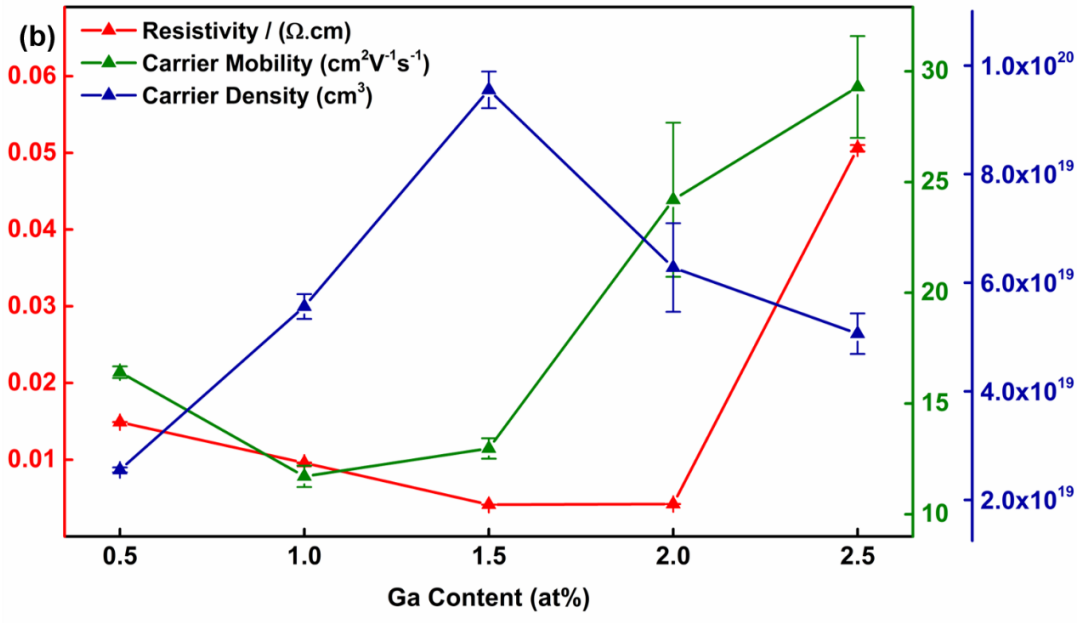

Figure 64 Electrical properties of (a) microwave annealed and (b) radiant annealed GZO pellets.

An increase in the carrier density from 0.5 at.% to 2.5 at.% dopant content of singly doped pellets was observed after the microwave heat treatment. This phenomenon is

understood as an effect of increasing the number of free carriers by substitutional or interstitial incorporation of Al^{3+} and Ga^{3+} in the ZnO structure.[45] The mobility of the carriers in highly doped pellets was seen to decrease, coinciding with lower conductivities. This could be a result of carrier-carrier scattering and ionized impurity scattering which could potentially take place at higher carrier densities ≥ 10^{19} cm^3.[290,291]

For conventional radiant annealed AZO and GZO samples, the carrier density peaks at 1.5 at.%, then decreases upon further doping. This effect is most likely due to the difference in heating time required for the two annealing techniques used in this work. Microwave annealing was carried out for 90s in the reducing atmosphere of 5% H_2/N_2 (~ O_2 5ppm), whilst the conventional heat treatment was carried out for much longer (3hours). During the longer conventional heat treatment, there is a greater chance of forming oxygen interstitials, by diffusion of trapped O^{2-} species (usually found at the surface of grain boundaries) into the crystal lattice, which may unfavourably affect the carrier density.[292,282,293] At the same time, the larger crystallite size formed by the longer heating time leads to a decrease in the grain boundary scattering and an improvement in the charge carrier mobility values.[45,294]

The effective doping of metal ions into ZnO, plays a key role in improving the electrical properties of doped-ZnO materials. The dopant substitution into the ZnO structure can be affected by the ionic radii of the dopants (r(Zn^{2+}) = 0.74 Å, r(Al^{3+}) = 0.54 Å, r(Ga^{3+}) = 0.62 Å) and the Madelung energy.[295,296] As the ionic radii of Al^{3+} and Ga^{3+} are both smaller than that of Zn^{2+}, the Al-O (1.81 Å) and Ga-O (1.90 Å) covalent bonds are shorter than Zn-O (2.00 Å) covalent bonds in the powders.[297] Therefore, increasing the dopant substitution can produce more crystal strain within the ZnO lattice, boosting the Madelung energy, making the structure unstable. Thus, a “saturation” point exists, beyond which the addition of further dopants, via the increase of the dopant concentration, could have a detrimental effect on the crystallinity.[258] Furthermore, due to the poor solubility of dopants in the ZnO structure at higher dopant levels, it is possible that segregation of a small secondary phase of non-conductive Al or Ga oxide is formed at the grain boundaries (of the respective doped-ZnO material), which may lead to the increase of resistivity seen for concentrations above 1.5 at% (Figure 63 and 64).[298]

In the case of AGZO, it is possible that the simultaneous introduction of both dopants in the lattice structure may lead to a compensation effect, whereby the difference in size of the two dopants helps to reduce some of the crystal strain, in turn allowing greater dopant solubility in the ZnO structure.[299] This improved doping of Al and Ga into the ZnO structure could reduce the formation of interstitials, non-conductive oxide phases and the accumulation of dopant elements, enhancing the electrical properties in AGZO. Correspondingly, the co-doping leads to a more pronounced drop in the resistivity (5.6 x 10^{-4} Ω.cm) compared to the single doped powders (table 8).

Table 8 Electrical properties of AGZO pellets.

	ρ (Ω.cm)	**μ ($cm^2V^{-1}s^{-1}$)**	**N (cm^3)**
Microwave AGZO	5.6 x 10^{-4}	8.32	8 x 10^{20}
Conventional AGZO	6.1 x 10^{-4}	12.74	6 x 10^{20}

Table 8 summarises the electrical properties of pelleted microwave synthesised AGZO powder samples after the post-synthesis heat treatment. The lowest resistivity values of 5.6 x 10^{-4} Ω.cm and 6.1 x 10^{-4} Ω.cm were observed for the pellets annealed by microwave and radiant annealing methods, respectively. As mentioned in the previous discussion, the reduced resistivity in AGZO is possibly due to the exceptional charge carrier properties achieved by the effective doping, with a minimal effect on ZnO crystalline lattice structure, as evident by the XPS and XRD analysis.

6.4 Conclusions

Al doped ZnO (AZO), Ga doped ZnO (GZO) and Al, Ga co-doped ZnO (AGZO) materials were successfully synthesised by a single-step microwave-assisted method. Studies conducted on all three pelleted powder samples indicate that co-doping leads to a more pronounced drop in the resistivity (5.6 x 10^{-4} Ω.cm) compared to the singly doped powders, which we propose is due to the exceptional charge carrier properties achieved by effective doping, with a minimal effect on the ZnO crystalline lattice structure. The

electrical properties of all samples illustrate that comparable resistivity values, for both singly doped and co-doped ZnO pellets, can be obtained via the energy efficient, rapid (i.e. 90s) microwave post-synthesis heat treatment rather than long (i.e. 3 hr) radiant annealing method. This could bring significant scientific, economic and environmental benefits for industrial scale up by saving cost and time. The highly stable nature of the microwave synthesized nanoparticle suspensions means that they could be useful in the preparation of ink formulations for inkjet printing. This study shows that there is significant potential to develop microwave synthesised Al, Ga co-doped ZnO as a promising alternative transparent conducting material, which is suitable to be used for both physical and solution processed thin film fabrication to make TCO coatings benefitting many applications where alternative TCO coatings are in significant demand.

Chapter 7

Transparent Conducting Film Fabrication of Al-Doped, Ga-Doped, and Al, Ga Co-doped ZnO and Application of Al, Ga Co-doped ZnO on Transparent Heaters

7.1 Overview

In addition to the more obvious uses in defrosting and demisting windows from moisture, metallic window heaters find applications in broad areas including temperature maintenance in industrial processes, heating of microchannel chips, sensors or displays and even painting conservation.[300] Transparent thin film heaters tend to outperform hydrophobic coatings for defrosting and anti-icing applications, mostly due to the poor mechanical and chemical stability of the hydrophobic coatings under extreme weather conditions.[301] The superior mechanical properties of transparent thin film heaters are also required in newer applications, such as in lab-on-chips and for wearable body heaters for personalized heating.[302,303] The latter, in particular, requires a coating of the transparent conducting material onto a flexible and stretchable substrate, which introduces the new demand for high mechanical flexibility and stretchability.[303] Transparent and smart windows are also considered key components for next generation energy efficient buildings.[304]

The ideal properties for a transparent thin film heater are low sheet resistance, high thermal stability and high transmittance. Additionally, excellent areal uniformity is required to achieve even heating from the thin film coating.[305] Indium tin oxide (ITO) has been widely used as a transparent thin film heater as it highly transparent (~90%) and conducting (10 Ω/sq),[305] however, it exhibits a slow thermal response and fails to perform in certain applications that require flexibility and robustness.[305] Significantly, due to the high production costs associated with the complex fabrication processes for ITO and the increasing price of indium sources, efforts have focused on finding inexpensive alternative materials.

In addition to the heating applications, TCO thin films fabricated on glass substrates have been fabricated in commercial quantities for flat panel displays, solar cells or in roll-to-roll coating operations for touch screens for decades. This increase has been enabled by the use of direct current (dc) magnetron sputtering systems. Apart from magnetron sputtering, deposition techniques including pulsed laser deposition (PLD),[30] chemical vapour deposition (CVD),[19,31,32,211] and radio frequency (RF) sputtering[34–36] have all been developed to deposit TCO films. Most of these deposition techniques are highly energy intensive, which require specially designed heated reactor lines and high vacuum systems. Therefore, alongside the hunt for alternative TCO materials, there is a significant interest directed towards emerging cost effective thin film fabrication methods to lower the overall production cost.

The materials properties of Al, Ga singly-doped and co-doped ZnO were discussed in detail in chapter 6, indicating the promising signs of utilising AGZO as a cost-effective alternative for replacing expensive ITO. To establish the practicality of using the conducting TCO nanoparticles for coatings, thin films were fabricated by the AACT technique.[306,257] The effect of the carrier gas flow rate, deposition time and deposition temperature were investigated to optimise the conductivity of the deposited thin films. Using these optimal deposition parameters for AZO, GZO and AGZO, respectively, thin films were fabricated and their opto-electric properties were compared. Out of the three doped-ZnO powders, AGZO showed the lowest resistivity, with a value of 5.7×10^{-3} Ω.cm for films with 90% visible transmittance.

Finally, AGZO thin films were fabricated into transparent thin film heaters and studied. A mean temperature of 132.3 °C was reached after applying a voltage of 18 V for 10 min, giving a power consumption of 2.11 W. These results show that AGZO thin films could easily be fabricated and used as transparent heaters to replace the more expensive indium tin oxide. There are not many reports on the use of doped ZnO in transparent heating applications.[307] To the best of the knowledge, this is the first report of Al, Ga co-doped ZnO for heater application.

7.2 Experimental details and characterization techniques

7.2.1 Synthesis of doped-ZnO Powders and Thin Film Fabrication

Conducting powders were synthesised, suspended and were then used to deposit thin films on glass substrates according to a recently published method using aerosol assisted chemical transport (AACT).[306] AZO, GZO and AGZO powders were synthesised in a microwave reactor (Anton Paar Multiwave PRO, 2.45 GHz, 1500W) from a precursor solution containing $Zn(CH_3COO).2H_2O$ (1.00 g) (BDH Chemicals), $AlCl_3.6H_2O$ (0.0165 g) (Sigma-Aldrich) and $Ga(NO_3)_3.xH_2O$ (0.0175 g) (Sigma-Aldrich) dissolved in diethylene glycol (DEG) (45 mL) (Sigma-Aldrich) and deionized water (5 ml). The clear precursor solution was transferred to a fluorocarbon polymer (TFM) vessel and was purged with Ar for 5 min. The reaction vessel was heated to 200 °C for 30 mins at a ramp rate of 20 °C min^{-1}, resulting in an opaque suspension. Upon cooling, the powder was collected by centrifuging and was washed with ethanol and allowed to dry in an oven for 1 hour at 60 °C.

For thin film fabrication by AACT, the doped-ZnO powder (0.2 g) was dispersed in 50 ml of methanol (100%, VWR Chemicals). Formic acid (0.05 ml) was added to aid in the formation of a suspension and ethyl cellulose (0.01g) was added as a binder.[308,251] The suspension was sonicated for 5 min using a sonicator probe (S-4000, Misonix, Inc, USA). Prior to the deposition, the glass substrates (1.5 x 2 cm) were cleaned ultrasonically with doubly distilled water, acetone, propan-2-ol, and then stored in ethanol. In the deposition, an ultrasonically produced aerosol of the suspension was directed via an N_2 + 5%H_2 gas flow (BOC, UK) towards the heated glass substrate in a tube furnace (MTF-10-25-130, Carbolite, UK). Iterative manipulation of the key deposition parameters (deposition time, carrier gas flow rate and the deposition temperature) was used to determine the optimum deposition parameters for AZO, GZO and AGZO. Subsequent depositions of these three materials were carried out under these optimised conditions.

7.2.2 Thin Films Characterisation

X-ray diffraction (XRD) measurements were conducted on a Bruker AXS Advance X-ray diffractometer with primary monochromatic high intensity Cu Kα (λ = 1.541 Å) radiation and a position sensitive detector. The electrical properties were measured by a four-point probe conductivity meter (Jandel, HM20, Jandel Engineering Ltd., Linslade, UK) and by a Hall effect measurement system (ECOPIA Hall effect measurement system, HMS-3000), using the Van der Pauw method to determine the bulk resistivity of the thin films. The surface and cross-sectional morphology of the thin films were investigated using a Leo 1530 VP field emission gun scanning electron microscope (FEG-SEM) at an accelerating voltage of 5 kV and a working distance of 5 mm. Optical transmittance measurements of the thin films were conducted using a dual beam Perkin-Elmer Lambda 35 UV-Vis spectrometer (Perkin Elmer, Massachusetts, US) over the wavelength range of 300 nm – 800 nm.

7.2.3 Transparent Heater Characterisation

Conducting silver paint (agar scientific) was used to make electrical connections either side of the AGZO thin film. The AGZO region between the silver contacts was 1.5 cm^2. The sheet resistance across the two silver terminals was 126.7 Ω/sq. Crocodile clips were used to connect the terminals to a DC power supply. A thermal imaging camera (Micro-Epsilon TIM 400T1500 with 13° optics) was used to measure the heating and cooling temperature profiles. A potential was applied for 600 seconds and then was turned off and the sample was allowed to cool to room temperature (~600 seconds). Heating and cooling profiles were recorded using applied potentials of 6, 9, 12 and 18 V. The reported temperatures are the average over the active area.

7.3 Results and Discussion

7.3.1 Thin Film Fabrication and Optimization of the Key Deposition Parameters

Al and Ga doped ZnO powder was used for the optimisation of key deposition parameters in the AACT technique, as it showed the best conductivity among all of the

metal doped-ZnO powders. The key deposition parameters were methodically studied to improve the conductivity. The surface coverage and the morphology of the film were controlled by iteratively modifying the deposition time, carrier gas flow rate and the deposition temperature respectively. The methanolic suspensions with 0.2 g of powder were found to yield a suspension that was stable for over 1 hr, so this was adopted for use throughout the rest of this work.

Initially, the carrier gas flow rate was varied from 108.54 ml min^{-1} to 367.60 ml min^{-1} keeping the other parameters constant (i.e. deposition time 30 min and temperature 50 °C). The FEG-SEM images (figure 65) show the surface morphology of AGZO thin films deposited using N_2 + 5% H_2 carrier gas at 108.54, 219.87 and 323.27 ml min^{-1} flow rates respectively. It can be observed that as the flow rate increases the surface coverage improves. This may be because larger particles are carried towards the heated substrate at higher flow rates, which cause greater nucleation and hence more deposition on the surface of the substrate, improving coverage. No sheet resistance values were observed for the lower flow rates (108.54 or 219.87 ml min^{-1}), most likely due to the poor surface coverage. The film deposited at 323.27 ml min^{-1} gave the lowest sheet resistance (i.e. 2.3 MΩ/sq) among the remaining films. The film deposited at 367.60 ml min^{-1} appeared to have a higher surface coverage in the SEM, but had a far higher sheet resistance than the other films (3.7 MΩ/sq). This high resistance was likely due to poor interparticle connectivity caused by the poor adhesion of the larger particles to the substrate, which is far more numerous at higher flow rates. The poor adhesion is supported by the fact that films fabricated at the highest flow rate were powdery and rubbed off easily, which was unlike the other thin films.

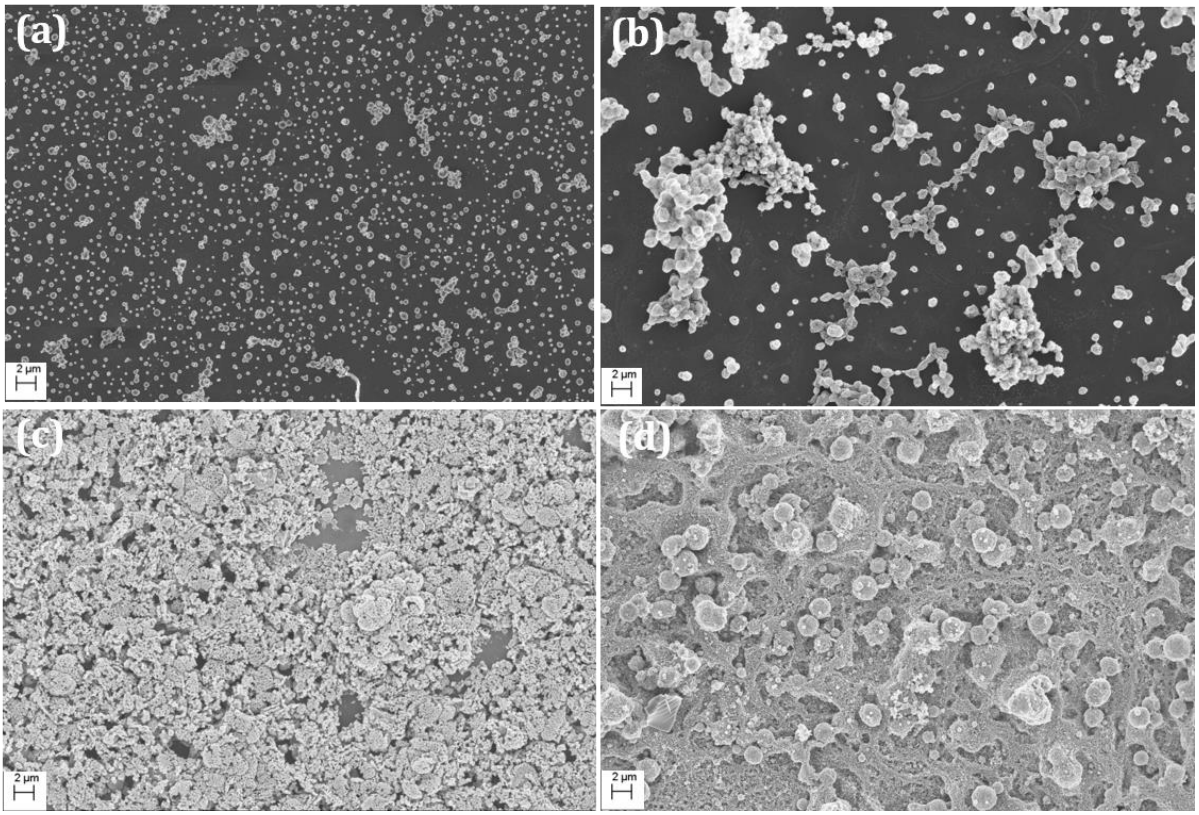

Figure 65 FEG-SEM images of AGZO thin films deposited for 30 min at 50 °C by AACT using carrier gas flow rates of (a) 108.54 ml min^{-1}, (b)219.87 ml min^{-1}, (c) 323.27 ml min^{-1} and (d) 367.60 ml min^{-1}.

Figure 66 shows the surface topographical SEM images of AGZO films deposited at different deposition times by AACT. The deposition time was varied from 30 to 75 mins, whilst maintaining a constant aerosol flow rate. As shown in figure 66b, it was found that the films prepared over 60 and 75 min deposition times, had a complete surface coverage and lower sheet resistance values than the film deposited at 30 min. As there was a negligible difference in the sheet resistance of the 60 and 75 mins films, 60 mins was adopted as the optimal deposition time. The sheet resistance values for both 60 and 75 mins films were 121 kΩ/sq and 122 kΩ/sq respectively.

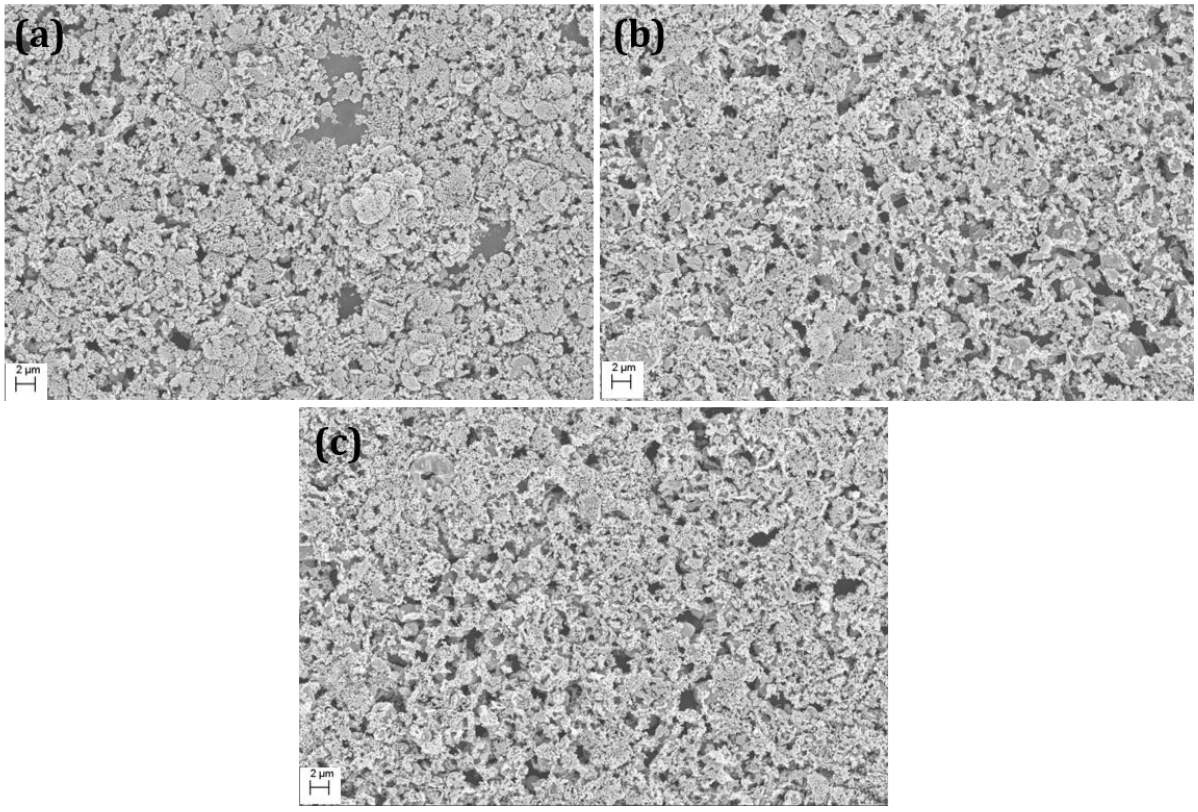

Figure 66 Surface topographical SEM images of AGZO thin films deposited at 50 °C with a 323.27 ml min^{-1} for different deposition times (a) 30 min, (b) 60 min, and (c) 75 min.

To further improve the conductivity, higher deposition temperatures were investigated. The deposition temperatures were varied from 50 °C to 500 °C. Figure 67 shows the SEM images of AGZO thin films deposited at 50 °C, 100 °C, 200 °C and 300 °C and figure 68 shows the morphology of the film deposited at 400 °C.

As the temperature increases, the particles in the films appeared to be fusing together to form a more compact and well adhered film with improved surface coverage. The SEM image of the film deposited at 400 °C shows uniform features which consist of sintered AGZO particles. The cross-sectional image in figure 68b also shows the good uniformity of the film thickness. The film thickness after 60 min deposition time was around 400 nm, indicating an average growth rate of ~7 nm/min. The film uniformity has a great importance in TCO thin films, especially in heater applications as differences in the thickness and coverage of the thin film can cause the film to heat unevenly.

At the elevated temperatures inside the decomposition chamber of the AACT apparatus thin films formation can be assumed to occur through 3 steps.

1. solvent evaporation
2. nano-particles land on the substrate
3. nanoparticles begin to fuse together with the help of EC binder linked to the particles.

During the deposition period, steps 1 – 3 are repeated continuously to form the thin film. The rate of these individual processes affects the end morphology and thickness of the resultant film. Increasing the temperature affects the rates, particularly of step 3, leading to improved fusion and interparticle necking.

The sheet resistance of the films decreased upon increasing the deposition temperature and gave the lowest resistance of 142.5 Ω/sq at 400 °C (figure 69). This could be a result of the improved electrical connection between individual particles themselves. As it is reported, the increase of deposition temperature could accelerate the nucleation, subsequently improves the inter-particle and particle-substrate connections leading to a better conductivity.[309] However, an increase in the sheet resistance was noticed for the film deposited above 400 °C, which possibly is due to an unfavourable alteration in the crystal structure of ZnO that occurs at high temperatures.[310,311] Since the lowest sheet resistance was observed at 400 °C it was adopted as the optimal temperature for further depositions.

Unlike thin films fabricated at lower temperatures, the thin films fabricated at 400 °C were found to be much more mechanically stable. Standard Scotch Tape tests were used to assess the adherence of the coating as shown in figure 70 and there was no change in the sheet resistance of the films after the scotch tape test confirming the good film adherence.

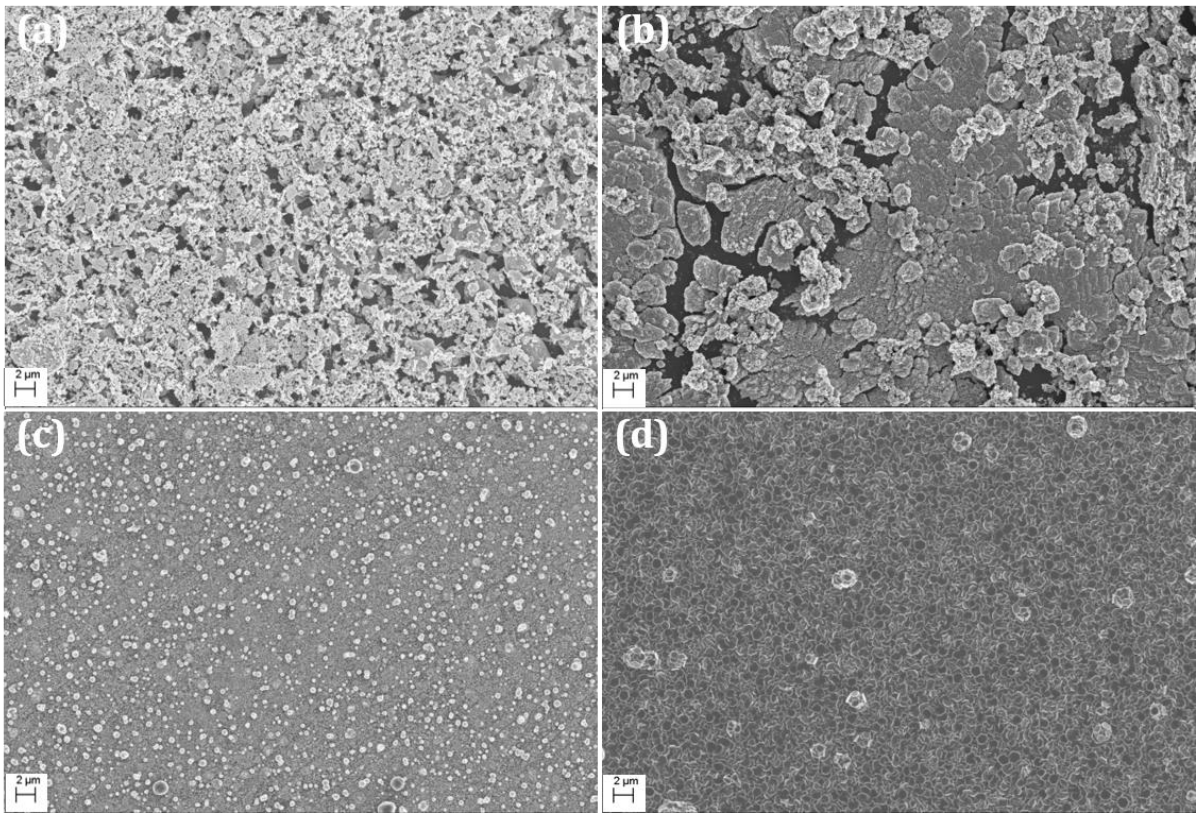

Figure 67 FEG-SEM images of AGZO thin films deposited for 60 min using 323.27 ml min^{-1} carrier gas flow for deposition temperatures of (a) 50 °C, (b) 100 °C, (c) 200 °C and (d) 300 °C.

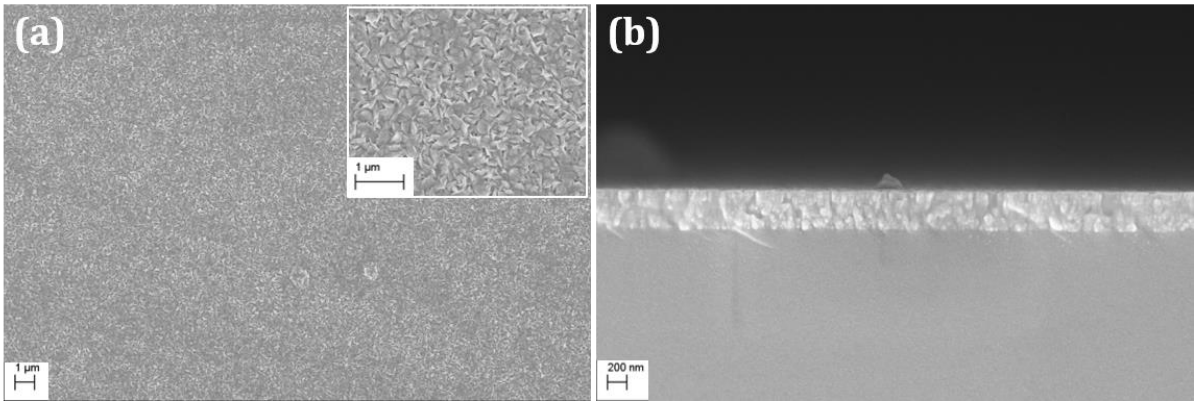

Figure 68 Optimized AGZO thin film at 400 °C for 60 min using 323.27 ml min^{-1} carrier gas flow with (a) surface FEG-SEM images with 10 K X, insert 20 K X magnifications and (b) cross-sectional FEG-SEM image of an AGZO thin film deposited by aerosol assisted chemical transport.

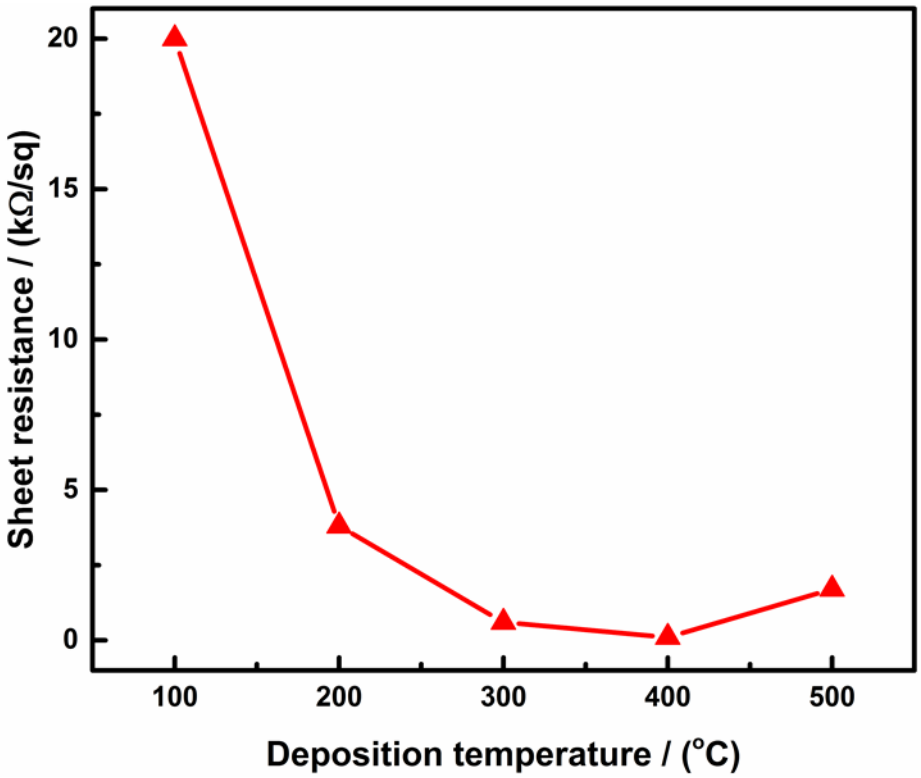

Figure 69 Variation of sheet resistance against different deposition temperatures.

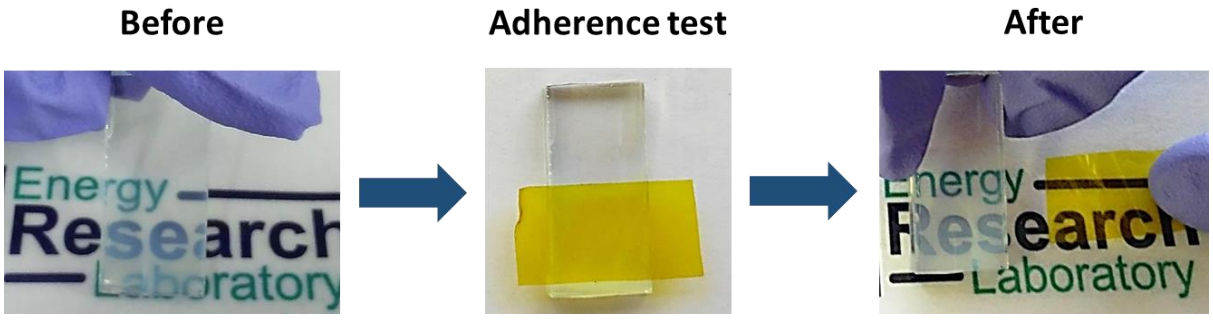

Figure 70 Images of the scotch tape test for the optimized AGZO thin film deposited by AACT.

7.3.2 Opto-electrical Properties and Characterization of Optimized Thin Films

AZO, GZO and AGZO thin films were fabricated using the optimised AACT parameters as discussed above. The surface morphological images of the AACT deposited AZO, GZO and AGZO films are illustrated in figure 71, 72 and 68 respectively. The images indicated that the deposited films showed a good surface coverage with fused nanoparticles deposited at 400 °C. Electrical properties obtained by the Hall effect measurements are presented in table 9. The lowest film resistivity values obtained for AZO and GZO were $1.2x10^{-2}$ Ω.cm (for the film thickness of 500 nm) and $1.6x10^{-2}$ Ω.cm (for the film thickness of 400 nm) respectively. Both films showed over 85% transmission in the visible region. The best conductivity was achieved for the thin film coatings fabricated using co-doped AGZO powders with the optimal doping levels of 1.5 at.% for Al and Ga. A film resistivity of 5.7×10^{-3} Ω.cm was observed for AGZO (for the film thickness of 400 nm) with an average transparency of 90% in the visible region of the spectrum as shown in figure 73.

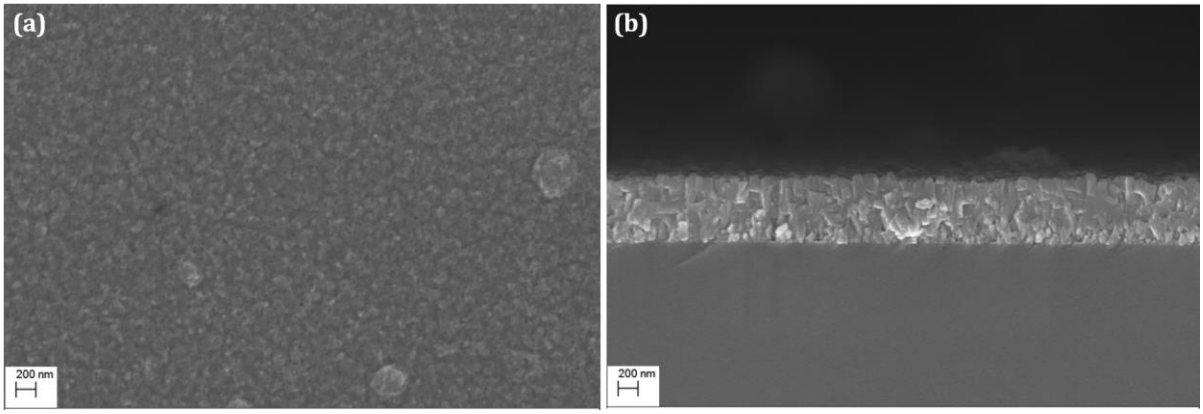

Figure 71 Surface (a) and cross-sectional (b) images of AZO thin film deposited by aerosol assisted chemical transport using optimal deposition parameters.

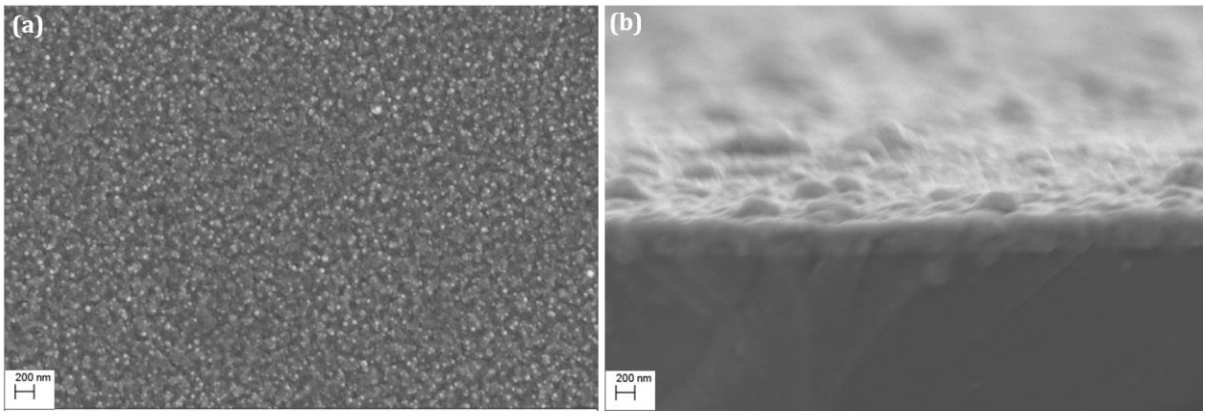

Figure 72 Surface (a) and cross-sectional (b) images of GZO thin film deposited by aerosol assisted chemical transport using optimal deposition parameters.

As discussed, the conductivity is a concerted effect of the carrier concentration and the Hall mobility of donors. Hence, the variation in the resistivity of the thin films compared to the pellets is possibly due to the drop in the carrier density or/and hall mobility. A similar effect has been observed by other groups for the sputter coated films at temperatures above 250 °C.[312,313] According to their reports, dopant can migrate at grain boundaries, forming small regions of non-conducting oxides, which in turn act as scattering centres. This can influence both the carrier density and the mobility unfavourably, causing an increase in the resistivity. Furthermore, this could also create defects in the crystal structure, adversely affecting the crystallinity. We believe that a similar phenomenon may affect the electrical properties of the AACT films, hence increase the resistivity in the thin films compared to that of in the pellets.

Table 9 Properties of the AACT deposited thin films; Resistivity (ρ), Hall mobility (μ) and carrier concentration (*n*).

Thin film	**ρ (Ω.cm)**	***n*** **(cm^3)**	**μ ($cm^2V^{-1}s^{-1}$)**
AZO	$1.2x10^{-2}$	$1.7x10^{19}$	2.8
GZO	$1.6x10^{-2}$	$6.1x10^{19}$	6.5
AGZO	$5.7x10^{-3}$	$7.0x10^{19}$	14.4

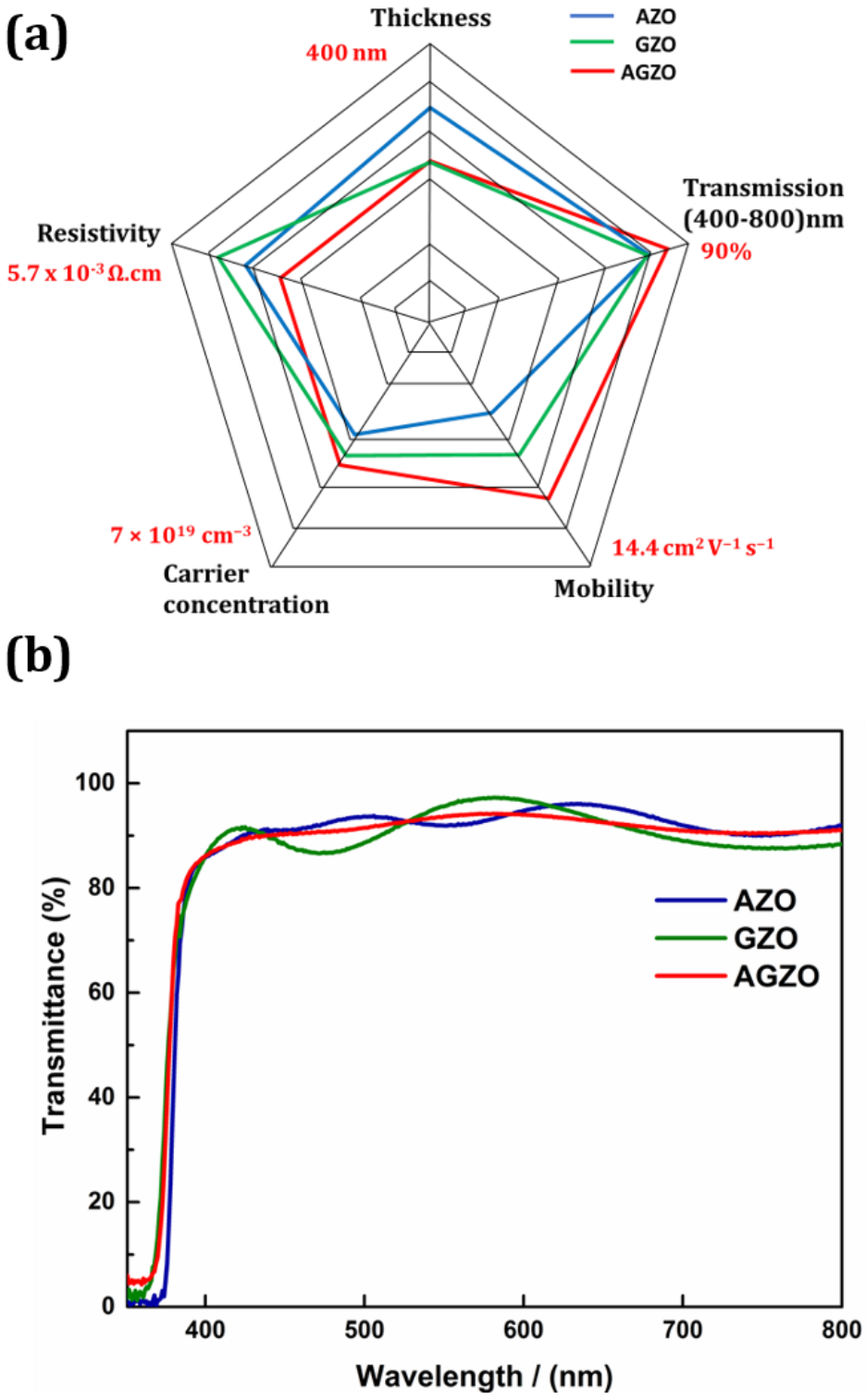

Figure 73 (a) State of art values and (b) optical transmission spectrum of AACT deposited AZO, GZO and AGZO thin films.

XRD analysis of thin films indicates that the ZnO thin film grows in the wurtzite phase, preferentially along the 'c' axis with a prominent peak from the (002) plane (Figure 74).

No impurity phases were detected in the XRD pattern of the thin films.[312] It was also noticed that the intensity of some of the ZnO reflections decreased after the thin film fabrication (compared to the doped-ZnO powder XRD in chapter 6), indicating an alteration in the crystallinity and further suggesting that higher deposition temperature could be affecting the electrical properties.

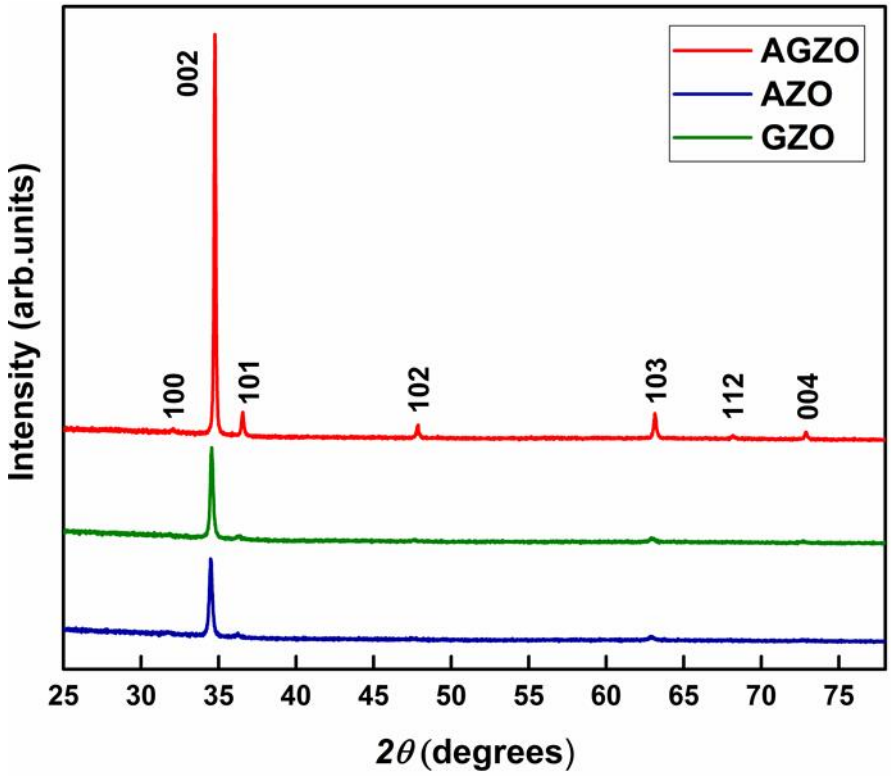

Figure 74 XRD diffractograms of AZO, GZO and AGZO thin films deposited by AACT.

The band gap energies were obtained from the Tauc plots, produced using the transmission-diffuse reflectance spectra of the thin films (Figure 75). The optical band gap energies of AZO, GZO and AGZO thin films are 3.24, 3.26 and 3.31 eV respectively. The band gap value (Eg) can be evaluated by the formulation given as below:

$$(\alpha h\nu)^2 = C\,(h\nu - Eg) \qquad (29)$$

where C is a constant, $h\nu$ is photon energy, and α is absorption coefficient, which is derived using the expression:

$$\alpha = \ln(1/T)/d \qquad (30)$$

Here T and d represent transmissivity and thickness, respectively. By drawing a line along the linearity part of the curve of $(\alpha h\nu)^2$ versus $(h\nu)$ and intercepting the x-axis, the x value equal to E_g is obtained.[314] According to the Burstein–Moss theory, the optical band gap value closely correlates with carrier density.[315] Since the lowest localized state density in the band gap of ZnO is only 3.68×10^{18} cm^{-3},[316] when the carrier concentration is larger than this, electrons are promoted and occupy the bottom of the conduction band. As the Pauli exclusion principle applies, further electrons must be promoted to higher energy levels, requiring more energy. This is observed through a broadening in the observed band gap. The wide band gaps contribute towards the high optical transmittance of TCO thin films.

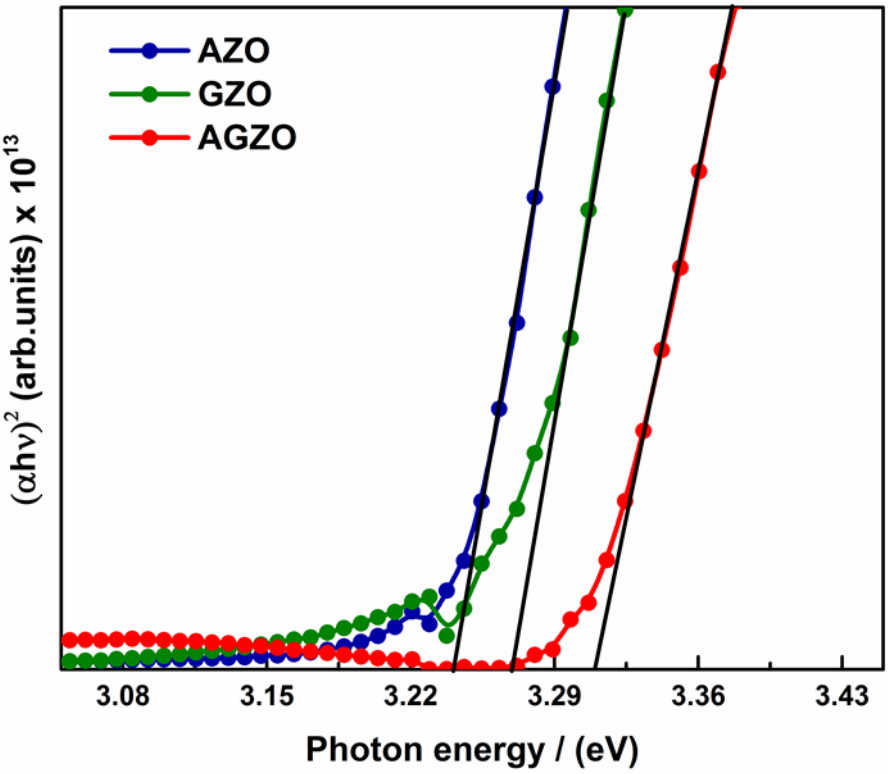

Figure 75 Tauc plot for AACT deposited AZO, GZO and AGZO thin films

7.3.3 Fabrication of Transparent Heater using Al, Ga Co-doped ZnO Thin Films

The most important factor for a thin film heater is the sheet resistance of the material, the lower the value, the better its power efficiency. The sheet resistance of the AGZO thin film was 142.5 Ω/sq at a thickness of 400 nm, giving a resistivity of 5.7 x 10^{-3} Ω.cm. Temperature-time profiles of the AGZO thin film (with an active area of 1.5 cm^2) for applied potentials of 6, 9, 12, 15 and 18 V were measured using a thermal imaging camera. The thin films were allowed to heat for 10 mins and then cool back to room temperature as shown in figure 76a. The average temperature of the thin film after 10 min of heating is plotted as a function of applied voltage in figure 76b; average temperatures of 46.6, 58.6, 79.3, 104.0 and 132.3 °C were reached after applying 6, 9, 12, 15 and 18 V, respectively. The power consumption, P, and the resistance, R, of the AGZO thin film heater can be determined from equations 31 and 32, where I is the current passing through the AGZO thin film, ρ is the resistivity, L is the distance separation between the electrodes, A is the area of the AGZO thin film, δ is the film thickness and W is the width.

$$P = I^2R \qquad (31)$$

$$R = \rho\frac{L}{A} = \rho\frac{L}{\delta W} \qquad (32)$$

The current passing through the AGZO heater plotted as a function of applied voltage is shown in figure 76b. The sheet resistance between the two electrodes was calculated to be 95 Ω/sq. The power consumption of the AGZO heater was 0.267, 0.578, 0.950, 1.56 and 2.11 W for applied voltages of 6, 9, 12, 15 and 18 V, respectively.

Whilst the thermal properties of the thin film heater depend on the electrical and thermal conductivity and specific heat capacity of the active material, to a large extent, the heating performance is ultimately decided by the substrate properties (substrate type and thickness).[305] More specifically, the response time of the heater depends on the additional mass which can be the substrate or the encapsulating material which is covering the heater.[305] Different substrates and thicknesses are used depending on the

application, which makes comparisons with other materials and work in the literature difficult. The thicker the substrate, the longer the response time of the heater will be, due to heat loss to the substrate by conduction. Therefore, thicker substrates will take longer to reach a temperature plateau compared with thinner substrates. The thickness of the glass substrate used in this study was 3 mm, which is the typical thickness used for glazing applications. Thus, it gives a realistic insight into the response time of heated windows if our material was to be used in a scaled-up application.

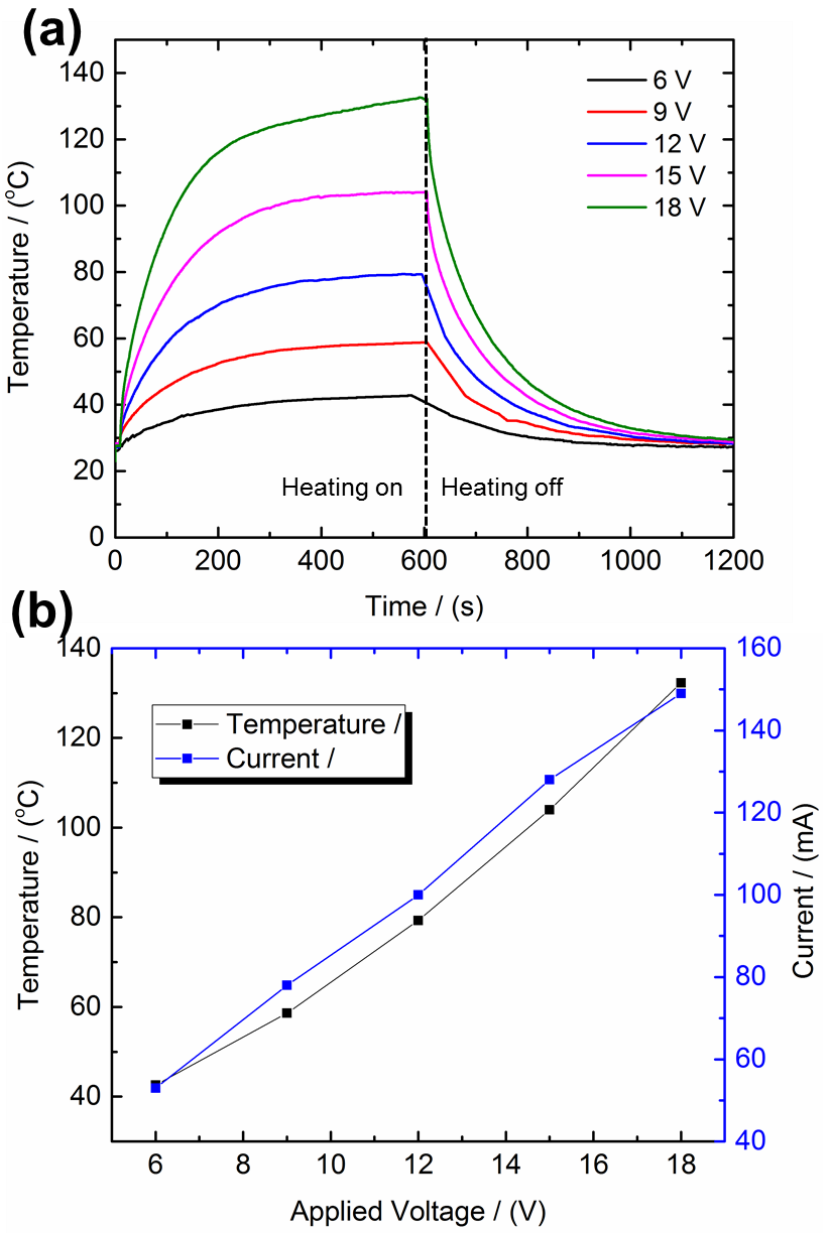

Figure 76(a) Heating and cooling temperature profiles of the AGZO thin film heater at various voltages. (b) Average temperature and current as a function of applied voltage.

A thermal image of the AGZO heater is shown in figure 77 along with a histogram of the temperature distribution after 10 min of heating at an applied voltage of 18 V. The mean thin film temperature was 132.3 °C with a standard deviation of 9.7 °C. There were some hotspots in the film which reached up to 156.7 °C and some cooler areas which were around 100 °C, however, these areas accounted for less than 0.2 % of the total film area. The broad temperature distribution is likely to stem from variation in the AGZO thin film thickness and homogeneity.

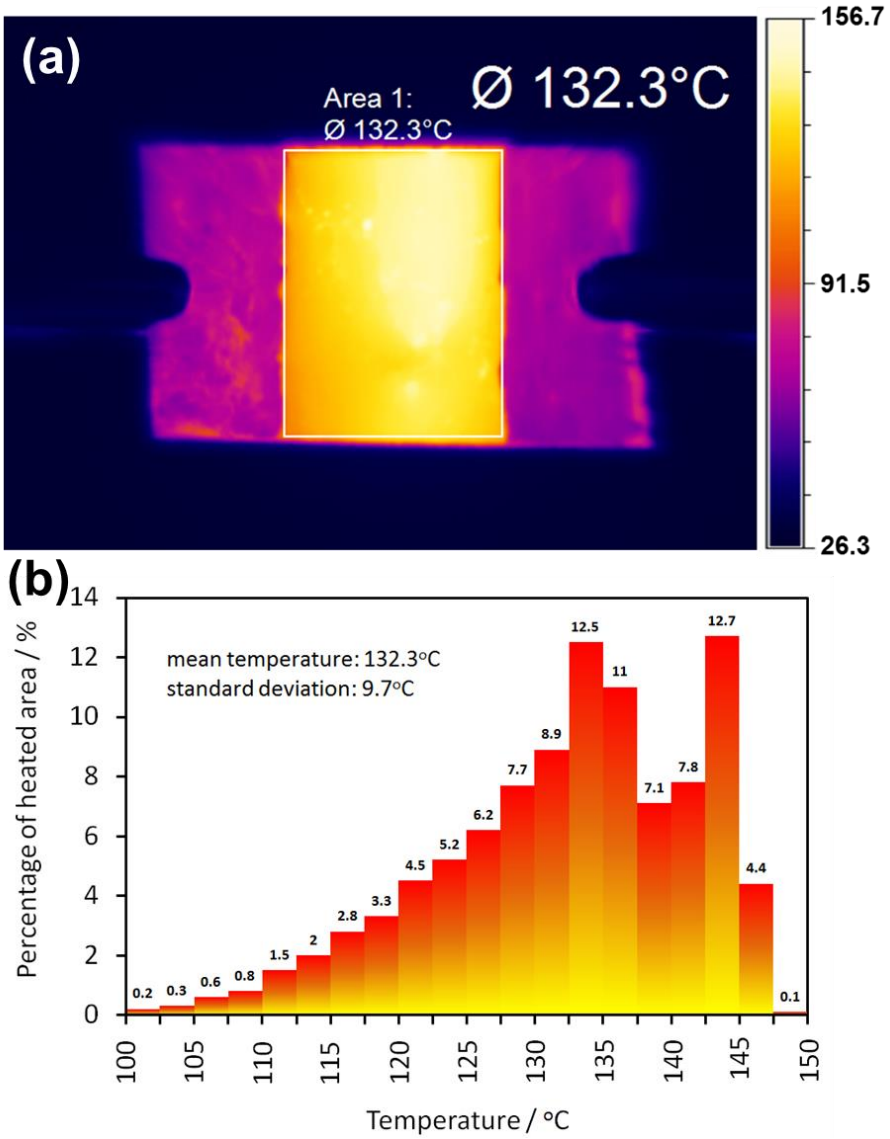

Figure 77(a) Thermal image and (b) histogram of the temperature distribution of the AZGO thin film heater at an applied voltage of 18 V after 600s of heating.

7.4 Conclusions

This study demonstrates a new and simple aerosol assisted physical vapour deposition technique (i.e. AACT) to fabricate TCO films by using doped-ZnO powders. AZO, GZO and AGZO thin films were fabricated on float glass substrates from a nanoparticle suspension using a new and inexpensive deposition technique. The influence of the carrier gas flow rate, deposition time and deposition temperature on optimising the conductivity of the deposited thin films were investigated. The SEM images showed that uniform films with higher surface coverage can be obtained at elevated deposition temperatures. As the particles fuse together at higher deposition temperatures, inter-particle connections improve to give rise to a better conductivity. AZO GZO and AGZO thin films were fabricated by using the optimal deposition parameters and the opto-electronic properties were compared. Among all three doped-ZnO powders, the lowest resistivity of 5.7 x 10^{-3} Ω.cm was obtained for AGZO with 90% visible transmittance. Moreover, the AGZO films were investigated for use as transparent thin film heaters; average temperatures of 46.6, 58.6, 79.3, 104.0 and 132.3 °C were reached after applying 6, 9, 12, 15 and 18 V, respectively, for 10 min. The power consumption of the heater at 18 V was 2.11 W. The results show that the Al, Ga co-doped ZnO thin film can be used as an alternative material for indium in oxide, which is suitable to be used for both physical and solution processed thin film fabrication to make TCO coatings benefitting many applications including transparent thin film heaters.

Chapter 8

Conclusions

Over the past few years there has been a significant increase in research into the synthesis and thin film fabrication of doped metal oxides for transparent conducting applications. Currently, the most widely used TCO material is indium tin oxide due to its excellent optical and electrical properties. ITO, however, also has distinct disadvantages including high costs, associated with the scarcity of indium. The demand for low-cost conducting thin films has pushed research towards new TCO materials. Similarly, efforts to reduce the processing costs associated with thin film fabrication has driven research towards low-cost synthesis and post-sintering technologies. With this in mind, this thesis has focussed projects on the development of a new low-cost aerosol assisted physical deposition method, which can be used for TCO thin film fabrication, in addition to projects producing highly conducting doped metal oxide materials, as potential ITO replacements in TCO applications.

The first project reported in this thesis outlines efforts to develop a new and simple aerosol assisted physical vapour deposition technique. This technique was used to fabricate TCO films using TCO nanoparticle suspensions. Specifically, Sn-doped In_2O_3 (ITO) thin films were fabricated on plain glass substrates from a nanoparticle suspension using a new and inexpensive aerosol-assisted chemical transport (AACT) process. The influence of solvent type, loading level and film deposition time on the structural, electrical and optical properties of the deposited thin films was investigated. Analysis of the surface morphology confirmed that by using methanol as the appropriate solvent, with the optimal loading level (0.20 wt/vol%), there is a significant improvement in the film nanoparticle coverage. This correspondingly gives rise to improved electrical properties in the thin films. Furthermore, the SEM images of the films prepared using a 30 min deposition time, with a 0.20% (wt/vol%) methanolic ITO

suspension, provided a better surface coverage compared to the other deposition times investigated.

In a follow up investigation, the effect of a post-deposition heat-treatment step on the resistivity and transparency of the ITO films was investigated. Microwave radiation and conventional radiant heat-treated films were compared with one another. Microwave heat treatment can be carried out in a much shorter time and is therefore known to have a significantly reduced energy footprint, compared to the conventional radiant heat treatment. The ITO films fabricated through the optimal deposition parameters were heat-treated with either microwaves or conventional radiant heating in order to improve the inter-particle connections and film adherence. The XRD diffractograms confirmed that post-deposition heat treatment of ITO films helped to enhance the purity of the desired phase. ITO films heat treated with microwave annealing post-deposition exhibited an average transmittance of over 85% in the visible region, with a resistivity of 12 Ω.cm and a carrier concentration of 3.7 x 10^{16} cm^3, which was superior to films that were heat-treated using the more conventional thermal processing (despite the shorter processing time for the microwave process). The resistivity of ITO films was further decreased to 6.0 x 10^{-2} Ω.cm with an increased carrier concentration of -8.0 x 10^{18} cm^3 when ethyl cellulose was added to the ITO suspension prior to the AACT deposition. The enhanced conductivity of these films was hypothesised to be due to the improved particle-particle and particle-substrate connections, which was indicated by SEM imaging. The resistivity of the microwave heat treated AACT-ITO films showed comparable results to films reported in the literature, fabricated by a commonly used sol-gel method.

In an effort to develop alternative materials to ITO ZnO powders were fabricated with a range of metal dopants. Specifically, Al doped ZnO (AZO), Ga doped ZnO (GZO), Si doped ZnO (SZO), Cu doped ZnO (CZO) and Mn doped ZnO (MZO) powders were all synthesised and processed using microwave radiation and subsequently evaluated to determine their electrical properties. The respective dopant amounts were varied to tune the conductivity. Resistivity trends were constructed to detect the optimal doping of the powders. In general, the resistivity trends showed an initial decrease in the resistivity with an increase in the dopant content, to a point, whereby further increases

in dopant concentration led to an increase in the resistance. The fact that the trend passes through a minimum could be related to a kinetic equilibrium process, whereby higher concentrations of metal dopants could be nucleated with oxygen ions and form bigger impurity particles. Larger particles would be difficult to be incorporated into the ZnO lattice, particularly at higher concentrations. Subsequent measurements of the carrier density and electron mobility of the pellets were obtained using the van der Pauw method. In addition, structural and surface analysis was carried out by using XPS, XRD and SEM for the optimally doped ZnO powders. XPS confirmed the presence of the relevant elements in each metal doped ZnO samples and showed no other additional peaks, indicating that there is a single phase of ZnO in all the samples, which agrees with the XRD results. Apart from MZO, SEM images of all the other powders show a structure of mostly agglomerated spherical nanoparticles. MZO exhibited a much broader particle size distribution compared to the other powders. Formation of these agglomerated clusters could be due to the solvent evaporation. Among all the microwave synthesised singly doped-ZnO powders, AZO and GZO showed significantly better optoelectronic properties and was therefore chosen for more in-depth study.

To fully explore the AZO and GZO materials, a more expansive study was conducted. Al doped ZnO (AZO) and Ga doped ZnO (GZO) were synthesised by a single-step microwave-assisted method to carry out these detailed studies. In an effort to enhance the conductivity of the metal doped ZnO materials, co-doping of the powders was undertaken with both the Al and Ga dopants. The resulting pelleted powders were found to have a significantly lower resistivity (5.6×10^{-4} Ω.cm) compared to the singly-doped powders, which is due to the exceptional charge carrier properties achieved by effective doping with a minimal effect on the ZnO crystalline lattice structure. This was hypothesised to be due to the simultaneous introduction of both dopants in the lattice structure, which may lead to a compensation effect, whereby the difference in size of the two dopants works to reduce some of the crystal strain, in turn allowing greater dopant solubility in the ZnO structure.

To determine the practicality of using these conducting TCO nanoparticles for coatings, thin films were fabricated by the previously validated AACT technique. The effect of the carrier gas flow rate, deposition time and deposition temperatures were investigated to

optimise the conductivity of the deposited thin films. Using the optimal deposition parameters AZO, GZO and AGZO thin films were fabricated and their optoelectronic properties were compared. Out of the three doped-ZnO powders, AGZO showed the lowest resistivity, with a value of 5.7 x 10^{-3} Ω.cm for films with 90% visible transmittance. This study indicates that there is a significant potential to develop microwave synthesised AGZO as a promising alternative transparent conducting material, which is suitable to be used for both physical and solution based thin film fabrication techniques.

Lastly, AGZO thin films were fabricated and tested to be used as transparent thin film heaters, as an example application for TCOs. A mean temperature of 132.3 °C was reached after applying a voltage of 18 V for 10 min, giving a power consumption of 2.11 W. These results show that AGZO thin films could easily be fabricated and used as transparent heaters to replace the more expensive ITO. The results show that the Al, Ga co-doped ZnO thin film can readily be used as an alternative to ITO. It has been shown that the material can be fabricated using less energy, is highly transparent and conductive and is also applicable to a wide variety of TCO applications.

Chapter 9

References

(1) Lewis, B. G.; Paine, D. C. Applications and Processing of Transparent Conducting Oxides. *MRS Bull.* **2011**, *25* (8), 22–27.

(2) Chinnock, C. The End of ITO Dominance is in Sight http://www.insightmedia.info/the-end-of-ito-dominance-is-in-sight/ (accessed Jul 6, 2015).

(3) Granqvist, C. G.; Hultåker, A. Transparent and conducting ITO films: new developments and applications. *Thin Solid Films* **2002**, *411* (1), 1–5.

(4) Materion. Transparent Conductive Oxide Thin Films.

(5) Askari, H.; Fallah, H.; Askari, M.; Mohmmadieyh, M. C. Electrical and optical properties of ITO thin films prepared by DC magnetron sputtering for low-emitting coatings. **2014**.

(6) Wang, Y.; Overvig, A. C.; Shrestha, S.; Zhang, R.; Wang, R.; Yu, N.; Dal Negro, L. Tunability of indium tin oxide materials for mid-infrared plasmonics applications. *Opt. Mater. Express* **2017**, *7* (8), 2727.

(7) Fang, V.; Kennedy, J.; Futter, J.; Manning, J. *A review of near infrared reflectance properties of metal oxide nanostructures*; 2013.

(8) Fortunato, E.; Ginley, D.; Hosono, H.; Paine, D. C. Transparent Conducting Oxides for Photovoltaics. *MRS Bull.* **2011**, *32* (3), 242–247.

(9) Ginley, D. S.; Bright, C. Transparent Conducting Oxides. *MRS Bull.* **2011**, *25* (8), 15–18.

(10) Minami, T. New n-Type Transparent Conducting Oxides. *MRS Bull.* **2011**, *25* (8), 38–44.

(11) Wang, J. T.; Shi, X. L.; Liu, W. W.; Zhong, X. H.; Wang, J. N.; Pyrah, L.; Sanderson, K. D.; Ramsey, P. M.; Hirata, M.; Tsuri, K. Influence of Preferred Orientation on the Electrical Conductivity of Fluorine-Doped Tin Oxide Films. *Sci. Rep.* **2015**, *4* (1), 3679.

(12) Minami, T. Substitution of transparent conducting oxide thin films for indium tin oxide transparent electrode applications. *Thin Solid Films* **2008**, *516* (7), 1314–1321.

(13) Minami, T.; C, D. A. L. and J. J.; Chopra K L, M. S. and P. D. K.; Hartnagel H L, D. A. L. J. A. K. J. C.; T, M.; Freeman A J, P. K. R. M. T. O. C. R. P. H. and M. T. J.; G, G. R.; Coutts T J, Y. D. L. and L. X.; Minami T, N. H. and T. S.; Minami T, N. H. and T. S.; et al. Transparent conducting oxide semiconductors for transparent electrodes. *Semicond. Sci. Technol.* **2005**, *20* (4), S35–S44.

(14) Fallah, H. R.; Ghasemi, M.; Hassanzadeh, A.; Steki, H. The effect of annealing on structural, electrical and optical properties of nanostructured ITO films prepared by e-beam evaporation. *Mater. Res. Bull.* **2007**, *42* (3), 487–496.

(15) Diebold, U. The surface science of titanium dioxide. *Surf. Sci. Rep.* **2003**, *48* (5–8), 53–229.

(16) Zeng, H.; Yang, S.; Cai, W. Reshaping Formation and Luminescence Evolution of ZnO Quantum Dots by Laser-Induced Fragmentation in Liquid. *J. Phys. Chem. C* **2011**, *115* (12), 5038–5043.

(17) Zeng, H.; Du, X.-W.; Singh, S. C.; Kulinich, S. A.; Yang, S.; He, J.; Cai, W. Nanomaterials via Laser Ablation/Irradiation in Liquid: A Review. *Adv. Funct. Mater.* **2012**, *22* (7), 1333–1353.

(18) Noor, N.; Parkin, I. P. Enhanced transparent-conducting fluorine-doped tin oxide films formed by Aerosol-Assisted Chemical Vapour Deposition. *J. Mater. Chem. C* **2013**, *1* (5), 984–996.

(19) Bhachu, D. S.; Sankar, G.; Parkin, I. P. Aerosol Assisted Chemical Vapor Deposition of Transparent Conductive Zinc Oxide Films. *Chem. Mater.* **2012**, *24* (24), 4704–

4710.

(20) Peiris, T. A. N. Microwave-assisted processing of solid materials for sustainable energy related electronic and optoelectronic applications. Loughborough University 2014.

(21) Bhatti, I. A.; Nirmal Peiris, T. A.; Smith, T. D.; Upul Wijayantha, K. G. Hierarchical ZnO nanorod electrodes: Effect of post annealing on structural and photoelectrochemical performance. *Mater. Lett.* **2013**, *93*, 333–336.

(22) Dhar, A.; Alford, T. L. Controlled Microwave Processing of IGZO Thin Films for Improved Optical and Electrical Properties. *JOM* **2015**, *67* (7), 1624–1628.

(23) Fuh, C.-S.; Liu, P.-T.; Teng, L.-F.; Huang, S.-W.; Lee, Y.-J.; Shieh, H.-P. D.; Sze, S. M. Effects of Microwave Annealing on Nitrogenated Amorphous In-Ga-Zn-O Thin-Film Transistor for Low Thermal Budget Process Application. *IEEE Electron Device Lett.* **2013**, *34* (9), 1157–1159.

(24) Hwang, M.; Jeong, B.; Moon, J.; Chun, S.-K.; Kim, J. Inkjet-printing of indium tin oxide (ITO) films for transparent conducting electrodes. *Mater. Sci. Eng. B* **2011**, *176* (14), 1128–1131.

(25) Papavassiliou, G. C. Three- and low-dimensional inorganic semiconductors. *Prog. Solid State Chem.* **1997**, *25* (3–4), 125–270.

(26) Deen, M. J.; Pascal, F. Electrical characterization of semiconductor materials and devices—review. *J. Mater. Sci. Mater. Electron.* **2006**, *17* (8), 549–575.

(27) Bott, A. W. Electrochemistry of Semiconductors. *Curr. Sep.* **1998**, *17:3*, 87–91.

(28) Bard, A. J.; Faulkner, L. R. *Electrochemical Methods Fundamentals and Applications*; 1980.

(29) Bädeker, K. Über die elektrische Leitfähigkeit und die thermoelektrische Kraft einiger Schwermetallverbindungen. *Ann. Phys.* **1907**, *327* (4), 749–766.

(30) Agura, H.; Suzuki, A.; Matsushita, T.; Aoki, T.; Okuda, M. Low resistivity transparent conducting Al-doped ZnO films prepared by pulsed laser deposition.

Thin Solid Films **2003**, *445* (2), 263–267.

(31) Knapp, C. E.; Hyett, G.; Parkin, I. P.; Carmalt, C. J. Aerosol-Assisted Chemical Vapor Deposition of Transparent Conductive Gallium–Indium–Oxide Films. *Chem. Mater.* **2011**, *23* (7), 1719–1726.

(32) Tahir, A. A.; Peiris, T. A. N.; Wijayantha, K. G. U. Enhancement of Photoelectrochemical Performance of AACVD-produced TiO2 Electrodes by Microwave Irradiation while Preserving the Nanostructure. *Chem. Vap. Depos.* **2012**, *18* (4–6), 107–111.

(33) Ehsan, M. A.; Peiris, T. A. N.; Wijayantha, K. G. U.; Olmstead, M. M.; Arifin, Z.; Mazhar, M.; Lo, K. M.; McKee, V. Development of molecular precursors for deposition of indium sulphide thin film electrodes for photoelectrochemical applications. *Dalton Trans.* **2013**, *42* (30), 10919–10928.

(34) Minami, T. Present status of transparent conducting oxide thin-film development for Indium-Tin-Oxide (ITO) substitutes. *Thin Solid Films* **2008**, *516* (17), 5822–5828.

(35) Minami, T. Properties of transparent zinc-stannate conducting films prepared by radio frequency magnetron sputtering. *J. Vac. Sci. Technol. A Vacuum, Surfaces, Film.* **1995**, *13* (3), 1095.

(36) Isherwood, P. J. M.; Walls, J. M. Cupric Oxide-based p-type Transparent Conductors. *Energy Procedia* **2014**, *60*, 129–134.

(37) Wang, T.; Liu, Y.; Fang, Q.; Wu, M.; Sun, X.; Lu, F. Low temperature synthesis wide optical band gap Al and (Al, Na) co-doped ZnO thin films. *Appl. Surf. Sci.* **2011**, *257* (6), 2341–2345.

(38) Ellmer, K.; Vollweiler, G. Electrical transport parameters of heavily-doped zinc oxide and zinc magnesium oxide single and multilayer films heteroepitaxially grown on oxide single crystals. *Thin Solid Films* **2006**, *496* (1), 104–111.

(39) Joshi, U. S.; Matsumoto, Y.; Itaka, K.; Sumiya, M.; Koinuma, H. Combinatorial synthesis of Li-doped NiO thin films and their transparent conducting properties.

Appl. Surf. Sci. **2006**, *252* (7), 2524–2528.

(40) Lau, C. H.; Zhuang, L.; Wong, K. H. In-doped transparent and conducting cubic magnesium zinc oxide thin films grown by pulsed laser deposition. *Phys. status solidi* **2007**, *244* (5), 1533–1537.

(41) Arca, E.; Fleischer, K.; Shvets, I. V. Magnesium, nitrogen codoped Cr2O3: A p-type transparent conducting oxide. *Appl. Phys. Lett.* **2011**, *99* (11), 111910.

(42) Götzendörfer, S.; Löbmann, P. Influence of single layer thickness on the performance of undoped and Mg-doped CuCrO2 thin films by sol–gel processing. *J. Sol-Gel Sci. Technol.* **2010**, *57* (2), 157–163.

(43) Wang, T.; Liu, Y.; Li, G.; Sun, Z.; Lu, J.; Liu, B.; Wu, M. Synthesis of highly-transparent Al-doped ZnO porous network thin films. *CrystEngComm* **2011**, *13* (7), 2661.

(44) Hagendorfer, H.; Lienau, K.; Nishiwaki, S.; Fella, C. M.; Kranz, L.; Uhl, A. R.; Jaeger, D.; Luo, L.; Gretener, C.; Buecheler, S.; et al. Highly transparent and conductive ZnO: Al thin films from a low temperature aqueous solution approach. *Adv. Mater.* **2014**, *26* (4), 632–636.

(45) Jun, M.-C.; Park, S.-U.; Koh, J.-H. Comparative studies of Al-doped ZnO and Ga-doped ZnO transparent conducting oxide thin films. *Nanoscale Res. Lett.* **2012**, *7* (1), 639.

(46) Williams, V. O.; DeMarco, E. J.; Katz, M. J.; Libera, J. A.; Riha, S. C.; Kim, D. W.; Avila, J. R.; Martinson, A. B. F.; Elam, J. W.; Pellin, M. J.; et al. Fabrication of transparent-conducting-oxide-coated inverse opals as mesostructured architectures for electrocatalysis applications: a case study with NiO. *ACS Appl. Mater. Interfaces* **2014**, *6* (15), 12290–12294.

(47) Kawazoe, H.; Yasukawa, M.; Hyodo, H.; Kurita, M.; Yanagi, H.; Hosono, H. P-type electrical conduction in transparent thin films of CuAlO2. **1997**, *389* (6654), 939–942.

(48) Braunstein, G.; Muraviev, a.; Saxena, H.; Dhere, N.; Richter, V.; Kalish, R. P type

doping of zinc oxide by arsenic ion implantation. *Appl. Phys. Lett.* **2005**, *87* (19), 1–3.

(49) Hitosugi, T.; Yamada, N.; Nakao, S.; Hirose, Y.; Hasegawa, T. Properties of TiO2-based transparent conducting oxides. *Phys. Status Solidi* **2010**, *207* (7), 1529–1537.

(50) Perkins, J. D.; Hest, M. f. a. m.; Teplin, C. W.; Alleman, J. L.; Dabney, M. S.; Gedvilas, L. M.; Keyes, B. M.; To, B.; Ginley, D. S.; Taylor, M. P.; et al. Amorphous Transparent Conducting Oxides (TCOS) Deposited at T ⩽ 100 oC. In *2006 IEEE 4th World Conference on Photovoltaic Energy Conference*; IEEE, 2006; Vol. 1, pp 202–204.

(51) Mizoguchi, H.; Kamiya, T.; Matsuishi, S.; Hosono, H. A germanate transparent conductive oxide. *Nat. Commun.* **2011**, *2*, 470.

(52) Search, H.; Journals, C.; Contact, A.; Iopscience, M.; Address, I. P. Transparent conducting oxide. *System* **2005**, *35*.

(53) Chen, W.-J.; Liu, W.-L.; Hsieh, S.-H.; Hsu, Y.-G. Synthesis of ZnO:Al Transparent Conductive Thin Films Using Sol-gel Method. *Procedia Eng.* **2012**, *36*, 54–61.

(54) Gómez, H.; Maldonado, a.; Castanedo-Pérez, R.; Torres-Delgado, G.; de la L. Olvera, M. Properties of Al-doped ZnO thin films deposited by a chemical spray process. *Mater. Charact.* **2007**, *58* (8–9 SPEC. ISS.), 708–714.

(55) Chang, J. F.; Lin, W. C.; Hon, M. H. Effects of post-annealing on the structure and properties of Al-doped zinc oxide films. *Appl. Surf. Sci.* **2001**, *183* (1–2), 18–25.

(56) Oh, B. Y.; Jeong, M. C.; Kim, D. S.; Lee, W.; Myoung, J. M. Post-annealing of Al-doped ZnO films in hydrogen atmosphere. *J. Cryst. Growth* **2005**, *281* (2–4), 475–480.

(57) Sathasivam, S.; Bhachu, D. S.; Lu, Y.; Chadwick, N.; Althabaiti, S. A.; Alyoubi, A. O.; Basahel, S. N.; Carmalt, C. J.; Parkin, I. P. Tungsten Doped TiO2 with Enhanced Photocatalytic and Optoelectrical Properties via Aerosol Assisted Chemical Vapor Deposition. *Sci. Rep.* **2015**, *5*, 10952.

(58) Hammarberg, E.; Prodi-Schwab, A.; Feldmann, C. Microwave-assisted synthesis of

indium tin oxide nanocrystals in polyol media and transparent, conductive layers thereof. *Thin Solid Films* **2008**, *516* (21), 7437–7442.

(59) Luo, L.; Rossell, M. D.; Xie, D.; Erni, R.; Niederberger, M. Microwave-Assisted Nonaqueous Sol–Gel Synthesis: From Al:ZnO Nanoparticles to Transparent Conducting Films. *ACS Sustain. Chem. Eng.* **2013**, *1* (1), 152–160.

(60) Potter, D. B.; Powell, M. J.; Darr, J. A.; Parkin, I. P.; Carmalt, C. J.; Edwards, P. P.; Kafafi, Z. H.; Chrisey, D. B.; Mork, H. Transparent conducting oxide thin films of Si-doped ZnO prepared by aerosol assisted CVD. *RSC Adv.* **2017**, *7* (18), 10806–10814.

(61) Howard, D. P.; Marchand, P.; Mcca, L.; Carmalt, C. J.; Parkin, I. P.; Darr, J. A. High-Throughput Continuous Hydrothermal Synthesis of Transparent Conducting Aluminum and Gallium Co-doped Zinc Oxides. *ACS Comb. Sci.* **2017**, http://dx.doi.org/10.1021/acscombsci.6b00118.

(62) Dixon, S. C.; Scanlon, D. O.; Carmalt, C. J.; Parkin, I. P.; Lifka, H.; Gierth, R.; Ruske, M.; Moet, D.; Hessler-Wyser, A.; Ballif, C.; et al. n-Type doped transparent conducting binary oxides: an overview. *J. Mater. Chem. C* **2016**, *4* (29), 6946–6961.

(63) Scanlon, D. O.; Watson, G. W.; Hamada, N.; Hirano, H.; Kikuchi, M.; Yanagi, H.; Kamiya, T.; Hosono, H.; Zunger, A.; Perry, N. H.; et al. On the possibility of p-type SnO2. *J. Mater. Chem.* **2012**, *22* (48), 25236.

(64) Walsh, A.; Buckeridge, J.; Catlow, C. R. A.; Jackson, A. J.; Keal, T. W.; Miskufova, M.; Sherwood, P.; Shevlin, S. A.; Watkins, M. B.; Woodley, S. M.; et al. Limits to Doping of Wide Band Gap Semiconductors. *Chem. Mater.* **2013**, *25* (15), 2924–2926.

(65) Freeman, A. J.; Poeppelmeier, K. R.; Mason, T. O.; Chang, R. P. H.; Marks, T. J. Chemical and Thin-Film Strategies for New Transparent Conducting Oxides. *MRS Bull.* **2000**, *25* (8), 45–51.

(66) Hautier, G.; Miglio, A.; Waroquiers, D.; Rignanese, G.-M.; Gonze, X. How Does Chemistry Influence Electron Effective Mass in Oxides? A High-Throughput Computational Analysis. *Chem. Mater.* **2014**, *26* (19), 5447–5458.

(67) Edwards, P. P.; Porch, A.; Jones, M. O.; Morgan, D. V.; Perks, R. M.; Poeppelmeier, K. R.; Williamson, D. L.; Marshall, J. H.; W. F. Peck, J.; Rapkine, D. H. Basic materials physics of transparent conducting oxides. *Dalt. Trans.* **2004**, *90* (19), 2995.

(68) Wong, F. L.; Fung, M. K.; Tong, S. W.; Lee, C. S.; Lee, S. T. Flexible organic light-emitting device based on magnetron sputtered indium-tin-oxide on plastic substrate. *Thin Solid Films* **2004**, *466* (1–2), 225–230.

(69) Fan, J. C. C.; Goodenough, J. B. X-ray photoemission spectroscopy studies of Sn-doped indium-oxide films. *J. Appl. Phys.* **1977**, *48* (8), 3524–3531.

(70) Prewitt, C. T.; Shannon, R. D.; Rogers, D. B.; Sleight, A. W. C rare earth oxide-corundum transition and crystal chemistry of oxides having the corundum structure. *Inorg. Chem.* **1969**, *8* (9), 1985–1993.

(71) Farahamndjou, M. The study of electro-optical properties of nanocomposite ITO thin films prepared by e-beam evaporation. *Mex. J. Phys.* **2013**, No. 59, 205–207.

(72) Nadaud, N.; Lequeux, N.; Nanot, M.; Jov?, J.; Roisnel, T. Structural Studies of Tin-Doped Indium Oxide (ITO) and In4Sn3O12. *J. Solid State Chem.* **1998**, *135* (1), 140–148.

(73) Lee, J.-S.; Choi, S.-C. Solvent effect on synthesis of indium tin oxide nano-powders by a solvothermal process. *J. Eur. Ceram. Soc.* **2005**, *25* (14), 3307–3314.

(74) Nath, P.; Bunshah, R. F. Preparation of In2O3 and tin-doped In2O3 films by a novel activated reactive evaporation technique. *Thin Solid Films* **1980**, *69* (1), 63–68.

(75) Kim, S.-M.; Seo, K.-H.; Lee, J.-H.; Kim, J.-J.; Lee, H. Y.; Lee, J.-S. Preparation and sintering of nanocrystalline ITO powders with different SnO2 content. *J. Eur. Ceram. Soc.* **2006**, *26* (1–2), 73–80.

(76) Udawatte, C. P.; Yanagisawa, K.; Nasu, S. Sintering of Additive Free Hydrothermally Derived Indium Tin Oxide Powders in Air. *J. Solid State Chem.* **2000**, *154* (2), 444–450.

(77) Gupta, L.; Mansingh, A.; Srivastava, P. K. Band gap narrowing and the band

structure of tin-doped indium oxide films. *Thin Solid Films* **1989**, *176* (1), 33–44.

(78) Gheidari, A. M.; Soleimani, E. A.; Mansorhoseini, M.; Mohajerzadeh, S.; Madani, N.; Shams-Kolahi, W. Structural properties of indium tin oxide thin films prepared for application in solar cells. *Mater. Res. Bull.* **2005**, *40* (8), 1303–1307.

(79) Bae, J. W.; Kim, H. J.; Kim, J. S.; Lee, Y. H.; Lee, N. E.; Yeom, G. Y.; Ko, Y. W. Tin-doped indium oxide thin film deposited on organic substrate using oxygen ion beam assisted deposition. *Surf. Coatings Technol.* **2000**, *131* (1–3), 196–200.

(80) Tahar, R. B. H.; Ban, T.; Ohya, Y.; Takahashi, Y. Tin doped indium oxide thin films: Electrical properties. *J. Appl. Phys.* **1998**, *83* (5), 2631.

(81) Liu, Y.; Li, Y.; Zeng, H. ZnO-Based Transparent Conductive Thin Films: Doping, Performance, and Processing. *J. Nanomater.* **2013**, *2013*, 1–9.

(82) Janotti, A.; Van de Walle, C. G. Fundamentals of zinc oxide as a semiconductor. *Reports Prog. Phys.* **2009**, *72* (12), 126501.

(83) Reynolds, D. C.; Look, D. C.; Jogai, B. Optically pumped ultraviolet lasing from ZnO. *Solid State Commun.* **1996**, *99* (12), 873–875.

(84) Kamble, A. S.; Sinha, B. B.; Chung, K.; Gil, M. G.; Burungale, V.; Park, C.-J.; Kim, J. H.; Patil, P. S. Effect of hydroxide anion generating agents on growth and properties of ZnO nanorod arrays. *Electrochim. Acta* **2014**, *149*, 386–393.

(85) Selim, F. A.; Weber, M. H.; Solodovnikov, D.; Lynn, K. G. Nature of Native Defects in ZnO. *Phys. Rev. Lett.* **2007**, *99* (8), 85502.

(86) Ton-That, C.; Weston, L.; Phillips, M. R. Characteristics of point defects in the green luminescence from Zn- and O-rich ZnO. *Phys. Rev. B* **2012**, *86* (11), 115205.

(87) Zinc oxide: Perfect pair of defects. *NPG Asia Mater.* **2009**.

(88) Shi, D. *Functional thin films and functional materials : new concepts and technologies*; Springer, 2003.

(89) Horikoshi, S.; Serpone, N. *Microwaves in nanoparticle synthesis : fundamentals and*

applications; Wiley-VCH, 2013.

(90) Cushing, B. L.; Kolesnichenko, V. L.; O'Connor, C. J. Recent Advances in the Liquid-Phase Syntheses of Inorganic Nanoparticles. *Chem. Rev.* **2004**, *104* (9), 3893–3946.

(91) Han, C.-H.; Han, S.-D.; Gwak, J.; Khatkar, S. P. Synthesis of indium tin oxide (ITO) and fluorine-doped tin oxide (FTO) nano-powder by sol–gel combustion hybrid method. *Mater. Lett.* **2007**, *61* (8–9), 1701–1703.

(92) Feldmann, C. Polyol-Mediated Synthesis of Nanoscale Functional Materials. *Adv. Funct. Mater.* **2003**, *13* (2), 101–107.

(93) Hammarberg, E. Nanoscale Transparent Conductive Oxides via Microwave-assisted Polyol Synthesis, 2008.

(94) Fievet, F.; Lagier, J.; Blin, B.; Beaudoin, B.; Figlarz, M. Homogeneous and heterogeneous nucleations in the polyol process for the preparation of micron and submicron size metal particles. *Solid State Ionics* **1989**, *32–33*, 198–205.

(95) Jézéquel, D.; Guenot, J.; Jouini, N.; Fiévet, F. Submicrometer zinc oxide particles: Elaboration in polyol medium and morphological characteristics. *J. Mater. Res.* **1995**, *10* (1), 77–83.

(96) Gabriel, C.; Gabriel, S.; H. Grant, E.; H. Grant, E.; S. J. Halstead, B.; Michael P. Mingos, D. Dielectric parameters relevant to microwave dielectric heating. *Chem. Soc. Rev.* **1998**, *27* (3), 213.

(97) Palchik, O.; Kerner, R.; Gedanken, A.; Weiss, A. M.; Slifkin, M. A.; Palchik, V. Microwave-assisted polyol method for the preparation of CdSe "nanoballs." *J. Mater. Chem.* **2001**, *11* (3), 874–878.

(98) Tsuji, M.; Miyamae, N.; Hashimoto, M.; Nishio, M.; Hikino, S.; Ishigami, N.; Tanaka, I. Shape and size controlled synthesis of gold nanocrystals using oxidative etching by AuCl4− and Cl− anions in microwave-polyol process. *Colloids Surfaces A Physicochem. Eng. Asp.* **2007**, *302* (1–3), 587–598.

(99) Dong, H.; Chen, Y.-C.; Feldmann, C. Polyol synthesis of nanoparticles: status and

options regarding metals, oxides, chalcogenides, and non-metal elements. *Green Chem.* **2015**, *17* (8), 4107–4132.

(100) Haynes, W. M. *CRC handbook of chemistry and physics : a ready-reference book of chemical and physical data.*; CRC, 2012.

(101) Blasse, G.; Grabmaier, B. C. *Luminescent Materials*; Springer Berlin Heidelberg: Berlin, Heidelberg, 1994.

(102) Brinker, C. J.; Scherer, G. W. *Sol-Gel Science: The Physics and Chemistry of Sol-Gel Processing*; Academic press, inc, 1990.

(103) Niederberger, M.; Garnweitner, G. Organic reaction pathways in the nonaqueous synthesis of metal oxide nanoparticles. *Chemistry* **2006**, *12* (28), 7282–7302.

(104) Niederberger, M. Nonaqueous sol-gel routes to metal oxide nanoparticles. *Acc. Chem. Res.* **2007**, *40* (9), 793–800.

(105) Park, J.; Joo, J.; Kwon, S. G.; Jang, Y.; Hyeon, T. Synthesis of monodisperse spherical nanocrystals. *Angew. Chem. Int. Ed. Engl.* **2007**, *46* (25), 4630–4660.

(106) Fu, L.; Liu, H.; Li, C.; Wu, Y.; Rahm, E.; Holze, R.; Wu, H. Electrode materials for lithium secondary batteries prepared by sol–gel methods. *Prog. Mater. Sci.* **2005**, *50* (7), 881–928.

(107) Znaidi, L. Sol–gel-deposited ZnO thin films: A review. *Mater. Sci. Eng. B* **2010**, *174* (1–3), 18–30.

(108) Kołodziejczak-Radzimska, A.; Jesionowski, T. Zinc Oxide—From Synthesis to Application: A Review. *Materials (Basel).* **2014**, *7* (4), 2833–2881.

(109) Zhang, Y.; Cao, H.; Zhang, J.; Xia, B. Synthesis of LiNi0.6Co0.2Mn0.2O2 cathode material by a carbonate co-precipitation method and its electrochemical characterization. *Solid State Ionics* **2006**, *177* (37–38), 3303–3307.

(110) Cho, T.-H.; Shiosaki, Y.; Noguchi, H. Preparation and characterization of layered LiMn1/3Ni1/3Co1/3O2 as a cathode material by an oxalate co-precipitation method. *J. Power Sources* **2006**, *159* (2), 1322–1327.

(111) Rahaman, M. N. Ceramic processing and sintering. *Mater. Corros.* **1996**, *47* (5), 284–284.

(112) Rao, C. N. R.; Muller, A.; Cheetham, A. K. *The Chemistry of Nanomaterials: Synthesis, Properties and Applications, 2 Volumes*; 2004.

(113) Gao, Z.; Gao, Y.; Li, Y.; Li, Y. Effects of heat treatment on the microstructure of nanophase indium-tin oxide. *Nanostructured Mater.* **1999**, *11* (5), 611–616.

(114) Li, S.; Qiao, X.; Chen, J.; Wang, H.; Jia, F.; Qiu, X. Effects of temperature on indium tin oxide particles synthesized by co-precipitation. *J. Cryst. Growth* **2006**, *289* (1), 151–156.

(115) Gaikwad, A. B.; Navale, S. C.; Samuel, V.; Murugan, A. V.; Ravi, V. A co-precipitation technique to prepare BiNbO4, MgTiO3 and Mg4Ta2O9 powders. *Mater. Res. Bull.* **2006**, *41* (2), 347–353.

(116) Zawrah, M. F.; Hamaad, H.; Meky, S. Synthesis and characterization of nano MgAl2O4 spinel by the co-precipitated method. *Ceram. Int.* **2007**, *33* (6), 969–978.

(117) Kim, K. Y.; Park, S. Bin. Preparation and property control of nano-sized indium tin oxide particle. *Mater. Chem. Phys.* **2004**, *86* (1), 210–221.

(118) Gersten, B. Solvothermal Synthesis of Nanoparticles.

(119) Byrappa, K.; Adschiri, T. Hydrothermal technology for nanotechnology. *Prog. Cryst. Growth Charact. Mater.* **2007**, *53* (2), 117–166.

(120) Lee, J.-S.; Choi, S.-C. Crystallization behavior of nano-ceria powders by hydrothermal synthesis using a mixture of H2O2 and NH4OH. *Mater. Lett.* **2004**, *58* (3–4), 390–393.

(121) Piticescu, R. R.; Monty, C.; Taloi, D.; Motoc, A.; Axinte, S. Hydrothermal synthesis of zirconia nanomaterials. *J. Eur. Ceram. Soc.* **2001**, No. 21, 2057–2060.

(122) Shimada, S.; Mackenzie, K. J. D. A novel method for crystal growth of indium oxide, In2O3, from the vapour phase. *J. Cryst. Growth* **1981**, *55* (3), 453–456.

(123) Howard, D. P.; Marchand, P.; Johnson, I. D.; Carmalt, C. J.; Parkin, I. P.; Darr, J. A.; Edwards, P. P.; Porch, A.; Jones, M. O.; Morgan, D. V.; et al. Conducting Al and Ga-doped zinc oxides; rapid optimisation and scale-up. *J. Mater. Chem. A* **2016**, *4* (33), 12774–12780.

(124) Ghanizadeh, S.; Peiris, T. A. N.; Jayathilake, D. S. Y.; Hutt, D. A.; Wijayantha, K. G. U.; Southee, D. J.; Conway, P. P.; Marchand, P.; Darr, J. A.; Parkin, I. P.; et al. Dispersion and microwave processing of nano-sized ITO powder for the fabrication of transparent conductive oxides. *Ceram. Int.* **2016**, *42* (16), 18296–18302.

(125) Lee, C.; Lee, W.; Kim, H.; Kim, H. W. Influence of annealing atmosphere on the structure, resistivity and transmittance of InZnO thin films. *Ceram. Int.* **2008**, *34* (4), 1089–1092.

(126) Yim, K.; Kim, H. W.; Lee, C. Effects of annealing on structure, resistivity and transmittance of Ga doped ZnO films. *Mater. Sci. Technol.* **2007**, *23* (1), 108–112.

(127) Huang, C. J.; Shih, W. C. Influence of H2- and N2-ambient annealing of indium-tin oxide film on plastic substrate for organic light-emitting diode. *J. Electron. Mater.* **2003**, *32* (10), L9–L13.

(128) Mason, T. O.; Gonzalez, G. B.; Kammler, D. R.; Mansourian-Hadavi, N.; Ingram, B. J. Defect chemistry and physical properties of transparent conducting oxides in the CdO-In2O3-SnO2 system. *Thin Solid Films* **2002**, *411* (1), 106–114.

(129) González, G. B.; Cohen, J. B.; Hwang, J.-H.; Mason, T. O.; Hodges, J. P.; Jorgensen, J. D. Neutron diffraction study on the defect structure of indium–tin–oxide. *J. Appl. Phys.* **2001**, *89* (5), 2550–2555.

(130) Zhang, K.; Zhu, F.; Huan, C. H. A.; Wee, A. T. S. Effect of hydrogen partial pressure on optoelectronic properties of indium tin oxide thin films deposited by radio frequency magnetron sputtering method. *J. Appl. Phys.* **1999**, *86* (2).

(131) Meredith, R. *Engineers' handbook of industrial microwave heating*; 1998.

(132) Electronics | HowStuffWorks http://electronics.howstuffworks.com/cell-phone-radiation1.htm (accessed Sep 19, 2017).

(133) Gupta, M.; Wai Leong, E. W. Introduction to Microwaves. In *Microwaves and Metals*; John Wiley & Sons (Asia) Pte Ltd: Singapore, 2011; pp 1–23.

(134) Jacob, J.; Chia, L. H. L.; Boey, F. Y. C. Thermal and non-thermal interaction of microwave radiation with materials. *J. Mater. Sci.* **1995**, *30* (21), 5321–5327.

(135) Sun, J.; Wang, W.; Yue, Q. Review on Microwave-Matter Interaction Fundamentals and Efficient Microwave-Associated Heating Strategies. *Materials (Basel).* **2016**, *9* (4), 231.

(136) Saxena, V. K.; Chandr, U. Microwave Synthesis: a Physical Concept. In *Microwave Heating*; InTech, 2011.

(137) Pueschner http://www.pueschner.com/basics/phys_basics_en.php (accessed Aug 19, 2017).

(138) Oghbaei, M.; Mirzaee, O. Microwave versus conventional sintering: A review of fundamentals, advantages and applications. *J. Alloys Compd.* **2010**, *494* (1), 175–189.

(139) Hart, J. N.; Menzies, D.; Cheng, Y.-B.; Simon, G. P.; Spiccia, L. Microwave processing of TiO2 blocking layers for dye-sensitized solar cells. *J. Sol-Gel Sci. Technol.* **2006**, *40* (1), 45–54.

(140) Lidström, P.; Tierney, J.; Wathey, B.; Westman, J. Microwave assisted organic synthesis—a review. *Tetrahedron* **2001**, *57* (45), 9225–9283.

(141) Bilecka, I.; Niederberger, M. Microwave chemistry for inorganic nanomaterials synthesis. *Nanoscale* **2010**, *2* (8), 1358.

(142) Clark, D. E.; Folz, D. C.; West, J. K. Processing materials with microwave energy. *Mater. Sci. Eng. A* **2000**, *287* (2), 153–158.

(143) Stuerga, D. Microwave-Material Interactions and Dielectric Properties, Key Ingredients for Mastery of Chemical Microwave Processes. In *Microwaves in Organic Synthesis*; Wiley-VCH Verlag GmbH: Weinheim, Germany; pp 1–61.

(144) Bruce, R. W. New Frontiers in the Use of Microwave Energy: Power and Metrology.

MRS Proc. **1988**, *124*, 3.

(145) Chen, M.; Siochi, E. J.; Ward, T. C.; McGrath, J. E. Basic ideas of microwave processing of polymers. *Polym. Eng. Sci.* **1993**, *33* (17), 1092–1109.

(146) Hong, S. M.; Park, J. K.; Teeradej, N.; Lee, Y. O.; Cho, Y. K.; Park, C. H. Pretreatment of sludge with microwaves for pathogen destruction and improved anaerobic digestion performance. *Water Environ. Res.* **2006**, *78* (1), 76–83.

(147) Meredith, R. J. (Roger J. .; Institution of Electrical Engineers. *Engineers' handbook of industrial microwave heating*; Institution of Electrical Engineers, 1998.

(148) von Hippel Arthur Robert. *Dielectrics and waves*; John Wiley, New York, 1954.

(149) Rao, K. J.; B. Vaidhyanathan; M. Ganguli, A.; Ramakrishnan, P. A. Synthesis of Inorganic Solids Using Microwaves. *Chem. Mater.* **1999**, *11* (4), 882–895.

(150) Ramesh, P. D.; Brandon, D.; Schächter, L. Use of partially oxidized SiC particle bed for microwave sintering of low loss ceramics. *Mater. Sci. Eng. A* **1999**, *266* (1–2), 211–220.

(151) Vos, B.; Mosman, J.; Zhang, Y.; Poels, E.; Bliek, A. Impregnated carbon as a susceptor material for low loss oxides in dielectric heating. *J. Mater. Sci.* **2003**, *38* (1), 173–182.

(152) Horikoshi, S.; Matsubara, A.; Takayama, S.; Sato, M.; Sakai, F.; Kajitani, M.; Abe, M.; Serpone, N. Characterization of microwave effects on metal-oxide materials: Zinc oxide and titanium dioxide. *Appl. Catal. B Environ.* **2009**, *91* (1–2), 362–367.

(153) Ma, J.; Fang, M.; Li, P.; Zhu, B.; Lu, X.; Lau, N. T. Microwave-assisted catalytic combustion of diesel soot. *Appl. Catal. A Gen.* **1997**, *159* (1–2), 211–228.

(154) Jones, D. A.; Lelyveld, T. P.; Mavrofidis, S. D.; Kingman, S. W.; Miles, N. J. Microwave heating applications in environmental engineering—a review. *Resour. Conserv. Recycl.* **2002**, *34* (2), 75–90.

(155) Gupta, M.; Wai Leong Eugene, W. *Microwaves and Metals*; John Wiley & Sons (Asia) Pte Ltd: Singapore, 2007.

(156) Thostenson, E. T.; Chou, T.-W. Microwave processing: fundamentals and applications. *Compos. Part A Appl. Sci. Manuf.* **1999**, *30* (9), 1055–1071.

(157) Yarahmadi, S. Preparation and performance of nanostructured iron oxide thin films for solar hydrogen generation, Loughborough University, 2011.

(158) Manseki, K.; Sugiura, T.; Yoshida, T. Microwave synthesis of size-controllable SnO2 nanocrystals for dye-sensitized solar cells. *New J. Chem.* **2014**, *38* (2), 598.

(159) Lagashetty, A.; Havanoor, V.; Basavaraja, S.; Balaji, S. D.; Venkataraman, A. Microwave-assisted route for synthesis of nanosized metal oxides. *Sci. Technol. Adv. Mater.* **2007**, *8* (6), 484–493.

(160) Rao, C. N. R.; Müller, A.; Cheetham, A. K. *The Chemistry of Nanomaterials: Synthesis, Properties and Applications*; The Chemical of Nanomaterials, 2004.

(161) Kitchen, H. J.; Vallance, S. R.; Kennedy, J. L.; Tapia-Ruiz, N.; Carassiti, L.; Harrison, A.; Whittaker, A. G.; Drysdale, T. D.; Kingman, S. W.; Gregory, D. H. Modern microwave methods in solid-state inorganic materials chemistry: from fundamentals to manufacturing. *Chem. Rev.* **2014**, *114* (2), 1170–1206.

(162) de la Hoz, A.; Díaz-Ortiz, Á.; Moreno, A.; Jiménez, J. L.; Palacios, J. C.; Cossío, F. P.; Arrieta, A.; Vivanco, S.; Foces-Foces, C. Microwaves in organic synthesis. Thermal and non-thermal microwave effects. *Chem. Soc. Rev.* **2005**, *34* (2), 164–178.

(163) Shpil'ko, A. V.; Kirilenko, E. V.; Soltis, M. V.; Petrovskii, V. Y. Microwave absorptivity of refractory powders depending on particle size. *Powder Metall. Met. Ceram.* **2010**, *49* (5–6), 304–316.

(164) Baghbanzadeh, M.; Carbone, L.; Cozzoli, P. D.; Kappe, C. O. Microwave-Assisted Synthesis of Colloidal Inorganic Nanocrystals. *Angew. Chemie Int. Ed.* **2011**, *50* (48), 11312–11359.

(165) Jones, D. A.; Lelyveld, T. P.; Mavrofidis, S. D.; Kingman, S. W.; Miles, N. J. Microwave heating applications in environmental engineering—a review. *Resour. Conserv. Recycl.* **2002**, *34* (2), 75–90.

(166) Kappe, C. O.; Dallinger, D. The impact of microwave synthesis on drug discovery. *Nat. Rev. Drug Discov.* **2006**, *5* (1), 51–63.

(167) Hammarberg, E.; Prodi-Schwab, A.; Feldmann, C. Microwave-assisted polyol synthesis of aluminium- and indium-doped ZnO nanocrystals. *J. Colloid Interface Sci.* **2009**, *334* (1), 29–36.

(168) Bühler, G.; Thölmann, D.; Feldmann, C. One-Pot Synthesis of Highly Conductive Indium Tin Oxide Nanocrystals. *Adv. Mater.* **2007**, *19* (17), 2224–2227.

(169) Conrad, F.; Zhou, Y.; Yulikov, M.; Hametner, K.; Weyeneth, S.; Jeschke, G.; Günther, D.; Grunwaldt, J.-D.; Patzke, G. R. Microwave-Hydrothermal Synthesis of Nanostructured Zinc-Copper Gallates. *Eur. J. Inorg. Chem.* **2010**, *2010* (13), 2036–2043.

(170) Glaspell, G.; Fuoco, L.; El-Shall, M. S. Microwave synthesis of supported Au and Pd nanoparticle catalysts for CO oxidation. *J. Phys. Chem. B* **2005**, *109* (37), 17350–17355.

(171) Shojaie, A. F.; Loghmani, M. H. La3+ and Zr4+ co-doped anatase nano TiO2 by sol-microwave method. *Chem. Eng. J.* **2010**, *157* (1), 263–269.

(172) Smith, D. *Thin-Film Deposition: Principles and Practice*; 1995.

(173) Hitchman, M. L.; Jensen, K. F. *Chemical Vapor Deposition: Principles and Applications*; 1999.

(174) Stradling, R.; Klipstein, P. *Growth and Characterisation of Semiconductors*; 1990.

(175) Mat-Teridi, M. A.; Tahir, A. A.; Senthilarasu, S.; Wijayantha, K. G. U.; Sulaiman, M. Y.; Ahmad-Ludin, N.; Ibrahim, M. A.; Sopian, K. Fabrication of NiO photoelectrodes by aerosol-assisted chemical vapour deposition (AACVD). *Phys. status solidi - Rapid Res. Lett.* **2014**, *8* (12), 982–986.

(176) Jakšić, Z. Nanomembrane-based plasmonics. *J. Nanophotonics* **2011**, *5* (1), 51818.

(177) Cho, H.; Yun, Y.-H. Characterization of indium tin oxide (ITO) thin films prepared by a sol–gel spin coating process. *Ceram. Int.* **2011**, *37* (2), 615–619.

(178) Zhang, J.; Nakamura, K. Effect of annealing temperature on properties of spin coated AZO films. *Mater. Res. Innov.* **2014**, *18* (S4), S4-674-S4-676.

(179) Kurdesau, F.; Khripunov, G.; da Cunha, A. F.; Kaelin, M.; Tiwari, A. N. Comparative study of ITO layers deposited by DC and RF magnetron sputtering at room temperature. *J. Non. Cryst. Solids* **2006**, *352* (9–20), 1466–1470.

(180) Crick, C. R.; Parkin, I. P. Water droplet bouncing--a definition for superhydrophobic surfaces. *Chem. Commun. (Camb).* **2011**, *47* (44), 12059–12061.

(181) Kodas, T. T.; Hampden-Smith, M. J. *The Chemistry of Metal CVD*; 2007.

(182) McCurdy, R. J. Successful implementation methods of atmospheric CVD on a glass manufacturing line. *Thin Solid Films* **1999**, *351* (1–2), 66–72.

(183) Kodas, T. T.; Hampden-Smith, M. J. *Aerosol Processing of Materials*; 1999.

(184) Hu, Y. H.; Zhang, L. Amorphization of metal-organic framework MOF-5 at unusually low applied pressure. *Phys. Rev. B* **2010**, *81* (17), 174103.

(185) Jensen, K. F. Modeling and Analysis of Low Pressure CVD Reactors. *J. Electrochem. Soc.* **1983**, *130* (9), 1950.

(186) Potts, S. E.; Carmalt, C. J.; Blackman, C. S.; Abou-Chahine, F.; Pugh, D.; Davies, H. O. Synthesis of Zirconium Guanidinate Complexes and the Formation of Zirconium Carbonitride via Low Pressure CVD. *Organometallics* **2009**, *28* (6), 1838–1844.

(187) Mädler, L.; Kammler, H. K.; Mueller, R.; Pratsinis, S. E. Controlled synthesis of nanostructured particles by flame spray pyrolysis. *J. Aerosol Sci.* **2002**, *33* (2), 369–389.

(188) Waugh, M. R.; Hyett, G.; Parkin, I. P. Zinc Oxide Thin Films Grown by Aerosol Assisted CVD. *Chem. Vap. Depos.* **2008**, *14* (11–12), 366–372.

(189) Choy, K. Chemical vapour deposition of coatings. *Prog. Mater. Sci.* **2003**, *48* (2), 57–170.

(190) Mattox, D. M. *Handbook of Physical Vapor Deposition (PVD) Processing*; Elsevier,

2010.

(191) Joan, B. Difference Between PVD and CVD. DifferenceBetween.net. http://www.differencebetween.net/technology/industrial/difference-between-pvd-and-cvd/.

(192) Sharafutdinov, R.; Khmel, S.; Shchukin, V.; Ponomarev, M.; Baranov, E.; Volkov, A.; Semenova, O.; Fedina, L.; DOBROVOLSKY, P.; KOLESOV, B. Gas-jet electron beam plasma chemical vapor deposition method for solar cell application. *Sol. Energy Mater. Sol. Cells* **2005**, *89* (2–3), 99–111.

(193) Park, S.-M.; Ikegami, T.; Ebihara, K.; Shin, P.-K. Structure and properties of transparent conductive doped ZnO films by pulsed laser deposition. *Appl. Surf. Sci.* **2006**, *253* (3), 1522–1527.

(194) Feldmann, C.; Jungk, H.-O. Polyol-Mediated Preparation of Nanoscale Oxide Particles. *Angew. Chemie Int. Ed.* **2001**, *40* (2), 359–362.

(195) Anton Paar http://www.anton-paar.com/uk-en/products/details/microwave-reaction-system-multiwave-pro/ (accessed Aug 7, 2017).

(196) Suryanarayana, C.; Norton, M. G. *X-ray Diffraction: A Practical Approach*; 1998.

(197) Kopeliovich, D. Substech http://www.substech.com/Scanning Electron Microscope (accessed Aug 22, 2017).

(198) Han, S. S. and Y. S. *Organic Light Emitting Diode - Material, Process and Devices*; Ko, S. H., Ed.; InTech, 2011.

(199) Ginley, D. S. (David S. . *Handbook of transparent conductors*; Springer, 2010.

(200) Ummartyotin, S.; Juntaro, J.; Wu, C.; Sain, M.; Manuspiya, H. Deposition of PEDOT: PSS Nanoparticles as a Conductive Microlayer Anode in OLEDs Device by Desktop Inkjet Printer. *J. Nanomater.* **2011**, *2011*, 1–7.

(201) Volume Resistivity vs. Volume Conductivity vs. Surface Resistivity https://www.caplinq.com/blog/linqstat-volume-resistivity-vs-volume-conductivity-vs-surface-resistivity_267/ (accessed Jul 10, 2017).

(202) van der Pauw, L. J. A Method of Measuring Specific Resistivity and Hall Effect of Discs of Arbitrary Shape. In *Semiconductor Devices: Pioneering Papers*; WORLD SCIENTIFIC, 1991; pp 174–182.

(203) Nanoscience http://www.nanoscience.com/products/optical-profilometry/technology-overview/stylus-profilometry/ (accessed Jul 20, 2017).

(204) Morrison, I. D.; Ross, S. *Colloidal Dispersions: Suspensions, Emulsions, and Foams*; 2002.

(205) Kissa, E. *Dispersions: Characterization, Testing, and Measurement*; 1999.

(206) Yuan, C.; Wu, H. Bin; Xie, Y.; Lou, X. W. D. Mixed transition-metal oxides: design, synthesis, and energy-related applications. *Angew. Chem. Int. Ed. Engl.* **2014**, *53* (6), 1488–1504.

(207) Ellmer, K. Past achievements and future challenges in the development of optically transparent electrodes. *Nat. Photonics* **2012**, *6* (12), 809–817.

(208) Llordés, A.; Garcia, G.; Gazquez, J.; Milliron, D. J. Tunable near-infrared and visible-light transmittance in nanocrystal-in-glass composites. *Nature* **2013**, *500* (7462), 323–326.

(209) Hoertz, P. G.; Chen, Z.; Kent, C. A.; Meyer, T. J. Application of high surface area tin-doped indium oxide nanoparticle films as transparent conducting electrodes. *Inorg. Chem.* **2010**, *49* (18), 8179–8181.

(210) Bagheri-Mohagheghi, M.-M.; Shokooh-Saremi, M. The effect of high acceptor dopant concentration of Zn 2 on electrical, optical and structural properties of the In 2 O 3 transparent conducting thin films. *Semicond. Sci. Technol.* **2003**, *18* (2), 97–103.

(211) Ehsan, M. A.; Peiris, T. A. N.; Upul Wijayantha, K. G.; Olmstead, M. M.; Arifin, Z.; Mazhar, M.; Lo, K. M.; Mckee, V. Development of molecular precursors for deposition of indium sulphide thin film electrodes for photoelectrochemical applications. **2013**, *42*.

(212) Tahir, A. A.; Wijayantha, K. G. U.; Saremi-Yarahmadi, S.; Mazhar, M.; McKee, V. Nanostructured α-Fe 2 O 3 Thin Films for Photoelectrochemical Hydrogen Generation. *Chem. Mater.* **2009**, *21* (16), 3763–3772.

(213) Alam, M. .; Cameron, D. . Optical and electrical properties of transparent conductive ITO thin films deposited by sol–gel process. *Thin Solid Films* **2000**, *377–378*, 455–459.

(214) Valencia, H. Y.; Moreno, L. C.; Ardila, A. M. Structural, electrical and optical analysis of ITO thin films prepared by sol–gel. *Microelectronics J.* **2008**, *39* (11), 1356–1357.

(215) Predoana, L.; Preda, S.; Nicolescu, M.; Anastasescu, M.; Calderon-Moreno, J. M.; Duta, M.; Gartner, M.; Zaharescu, M. Influence of the substrate type on the microstructural, optical and electrical properties of sol–gel ITO films. *J. Sol-Gel Sci. Technol.* **2014**, *71* (2), 303–312.

(216) Brack, P.; Sagu, J. S.; Peiris, T. A. N.; McInnes, A.; Senili, M.; Wijayantha, K. G. U.; Marken, F.; Selli, E. Aerosol-Assisted CVD of Bismuth Vanadate Thin Films and Their Photoelectrochemical Properties. *Chem. Vap. Depos.* **2015**, *21* (1-2–3), 41–45.

(217) Mat-Teridi, M. Construction of photosensitised semiconductor cathodes, Loughborough University, 2012.

(218) Peiris, T. A. N.; Sagu, J. S.; Hazim Yusof, Y.; Wijayantha, K. G. U. Microwave-assisted Low Temperature Fabrication of ZnO Thin Film Electrodes for Solar Energy Harvesting. *Thin Solid Films* **2015**, *590*, 293–298.

(219) Bhatti, I. A.; Nirmal Peiris, T. A.; Smith, T. D.; Upul Wijayantha, K. G. Hierarchical ZnO nanorod electrodes: Effect of post annealing on structural and photoelectrochemical performance. *Mater. Lett.* **2013**, *93*, 333–336.

(220) Thostenson, E. T.; Chou, T.-W. Microwave processing: fundamentals and applications. *Compos. Part A Appl. Sci. Manuf.* **1999**, *30* (9), 1055–1071.

(221) Marchand, P.; Makwana, N. M.; Tighe, C. J.; Gruar, R. I.; Parkin, I. P.; Carmalt, C. J.;

Darr, J. A. High-Throughput Synthesis, Screening and Scale-Up of Optimised Conducting Indium Tin Oxides. *ACS Comb. Sci.* **2016**, *18* (2), 130–137.

(222) Gruar, R. I.; Tighe, C. J.; Darr, J. A. Scaling-up a Confined Jet Reactor for the Continuous Hydrothermal Manufacture of Nanomaterials. *Ind. Eng. Chem. Res.* **2013**, *52* (15), 5270–5281.

(223) Das, S. D. Prospects of Microwave Heating in Silicon Solar Cell Fabrication – A Review. *IOSR J. Electr. Electron. Eng.* **2013**, *6* (3), 28–38.

(224) Mittal, K. L. Adhesion Measurement of Thin Films. *Electrocompon. Sci. Technol.* **1976**, *3* (C), 21–42.

(225) Shen, X. S.; Wang, G. Z.; Hong, X.; Zhu, W. Nanospheres of silver nanoparticles: agglomeration, surface morphology control and application as SERS substrates. *Phys. Chem. Chem. Phys.* **2009**, *11* (34), 7450–7454.

(226) Faure, B.; Salazar-Alvarez, G.; Ahniyaz, A.; Villaluenga, I.; Berriozabal, G.; Miguel, Y. R. De; Bergström, L. Dispersion and surface functionalization of oxide nanoparticles for transparent photocatalytic and UV-protecting coatings and sunscreens. *Science and Technology of Advanced Materials*. Taylor & Francis January 12, 2016.

(227) Saremi-Yarahmadi, S.; Vaidhyanathan, B.; Wijayantha, K. G. U. Microwave-assisted low temperature fabrication of nanostructured α-Fe2O3 electrodes for solar-driven hydrogen generation. *Int. J. Hydrogen Energy* **2010**, *35* (19), 10155–10165.

(228) Tang, B.; Si, F.; Li, Y.; Liu, L.; Zhang, S. Preparation and characterization of Ba0.2Sr0.8La4Ti4+xO15 microwave dielectric ceramics. *J. Mater. Sci. Mater. Electron.* **2015**, *26* (5), 2719–2725.

(229) Binner, J.; Vaidhyanathan, B.; Paul, A.; Annaporani, K.; Raghupathy, B. Compositional Effects in Nanostructured Yttria Partially Stabilized Zirconia. *Int. J. Appl. Ceram. Technol.* **2011**, *8* (4), 766–782.

(230) Torgovnikov, G. *Dielectric Properties of Wood and Wood-Based Materials*; Springer Science & Business Media, 2012.

(231) McLean, T. P.; Paige, E. G. S. A theory of the effects of carrier-carrier scattering on mobility in semiconductors. *J. Phys. Chem. Solids* **1960**, *16* (3–4), 220–236.

(232) Malik, A.; Seco, A.; Fortunato, E.; Martins, R. Selective optical sensors from 0.25 to 1.1 um based on metal oxide-semiconductor heterojunctions. *Sensors Actuators, A Phys.* **1998**, *68* (1–3 pt 2), 333–337.

(233) Kim, N.-R.; Lee, J.-H.; Lee, Y.-Y.; Nam, D.-H.; Yeon, H.-W.; Lee, S.-Y.; Yang, T.-Y.; Lee, Y.-J.; Chu, A.; Nam, K. T.; et al. Enhanced conductivity of solution-processed indium tin oxide nanoparticle films by oxygen partial pressure controlled annealing. *J. Mater. Chem. C* **2013**, *1* (37), 5953.

(234) Lannoo, M.; Bourgoin, J. *Point Defects in Semiconductors I*; Springer Series in Solid-State Sciences; Springer Berlin Heidelberg: Berlin, Heidelberg, 1981; Vol. 22.

(235) Bourgoin, J.; Lannoo, M. *Point Defects in Semiconductors II*; Springer Series in Solid-State Sciences; Springer Berlin Heidelberg: Berlin, Heidelberg, 1983; Vol. 35.

(236) Stavola, M. *Identification of defects in semiconductors*; Academic Press, 1998.

(237) Pantelides, S. T. *Deep centers in semiconductors : a state-of-the-art approach*, 2nd ed.; Gordon and Breach Science Publishers: Yverdon, Switzerland ;, 1992.

(238) Van de Walle, C. G. Hydrogen as a Cause of Doping in Zinc Oxide. *Phys. Rev. Lett.* **2000**, *85* (5), 1012–1015.

(239) Janotti, A.; Van de Walle, C. G. Hydrogen multicentre bonds. *Nat. Mater.* **2007**, *6* (1), 44–47.

(240) Look, D. C. Recent advances in ZnO materials and devices. *Mater. Sci. Eng. B* **2001**, *80* (1–3), 383–387.

(241) Özgür, Ü.; Alivov, Y. I.; Liu, C.; Teke, A.; Reshchikov, M. A.; Doğan, S.; Avrutin, V.; Cho, S.-J.; Morkoç, H. A comprehensive review of ZnO materials and devices. *J. Appl. Phys.* **2005**, *98* (4), 41301.

(242) Jagadish, C.; Pearton, S. J. *Zinc oxide bulk, thin films and nanostructures : processing, properties and applications*; Elsevier, 2006.

(243) Norbert H. Nickel; Evgenii Terukov. *Zinc Oxide - A Material for Micro- and Optoelectronic Applications*; Nickel, N. H., Terukov, E., Eds.; NATO Science Series II: Mathematics, Physics and Chemistry; Springer Netherlands: Dordrecht, 2005; Vol. 194.

(244) Ogale, S. B. *Thin Films and Heterostructures for Oxide Electronics*; Multifunctional Thin Film Series; Springer-Verlag: New York, 2005.

(245) Wardle, M. G.; Goss, J. P.; Briddon, P. R. Theory of Li in ZnO: A limitation for Li-based p-type doping. *Phys. Rev. B* **2005**, *71* (15), 155205.

(246) Park, C. H.; Zhang, S. B.; Wei, S.-H. Origin of p-type doping difficulty in ZnO: The impurity perspective. *Phys. Rev. B* **2002**, *66* (7), 73202.

(247) Islam, M. N.; Ghosh, T. B.; Chopra, K. L.; Acharya, H. N. XPS and X-ray diffraction studies of aluminum-doped zinc oxide transparent conducting films. *Thin Solid Films* **1996**, *280* (1–2), 20–25.

(248) Sato, H.; Minami, T.; Takata, S. Highly transparent and conductive group IV impurity?doped ZnO thin films prepared by radio frequency magnetron sputtering. *J. Vac. Sci. Technol. A Vacuum, Surfaces, Film.* **1993**, *11* (6), 2975–2979.

(249) Wu, H.-C.; Peng, Y.-C.; Shen, T.-P. Electronic and Optical Properties of Substitutional and Interstitial Si-Doped ZnO. *Materials (Basel).* **2012**, *5* (12), 2088–2100.

(250) Thaweesaeng, N.; Supankit, S.; Techidheera, W.; Pecharapa, W. Structure Properties of As-synthesized Cu-doped ZnO Nanopowder Synthesized by Co-precipitation Method. *Energy Procedia* **2013**, *34*, 682–688.

(251) Nirmal Peiris, T. A.; Ghanizadeh, S.; Jayathilake, D. S. Y.; Hutt, D. A.; Wijayantha, K. G. U.; Conway, P. P.; Southee, D. J.; Parkin, I. P.; Marchand, P.; Darrd, J. A.; et al. Aerosol-assisted fabrication of tin-doped indium oxide ceramic thin films from nanoparticle suspensions. *J. Mater. Chem. C* **2016**, *4* (24), 5739–5746.

(252) Larson, A. C.; Von Dreele, R. B. *General Structure Analysis System (GSAS)*; 2000.

(253) Toby, B. H. EXPGUI, a graphical user interface for GSAS. *J. Appl. Cryst* **2001**, *34*, 210–213.

(254) Thermo Scientific XPS: Knowledge Base http://xpssimplified.com/periodictable.php (accessed Jun 16, 2017).

(255) Xiong, H.; Zhang, C.; Zhang, K.; Shao, X. Effects of Atomization Injection on Nanoparticle Processing in Suspension Plasma Spray. *Nanomaterials* **2016**, *6* (5), 94.

(256) Tan, T. L.; Lai, C. W.; Abd Hamid, S. B. Tunable Band Gap Energy of Mn-Doped ZnO Nanoparticles Using the Coprecipitation Technique. *J. Nanomater.* **2014**, *2014*, 1–6.

(257) Jayathilake, D. S. Y.; Peiris, T. A. N.; Sagu, J. S.; Potter, D. B.; Wijayantha, K. G. U.; Carmalt, C. J.; Southee, D. J. Microwave-Assisted Synthesis and Processing of Al-Doped, Ga-Doped, and Al, Ga Codoped ZnO for the Pursuit of Optimal Conductivity for Transparent Conducting Film Fabrication. *ACS Sustain. Chem. Eng.* **2017**, *5* (6), 4820–4829.

(258) Ebrahimifard, R.; Golobostanfard, M. R.; Abdizadeh, H. Sol–gel derived Al and Ga co-doped ZnO thin films: An optoelectronic study. *Appl. Surf. Sci.* **2014**, *290*, 252–259.

(259) Labhane, P. K.; Huse, V. R.; Patle, L. B.; Chaudhari, A. L.; Sonawane, G. H. Synthesis of Cu Doped ZnO Nanoparticles: Crystallographic, Optical, FTIR, Morphological and Photocatalytic Study. *J. Mater. Sci. Chem. Eng.* **2015**, *3* (7), 39–51.

(260) Milenova, K. I.; Nikolov, P. M.; Kasabova, N. A.; Avramova, I. A. Ozone decomposition on ZnO catalysts obtained from different precursors. *Polish J. Chem. Technol.* **2014**, *16* (4), 55–59.

(261) Suja, M.; Bashar, S. B.; Morshed, M. M.; Liu, J. Realization of Cu-Doped p-Type ZnO Thin Films by Molecular Beam Epitaxy. *ACS Appl. Mater. Interfaces* **2015**, *7* (16), 8894–8899.

(262) Kaur, G.; Mitra, A.; Yadav, K. L. Pulsed laser deposited Al-doped ZnO thin films for

optical applications. *Prog. Nat. Sci. Mater. Int.* **2015**, *25* (1), 12–21.

(263) Xiu, S.; Wei, T.; Yang, Y.; Zhang, T.; Li, J.; Song, W. Preparation of AZO nanoparticles, ceramic targets and thin films by a Co-precipitaition method. *J. Wuhan Univ. Technol. Sci. Ed.* **2015**, *30* (6), 1134–1139.

(264) Lv, J.; Li, C. Evidences of VO, VZn, and Oi defects as the green luminescence origins in ZnO. *Appl. Phys. Lett.* **2013**, *103* (23), 232114.

(265) Zhang, Z.; Look, D. C.; Schifano, R.; Johansen, K. M.; Svensson, B. G.; Brillson, L. J.; C, L. D.; Pearton S J, N. D. P. I. L. H. Y. W. and S. T.; Look D C, H. J. W. and S. J. R.; G, J. A. and V. de W. C.; et al. Process dependence of H passivation and doping in H-implanted ZnO. *J. Phys. D. Appl. Phys.* **2013**, *46* (5), 55107.

(266) Wang, Y. G.; Lau, S. P.; Lee, H. W.; Yu, S. F.; Tay, B. K.; Zhang, X. H.; Hng, H. H. Photoluminescence study of ZnO films prepared by thermal oxidation of Zn metallic films in air. *J. Appl. Phys.* **2003**, *94* (1), 354.

(267) Hussain, S.; Khan, Y.; Khranovskyy, V.; Muhammad, R.; Yakimova, R. Effect of oxygen content on the structural and optical properties of ZnO films grown by atmospheric pressure MOCVD. *Prog. Nat. Sci. Mater. Int.* **2013**, *23* (1), 44–50.

(268) Rao, T. P.; Raj, S. G.; Kumar, M. C. S. Effect of Annealing Atmosphere on Structural and Optical Properties of Nd:ZnO Thin Films. *Procedia Mater. Sci.* **2014**, *6*, 1631–1638.

(269) Zhang, Z.; Look, D. C.; Schifano, R.; Johansen, K. M.; Svensson, B. G.; Brillson, L. J. Process dependence of H passivation and doping in H-implanted ZnO. *J. Phys. D. Appl. Phys.* **2013**, *46* (5), 55107.

(270) Janotti, A.; Walle, C. G. Van De. Native point defects in ZnO. *Phys. Rev. B* **2007**, *76*, 165202-1–22.

(271) Look, D. C.; Farlow, G. C.; Reunchan, P.; Limpijumnong, S.; Zhang, S. B.; Nordlund, K. Evidence for Native-Defect Donors in n -Type ZnO. *Phys. Rev. Lett.* **2005**, *95* (22), 225502.

(272) Ogata, K.; Sakurai, K.; Fujita, S.; Fujita, S.; Matsushige, K. Effects of thermal annealing of ZnO layers grown by MBE. *J. Cryst. Growth* **2000**, *214*, 312–315.

(273) Cho, J.; Nah, J.; Oh, M.-S.; Song, J.-H.; Yoon, K.-H.; Jung, H.-J.; Choi, W.-K. Enhancement of Photoluminescence and Electrical Properties of Ga-Doped ZnO Thin Film Grown on α-Al2O3(0001) Single-Crystal Substrate by rf Magnetron Sputtering through Rapid Thermal Annealing. *Jpn. J. Appl. Phys.* **2001**, *40*, L1040–L1043.

(274) Shu-wen, X. A Study of Annealing Time Effects on the Properties of Al:ZnO. *Phys. Procedia* **2012**, *25*, 345–349.

(275) Kim, J.; Yun, J.-H.; Park, Y. C.; Anderson, W. A. Transparent and crystalline Al-doped ZnO film-embedded heterojunction Si solar cell. *Mater. Lett.* **2012**, *75*, 99–101.

(276) Nomoto, J.; Konagai, M.; Miyata, T.; Minami, T. Resistivity characteristics of transparent conducting impurity-doped ZnO films for use in oxidizing environments at high temperatures. *J. Vac. Sci. Technol. A Vacuum, Surfaces, Film.* **2010**, *28* (4), 861.

(277) Wu, R.; Zhang, W.; Zhang, H.; Song, D.; Ma, Q.; Liu, J.; Ma, X.; Zhang, L.; Zhang, L.; Song, H. Investigation of aluminum and gallium co-doped ZnO powders and their effects on the properties of targets. *Mater. Sci. Semicond. Process.* **2014**, *19*, 24–31.

(278) Wang, J.; Wang, Y.; Xie, S.; Qiao, M.; Li, H.; Fan, K. Partial hydrogenation of benzene to cyclohexene on a Ru–Zn/m-ZrO2 nanocomposite catalyst. *Appl. Catal. A Gen.* **2004**, *272* (1), 29–36.

(279) Kim, J.-P.; Lee, S.-A.; Bae, J. S.; Park, S.-K.; Choi, U.-C.; Cho, C.-R. Electric properties and surface characterization of transparent Al-doped ZnO thin films prepared by pulsed laser deposition. *Thin Solid Films* **2008**, *516* (16), 5223–5226.

(280) Prasada Rao, T.; C. Santhosh Kumar, M. Resistivity Stability of Ga Doped ZnO Thin Films with Heat Treatment in Air and Oxygen Atmospheres. *J. Cryst. Process Technol.* **2012**, *2* (2), 72–79.

(281) Chen, M.; Wang, X.; Yu, Y. H.; Pei, Z. L.; Bai, X. D.; Sun, C.; Huang, R. F.; Wen, L. S. X-ray photoelectron spectroscopy and auger electron spectroscopy studies of Al-doped ZnO films. *Appl. Surf. Sci.* **2000**, *158* (1), 134–140.

(282) Hai-Bo, F.; Shao-Yan, Y.; Pan-Feng, Z.; Hong-Yuan, W.; Xiang-Lin, L.; Chun-Mei, J.; Qin-Sheng, Z.; Yong-Hai, C.; Zhan-Guo, W. Investigation of Oxygen Vacancy and Interstitial Oxygen Defects in ZnO Films by Photoluminescence and X-Ray Photoelectron Spectroscopy. *Chinese Phys. Lett.* **2007**, *24* (7), 2108–2111.

(283) Liu, C. P.; Jeng, G. R. Properties of aluminum doped zinc oxide materials and sputtering thin films. *J. Alloys Compd.* **2009**, *468* (1), 343–349.

(284) Hasanpoor, M.; Aliofkhazraei, M.; Delavari, H. Microwave-assisted Synthesis of Zinc Oxide Nanoparticles. *Procedia Mater. Sci.* **2015**, *11*, 320–325.

(285) Meire, M.; Van Der Voort, P.; Van Driessche, I.; Lommens, P. Microwave assisted synthesis of mesoporous titania and relevant surface interactions with dye molecules. *Belgian Ceram. Soc. Annu. Meet. Abstr.* **2014**.

(286) Farzadi, A.; Solati-Hashjin, M.; Bakhshi, F.; Aminian, A. Synthesis and characterization of hydroxyapatite/β-tricalcium phosphate nanocomposites using microwave irradiation. *Ceram. Int.* **2011**, *37* (1), 65–71.

(287) Zhao, B.; Tang, L.; Wang, B.; Liu, B.; Feng, J. Optical and electrical characterization of gradient AZO thin film by magnetron sputtering. *J. Mater. Sci. Mater. Electron.* **2016**, 1–5.

(288) Mkawi, E. M.; Ibrahim, K.; Ali, M. K. M.; Farrukh, M. A.; Mohamed, A. S. The effect of dopant concentration on properties of transparent conducting Al-doped ZnO thin films for efficient Cu2ZnSnS4 thin-film solar cells prepared by electrodeposition method. *Appl. Nanosci.* **2015**, *5* (8), 993–1001.

(289) Wojnarowicz, J.; Kusnieruk, S.; Chudoba, T.; Gierlotka, S.; Lojkowski, W.; Knoff, W.; Lukasiewicz, M. I.; Witkowski, B. S.; Wolska, A.; Klepka, M. T.; et al. Paramagnetism of cobalt-doped ZnO nanoparticles obtained by microwave solvothermal synthesis. *Beilstein J. Nanotechnol.* **2015**, *6* (1), 1957–1969.

(290) Sanon, G.; Rup, R.; Mansingh, A. Growth and characterization of tin oxide films prepared by chemical vapour deposition. *Thin Solid Films* **1990**, *190* (2), 287–301.

(291) Malik, A.; Sêco, A.; Fortunato, E.; Martins, R. New UV-enhanced solar blind optical sensors based on monocrystalline zinc sulphide. *Sensors Actuators A Phys.* **1998**, *67* (1–3), 68–71.

(292) Ruske, F.; Roczen, M.; Lee, K.; Wimmer, M.; Gall, S.; Hüpkes, J.; Hrunski, D.; Rech, B. Improved electrical transport in Al-doped zinc oxide by thermal treatment. *J. Appl. Phys.* **2010**, *107* (1), 13708.

(293) Erhart, P.; Albe, K. First-principles study of migration mechanisms and diffusion of oxygen in zinc oxide. *Phys. Rev. B* **2006**, *73* (11), 115207.

(294) Kykyneshi, R. Pulsed laser deposition and thin film properties of p-type barium copper sulfur fluoride, barium copper selenium fluoride, barium copper tellurium fluoride and n-type zinc indium oxide wide band-gap semiconductors, 2007.

(295) Kuo, S.-Y.; Chen, W.-C.; Lai, F.-I.; Cheng, C.-P.; Kuo, H.-C.; Wang, S.-C.; Hsieh, W.-F. Effects of doping concentration and annealing temperature on properties of highly-oriented Al-doped ZnO films. *J. Cryst. Growth* **2006**, *287* (1), 78–84.

(296) *ZnO Nanocrystals and Allied Materials*; Rao, M. S. R., Okada, T., Eds.; Springer Series in Materials Science; Springer India: New Delhi, 2014; Vol. 180.

(297) Chen, C.-C.; Wu, H.-C. Electronic Structure and Optical Property Analysis of Al/Ga-Codoped ZnO through First-Principles Calculations. *Materials (Basel).* **2016**, *9* (3), 164.

(298) Mousavi, S. H.; Müller, T. S.; de Oliveira, P. W. The effects of the aluminium concentration on optical and electrical properties of AZO thin films as a transparent conductive layer. *J. Mater. Sci. Mater. Electron.* **2013**, *24* (9), 3338–3343.

(299) Vorobyeva, N. A.; Rumyantseva, M. N.; Vasiliev, R. B.; Kozlovskiy, V. F.; Soshnikova, Y. M.; Filatova, D. G.; Zaytsev, V. B.; Zaytseva, A. V.; Gaskov, A. M. Doping effects on electrical and optical properties of spin-coated ZnO thin films. *Vacuum* **2015**, *114*,

198–204.

(300) Hong, S.; Lee, H.; Lee, J.; Kwon, J.; Han, S.; Suh, Y. D.; Cho, H.; Shin, J.; Yeo, J.; Ko, S. H. Highly Stretchable and Transparent Metal Nanowire Heater for Wearable Electronics Applications. *Adv. Mater.* **2015**, *27* (32), 4744–4751.

(301) Lv, J.; Song, Y.; Jiang, L.; Wang, J. Bio-Inspired Strategies for Anti-Icing. *ACS Nano* **2014**, *8* (4), 3152–3169.

(302) Petrucci, G.; Caputo, D.; Nascetti, A.; Lovecchio, N.; Parisi, E.; Alameddine, S.; de Cesare, G.; Zahra, A. Thermal characterization of thin film heater for lab-on-chip application. In *2015 XVIII AISEM Annual Conference*; IEEE, 2015; pp 1–4.

(303) An, B. W.; Gwak, E.-J.; Kim, K.; Kim, Y.-C.; Jang, J.; Kim, J.-Y.; Park, J.-U. Stretchable, Transparent Electrodes as Wearable Heaters Using Nanotrough Networks of Metallic Glasses with Superior Mechanical Properties and Thermal Stability. *Nano Lett.* **2016**, *16* (1), 471–478.

(304) Park, S.-H.; Lee, S.-M.; Ko, E.-H.; Kim, T.-H.; Nah, Y.-C.; Lee, S.-J.; Lee, J. H.; Kim, H.-K. Roll-to-Roll sputtered ITO/Cu/ITO multilayer electrode for flexible, transparent thin film heaters and electrochromic applications. *Sci. Rep.* **2016**, *6*, 33868.

(305) Gupta, R.; Rao, K. D. M.; Kiruthika, S.; Kulkarni, G. U. Visibly Transparent Heaters. *ACS Appl. Mater. Interfaces* **2016**, *8* (20), 12559–12575.

(306) Jayathilake, D. S. Y.; Peiris, T. A. N.; Sagu, J. S.; Potter, D. B.; Wijayantha, K. G. U.; Carmalt, C. J.; Southee, D. J. Microwave Assisted Synthesis and Processing of Al, Ga and Al,Ga Co-doped ZnO for the Pursuit of Optimal Conductivity for Transparent Conducting Film Fabrication. *ACS Sustain. Chem. Eng.* **2017**, acssuschemeng.7b00263.

(307) Kim, J. H.; Ahn, B. Du; Kim, C. H.; Jeon, K. A.; Kang, H. S.; Lee, S. Y. Heat generation properties of Ga doped ZnO thin films prepared by rf-magnetron sputtering for transparent heaters. *Thin Solid Films* **2008**, *516* (7), 1330–1333.

(308) Grubbs, R. B. Roles of Polymer Ligands in Nanoparticle Stabilization. *Polym. Rev.* **2007**, *47* (2), 197–215.

(309) Chen, S.; Noor, N.; Parkin, I. P.; Binions, R. Temperature and thickness-dependent growth behaviour and opto-electronic properties of Ga-doped ZnO films prepared by aerosol-assisted chemical vapour deposition. *J. Mater. Chem. A* **2014**, *2* (40), 17174–17182.

(310) Husna, J.; Aliyu, M. M.; Islam, M. A.; Chelvanathan, P.; Hamzah, N. R.; Hossain, M. S.; Karim, M. R.; Amin, N. Influence of Annealing Temperature on the Properties of ZnO Thin Films Grown by Sputtering. *Energy Procedia* **2012**, *25*, 55–61.

(311) Bao, D.; Gu, H.; Kuang, A. Preparation and microstructure of ZnO thin films by SOL-GEL process. *Ferroelectrics* **1996**, *186* (1), 211–214.

(312) Isherwood, P. J. M.; Neves, N.; Bowers, J. W.; Newbatt, P.; Walls, J. M. High quality aluminium doped zinc oxide target synthesis from nanoparticulate powder and characterisation of sputtered thin films. *Thin Solid Films* **2014**, *566*, 108–114.

(313) Chang, J. F.; Hon, M. H. The effect of deposition temperature on the properties of Al-doped zinc oxide thin films. *Thin Solid Films* **2001**, *386* (1), 79–86.

(314) Liu, J.; Zhang, W.; Song, D.; Ma, Q.; Zhang, L.; Zhang, H.; Ma, X.; Song, H. Comparative study of the sintering process and thin film sputtering of AZO, GZO and AGZO ceramics targets. *Ceram. Int.* **2014**, *40* (8), 12905–12915.

(315) Banerjee, P.; Lee, W.-J.; Bae, K.-R.; Lee, S. B.; Rubloff, G. W. Structural, electrical, and optical properties of atomic layer deposition Al-doped ZnO films. *J. Appl. Phys.* **2010**, *108* (4), 43504.

(316) Lu, J. G.; Fujita, S.; Kawaharamura, T.; Nishinaka, H.; Kamada, Y.; Ohshima, T.; Ye, Z. Z.; Zeng, Y. J.; Zhang, Y. Z.; Zhu, L. P.; et al. Carrier concentration dependence of band gap shift in n-type ZnO:Al films. *J. Appl. Phys.* **2007**, *101* (8), 83705.

Chapter 10

Appendix

10.1 Conference presentations

1. T. A. Nirmal Peiris, **Subhashi Jayathilake**, Hussain Alessa and Upul Wijayantha, Transition to Renewable Energy Systems; Efficient Flexible Solar Cells, Chemistry Research Day 2014, Loughborough University, 21 May 2014.

2. T. A. Nirmal Peiris, **Subhashi Jayathilake**, Hussain Alessa and Upul Wijayantha, Transition to Renewable Energy Systems; Efficient Flexible Solar Cells, Science Matters 2014, Loughborough University, 22 May 2014.

3. T. A. Nirmal Peiris, **Subhashi Jayathilake**, Hussain Alessa, Jorge García-Cañadas and Upul Wijayantha, Electrochemical Analysis of the Effect of Electrodeposited Mg(OH)2; Efficient Solar Cells, Great Western Electrochemistry Meeting, University of Bath, 2 June 2014.

4. T. A. Nirmal Peiris, **Subhashi Jayathilake**, Hussain Alessa, Jagdeep S Sagu, Jorge García-Cañadas and Upul Wijayantha, Flexible High Efficiency Dye-sensitised and Perovskite based Solar Cells, Regional Postgraduate Symposium: Great Western Photoelectrochemistry Meeting, University of Bath, 9 June 2014.

5. T. A. Nirmal Peiris, **Subhashi Jayathilake**, Hussain Alessa and Upul Wijayantha, Transition to Renewable Energy Systems; Efficient Solar Cells, Research That Matters: Research Challenges in Focus, Loughborough University, 18 June 2014.

6. T. A. Nirmal Peiris, **Subhashi Jayathilake**, Upul Wijayantha and Jorge García-Cañadas, The effect of electrodeposited Mg(OH)2 layer on flexible and glass based solar cells, Electrochem 2014, Loughborough University, 7-9 September 2014.

7. **Subhashi Jayathilake**, Hussain Alessa, T.A. Nirmal Peiris and Upul Wijayantha, Perovskite solar cells, RSC Early Career Symposium, Rolls-Royce Learning & Career Development Centre Derby, 06 February 2015.

8. **Subhashi Jayathilake**, Hussain Alessa, T.A. Nirmal Peiris and Upul Wijayantha, Harnessing solar energy to electricity; Perovskite solar cells, Science Matters 2015, Loughborough University, 04 June 2015.

9. **Subhashi Jayathilake**, Hussain Alessa, T.A. Nirmal Peiris and Upul Wijayantha, Harnessing solar energy to electricity; Perovskite solar cells, Summer Showcase 2015, Loughborough University, 17 June 2015.

10. **Subhashi Jayathilake**, T.A. Nirmal Peiris and Upul Wijayantha, Transparent conducting oxides, Plasma Surfaces and Thin Films; Early career researchers meeting, Loughborough University, 17 June 2015.

11. **Subhashi Jayathilake**, Hussain Alessa, T. A. Nirmal Peiris and K. G. U Wijayantha, Dual functionality of Perovskite in Perovskite solar cells, Midlands Electrochemistry Group Meeting 2015, Warwick University, 22 June 2015.

12. **Subhashi Jayathilake,** T.A. Nirmal Peiris, Upul Wijayantha, Darren Southee, Towards fabrication of novel and low cost transparent conducting oxides for electrochemical devices, Electrochem 2015, Durham University, 13-15 August 2015.

13. **Subhashi Jayathilake,** T.A. Nirmal Peiris, Upul Wijayantha, Darren Southee, Towards fabrication of novel and low cost transparent conducting oxides for electrochemical devices, RSC Early Career Symposium, Royal Society of Chemistry Burlington House London, 16 February 2016.

14. **Subhashi Jayathilake,** T.A. Nirmal Peiris, Upul Wijayantha, Darren Southee, Fabrication of novel and low cost transparent conducting oxides, Plasma Surfaces and Thin Films; Early career researchers meeting, Loughborough University, 6 April 2016.

15. **Subhashi Jayathilake,** T.A. Nirmal Peiris, Jagdeep Sagu, Upul Wijayantha, Darren Southee, Microwave assisted synthesis and processing of transparent conducting oxides, Design School Research Student Conference, Loughborough University, 13 April 2016.

16. **Subhashi Jayathilake,** T.A. Nirmal Peiris, Jagdeep Sagu, Upul Wijayantha, Darren Southee, Microwave assisted synthesis and processing of transparent conducting oxides, Midlands Electrochemistry Group Meeting 2016, Leicester University, 25 May 2016.

17. **Subhashi Jayathilake,** T.A. Nirmal Peiris, Jagdeep Sagu, Upul Wijayantha, Darren Southee, Microwave assisted synthesis and processing of transparent conducting oxides, Science matters 2016, Loughborough University, 20 June 2016.

18. **Subhashi Jayathilake**, T.A. Nirmal Peiris, Jagdeep Sagu, Upul Wijayantha, Darren Southee, Microwave assisted synthesis and processing of transparent conducting oxides, Summer Showcase 2016, Loughborough University, 22 June 2016.

19. **Subhashi Jayathilake,** T.A. Nirmal Peiris, Jagdeep Sagu, Upul Wijayantha, Darren Southee, Microwave assisted synthesis and processing of transparent conducting oxides, HOPV16, Swansea University, 28 June-1 July 2016.

10.2 Awards

1. People's choice poster award 2015, Summer Showcase 2015, Loughborough University, 17 June 2015
2. RSC travel bursary to attend RSC energy Sector early career chemists meeting 16 February 2016.
3. Supergen SuperSolar bursary to attend International conference on hybrid and organic photovoltaics (HOPV16).
4. Solar Fuels Network bursary to attend the International conference on hybrid and organic photovoltaics (HOPV16).
5. RSC energy sector travel grant to attend the International conference on hybrid and organic photovoltaics (HOPV16).

10.3 Articles Published in Scientific Journals

1. **D. S. Y. Jayathilake**, T. A. Nirmal Peiris, Jagdeep S. Sagu, Dominic B. Potter, K. G U. Wijayantha, Claire J. Carmalt, Darren J. Southee, Microwave-Assisted Synthesis and Processing of Al-Doped, Ga-Doped, and Al, Ga Codoped ZnO for the Pursuit of Optimal Conductivity for Transparent Conducting Film Fabrication, ACS Sustainable Chemistry & Engineering, 2017, 5 (6), 4820–4829.

2. T. A. Nirmal Peiris, Shaghayegh Ghanizadeh, **D. S. Y. Jayathilake**, David A. Hutt, K. G. U. Wijayantha, Paul P. Conway, Darren J. Southee, I. P. Parkin, P. Marchand, J. A. Darr, C. J. Carmalt, Aerosol-assisted fabrication of tin-doped indium oxide ceramic thin films from nanoparticle suspensions, Journal of Materials Chemistry C, 2016, 4 (24), 5739-5746.

3. Shaghayegh Ghanizadeh, T. A. Nirmal Peiris, **D. S. Y. Jayathilake**, David A. Hutt, K. G. U. Wijayantha, Darren J. Southee, Paul P. Conway, P. Marchand, J. A. Darr, I. P. Parkin, C. J. Carmalt, Ceramics International, 2016, 42 (16), 18296-18302.

4. W. M. Tilakaratne, B. S. M. S. Siriwardena, **D. S. Y. Jayathilake**, T. N. Pitakotuwage, R. P. Illeperuma, Demographic and Histopathological Differences of Oral Squamous Cell Carcinoma; Analysis of 4394 Cases from Sri Lanka, Journal of Clinical & Experimental Oncology, 2015, 4,1-7.

5. Rasika Pawiththra Illeperuma, Samadarani Siriwradena, **D. S. Y. Jayathilake**, Nilmini Pitakotuwage, Ranjith Kumarasiri, Manjula Attygala, Roshan Peiris, Aruni Tilakaratne, Wanninayake Mudiyanselage Tilakaratne, Analysis of Oral Cancer Cases of Sri Lanka for 13 Years, Oral Surgery, Oral Medicine, Oral Pathology and Oral Radiology, 2015, 119(3), 163-164.

10.4 Articles in Preparation

1. **D. S. Y. Jayathilake**, Jagdeep S. Sagu, and K. G. U. Wijayantha, Transparent Heater Based on Al, Ga Co-doped ZnO Thin Films, 2017.

2. S. Ghanizadeh, T. A. Nirmal Peiris, **D. S. Y. Jayathilake**, D. A. Hutt, K. G. U. Wijayantha, P. P. Conway, D. J. Southee, P. Marchand, J. A. Darr, I. P. Parkin, C. J. Carmalt, Preparation and microwave-assisted heating of Nb-doped TiO_2 thin films, 2017.